Year : 2020

An automated data integration framework for stochastic downscaling of coarse-resolution digital elevation models

Rasera Luiz Gustavo

UNIL | Université de Lausanne

Faculty of Geosciences and Environment
Institute of Earth Surface Dynamics

An automated data integration framework for stochastic downscaling of coarse-resolution digital elevation models

Ph.D. thesis

Presented at the
Faculty of Geosciences and Environment
Institute of Earth Surface Dynamics
of the University of Lausanne
by

Luiz Gustavo Rasera

Master of Science in Mining Engineering
Bachelor of Science in Geology
Federal University of Rio Grande do Sul

Jury

Prof. Dr. Gregoire Mariethoz, Thesis director
Prof. Dr. Stuart N. Lane, Thesis co-director
Prof. Dr. Alessandro Comunian, Expert
Prof. Dr. Julian M. Ortiz, Expert
Prof. Dr. Philippe Renard, Expert
Prof. Dr. Christian Kull, Jury president

Lausanne, 2020

IMPRIMATUR

Vu le rapport présenté par le jury d'examen, composé de

Président de la séance publique :	M. le Professeur Christian Kull
Président du colloque :	M. le Professeur Christian Kull
Directeur de thèse :	M. le Professeur Grégoire Mariéthoz
Co-directeur de thèse :	M. le Professeur Stuart Lane
Expert externe :	M. le Professeur Alessandro Comunian
Expert externe :	M. le Professeur Julian Ortiz
Expert externe :	M. le Professeur Philippe Renard

Le Doyen de la Faculté des géosciences et de l'environnement autorise l'impression de la thèse de
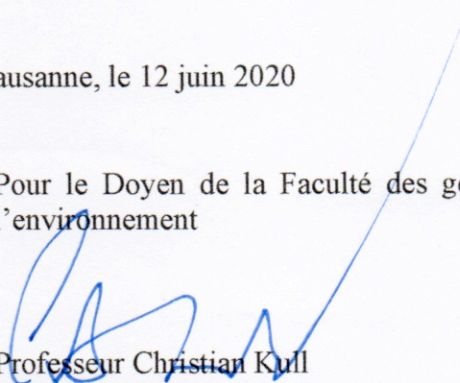
Monsieur Luiz Gustavo RASERA

Titulaire d'un
Master en ingénierie
De l'Université fédérale du Rio Grande do Sul

intitulée

An automated data integration framework for stochastic downscaling of coarse-resolution digital elevation models

Lausanne, le 12 juin 2020

Pour le Doyen de la Faculté des géosciences et de l'environnement

Professeur Christian Kull

Abstract

Spaceborne remote sensing has enabled near-global mapping of the Earth's topography. However, satellite-derived digital elevation models (DEMs) are unsuited for modeling fine-scale Earth surface processes due to their limited spatial resolution. To this day, fine-resolution DEMs remain sparsely distributed across the planet owing to the technical challenges and substantial costs for producing densely sampled data sets. Over the last decade, multispectral satellite imagery (MSI) has become widely available, providing abundant fine-resolution data for monitoring the Earth's surface. Although rendering no elevation information, MSI has the potential to provide indirect fine-scale information about topography. Statistical downscaling enables prediction of attributes at scales finer than that of the input data. Multiple-point statistics (MPS) simulation is a powerful alternative for stochastic downscaling due to its ability to replicate complex spatial patterns and assess the uncertainty of the predictions. Conceptually, MPS simulation methods could be employed for downscaling of coarse-resolution DEMs by extracting spatial information from available fine-resolution DEMs and MSI of better-measured data sets. The application of MPS simulation for downscaling of DEMs is compelling, but there are many issues to be addressed. Trends in elevation pose a challenge for stochastic downscaling of mountainous terrain. MPS simulation algorithms are also notably difficult to parameterize, often requiring manual parameter calibration. As a result, the integration of disparate data sources, such as DEMs and MSI, into the downscaling becomes a daunting task.

Addressing these challenges requires the development of an automated data integration approach. In this thesis, a MPS-driven data integration framework for stochastic downscaling of coarse-resolution DEMs is developed. The approach is composed of algorithms designed for three primary tasks: the statistical downscaling of data sets with trends, the automation of the downscaling process, and the integration of secondary data into the downscaling. The first contribution of this thesis is a novel MPS-driven downscaling algorithm with inbuilt capabilities for handling data sets with trends. Terrain elevation is

modeled as a spatial signal expressed as the sum of a deterministic trend and a stochastic residual component. The approach enables accurate downscaling of coarse-resolution DEMs of either flat or steep terrain. The second contribution addresses the parametrization of the MPS-driven downscaling algorithm. An automation routine is used to infer optimal algorithm parameters by framing the parameter calibration task as an optimization problem. The framework provides an efficient alternative for automatic generation of statistically accurate fine-resolution DEMs. The third contribution builds upon the two aforementioned developments by integrating finer-resolution MSI-sourced data as secondary information into the downscaling process. Elevation and MSI data with varying spatial resolutions are integrated based on a probabilistic framework. The approach enables to enhance the structural accuracy of the fine-resolution simulated DEMs and to reduce the inherent uncertainty associated with the downscaling.

Developments in this thesis provide an efficient, low-cost alternative for fine-scale probabilistic topographic mapping based on the integration of available finer-resolution terrain and imagery data. Future research should focus on evaluating potential applications of the downscaled DEMs for the study of Earth surface processes, the planning and design of infrastructures, and the risk assessment of natural hazards.

Résumé

La télédétection spatiale a permis une cartographie quasi globale de la topographie terrestre. Cependant, les modèles numériques d'élévation (MNE) dérivés des satellites ne sont pas adaptés à la modélisation des processus de surface à petite échelle en raison de leur faible résolution spatiale. À ce jour, les MNE à haute résolution sont répartis de manière lacunaire sur la planète en raison des défis techniques et des coûts substantiels d'acquisition d'un ensemble de données à cette haute résolution. Au cours de la dernière décennie, l'imagerie satellitaire multispectrale (ISM) est devenue massivement disponible, fournissant d'abondantes données d'observation de la surface terrestre à haute résolution. Bien qu'il ne donne aucune information sur l'élévation, l'ISM a le potentiel de fournir des informations indirectes sur la topographie à haute résolution. L'interpolation statistique permet de prédire les attributs à des échelles plus fines. Les simulations statistiques multipoints (MPS) sont une alternative crédible pour l'amélioration stochastique de la résolution, en raison de sa capacité à reproduire des modèles spatiaux complexes et à évaluer l'incertitude des prévisions. Sur le plan conceptuel, les MNE basses résolution peuvent être amélioré en ajoutant à l'aide de MPS les informations présentes dans des MNE et ISM a haute résolution. L'application de MPS pour le downscaling stochastique des MNE est crédible, mais de nombreux problèmes doivent être résolus. Les trends de l'altitude posent un défi pour le downscaling stochastique du terrain montagneux. Les algorithmes de simulation MPS sont également particulièrement difficiles à paramétrer, nécessitant souvent un étalonnage manuel. Par conséquent, l'intégration de données disparates, telles que MNE et ISM, devient une tâche ardue.

Relever ces défis nécessite le développement d'une approche automatisée d'intégration des données. Dans cette thèse, un framework d'intégration de données basée sur les MPS est développé pour le downscaling stochastique des MNE basse résolution. L'approche est composée d'algorithmes conçus pour trois tâches principales: le downscaling statistique des ensembles de données avec trends, l'automatisation du processus de downscaling

et l'intégration des données secondaires dans le processus. La première contribution de cette thèse est un nouvel algorithme MPS de downscaling avec la capacité de gérer des données avec des trends. L'élévation du terrain est modélisée comme un signal spatialisé exprimé comme la somme d'un trend déterministe et d'une composante résiduelle stochastique. L'approche permet le downscaling des MNE de terrain plat aussi bien qu'escarpé. La deuxième contribution traite de l'automatisation de la paramétrisation de l'algorithme, en l'exprimant comme un problème d'optimisation. Le framework fournit une alternative efficace pour la génération automatique de MNE à haute résolution statistiquement correcte. La troisième contribution s'appuie sur les deux développements susmentionnés en intégrant des données ISM à haute résolution en tant qu'informations secondaires dans le processus de downscaling. Les données d'élévation et radiométriques avec différentes résolutions spatiales sont intégrées en utilisant une approche probabiliste. L'approche permet d'améliorer la précision structurelle des MNE simulés et de réduire l'incertitude inhérente au downscaling.

Les développements de cette thèse fournissent une alternative efficace et bon marché à l'acquisition de donnée topographique à haute résolution basée sur l'intégration de données de terrain et d'imagerie multispectraux à plus haute résolution. Les recherches futures devraient se concentrer sur l'évaluation des applications potentielles des MNE à haute résolution pour l'étude des processus de surface terrestre, la planification et la conception des infrastructures, et l'évaluation des risques naturels.

Preface

Parts of this thesis have been either previously published as original research articles or are in preparation for submission as original research articles.

Chapter 3 is composed in part by Rasera, L.G., Gravey, M., Lane, S.N. and Mariethoz, G., *Stochastic Downscaling of Images with Trends using Multiple-Point Statistics Simulation: An Application to Digital Elevation Models*, and Rasera, L.G., Gravey, M., Lane, S.N. and Mariethoz, G., *Correction to: Stochastic Downscaling of Images with Trends using Multiple-Point Statistics Simulation: An Application to Digital Elevation Models*, published by Mathematical Geosciences as original research articles.

Chapter 4 consists of an extended version of a manuscript in preparation for submission as an original research article to Mathematical Geosciences. The chapter is composed in part by Rasera, L.G., Mariethoz, G. and Lane, S.N. (2018) Data-Driven Fusion of Multi-Resolution Digital Elevation Models and Remote Sensing Imagery, presented at 19th Annual International Association for Mathematical Geosciences Conference in Olomouc, Czech Republic, as an original work.

Chapter 5 consists of an extended version of a manuscript in preparation for submission as an original research article to Earth and Space Science. The chapter is composed in part by Rasera, L.G., Mariethoz, G. and Lane, S.N. (2018) Stochastic Fusion of Multi-Resolution Digital Elevation Models and Satellite Imagery Data, presented at the American Geophysical Union 2018 Fall Meeting in Washington DC, USA, as an original work.

Contents

List of Tables

List of Figures

Chapter 1

Introduction

1.1 Problem setting and background

Terrain surface features play a fundamental role in regulating atmospheric, hydrologic, geomorphic, and ecological processes operating on, or near, the Earth's surface (Wilson, 2012). Our understanding of the physical nature and magnitude of these processes may be advanced by an accurate representation of the terrain surface. Topography, or hypsometry, is the field of geoscience and planetary science concerned with the study of the shape and features of land surfaces. Topography focuses on the measurement of land elevation relative to mean sea level, while bathymetry concentrates on the measurement of the underwater depth of lake and ocean floors. Geomorphometry is the branch of applied science concerned with the acquisition, processing, representation, and quantitative analysis of terrain elevation data (Wilson and Gallant, 2000; Li et al., 2005; Hengl and Reuter, 2008).

Spatial scaling has an important role in geomorphology and surface hydrology (Goodchild, 2011). Digital elevation models (DEMs) serve as the prime input data for many terrain modeling studies, and their spatial resolution has a direct impact on several applications in geoscience and geotechnical engineering, such as hydrological modeling (Jarihani et al., 2015), prediction of surface saturation zones (Barling et al., 1994), landscape erosion-deposition models (Schoorl et al., 2000), sediment transport (Lane et al., 1996), hillslope stability and landslide modeling (Montgomery and Dietrich, 1994; Claessens et al., 2005).

Remote sensing techniques have experienced a major technological evolution over the

past decade enabling rapid and precise acquisition of fine-resolution DEMs. Yet, fine-resolution data sets are relatively sparse and unevenly distributed across the planet. This is mostly due to the technical limitations associated with different acquisition techniques. Sensors designed to measure elevation data offer a wide range of spatial resolutions and coverage capabilities. Terrestrial light detection and ranging (LiDAR) surveys, for example, allow the acquisition of fine-resolution DEMs with centimeter- to millimeter-level precision, but only within small spatial extents and often with dead ground problems (i.e. when parts of the terrain are hidden from the observer due to topographic undulations) (Becker et al., 2009; Doria and Radke, 2012). Consequently, carrying out extensive fine-resolution surveys entails substantial costs. By contrast, satellite-mounted synthetic-aperture radar (SAR) systems are able to gather elevation measurements over large areas, often with regular repeat coverage, but with limited spatial resolution and precision (Wilson, 2012; Yamazaki et al., 2017). These limitations prevent extensive characterization of terrain properties and processes at scales finer than the spatial resolution provided by spaceborne imaging sensors. In the last decade, however, fine-resolution multispectral satellite imagery (MSI) has become widely available, providing abundant data for monitoring the Earth's surface (Gorelick et al., 2017). Although rendering no elevation information, fine-resolution MSI may provide indirect information about topographic features at scales finer than the spatial resolution of spaceborne DEMs.

Downscaling refers to an increase in the spatial resolution of remotely sensed images. Statistical downscaling, in particular, plays an important role in science and engineering because it enables prediction of spatial attributes at scales finer than that of the original input data. Being an ill-posed problem, downscaling calls for a probabilistic framework to address its inherent underdetermination (i.e. multiple fine-resolution images may correspond to the same coarse-resolution image). Geostatistical simulation techniques offer a suitable framework for downscaling owing to their excellent data conditioning capabilities, relative low computational cost, and ability to provide uncertainty estimates for the predictions. Casting downscaling as a probabilistic problem enables to propagate the impact of the small-scale uncertainty about the imaged attribute to the response of a target physical process or engineering workflow.

In the last decade, a specific branch of geostatistics, known as multiple-point statistics (MPS) simulation, emerged as a powerful alternative for downscaling due to its ability to replicate the complex low-entropy textures (i.e. textures characterized by spatial connectivity between low and high values) often found in geophysical and remote sensing images. Fine-resolution simulations of a target random field are constructed by stochastic transfer

of fine-scale spatial structures from a better-informed training data set. This framework could be potentially extended for the statistical downscaling of a coarse-resolution target DEM by importing terrain elevation data from a better-measured area mapped at multiple scales.

The application of MPS simulation for the downscaling of coarse-resolution DEMs is compelling, but there are many issues to be addressed. Large-scale variations in the amplitude of the imaged physical properties (e.g. changes in elevation of a mountainous DEM), known as trends, pose a challenge for accurate modeling of fine-scale spatial structures. Moreover, MPS simulation algorithms are notably difficult to parameterize, often requiring manual parameter tuning and laborious sensitivity analyses. This task becomes even more troublesome when one has to integrate a large number of disparate data sources with varying spatial resolution and quality (e.g. DEMs and MSI). Nonetheless, any type of additional information about the target physical property should be integrated in order to produce more accurate predictions and data-consistent models.

In this thesis, the emphasis is on challenges associated with the automatic integration of different types of remote sensing data for the downscaling of coarse-resolution DEMs. The aim of this thesis is to develop a novel framework for efficient, low-cost generation of statistically accurate fine-resolution digital terrain models from limited information data in the form of coarse-resolution DEMs and fine-resolution MSI. These challenges are tackled from a geostatistical perspective. Numerical experiments illustrated by case studies are validated using well-established and state-of-the-art spatial statistics. An analysis on the impact of the resolved sub-pixel terrain features for modeling Earth surface processes, or land surface parameters, is beyond the scope of this thesis.

Understanding the aforementioned challenges and objectives requires appreciation of the importance of fine-resolution digital terrain data to the Earth sciences. Subsection 1.1.1 provides an overview on the principal digital terrain data acquisition techniques and data products. Subsection 1.1.2 discusses the importance of fine-resolution DEMs for the study of Earth's surface processes and the risk assessment of natural hazards.

1.1.1 Digital terrain modeling

Over the past three decades, the acquisition and processing methods for gathering topographic data have evolved significantly (Wilson, 2012). Nowadays, digital elevation data

may be acquired by a wide range of techniques. Nelson et al. (2009) define three general classes of methods for data collection: i. ground survey techniques (e.g. electronic theodolites, total stations, electronic distance measurement (EDM) devices, and global positioning system (GPS) units); ii. digitization of existing hardcopy topographic maps for deriving contour lines, stream networks, and spot heights; and iii. remote sensing techniques based on airborne and spaceborne systems using either active sensing, such as LiDAR and interferometric synthetic aperture radar (InSAR), or passive optical sensing, such as photogrammetric range imaging. Bathymetric data are commonly acquired with echosounders (e.g. sonars) mounted on a vessel, or by airborne LiDAR systems.

Terrain elevation data can be clustered into four main formats: point clouds, contours/breaklines, raster- and vector-based DEMs. DEMs are probably the most common data structures used for production of digital relief maps. A DEM consists of a 2.5- or 3-dimensional numerical representation of the Earth's (or another telluric planet, moon, or asteroid) surface generated from elevation measurements. Typically, DEMs are represented either as rasters (also known as heightmaps) or as vector-based triangular irregular networks (TINs). Raster-type DEMs consist of dot matrix data structures in the form of regular grids of square pixels. By contrast, TIN DEMs represent continuous surfaces by tessellation of triangular facets. TIN data sets are often referred to as primary (or measured) DEMs, whereas raster-type products are designated as secondary (or computed) DEMs. Although TINs offer a more accurate, flexible, and compact alternative for the representation of terrain features by allowing the generation of relief models with spatially variable data density, raster-type DEMs are often preferred in various types of geographic information systems (GIS) applications due to their computational convenience.

Most data providers and publications in the scientific literature use the term DEM as a generic term for both digital surface models (DSMs) and digital terrain models (DTMs). DEMs typically provide height information without any further definition about the surface properties. DSMs represent the Earth's surface including natural and man-made objects on it, whereas DTMs represent only the bare ground surface (Li et al., 2005). DSMs are commonly used, for example, as input data for landscape visualization and environmental simulation (Lindquist et al., 2016), and wind flow modeling in urban areas (Li et al., 2019). Applications of DTMs include hydraulic modeling for flood assessment (Lamichhane and Sharma, 2018; Leitão and de Sousa, 2018), land-use studies (Tsai et al., 2018), and geological and planetary mapping (Putri et al., 2019). In general, terrain elevation measurements taken from satellites, airplanes, and unmanned aerial vehicles (UAVs) serve as input data to DSM production. Computer algorithms must be applied to convert DSMs into DTMs (Li et al.,

2005).

1.1.2 On the importance and sparsity of fine-resolution digital elevation models

Terrain elevation data on Earth are unevenly distributed in space and time. To this day, most of the Earth's terrain surface is mapped at relatively coarse spatial and temporal resolutions (Yamazaki et al., 2017). In many cases, coarse-resolution spaceborne DEMs (Wilson, 2012), such as the U.S. National Geospatial-Intelligence Agency (NGA) and NASA's Shuttle Radar Topography Mission (SRTM30) 1-arc second near-global DEM (Farr et al., 2007) and JAXA's Earth Observatory Research Center (EORC) 1-arc second global digital surface model ALOS World 3D-30m (AW3D30) (Tadono et al., 2016), comprise the only freely available data products in remote regions across the planet. Spaceborne DEMs provide essential data for the analysis of large-scale geological structures and surface processes but are unsuited for small-scale landscape representation and hydrological simulations (Zhang and Montgomery, 1994). Wechsler (2007) demonstrates that the spatial resolution of the input DEM has a significant impact on multiple hydrologic parameters. Moreover, studies in flood engineering suggest that the spatial resolution of DEMs plays a critical role in hydraulic modeling for flood warning systems (Lamichhane and Sharma, 2018) and urban flood assessment (Leitão and de Sousa, 2018).

Small-scale topography may play a fundamental role in modulating large-scale surface processes in mountainous environments. The connectivity caused by rills and gullies, for example, can affect surface water runoff and sediment flux in mountain drainage basins (Lane et al., 2017). Fine-resolution DEMs are one of the most important data sources for modeling fine-scale geomorphic processes (Hengl and Reuter, 2008). These products are typically acquired using either ground or airborne systems (Wilson, 2012). The availability of fine-resolution DEMs, coupled with geomorphometric approaches, expands the range of applications of topography-based modeling, allowing detailed characterization of drainage area, drainage patterns, and surface roughness, which is a proxy for sediment transport impedance (Cavalli et al., 2013). The spatial resolution of these products enables accurate extraction of drainage networks (McMaster, 2002), terrain derivatives (Kienzle, 2003), and topographic indexes (Vaze et al., 2010; Mukherjee et al., 2013). Fine-resolution DEMs are also important for the analysis of surface texture (Trevisani et al., 2012) and the spatial patterns of saturated areas (Hoang et al., 2018), as well as for estimating snow accumulation and melt (Sohrabi et al., 2019). The detailed mapping of topographic surfaces plays a

fundamental role in the individuation of sediment source areas (Cavalli et al., 2013), as well as for the quantitative modeling of sediment fluxes and connectivity (Brown et al., 2009; Bishop et al., 2012).

The analysis and modeling of the Earth's surface phenomena can also be biased if the processes being investigated are influenced by details smaller than the spatial resolution of the input DEM (Goodchild, 2011). Perron et al. (2008) analyzed two-dimensional Fourier spectra derived from fine-resolution DEMs and showed that the spectral properties of landscapes can deviate in many important ways from the fractal scaling (Mandelbrot, 1974) often assumed to describe topographic surfaces. The development of computer algorithms for integrating coarse- and fine-resolution terrain elevation data would offer an efficient, low-cost alternative for generating synthetic fine-resolution DEMs in remote and sparsely populated regions, where typically only coarse-scale measurements are available.

1.2 Thesis statement

To address the aforementioned challenges, an automated data integration framework for stochastic downscaling of coarse-resolution DEMs is proposed in this thesis. The proposed approach provides a framework for addressing the problems of: i. MPS-driven downscaling of two-dimensional images with trends, ii. automation of the downscaling process, and iii. integration of finer-resolution secondary data in the form of MSI into the downscaling. The thesis statement:

An automated data integration framework for stochastic downscaling of coarse-resolution DEMs which provides an efficient, low-cost alternative for fine-resolution probabilistic terrain mapping will contribute towards more accurate modeling of Earth's surface processes and risk assessment of natural hazards in sparsely-sampled regions across the planet.

The data integration approach is composed of algorithms for the statistical downscaling of data sets with trends, automation of the downscaling process, and integration of secondary information into the downscaling based on a probabilistic framework. The first contribution of this thesis is a novel MPS-driven downscaling algorithm with inbuilt capabilities for handling data sets with trends. Terrain elevation is modeled as a spatial signal expressed as the sum of a deterministic trend and a stochastic residual component. This enables accurate downscaling of coarse-resolution DEMs of either flat or steep terrain. The

second contribution addresses the automation of the downscaling algorithm. An automation routine based on simulated annealing and cross-validation techniques is used to infer optimal algorithm parameters by framing the parameter calibration task as an optimization problem. The third contribution is the development of an approach for integrating available finer-resolution MSI as secondary data to enhance the structural accuracy and reduce the inherent uncertainty associated with the downscaling. Spatial information derived from coarse- and fine-resolution DEMs and MSI is integrated based on a probability aggregation framework.

1.3 Thesis outline

Chapter 2 establishes key concepts in statistical downscaling and geostatistics, and reviews relevant literature on the application of geostatistical simulation to digital terrain modeling and remote sensing. Other important topics which form the basis of the algorithms developed in this thesis, including the geostatistical modeling of data sets with trends and the automation of MPS simulation methods, are discussed in this chapter.

Chapter 3 describes an MPS-driven algorithm for downscaling of two-dimensional digital images with trends. The method is illustrated by the downscaling of coarse-resolution DEMs from the South-Western Alps and the Jura Mountains in Switzerland. The framework introduces four novel aspects to MPS-driven downscaling: i. an inbuilt decomposition of the random variable into a trend and a residual component; ii. a multiple-scale quasi-pixel-based sequential simulation approach, iii. the application of kernel weighting techniques for computing distances between data events; and iv. a probabilistic approach for integrating coarse- and fine-resolution data based on a distance-to-probability transformation function. Simulated realizations are benchmarked against experimental results obtained from state-of-the-art two-point, multiple-point simulation, and deterministic interpolation methods.

Chapter 4 presents an automation framework for MPS-driven downscaling of coarse-resolution DEMs. The task of parameter optimization is cast as an optimization problem. The approach relies on the combination of simulated annealing and K-fold cross-validation techniques for optimizing the simulation parameters by minimization of a multiple-component objective function. Guidelines on the formulation of an objective function in the context of geomorphometry are discussed. The framework is demonstrated with an updated version of the algorithm introduced in Chapter 3. Three case studies using DEMs of the Alaska Range,

the Appalachians, and the Central Lowlands in South Australia illustrate the method.

Chapter 5 introduces an approach for integrating finer-resolution MSI to enhance the statistical downscaling of coarse-resolution DEMs. Fine-resolution MSI data are incorporated as auxiliary data for resolving sub-pixel features on a given target coarse-resolution DEM. Spatial and spectral information derived from DEMs and MSI are assimilated using probability aggregation operations. The method is demonstrated with the downscaling algorithm and the automation framework presented in Chapters 3 and 4, respectively. Case studies with DEMs and MSI of the Colorado Plateau and the San Gabriel Mountains in the Western United States illustrate the approach.

Finally, Chapter 6 contains the conclusions and recommendations. A brief summary of the previous chapters is provided. Research implications beyond the scope of this thesis are noted in this final chapter.

The three main Chapters (3 through 5) are each based upon scientific articles that have been already published (Chapter 3) or that will be submitted (Chapters 4 and 5). Each chapter has a preface that explains how it fits into the wider goals of the thesis.

Chapter 2

Fundamental concepts on downscaling and stochastic modeling

2.1 Statistical downscaling and data integration

Surface and subsurface surveys often need to estimate phenomena at scales finer than the spatial resolution provided by imaging sensors. Downscaling refers to a decrease in the pixel size of remotely sensed images (Atkinson, 2013). Conversely, upscaling refers to the coarsening of the image spatial resolution. The two approaches are often required for the integration of disparate data sets and for the calibration and validation of numerical models in various applications. Downscaling methods, in particular, play an important role in science and engineering because they enable performing predictions of spatial attributes at finer resolution than that of the original input data. The spatial predictions are often based on available fine-resolution data or prior knowledge about the small-scale variability.

Atkinson (2013) presents a comprehensive review of statistical downscaling techniques in the context of remote sensing applications. The author classifies downscaling methods in two main groups: area-to-point prediction and super-resolution mapping. Area-to-point techniques focus on the prediction of continuous properties, whereas super-resolution mapping focuses on the prediction of categorical variables. Area-to-point methods can be subdivided into regression-type approaches (Stathopoulou and Cartalis, 2009; Pouteau et al.,

2011), geostatistical estimation (Pardo-Igúzquiza et al., 2006, 2011), and geostatistical simulation (Kyriakidis and Yoo, 2005; Jha et al., 2013). Super-resolution mapping methods rely on pixel swapping algorithms (Atkinson, 2005; Thornton et al., 2006), Hopfield neural networks (Tatem, 2002; Nguyen et al., 2005), artificial neural networks and wavelets (Mertens, 2004), geostatistical simulation (Boucher and Kyriakidis, 2007; Boucher, 2009; Mariethoz et al., 2011), and Markov random fields (Kasetkasem et al., 2005; Tolpekin and Stein, 2009). In the field of computer vision, the term image super-resolution is generally associated with the increase of the spatial resolution of a given coarse image by superposing different views of the same scene.

Downscaling can be seen from an inverse problem perspective (Bertero and Boccacci, 1998), where the goal is to reconstruct an unknown fine-scale image from its corresponding known coarse-scale counterpart. From a statistical point of view, the forward problem of computing a coarse-resolution image from a given fine-resolution image is trivial as it may consists of a simple averaging process (e.g. linear, geometric, harmonic). On the other hand, downscaling a coarse-resolution image is an ill-posed problem because the upscaling of different fine-resolution images may result in the same coarse-resolution image. For that reason, any solution to downscaling calls for prior information, in the form of existing data, or as a model of sub-pixel spatial structure, in order to limit the problem underdetermination (Bertero and Boccacci, 1998; Boucher and Kyriakidis, 2007).

The prior sub-pixel structural model can assume the form of a mathematical model, such as a parametric variogram model (Goovaerts, 1997), a finer-resolution training image (Remy et al., 2009), or even a procedural algorithm linked to the parametric energy function of a Markov random field model (Kasetkasem et al., 2005), capable of generating statistically accurate scenarios, such that it allows to constrain a potentially large solution space. This model might be inferred or calibrated using textural information from available fine-scale analogs (Boucher and Kyriakidis, 2007; Boucher, 2009), or it may entirely rely on the structural information from the coarse-resolution image itself based on some sort of scale invariance assumption (Mariethoz et al., 2011). Note that the latter assumes a fractal scaling property (Mandelbrot, 1974) between coarse and fine structures, which is not valid in several applications (Gilbert, 1989; Perron et al., 2008). In some specific cases, where the extent of the spatial structures to be resolved is much larger than that of the coarse pixel (i.e. H-resolution type problem), other mechanisms based on a maximum spatial auto-correlation hypothesis (Woodcock and Strahler, 1987; Atkinson, 2005) might be applicable. Such model, however, is not flexible, and likely inappropriate for downscaling images in which the size of the patterns or objects to be resolved are finer than the spatial resolution

provided by the imaging sensor (i.e. L-resolution type problem) (Woodcock and Strahler, 1987; Atkinson, 2013).

After the prior structural model has been specified, a probabilistic framework is typically adopted as it offers the possibility to explore and model the inherent indetermination of the downscaling process. It is fundamental to realize that producing a single downscaled scenario does not reveal the uncertainty associated with its construction. In addition, the fact that direct information of the attribute of interest at the target fine scale is often non-existent, or is at best sparse, makes the task of reconstructing the unknown true fine-resolution image virtually impossible. Therefore, rather than trying to obtain the "perfect" prediction model which minimizes the per-pixel error with respect to the inaccessible true fine-resolution image, one should attempt to generate a series of possible scenarios that display the expected spatial features at the target fine scale, and analyze the variability associated with such predictions.

To this end, the problem is resolved by generating multiple synthetic fine-resolution images that are coherent with both the input coarse-resolution image and the prior fine-scale structural model. This framework enables the estimation of the conditional probability distribution of the attribute of interest, at any uninformed small-scale pixel, given the available coarse-scale data and the pre-specified structural model. This can be extended for determining the likelihood of the occurrence of specific spatial structures (i.e. a given configuration of pixel values) by computing their frequency of occurrence over the ensemble of simulated scenarios.

Nevertheless, the downscaling outputs themselves are seldom the end-goal of a study. Often, the generated fine-resolution scenarios serve as input data to another process or a more intricate chain of processes. The ensemble of simulated scenarios enables the determination of the uncertainty associated with the predictions, and the propagation of the impact of the small-scale uncertainty to the response of a target physical process or engineering simulation model (e.g. distributed runoff model, reservoir flow simulator, open-pit optimizer, wildfire propagation simulator). Ultimately, this allows the end-user to capitalize on such information and construct a probability distribution for the physical process or the engineering workflow outputs within a Monte Carlo framework.

2.1.1   Geostatistical simulation

Geostatistical simulation methods (Journel and Huijbregts, 1978; Goovaerts, 1997; Remy et al., 2009; Mariethoz and Caers, 2014) are one of the most prominent approaches for modeling spatially and temporally auto-correlated variables. These techniques are especially useful for characterizing partially known phenomena, or when the available data is imperfect or incomplete. Geostatistical methods find a wide range of applications owing to their excellent data conditioning capabilities and relative low computational cost. In the context of statistical downscaling, these techniques offer a suitable framework due to their ability to generate multiple scenarios and provide uncertainty estimates for the predictions.

A fundamental concept of geostatistics, and all of statistics and probability theory, is that of a random variable or random function. This model enables making uncertainty assessment about a partially known attribute or property. Unlike a deterministic variable, which takes only single outcome, thus leaving no room for uncertainty, a random variable may take a series of possible outcomes, each with a certain probability (Goovaerts, 1997; Remy et al., 2009). Random function models do not represent any of the natural or mechanistic processes responsible for generating the spatial and/or temporal distribution of the data. The application of such models is simply a matter of convenience for describing and making inferences about phenomena that are often sparsely sampled and not fully understood.

Another important aspect is the distinction between the concepts of estimation and simulation. In estimation, each unknown is evaluated independently of other estimates. Estimation aims at providing a minimum error variance prediction of any unsampled value. As predictions essentially consist of weighted averages of the input data, estimates tend to smooth out the original data variability. In this case, one is typically interested in performing either local or global predictions of the conditional expected value (e.g. mean) of the random variable under study. Conversely, simulation aims at characterizing the joint spatial distribution of all unknowns. This relates to making an assessment of the spatial variability and connectivity (i.e. texture) of the random variable in space and/or time.

In this thesis, the choice of a simulation framework is preferable as it enables to assess the uncertainty of the model predictions, and reproduce the data variability and spatial structure. This stems from the fact that the downscaled DEMs may serve as input data for modeling physical processes in which the texture of the terrain surface has an impact on the model outputs.

2.1.2 Downscaling with two-point statistics

Geostatistical simulation techniques can be broadly grouped into three main families of approaches: two-point, multiple-point, and object-based methods. Downscaling techniques based on two-point and multiple-point statistics are discussed in the forthcoming subsections. Object-based simulation is not specifically addressed in this thesis, as related methods are almost exclusively designed for niche-type applications, such as stochastic modeling of predefined objects (e.g. subsurface geological structures) in the presence of scarce conditioning data (Maharaja, 2008).

Two-point statistics techniques rely on parametric functions to generate simulated realizations of random fields (Kyriakidis and Yoo, 2005; Boucher and Kyriakidis, 2007; Liu and Journel, 2009). The spatial structure of the random field is characterized through covariance functions (Goovaerts, 1997), variogram models (Marcotte, 1996), or spatial entropy (Renard and Allard, 2013). In spatial modeling problems, these statistics essentially describe the probability of having a given value at a certain position as a function of a known value at another position. They allow characterization of spatial variability (i.e. roughness) and the preferential anisotropy of spatial features.

Two-point simulation methods have been used for several applications in the downscaling and integration of coarse- and fine-scale data (Journel, 1999; Kyriakidis and Yoo, 2005; Boucher and Kyriakidis, 2007; Liu and Journel, 2009; Zagayevskiy and Deutsch, 2015). In the context of terrain elevation modeling, these techniques have been employed for conflation of DEMs and spot height measurements (Kyriakidis et al., 1999), and downscaling of coarse-resolution DEMs using different kinds of auxiliary maps (Hengl et al., 2008). Nevertheless, two-point methods assume that second-order statistics suffice to describe and to model the spatial structure of the target random variable. Another aspect, often overlooked in practice, is that these methods implicitly adopt the higher-order statistics (Dimitrakopoulos et al., 2010) embedded in the simulation algorithms (Remy et al., 2009). These statistics are generally high-entropy in character, which leads to maximization of the spatial disorder beyond the input covariance function model (Journel and Deutsch, 1993).

These assumptions may not be entirely appropriate for modeling low-entropy Earth textures that display connectivity between high and low data values, such as permeability in porous media (Renard and Allard, 2013), geological structures (Strebelle, 2002), and topographic features (Rasera et al., 2020b,a). Curvilinear structures, such as drainage networks and channelized systems, are better characterized with spatial connectivity metrics.

Connectivity is often measured with multiple-point statistics and connectivity functions. Multiple-point statistics, such as multiple-point histograms (Boisvert et al., 2010) and high-order spatial cumulants (Dimitrakopoulos et al., 2010), enable the calculation of conditional probabilities by considering the joint spatial relationship between multiple data values.

2.1.3 Downscaling with multiple-point statistics

Multiple-point statistics (MPS) simulation methods (Remy et al., 2009; Mariethoz and Caers, 2014) comprise an alternative category of algorithms designed for simulating complex low-entropy Earth textures. These methods do not require the definition of an explicit random function model. Rather, the task of generating a simulated realization is formulated as a stochastic imaging problem. The structural model is typically referred to as a training image. The training image consists of either an analog or a conceptual representation of the phenomenon under study. They may be also fully computer-generated, obtained from process-based forward simulation runs (Mackey and Bridge, 1992), event-based modeling (Pyrcz et al., 2008), and unconditional object-based simulations (Maharaja, 2008). This framework enables the reproduction of more complex textures because the structural model is not limited to the descriptive capacity of a mere covariance function model, but it is instead replaced by an extensive, and potentially rich, database of spatial patterns. In terrain elevation modeling applications, the training image might be constructed from available DEMs (Tang et al., 2015; Rasera et al., 2020b,a) or landscape evolution model outputs (Coulthard, 2001; Tucker and Hancock, 2010).

Simulated realizations are produced following either a sequential simulation formalism (Strebelle, 2002) or a stochastic optimization framework (Deutsch and Cockerham, 1994). Sequential simulation-driven algorithms derive the spatial structure and statistics of the random field from the training image based on precomputed conditional probability distributions (Guardiano and Srivastava, 1993; Strebelle, 2002), or by direct sampling (Mariethoz et al., 2010). Spatial features are often simulated by resampling replicates from the training image through template matching. Conversely, optimization-driven algorithms rely on stochastic relaxation techniques and aim at minimizing an objective (or energy) function measuring the dissimilarity between the target spatial characteristics and those of a candidate realization generated using an iterative perturbation mechanism (Deutsch and Cockerham, 1994; Deutsch and Wen, 2000).

Over the past decade, MPS simulation algorithms have found application in a diverse range of downscaling problems, such as super-resolution of land cover maps derived

from satellite imagery (Boucher, 2009), downscaling based on scale-invariant multiple-point statistics (Mariethoz et al., 2011), downscaling of climate modeling simulations (Jha et al., 2013), and conditioning realizations to block-support data (Straubhaar et al., 2016). Applications relevant to the field of geomorphometry include the simulation of braided river DEM time series (Pirot et al., 2014), terrain elevation data fusion (Tang et al., 2015), and the downscaling of coarse-resolution DEMs (Rasera et al., 2020b,a).

2.1.4   Integrating fine-resolution data into the downscaling

Available fine-resolution data may be also integrated into the downscaling process. It enables generation of alternative scenarios that are consistent with both coarse-scale measurements and any additional, or previously mapped, fine-scale data. Such finer-resolution data provide valuable information about the spatial and/or temporal position of the physical property under study at the target resolution.

Additional fine-scale data can be obtained via direct surveys, archival data, or by another finer-resolution imaging technique. Such measurements may consist of either "hard" or "soft" data. Hard (or primary) data comprise direct measurements of the variable under study at the exact sample locations. Conversely, soft (or secondary) data encompass any type of indirect, and often less precise, measurement of the target variable. Disparate types of data sets are generally integrated following a probabilistic framework (Journel, 2002; Remy et al., 2009; Allard et al., 2012). Probabilities provide a unit-free, standardized, coding of information, which facilitates the task of data integration. As opposed to deterministic estimates, probabilities also include the information content of each individual data source and the uncertainty of its contribution for determining the conditional probability of a given event (Remy et al., 2009).

A classic example of fine-resolution data integration for the downscaling of remotely sensed images consists of pan-sharpening (Du et al., 2007; Thomas et al., 2008; Yokoya et al., 2017). Pan-sharpening techniques enable the creation of an artificial finer-resolution product by merging the small-scale spatial information from a fine-resolution panchromatic band (i.e. secondary data) with the spectral information content of coarser-resolution multispectral bands (i.e. primary data). Interestingly, the average scale ratio between primary and secondary data in pan-sharpening contrasts with traditional subsurface geology data integration problems (Deutsch and Wen, 2000; Liu and Journel, 2009; Straubhaar et al., 2016). In subsurface exploration, the spatial resolution of the secondary data (e.g. geophysical imagery, mining recovery, and reservoir production data) is often much coarser than

the resolution of the primary data (e.g. core samples).

Examples of fine-scale data integration in geostatistical downscaling of remote sensing imagery and topographic data include the assimilation of fine-scale GIS data, such as delineated water bodies, road networks, and previously mapped impervious surfaces, in super-resolution land cover mapping (Boucher and Kyriakidis, 2007; Boucher, 2009), multispectral image sharpening by cokriging (Pardo-Igúzquiza et al., 2006; Atkinson et al., 2008; Pardo-Igúzquiza et al., 2011), downscaling of DEMs based on auxiliary maps with regression kriging (Hengl et al., 2008), and the integration of point- and block-support data in two-point statistics simulation and estimation (Liu and Journel, 2009; Zagayevskiy and Deutsch, 2015).

2.2   Stochastic modeling in the presence of trends

Earth science data sets are often characterized by the presence of trends. Trends comprise large-scale variations, usually with relatively low temporal and/or spatial frequencies, of the physical property or attribute under study. Trends are commonly observed in various types of data, including time series and continuous signals (e.g. hydrographs, seismograms), piezometric data, geophysical and satellite imagery, and topographic data.

The most restrictive aspect of any probabilistic approach is the assumption of stationarity (Remy et al., 2009). Stationarity is a property of the random function model which enables making predictions about the outcome of a partially known variable. In its strictest sense, a stationary process is defined as a stochastic process whose unconditional joint probability distribution is invariant under any translation of the spatial and/or temporal coordinate lag vectors. This implies that the parameters associated with the stochastic process, such as its mean and variance, do not vary in space and/or time. Albeit extremely restrictive, the hypothesis of stationarity is also what allows one to scan the data set for replicates and to average them to infer the required statistics. Yet, in most cases, local information about the phenomenon under study calls for deviations from rigorous theory in order to account for the presence of trends in the data.

When dealing with trends, geostatistical methods usually model the target random variable as the sum of two components: a smoothly varying deterministic trend component, and a more rapidly varying stochastic residual component. The expected values of the random variable are modeled by a trend function. The formulation of the trend model

depends on the amount of available information and the type of problem in hand. In interpolation problems, the trend model may consists of, for example, a polynomial function of the spatial coordinates of the regionalized variable, or estimates of the random variable local expectations based on a correlated auxiliary variable. In extrapolation, however, predictions are attempted beyond the correlation range of any sample value. Naturally, such predictions are subject to a greater degree of uncertainty, thus making the functional type assumed for the trend model critical (Journel and Rossi, 1989).

In many applications, the physics underlying the studied phenomenon do not indicate that the observed data dissociate into a low-frequency trend component and a higher-frequency residual component (Journel and Rossi, 1989). This fact makes the choice of the trend model less evident. The decision to decouple the observed data into two components is most often subjective. Ultimately, such decision purely serves as a mathematical artifice to boost the accuracy and precision of the predictive model. In some cases, the choice of a particular trend model may be facilitated based on prior knowledge or indirect information about the property or phenomenon under study. In the end, one should ensure that the modeling decision does not yield biased estimates or affect the variability of the predictions.

The decomposition of the target random variable into two components can be either implicit or explicit. The ordinary kriging estimator (Journel and Huijbregts, 1978; Goovaerts, 1997), for example, performs an implicit decomposition by filtering the mean from the simple kriging estimator and imposing that the kriging weights sum to one in order to account for a locally variable expected value. Conversely, other estimators, such as kriging with a trend (Journel and Rossi, 1989; Goovaerts, 1997), and kriging with a locally varying mean (Goovaerts, 1997), rely on explicit trend function models. Although these methods enable trends in the data to be handled, they all maintain the covariance function model associated with the residual variable stationary. Such an assumption might not be suitable if the modeled physical property displays trends in the spatial and/or temporal structure of its corresponding residual component. The intrinsic random functions of order k approach (Dimitrakopoulos, 1990; Arroyo and Emery, 2015) is another alternative framework for modeling regionalized variables with trends, however it is based on random fields whose generalized increments of order k are assumed to be second-order stationary.

In the field of terrain elevation modeling, Rasera et al. (2020b,a) proposed a novel MPS-driven downscaling algorithm which includes an explicit decomposition of the terrain elevation data into a trend and a residual component at multiple scales. Both components are inferred from the input data based on spatial low-pass filtering operations. The trend

component is downscaled using a smooth deterministic interpolation, whereas the residual variable is downscaled with a sequential simulation framework. The stationary assumption for the residual component is relaxed by allowing an exhaustive search for replicates in the training image. Once the simulation process is finished, the downscaled data are restored by summing back together the trend and residual components at each scale.

2.3 Automation of multiple-point statistics simulation algorithms

One of the main issues hindering a more widespread usage of MPS simulation methods in practical applications is the difficulty associated with their parametrization. MPS algorithm parameters are often non-intuitive and cumbersome to set up. Moreover, parameters are algorithm-specific and their calibration is data dependent. In practice, extensive sensitivity analyses are generally employed (Liu, 2006; Meerschman et al., 2013). In addition, parameters must be re-calibrated if either the conditioning or training data are updated.

Nonlinear programming offers a potential framework for automatizing the calibration of MPS simulation algorithms. Dagasan et al. (2018) applied the simulated annealing algorithm (Kirkpatrick et al., 1983) to calibrate MPS simulation parameters. The approach focuses on the minimization of the dissimilarity between pattern statistics from the conditioning data and simulated realizations. The objective function employed in the study was the Jensen-Shannon divergence between multiple-point histograms (Boisvert et al., 2010) computed using the smooth histogram method (Melnikova et al., 2015). Baninajar et al. (2019) proposed the application of a stochastic optimization framework for calibrating parameters based on a sub-sampling cross-validation scheme (Hastie et al., 2009). Several gaps are randomly placed in the training image and subsequently simulated using the remaining parts of the data set as training data. The algorithm parameters are optimized using the simultaneous perturbation gradient approximation method (Spall, 1992) by minimizing the mean-squared error between the realizations and the original reference data in the gaps.

Although the two aforementioned approaches provide efficient automation routines for the determination of algorithm parameters, there are still several issues associated with both frameworks. The reliance on only the conditioning data for calibrating parameters may lead to biased pattern reproduction due to sample spacing, uneven sample density, and preferential sampling. If the sampling grid is sparse relative to the rate of spatial variation of a pattern, the reproduction of textural features finer than the sample spacing is

not explicitly taken into account in the optimization process. To enforce the reproduction of specific fine-scale structures, one must invoke external prior information in the form of a finer-resolution training image or expert knowledge.

One of the main issues with sub-sampling cross-validation techniques is that only a subset of the data is actually used for both training and validation. When dealing with non-stationary data sets, this strategy might be inappropriate as not all relevant spatial structures may be evaluated in the cross-validation process. In addition, the definition of an optimal setup for the dimensions, placement, and the number of gaps can be challenging.

2.3.1 Algorithm parameters and hyperparameters

In this thesis, the machine learning (Hastie et al., 2009) nomenclature is adopted for discerning the parameters intrinsic to the simulation algorithm from the parameters associated with the algorithm calibration or training process. The term parameter refers to a configuration variable that is internal to the simulation algorithm and whose value is calibrated from either the training data, or the conditioning data, when the latter is available. By contrast, a hyperparameter consists of a configuration variable that is external to the algorithm and whose value cannot be inferred from data.

Parameters are required by an algorithm in order to perform predictions. Fundamentally, they are an inherent part of the predictive model, and their configuration directly affects the predictive performance of the algorithm for a given data set. Algorithmic parameters are estimated from the training data, and are typically not set by the user. The development of an automatic framework for parameter calibration is a topic addressed by this thesis.

A hyperparameter is a parameter whose value is used to control the algorithm training or learning process. As a result, they must be specified before the training phase commences. Unlike algorithmic parameters, they are not inferred from data. Instead, they are often calibrated for a specific problem and serve to aid the inference of the algorithm parameters. Hyperparameters are commonly informed by the user, but they can also be estimated based on heuristics (Claesen and Moor, 2015). Hyperparameter optimization is a trending topic within the machine learning community because it is a crucial element for the development of fully automated, self-configuring algorithms and learning strategies. A detailed discussion on this topic is out of the scope of this thesis.

Chapter 3

Downscaling images with trends using multiple-point statistics simulation: An application to digital elevation models

Trends in elevation pose a challenge for stochastic downscaling of mountainous DEMs as they fundamentally violate the hypothesis of stationarity. This chapter proposes a solution for the first objective of this thesis: i. MPS-driven downscaling of two-dimensional images with trends.

In this chapter, a novel MPS downscaling algorithm with inbuilt capabilities for handling data sets with trends is proposed. The algorithm is illustrated using DEMs of two distinct mountain ranges. Terrain elevation is modeled as a spatial signal expressed as the sum of a deterministic trend and a stochastic residual component. The data decomposition enables the downscaling of steep terrains, and the MPS simulation framework offers a suitable alternative for reproduction of the low-entropy textures often present in fine-resolution DEMs.

This chapter has been published as: Rasera, L.G., Gravey, M., Lane, S.N., and Mariethoz, G. (2020). Downscaling images with trends using multiple-point statistics simulation: An application to digital elevation models. *Mathematical Geosciences*, 52(2):145–187, and

Rasera, L.G., Gravey, M., Lane, S.N., and Mariethoz, G. (2020). Correction to: Downscaling images with trends using multiple-point statistics simulation: An application to digital elevation models. *Mathematical Geosciences*, 52(2):189–189.

3.1   Introduction

Surface and subsurface investigations often need to estimate phenomena at scales finer than the spatial resolution provided by imaging sensors. Downscaling methods are commonly employed to achieve this. Atkinson (2013) provides an overview of statistical downscaling in remote sensing. From a statistical perspective, downscaling is an ill-posed problem because the upscaling of different fine-resolution images may result in the same coarse-scale image (Bertero and Boccacci, 1998; Boucher and Kyriakidis, 2007). The problem is resolved by producing multiple equiprobable synthetic fine-resolution images. This allows determination of the uncertainty associated with the sub-pixel predictions, and propagation of the impact of the fine-scale uncertainty to the response of a target transfer function. Therefore, the goal is to produce a finer resolution version of the original image, which is coherent with its low-resolution counterpart, and a given prior fine-scale structural model.

Geostatistical simulation provides a potential framework for stochastic downscaling problems. Traditional covariance-based simulation methods (Goovaerts, 1997) have been adapted for downscaling and integration of coarse- and fine-scale data (Journel, 1999; Kyriakidis and Yoo, 2005; Boucher and Kyriakidis, 2007; Liu and Journel, 2009; Zagayevskiy and Deutsch, 2015). Two-point simulation has also been applied for conflation and downscaling of terrain elevation data (Kyriakidis et al., 1999; Hengl et al., 2008). These methods assume that the second-order statistics characterized through variogram models are sufficient for describing the missing fine-scale structures. In addition, two-point statistics simulation approaches implicitly adopt the higher-order statistics embedded in the simulation algorithm (Remy et al., 2009). These higher-order statistics are often high-entropy in character, which leads to maximization of the spatial disorder beyond the input variogram model (Journel and Deutsch, 1993). Such assumptions may be inappropriate for modeling low-entropy Earth textures that depict spatial connectivity between extreme data values, such as permeability in porous media (Renard and Allard, 2013), curvilinear geological structures (Strebelle, 2002), and topographic features including surface drainage networks (Tang et al., 2015).

Multiple-point statistics (MPS) simulation (Remy et al., 2009) offers an alternative to

two-point statistics simulation for modeling low-entropy textures. It does not require the definition of an explicit random function model. Rather, the task of generating a simulated realization is formulated as a stochastic imaging problem. The structural model is commonly referred to as a training image, which consists of an analog or a conceptual representation of the studied phenomenon. The spatial structure and statistics of the random field are then extracted from the training image based on computed conditional probability distribution functions (CPDFs) (Guardiano and Srivastava, 1993; Strebelle, 2002), or by direct sampling (Mariethoz et al., 2010). Boucher (2009), Mariethoz et al. (2011), and Straubhaar et al. (2016) proposed different applications of MPS simulation for downscaling problems.

Another common characteristic of Earth science data sets is the presence of trends. Trends consist of large-scale variations, usually low spatial frequencies, of the physical property under study. In these cases, the expected values of the random variables (RVs) representing such properties are deemed unknown (Journel and Rossi, 1989). These local expectations are often modeled with a trend function (e.g. a locally varying mean) that can be a function of the spatial coordinates of the regionalized variable, or an estimate of the expected value based on a correlated auxiliary variable. The RV is thus decomposed into two components: a deterministic low-frequency trend and its associated complementary stochastic higher-frequency residual. Tang et al. (2015) used a similar approach for digital elevation data fusion based on MPS using a modified version of the simulation algorithm developed by Zhang et al. (2006).

The necessity to infuse complex fine-scale features in non-stationary coarse-resolution images requires the development of new statistical downscaling methods. In this contribution, we present a MPS simulation algorithm for downscaling coarse-resolution images with trends. The approach is inspired by the concept of image pyramids introduced by Burt and Adelson (1983) for image compression. Here, the pyramid data structure is adapted for enhancing the spatial resolution of a given target coarse-scale image. The missing fine-scale structures are imported from a multi-resolution training image, which contains structural information at several scales. The multi-resolution training image is constructed from a better-informed data set chosen based on additional prior information or expert knowledge. The spatial resolution of the target image is gradually enhanced through a series of conditional iterations of the downscaling algorithm. At each iteration, the algorithm generates features at a specific sub-pixel scale, such that the simulation of finer resolution features is conditioned to previously simulated coarser structures. This framework shares similarities with the multiple-grid approach proposed by Tran (1994). To address the presence of trends in the data set, at each scale, the input variable is decomposed into a trend and a residual

component. The trend component is downscaled with a smooth deterministic interpolation technique. The residual component is downscaled using a quasi-pixel-based sequential simulation approach. Realizations of the sub-pixel residual variable are generated by integrating coarse- and fine-scale information with a probability aggregation operator. After the simulation of each pyramid level, the trend and residual components are summed back together, and the procedure is repeated at the next scale. We illustrate the methodology with the downscaling of digital elevation models (DEMs) in two mountain ranges in Switzerland. The algorithm is benchmarked against two-point and multiple-point statistics simulation techniques, as well as a deterministic interpolation method. Results are validated by a series of statistical and structural metrics.

This chapter is organized as follows. In Section 3.2, we introduce the fundamental concepts of the methodology. The proposed downscaling algorithm is described in Section 3.3. In Section 3.4, we present the two case studies. The results are discussed in Section 3.5. Finally, in Section 3.6, we summarize the methodology and outline future work.

3.2   Stochastic downscaling

This section presents the fundamentals of the stochastic downscaling method. Subsection 3.2.1 introduces the concept of representing multi-resolution imagery data as a stochastic spatial signal. This signal can be decomposed into a deterministic low-frequency component (trend), and a stochastic higher-frequency component (residual). The term spatial frequency refers to a characteristic related to the scale of structural features on the image, which is interpreted as the inverse of structure scale. The trend component describes smooth large-scale structures on an image, whereas the residual component represents small-scale features. The downscaling of the trend and the residual components are presented in Subsection 3.2.2. Subsection 3.2.3 describes the conditional simulation of the fine-scale residual variable with the sequential simulation formalism. Subsection 3.2.4 focuses on the estimation of local conditional probabilities from distances between conditioning and training data events. Finally, the probability aggregation method for integrating coarse- and fine-scale information is discussed in Subsection 3.2.5.

3.2.1 Stochastic representation of imagery data

Let $z_V(\mathbf{u})$ be the sensor measurement of a physical property assigned to a coarse pixel V centered at the location $\mathbf{u}$ on a target coarse-resolution image denoted by z_V. In addition, let $z_v(\mathbf{u})$ be the small-scale measurement of the same property on a fine pixel v indexed on a target co-registered fine-resolution image z_v. The coarse-to-fine resolution ratio between z_V and z_v is defined as $G = \sqrt{|V|/|v|}$, where $|V|$ and $|v|$ are the areas of the coarse and fine pixels, respectively. The notation is presented in Table 3.1.

In this contribution, we make the assumption that any coarse datum $z_V(\mathbf{u}_i)$ corresponds to the linear average of the discrete set of G^2 co-registered fine-resolution pixel values $\mathbf{z}_v(\mathbf{u}_i) = [z_v(\mathbf{u}_g), g = 1, \ldots, G^2]$

$$z_V(\mathbf{u}_i) = \frac{1}{G^2} \sum_{g=1}^{G^2} z_v(\mathbf{u}_g) \qquad \forall i = 1, \ldots, N, \tag{3.1}$$

where $\mathbf{z}_v(\mathbf{u}_i)$ is referred as a patch (a square array of fine-scale pixel values) centered at the position $\mathbf{u}_i$ (Fig. 3.1), and N is the total number of pixels on z_V.
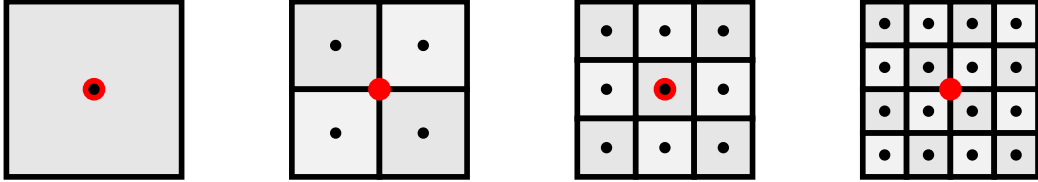
Figure 3.1: Pixels' configuration for multiple coarse-to-fine resolution ratios. *Left*: reference coarse pixel ($G = 1$). *Middle left*: co-registered patch of fine pixels ($G = 2$). *Middle right*: co-registered patch of fine pixels ($G = 3$). *Right*: co-registered patch of fine pixels ($G = 4$). Black dots indicate pixel centroids, red dots indicate patch centroids.

In geostatistics, $z_V(\mathbf{u})$ and $z_v(\mathbf{u})$ can be interpreted as realizations of the continuous RVs $Z_V(\mathbf{u})$ and $Z_v(\mathbf{u})$, respectively. The RV $Z(\mathbf{u})$ will be used to denote both $Z_V(\mathbf{u})$ and $Z_v(\mathbf{u})$ in expressions dealing with attributes at the same scale. Here, we propose to model $Z(\mathbf{u})$ as a spatial signal composed of two variables

$$Z(\mathbf{u}) = m(\mathbf{u}) + R(\mathbf{u}), \tag{3.2}$$

where $m(\mathbf{u})$ is a deterministic low-frequency signal (trend), and $R(\mathbf{u})$ is a RV representing its associated complementary stochastic higher-frequency signal (residual). It is assumed

Table 3.1: Notation.

Notation	Description
α	probability aggregation weight for fine-scale data
β	kernel weights normalizing constant
$\lambda(\mathbf{h}_j)$	kernel weight as a function of $\mathbf{h}_j$
σ	kernel shape parameter
$\phi(\cdot)$	distance-to-probability transformation function
Ψ	dual-resolution training image
Ω	conditioning data
$\boldsymbol{\theta}$	generic vector of algorithm parameters
$\boldsymbol{\Psi}$	multi-resolution training image
$\mathbf{h}_j$	coordinates offset of the j-th node from $\mathbf{u}$
$\mathbf{D}(\mathbf{u})$	local distance vector centered at $\mathbf{u}$
$\mathbf{D}_k(\mathbf{u})$	k-th element of the local distance vector
$\mathbf{R}_v(\mathbf{u})$	multivariate fine residual RV centered at $\mathbf{u}$
$\mathbf{r}_v(\mathbf{u})$	fine residual patch centered at $\mathbf{u}$
$\mathbf{u}$	data location
$\mathbf{z}_v(\mathbf{u})$	fine generic patch centered at $\mathbf{u}$
$D(\cdot)$	distance function
$d(\mathbf{u})$	data event centered at $\mathbf{u}$
$F(\cdot)$	MPS simulation algorithm
G	coarse-to-fine resolution ratio
K	number of data events for computing the local CPDF
$m(\mathbf{u})$	trend value centered at $\mathbf{u}$
m	trend image
N	number of pixels on z_V and r_V
$n(\mathbf{u})$	number of pixels in the search neighborhood centered at $\mathbf{u}$
q_k	rank of the k-th training data event
$R(\mathbf{u})$	residual RV centered at $\mathbf{u}$
$r(\mathbf{u})$	residual value centered at $\mathbf{u}$
r	residual image
(s)	superscript indicating simulated data
(t)	superscript indicating training data
V	subscript indicating coarse-scale data
v	subscript indicating fine-scale data
$Z(\mathbf{u})$	generic RV centered at $\mathbf{u}$
$z(\mathbf{u})$	generic datum value centered at $\mathbf{u}$
z	generic image
$\hat{}$	operator indicating estimated data

that $R(\mathbf{u})$ is a spatially auto-correlated RV, that is, it has some sort of spatial structure.

An estimate of $m(\mathbf{u})$ might be obtained by applying an appropriate spatial low-pass

filter on $z(\mathbf{u})$. The estimator $\hat{m}(\mathbf{u})$ is formulated as a weighted linear combination of $z(\mathbf{u})$ and its neighboring values $\{z(\mathbf{u} + \mathbf{h}_j), j = 1, \ldots, n\}$ within a moving search window

$$\hat{m}(\mathbf{u}) = \sum_{j=0}^{n} \lambda(\mathbf{h}_j)\, z(\mathbf{u} + \mathbf{h}_j) \quad \text{with} \quad \sum_{j=0}^{n} \lambda(\mathbf{h}_j) = 1, \tag{3.3}$$

where $\mathbf{h}_j$ is the set of $n+1$ coordinates lag vectors radiating from $\mathbf{u}$, with $z(\mathbf{u}) = z(\mathbf{u} + \mathbf{h}_0)$ and $n \ll N$. The weights $\lambda(\mathbf{h}_j)$ are precomputed based on a kernel and set as function of $\mathbf{h}_j$. The value of $r(\mathbf{u})$, which is interpreted as a realization of $R(\mathbf{u})$, is the complement of $\hat{m}(\mathbf{u})$.

3.2.2 Stochastic downscaling of images with trends

The goal of downscaling is to predict z_v such that the prediction is coherent with z_V and a given prior fine-scale structural model. In order to access the uncertainty of such prediction, a stochastic approach for downscaling is proposed. The objective is to estimate the unknown true value $z_v(\mathbf{u})$ by generating S realizations of $Z_v(\mathbf{u})$, denoted as $\{z_v^{(s)}(\mathbf{u}), s = 1, \ldots, S\}$, conditioned to coarse-resolution observations on z_V.

In practice, the fine-scale variables $\hat{m}_v(\mathbf{u})$ and $r_v(\mathbf{u})$ cannot be directly computed because one has no knowledge of $z_v(\mathbf{u})$. As a result, $m_v(\mathbf{u})$ has to be estimated from neighboring coarse-scale data. The sub-pixel trend estimator $\hat{m}_v(\mathbf{u})$ is thus obtained by downscaling $\hat{m}_V$ with a given deterministic interpolation method. Conversely, $R_V(\mathbf{u})$ is downscaled through stochastic simulation. A MPS simulation algorithm $F(\cdot)$ is used to generate conditional simulated realizations of $R_v(\mathbf{u})$, denoted as $r_v^{(s)}(\mathbf{u})$. This algorithm is parametrized by: a vector of parameters $\boldsymbol{\theta}$ associated with $F(\cdot)$, and a dual-resolution training image Ψ which describes the spatial relationship between the coarse and fine scales

$$R_v(\mathbf{u}|\Omega) = F(\boldsymbol{\theta}, \Psi \mid \Omega) \mapsto \{r_v^{(s)}(\mathbf{u} \mid \Omega), s = 1, \ldots, S\}, \tag{3.4}$$

where $|\Omega$ refers to the conditioning to both coarse measurements assigned on z_V and previously simulated fine-scale data on z_v.

The dual-resolution training image is constructed from a pair of co-registered coarse and fine-resolution images denoted by $z_V^{(t)}$ and $z_v^{(t)}$, respectively. It consists of an extensive multi-dimensional associative array listing all co-registered pairs of coarse and fine residual

data events present on $z_V^{(t)}$ and $z_v^{(t)}$. The residual training variables, indicated by $r_V^{(t)}(\mathbf{u})$ and $r_v^{(t)}(\mathbf{u})$, respectively, are filtered out from $z_V^{(t)}(\mathbf{u})$ and $z_v^{(t)}(\mathbf{u})$ with Equation (3.2).

The simulated sub-pixel variable $z_v^{(s)}(\mathbf{u})$ is reconstructed by rewriting Equation (3.2) as follows

$$z_v^{(s)}(\mathbf{u}) = \hat{m}_v(\mathbf{u}) + r_v^{(s)}(\mathbf{u}). \tag{3.5}$$

Figure 3.2 summarizes the methodology. Rounded white rectangles indicate the coarse-resolution target image and the training data. Processes are represented as gray rectangles and intermediate data structures are depicted as rounded gray rectangles. The downscaled image corresponds to the rounded black rectangle. The pre-processing step, indicated by the dashed rounded rectangle, encompasses all the processes and data required for the construction of the dual-resolution training image. This step is performed only once. The spatial low-pass filtering and deterministic interpolation processes are identical for both target and training images.
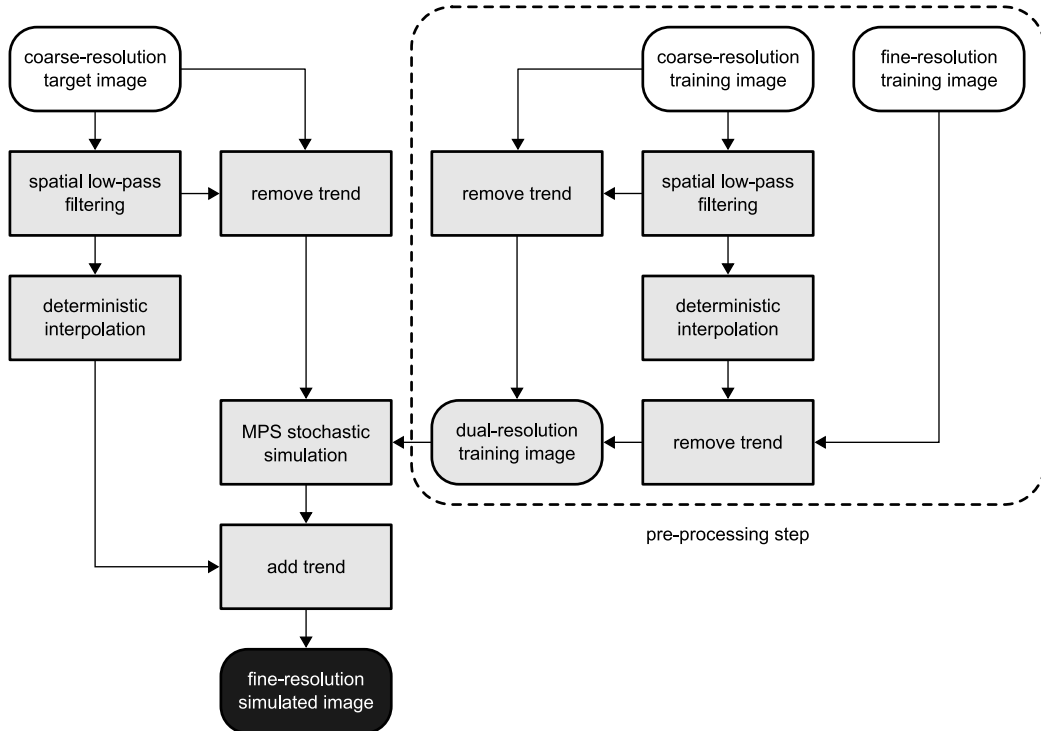
Figure 3.2: Methodology flowchart. The rounded white rectangles indicate the input images. Processes are represented as gray rectangles and intermediate data structures are depicted as rounded gray rectangles. The output downscaled image corresponds to the rounded black rectangle.

3.2.3   Downscaling with sequential simulation

Let $\mathbf{R}_v(\mathbf{u}_i) = [R_v(\mathbf{u}_g), g = 1, \ldots, G^2]$ denote the fine-resolution multivariate continuous RV co-registered with $r_V(\mathbf{u}_i)$. Hence, the fine-scale residual patch $\mathbf{r}_v(\mathbf{u}_i)$ is regarded as a joint realization of $\mathbf{R}_v(\mathbf{u}_i)$. The downscaling of $r_V(\mathbf{u}_i)$ is performed by generating a series of realizations of $\mathbf{R}_v(\mathbf{u}_i)$, denoted by $\mathbf{r}_v^{(s)}(\mathbf{u}_i)$, using sequential simulation (Goovaerts, 1997). The multivariate conditional probability $\Pr\{\mathbf{R}_v(\mathbf{u}_i) = \mathbf{r}_v \mid \Omega_{i-1}\}$ for $i = 1, \ldots, N$ is given by the recursive Bayes relation

$$
\Pr\{\mathbf{R}_v(\mathbf{u}_1) = \mathbf{r}_v, \ldots, \mathbf{R}_v(\mathbf{u}_N) = \mathbf{r}_v \mid \Omega_N\} \tag{3.6}
$$
$$
= \Pr\{\mathbf{R}_v(\mathbf{u}_1) = \mathbf{r}_v \mid \Omega_0\} \cdot \prod_{i=2}^{N-1} \Pr\{\mathbf{R}_v(\mathbf{u}_i) = \mathbf{r}_v \mid \Omega_{i-1}\},
$$

where $\mid \Omega_0$ refers to the conditioning of the first iteration of the downscaling to the initial set of coarse observations, and $\mid \Omega_{i-1}$ to the conditioning of the i-th iteration to the $i-1$ previously simulated patches of fine pixels and the initial low-resolution data. The index sequence $i = 1, \ldots, N$ defines the simulation path. The conditional probability $\Pr\{\mathbf{R}_v(\mathbf{u}_i) = \mathbf{r}_v \mid \Omega_{i-1}\}$ is approximated by the simulation algorithm $F(\cdot)$ based on Ψ.

3.2.4   Computing local conditional probabilities

Let $d_V(\mathbf{u}_i)$ denote the coarse-resolution target data event centered at the location $\mathbf{u}_i$. This data structure is comprised of the central value $r_V(\mathbf{u}_i)$ and its n_V neighboring coarse values

$$
d_V(\mathbf{u}_i) = \{r_V(\mathbf{u}_i + \mathbf{h}_j), j = 0, \ldots, n_V\}. \tag{3.7}
$$

A larger set of coordinates lag vectors is used to retrieve the co-registered fine-scale conditioning data event $d_v(\mathbf{u}_i)$

$$
d_v(\mathbf{u}_i) = \{r_v^{(s)}(\mathbf{u}_i + \mathbf{h}_j), j = 1, \ldots, n_v(\mathbf{u}_i)\}, \tag{3.8}
$$

where $r_v^{(s)}(\mathbf{u}_i + \mathbf{h}_j)$ corresponds to the current set of previously simulated fine pixels that

are collocated with $d_V(\mathbf{u}_i)$ (Fig. 3.3).
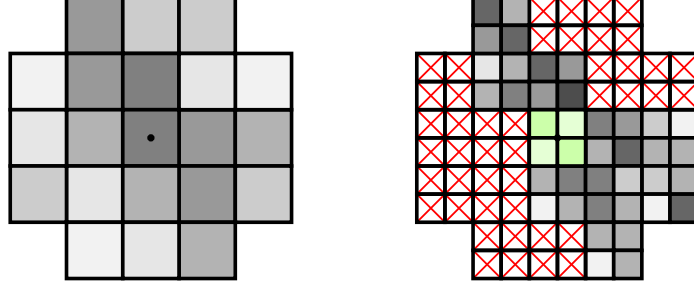
Figure 3.3: Pair of co-registered coarse- and fine-scale conditioning data events ($G = 2$). *Left*: coarse-scale data event. *Right*: incomplete fine-scale data event. Black dots indicate the data events' centroids. White pixels with red crosses denote non-informed values, green pixels indicate locations to be simulated.

Conditioning to the coarse information in $d_V(\mathbf{u}_i)$ is achieved by restricting the sampling of training data events $d_V^{(t)}(\mathbf{u})$ that minimize the coarse-scale distance function

$$D(d_V(\mathbf{u}_i), d_V^{(t)}(\mathbf{u})) = \left(\sum_{j=0}^{n_V} \lambda(\mathbf{h}_j) \left[r_V(\mathbf{u}_i + \mathbf{h}_j) - r_V^{(t)}(\mathbf{u} + \mathbf{h}_j) \right]^2 \right)^{1/2}, \qquad (3.9)$$

where $\lambda(\mathbf{h}_j)$ are the weights from a given kernel. Note that a kernel function that provides higher values for $\lambda(\mathbf{h}_0)$ ensures better conditioning of the downscaling to the local measurement $z_V(\mathbf{u}_i)$.

The reproduction of fine-scale spatial features is imposed by the minimization of the additional distance function

$$D(d_v(\mathbf{u}_i), d_v^{(t)}(\mathbf{u})) = \left(\sum_{j=1}^{n_v(\mathbf{u}_i)} \lambda(\mathbf{h}_j) \left[r_v^{(s)}(\mathbf{u}_i + \mathbf{h}_j) - r_v^{(t)}(\mathbf{u} + \mathbf{h}_j) \right]^2 \right)^{1/2}, \qquad (3.10)$$

where $d_v^{(t)}(\mathbf{u})$ corresponds to a fine-resolution training data event. Equation (3.10) ensures the sampling of compatible training data events by taking into account previously simulated fine-scale data.

In order to combine the two different sources of information given by Equations (3.9) and (3.10), both distances are converted into conditional probabilities. Most distance-based MPS simulation methods implicitly adopt a distance-to-probability transformation function.

Simulation algorithms that rely on a threshold distance value as a criterion for accepting a given training data event, for example, assume a uniform local CPDF. As proposed by Hoffimann et al. (2017), the local CPDFs can also be defined as a function of the distances between data events. In this case, the transformation function $\phi(\cdot)$ needs to be defined explicitly such that conditional probabilities can be assigned to each candidate training data event. Probabilities are made inversely proportional to the distances to a given target data event.

The transformation function $\phi(\cdot)$ also has to take into account the relative dispersion of distance values within the local pool of candidates. If all the K candidates are equally compatible with the conditioning data, the local CPDF should resemble a uniform distribution. By contrast, if only a small number of training data events is similar, the assignment of higher probabilities should be preferentially limited to this set of data events. This also applies to the opposite scenario (i.e. when several training data events are significantly dissimilar to the local conditioning data).

The coarse-scale conditional probability is thus expressed as

$$\Pr\{\mathbf{R}_v(\mathbf{u}_i) = \mathbf{r}_v^{(t)}(\mathbf{u}_k) \mid d_V(\mathbf{u}_i)\} \propto \phi(\mathbf{D}(\mathbf{u}_i)), \tag{3.11}$$

where $\mathbf{r}_v^{(t)}(\mathbf{u}_k)$ refers to the central patch of $d_v^{(t)}(\mathbf{u}_k)$, and $\mathbf{D}(\mathbf{u}_i)$ is a $(K \times 1)$ local vector that stores the distances between $d_V(\mathbf{u}_i)$ and the set of K best training data events $\{d_V^{(t)}(\mathbf{u}_k), k = 1, \ldots, K\}$ (i.e. the training data events that minimize Eq. (3.9)). Note that Equation (3.11) is also used to estimate $\Pr\{\mathbf{R}_v(\mathbf{u}_i) = \mathbf{r}_v^{(t)}(\mathbf{u}_k) \mid d_v(\mathbf{u}_i)\}$.

3.2.5   Integrating coarse- and fine-scale information

To simulate structures from the training image that are compatible with the conditioning data, we integrate the local conditional probabilities derived from coarse- and fine-scale information with the log-linear pooling operator (Allard et al., 2012). The conditional probability $\Pr\{\mathbf{R}_v(\mathbf{u}_i) = \mathbf{r}_v \mid \Omega_{i-1}\}$ in Equation (3.6) is approximated by

$$\Pr\{\mathbf{R}_v(\mathbf{u}_i) = \mathbf{r}_v \mid \Omega_{i-1}\} \approx \Pr\{\mathbf{R}_v(\mathbf{u}_i) = \mathbf{r}_v^{(t)}(\mathbf{u}) \mid d_V(\mathbf{u}_i), d_v(\mathbf{u}_i)\} \tag{3.12}$$
$$\propto \Pr\{\mathbf{R}_v(\mathbf{u}_i) = \mathbf{r}_v^{(t)}(\mathbf{u}_k) \mid d_V(\mathbf{u}_i)\}^{1-\alpha_i} \cdot \Pr\{\mathbf{R}_v(\mathbf{u}_i) = \mathbf{r}_v^{(t)}(\mathbf{u}_k) \mid d_v(\mathbf{u}_i)\}^{\alpha_i},$$

where $\alpha_i = \sum_{j=1}^{n_v(\mathbf{u}_i)} \lambda(\mathbf{h}_j)$.

The weight α_i controls the relative importance of previously simulated fine-resolution data during the aggregation process, based on the number of informed fine pixels and the kernel weights $\lambda(\mathbf{h}_j)$. The value of α_i changes throughout the simulation process. In the beginning of the simulation, conditional probabilities derived from coarse-resolution data tend to dominate the shape of the aggregated CPDFs, however as the simulation progresses and $r_v^{(s)}$ becomes more populated, the importance of fine-scale conditional probabilities gradually increases.

3.3   Algorithm

The following section aims at presenting the MPS simulation algorithm developed for downscaling. The simulation framework is later generalized as a multi-scale iterative process which allows the downscaling to handle large coarse-to-fine resolution ratios.

Algorithm 1 summarizes the downscaling of the target coarse-resolution image z_V using sequential simulation. The vector of algorithmic parameters $\boldsymbol{\theta}$ includes information related to the kernel function parameters for the spatial low-pass filters and distance functions, and the number of candidate training data events K used for computing the local CPDFs. For reproducibility, a seed is used to initialize a pseudo-random number generator which defines the order of the simulation path and the sampling of local CPDFs. Multiple conditional simulated realizations are generated by feeding the algorithm different random seeds.

Initially, the residual image r_V is extracted from z_V with Equation (3.2), and the fine-scale trend image $\hat{m}_v$ is estimated from $\hat{m}_V$ using a deterministic interpolation method. For each coarse pixel $r_V(\mathbf{u}_i)$ visited along the simulation path, the algorithm retrieves its corresponding pair of co-registered conditioning data events and computes the distance function in Equation (3.9) for all training data events stored in Ψ with fast Fourier transform (FFT) (Kwatra et al., 2003). The K best training data events are then sorted in ascending order according to the coarse-scale distance function. Subsequently, the distances between $d_V(\mathbf{u}_i)$ and this subset of training data events are stored in $\mathbf{D}(\mathbf{u}_i)$, which is later used to estimate the local CPDF. The same procedure is repeated for the co-registered fine-resolution conditioning data event, however, only for those K preselected locations. Once the simulation is finished, $z_v^{(s)}$ is restored with Equation (3.5) (line 12 of Algorithm 1).

When the coarse-to-fine resolution ratio is large (e.g. $G > 3$), Algorithm 1 has to be

---

Algorithm 1 Downscaling with sequential simulation

  input: a target coarse-resolution image z_V, a vector of algorithmic parameters $\boldsymbol{\theta}$, and the dual-resolution training image Ψ

  output: a conditional simulated realization $z_v^{(s)}$

1: Compute r_V and $\hat{m}_v$
2: Generate a path visiting $r_V(\mathbf{u}_i), i = 1, \ldots, N$
3: **for** each $r_V(\mathbf{u}_i), i = 1, \ldots, N$ along the path **do**
4:   Retrieve the data events $d_V(\mathbf{u}_i)$ and $d_v(\mathbf{u}_i)$
5:   Compute $D(d_V(\mathbf{u}_i), d_V^{(t)}(\mathbf{u}))$ for all training data events in Ψ
6:   Retrieve the K-best pairs of coarse and fine training data events
7:   Compute $D(d_v(\mathbf{u}_i), d_v^{(t)}(\mathbf{u}_k))$ for $k = 1, \ldots, K$
8:   Estimate $\Pr\{\mathbf{R}_v(\mathbf{u}_i) = \mathbf{r}_v^{(t)}(\mathbf{u}_k) \mid d_V(\mathbf{u}_i), d_v(\mathbf{u}_i)\}, k = 1, \ldots, K$
9:   Draw a simulated patch $\mathbf{r}_v^{(s)}(\mathbf{u}_i)$ from the local CPDF
10:   Add $\mathbf{r}_v^{(s)}(\mathbf{u}_i)$ to $r_v^{(s)}$
11: **end for**
12: $z_v^{(s)} \leftarrow \hat{m}_v + r_v^{(s)}$
13: **return** the conditional simulated realization $z_v^{(s)}$

---

adapted to allow a better reproduction of the different structures that can be found over a range of scales in $r_v^{(t)}$. To this end, we adopt a multi-scale iterative process based on smaller magnification factors. The downscaling of z_V is done through a series of hierarchical conditional simulations. This is accomplished by constraining simulations at finer resolutions to previously simulated coarser outputs. The process is interrupted when the downscaled image reaches a target spatial resolution of size $|v'|$ which is the fine pixel size of the finest dual-resolution training image available. Note that this iterative procedure entails replacing Ψ with a vector of dual-resolution training images.

The multi-scale downscaling of the target image z_V is summarized in Algorithm 2. The simulation of the sub-pixel residual variable is performed at multiple scales based on a series of conditional iterations of Algorithm 1. At the end of each iteration, the output realization $z_v^{(s)}$ is assigned as the new target coarse-scale image (line 3 of Algorithm 2). The process is repeated until the desired target spatial resolution is reached.

Algorithm 2 Multi-scale downscaling with sequential simulation

    input: a target coarse-resolution image z_V, a vector of algorithmic parameters $\boldsymbol{\theta}$, and the multi-resolution training image $\boldsymbol{\Psi}$

    output: a conditional simulated realization $z_v^{(s)}$

1: **while** $|V| > |v'|$ **do**
2:     Perform Algorithm 1 using the appropriate Ψ stored in $\boldsymbol{\Psi}$
3:     $z_V \leftarrow z_v^{(s)}$
4: **end while**
5: **return** the conditional simulated realization $z_v^{(s)}$

3.4   Case studies

The methodology is demonstrated with illustrative examples using DEMs from two mountain ranges in Switzerland. Our MPS-based downscaling method is used to generate fine-resolution conditional simulations. The coarse- and fine-resolution DEMs of both study areas consist of coarsened versions of the Swisstopo swissALTI3D DEM (Wiederkehr and Möri, 2013) produced with linear upscaling. Although there is a natural degree of similarity between both data sets as they originate from universal tectonic and surface processes, such as orogeny and mass wasting, they represent very distinct geomorphological settings. The maximum amplitude of the trend component in the two case studies is vastly different: In the Western Alps example it reaches 1.5 km, whereas in the Jura Mountains case it is only 300 m. The two mountain ranges are also characterized by contrasting landforms. The Western Alps are dominated by steep gradients, debris cones, and braided drainage systems, while the Jura Mountains are predominately karsts with lower gradients mainly driven by dissolution processes.

In Subsection 3.4.1, we define the kernel used for generating the weights for the spatial low-pass filter and distance functions as well as the distance-to-probability transformation function. The estimation of the sub-pixel trend image and the construction of multi-resolution training images are also discussed. Subsection 3.4.2 describes the setup of the other downscaling methods used for benchmarking. The statistical and structural metrics used to validate the results are discussed in Subsection 3.4.3. Subsection 3.4.4 presents an example using DEMs of the Western Alps, and Subsection 3.4.5 illustrates the method with DEMs from the Jura Mountains.

3.4.1 Kernels and distance-to-probability transformation function

In both case studies, a normalized Gaussian radial basis function is used for computing the kernel weights for the spatial low-pass filter (Eq. (3.3)) and distance functions (Eqs. (3.9) and (3.10))

$$\lambda(\mathbf{h}_j) = \frac{1}{2\pi\sigma^2\beta} \exp\left(-\frac{\|\mathbf{h}_j - \mathbf{h}_0\|_2^2}{2\sigma^2}\right), \tag{3.13}$$

where σ is the kernel shape parameter, and β is the normalizing constant (i.e. the sum of all kernel weights).

The transformation function $\phi(\cdot)$ assigns conditional probabilities to the local pool of candidate training data events. This function should be flexible enough to allow the sampling of either a large or a small portion of the K candidate training data events. The availability of a large pool of candidates for sampling is desirable for generating sub-pixel variability in the simulated realizations. However, a more thorough sampling might be important to enforce the reproduction of less frequent features present in the training image.

Based upon the aforementioned criteria, we formulated the following distance-to-probability transformation function

$$\phi(\mathbf{D}_k(\mathbf{u}_i)) \propto \left(\frac{\mathbf{D}_k(\mathbf{u}_i) - \min\left(\mathbf{D}(\mathbf{u}_i)\right)}{\max\left(\min\left(\mathbf{D}(\mathbf{u}_i)\right), c\right)} + 1\right)^{-q_k}, \tag{3.14}$$

where $\mathbf{D}_k(\mathbf{u}_i) = D(d_V(\mathbf{u}_i), d_V^{(t)}(\mathbf{u}_k))$ or $\mathbf{D}_k(\mathbf{u}_i) = D(d_v(\mathbf{u}_i), d_v^{(t)}(\mathbf{u}_k))$, c is a small constant inserted in the denominator to avoid division by zero, and q_k corresponds to the rank of $d_V^{(t)}(\mathbf{u}_k)$ or $d_v^{(t)}(\mathbf{u}_k)$ after the sorting operation.

Note that Equation (3.14) allows one to consider a variable number of candidate training data events at each location to be simulated. If all the distances stored in $\mathbf{D}(\mathbf{u}_i)$ are similar, a larger set of the K training data events is considered for sampling. Conversely, if such distances are significantly dissimilar, only the most compatible data events are likely to be drawn. The numerator of the base term in Equation (3.14) measures the dispersion within the pool of candidates by computing the difference in distance units between all the K elements against the best candidate training data event. The denominator converts the

absolute values into relative measurements towards the smallest element in the set. The exponent $-q_k$ scales the base such that higher conditional probabilities are assigned to the training data events that minimize the numerator. Adding $+1$ to the base term allows assigning uniform probabilities if all candidate training data events have roughly the same distance to the target data event. Computed conditional probabilities are later re-scaled to sum up to one.

The algorithm is driven by three parameters: one kernel shape parameter for the spatial low-pass filter denoted by σ_F, another shape parameter for the distance functions σ_D, and the number of candidate training data events K. Additionally, we compute $\hat{m}_v(\mathbf{u})$ and $\hat{m}_v^{(t)}(\mathbf{u})$ by downscaling the coarse-scale trend estimates with bicubic interpolation. At each scale, the decomposition between trend and residual is done using a spatial low-spatial filter with a radius that is proportional to the pixel size of the current coarse-scale. The sequential simulation process is performed using a random path.

In both examples, the multi-resolution training images are built directly from $z_v^{(t)}$ by linear upscaling. A discussion about the criteria for selecting input data to generate the dual-resolution training image is out of the scope of this work. In geomorphological applications, the training image can be built from a better-informed analog data set. In other research areas, where analogs are not commonly available, artificial training images may have to be employed.

3.4.2   Benchmarking against other techniques

The proposed algorithm is benchmarked against the two-point statistics area-to-point simulation method (Kyriakidis and Yoo, 2005), the direct sampling MPS simulation algorithm (Mariethoz et al., 2010), and the bicubic interpolation method (Keys, 1981). In order to carry a fair comparison between techniques, z_V is detrended prior to simulation. Realizations are conditioned to both r_V and previously simulated fine-resolution data. The downscaled DEMs are then restored by addition of the estimated trend component $\hat{m}_v$ computed with bicubic interpolation.

The downscaling by area-to-point simulation is performed with the error simulation framework (Journel and Huijbregts, 1978; Liu and Journel, 2009). As the simulation paradigm only applies to Gaussian variables, the reproduction of the fine-scale target histogram must be achieved through post-processing. The empirical CDF of $r_v^{(t)}$ is used as source distribution for a normal score transform. The histogram transformation morphs this

empirical CDF into a zero mean Gaussian distribution with unit variance through quantile mapping. An artificial coarse-scale Gaussian variable is constructed through linear upscaling of the transformed version of $r_v^{(t)}$. The histogram transformation is then applied to r_V using the previous Gaussian distribution as target CDF. Note that this approximation inherently introduces conditioning errors since the upscaling function between the original coarse- and fine-resolution residuals is actually non-linear. Unlike the trended component, each coarse-residual pixel value does not necessarily corresponds to the arithmetic mean of its co-registered fine residual patch due to the trend removal operation. Unconditional fine-resolution realizations of a zero mean Gaussian process are generated with the FFT moving average simulation algorithm (Ravalec et al., 2000). The inference of the fine-scale (i.e. point-support) variogram model is carried out as a two-step process. The first part consists of inferring the shape of the variogram model near the origin (i.e. for lags smaller than the coarse pixel size). This is performed based on the Gaussian transform of $r_v^{(t)}$. The second step is the inference of the variogram model geometric anisotropy, which is calibrated based on the transformed version of r_V. Each conditional realization is then back-transformed into the original variable space using the empirical CDF of $r_v^{(t)}$ as target distribution.

Downscaling with the direct sampling algorithm can be seen as a conditional simulation problem with an exhaustive secondary variable. The two required pre-processing steps are the resampling of the coarse-scale DEMs (in order to have co-located neighbors for both primary and secondary variables) and the variable normalization operations. In this study, r_V and $r_V^{(t)}$ are resampled at the fine-scale pixel size using nearest neighbor interpolation. The target and training residual DEMs are normalized using a min-max scaling. The minimum and maximum values are extracted from the training data. After simulation, output realizations are re-scaled.

Although not a geostatistical technique, the bicubic interpolation method is widely used in practical applications owing to its capability for generating smooth surfaces with a short processing time. Interpolations are performed based solely on z_V. Its application to the data sets hereby studied is straightforward, and it provides a reference point for comparison and analysis of the results.

3.4.3 Validation

The downscaled DEMs are evaluated based on a series of statistical and structural metrics. The reproduction of the reference fine-scale terrain elevation probability distribution is verified with empirical cumulative distribution functions (CDFs). The conditioning quality

of the simulations to the input coarse data is quantified based on the average mean error (ME) and root-mean-square error (RMSE) between the reference coarse-resolution DEMs and the upscaled realizations. The structural accuracy of the downscaling is assessed by computing empirical variograms, high-order cumulant maps (Dimitrakopoulos et al., 2010), probability of connection curves, and the mean structural similarity (SSIM) index (Wang et al., 2004) between simulated realizations and the reference residual DEMs. The topology of the realizations is described using the Euler characteristic. Detailed information about the probability of connection function and the Euler characteristic, and their application for the evaluation of continuous random fields can be found in Renard and Allard (2013). All the validation metrics, with exception of the ME and RMSE, are computed on the residual DEMs to remove the effect of large-scale topographic structures.

3.4.4   The Western Alps example

This example considers DEMs from a portion of the Western Swiss Alps. The topography in this region is characterized by a rough terrain with steep natural slopes, high altitude peaks, and glacially carved valleys. The reference DEMs and their respective residual DEMs are shown in Figure 3.4. The coarse DEM has dimensions of 64×64 pixels, and each pixel has size of 32×32 m, which is approximately the spatial resolution of the 1-arc second near-global DEM produced from the U.S. National Geospatial-Intelligence Agency (NGA) and NASA's Shuttle Radar Topography Mission (SRTM) (Farr et al., 2007). The medium and fine DEMs have dimensions of 128×128 pixels and 256×256 pixels, with pixel sizes of 16×16 m and 8×8 m, respectively. The footprint of the DEMs is roughly 4 km^2. The coarse DEM is used for conditioning, while the medium- and fine-resolution DEMs are used for validation of the simulations. The residual DEMs were computed using a spatial low-pass filter with $\sigma_F = 64$ m. Negative relief features in the residual variable represent gullies and drainage networks, whereas positive relief structures correspond to cliffs and mountain ridges.

Figure 3.5 illustrates the training DEMs and their respective residual DEMs. These DEMs are from a neighboring area that shares similar topographic features with the reference data set. The training data set has a larger footprint than the target area (≈ 16 km^2). The training DEMs should be extensive enough to include the expected range of relevant structural patterns to be determined. The coarse-, medium-, and fine-resolution DEMs have the following dimensions: 128×128 pixels, 256×256 pixels, 512×512 pixels, respectively, with the same pixel size configuration of the reference data set. The training
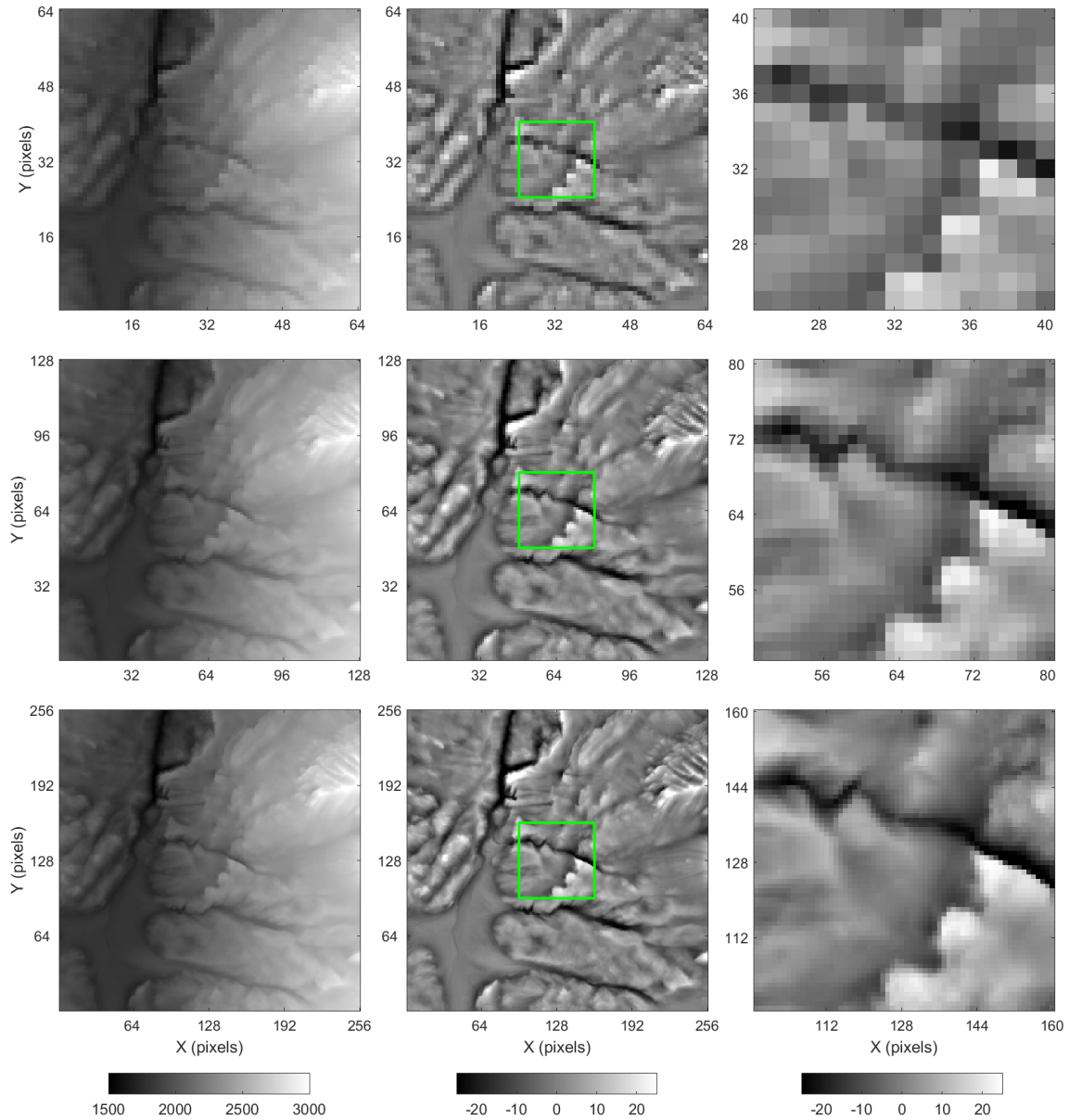
Figure 3.4: The Western Alps reference DEMs. *Top left*: coarse-resolution DEM. *Top center*: coarse-resolution residual DEM. *Top right*: coarse-resolution zoom. *Middle left*: medium-resolution DEM. *Middle center*: medium-resolution residual DEM. *Middle right*: medium-resolution zoom. *Bottom left*: fine-resolution DEM. *Bottom center*: fine-resolution residual DEM. *Bottom right*: fine-resolution zoom. The residual component of the trended DEMs has a vertical exaggeration factor of $8\times$. Green boxes highlight the magnified area. Colorbars' unit is m.

residual DEMs are displayed using the same spatial low-pass filter setup. Table 3.2 lists summary statistics from the target and training coarse-resolution DEMs used in both case studies. Note that all residual DEMs show similar mean values, but the training DEMs

have higher variance and range than their corresponding target data sets.

Table 3.2: Summary statistics of the target and training coarse-resolution DEMs from the Western Alps and the Jura Mountains examples.

Example	Data set	Mean	SD	Min.	Max.
Western Alps	Target	−0.38	5.94	−34.71	31.19
	Training	−0.11	7.81	−57.04	60.26
Jura Mountains	Target	−0.05	2.84	−14.66	13.11
	Training	−0.03	4.30	−18.00	27.66

Values are in residual elevation (in m)

An ensemble of 20 simulated realizations with a magnification factor of $4\times$ was generated based on two iterations of the algorithm. Since the pixel sizes of the multi-resolution training DEMs are all multiples of 2, the magnification factor per iteration was set equal to $G = 2$. The search window used by the spatial low-pass filter and the retrieval of data events at the coarse scale has dimensions of 5×5 pixels. The size of the corresponding fine-resolution search window is 10×10 pixels.

The parameters used for the two iterations of the downscaling of the Western Alps example are listed in Table 3.3. Parameters were chosen such that the algorithm performs reasonably well for both data sets. Typically, they may be inferred from the dual-resolution training image through cross-validation. The spatial low-pass filter kernel shape parameter σ_F is calibrated in order to generate an auto-correlated residual. The simulation of the fine-resolution residual component is only feasible if the spatial low-pass filter is applied to z_V prior to its interpolation. This leads to a significant improvement in the structural accuracy of the simulated realizations. The distance functions' kernel shape parameter σ_D is set such that the central pixel of the coarse-scale data events receives roughly half of the sum of the kernel weights. The weight given to the central pixel directly affects the conditioning quality of the downscaling to the target DEM. The number of candidate training data events K is adjusted to achieve a trade-off between the structural accuracy of the simulated realizations, sub-pixel variability, and computational efficiency.

The downscaling by area-to-point simulation is performed using a global search neighborhood. The fitted variogram model consists of a normalized anisotropic k-Bessel model whose parameters are listed in Table 3.4. The direct sampling algorithm parameters are configured to enforce the scanning of the entire training image. The normalized acceptance threshold is set to a small value to maximize the structural quality of the output

Table 3.3: Algorithm parameters used in the Western Alps and Jura Mountains examples.

Parameter	Unit	$G = 2$	$G = 4$
σ_F	m	64	32
σ_D	m	16	8
K	–	20	20

realizations. Table 3.5 lists the algorithm parameters used for the Western Alps and Jura Mountains examples. A standard configuration setup is employed which includes the use of an isotropic search radius for the retrieval of data events, and the L^2 norm for distance computation. The exponent in the distance function is set to zero. For a detailed description of the algorithm and its parameters, the reader is referred to Mariethoz et al. (2010) and Meerschman et al. (2013).

Table 3.4: Area-to-point simulation parameters used in the Western Alps and Jura Mountains examples.

Example	Parameter	Unit	$G = 2$	$G = 4$
Western Alps	σ_F	m	64	64
	Variogram model	–	k-Bessel	k-Bessel
	Max. range	m	22.4	20.8
	Min. range	m	19.2	17.6
	Azimuth	°	90	90
	Shape parameter	–	2	2
Jura Mountains	σ_F	m	64	64
	Variogram model	–	k-Bessel	k-Bessel
	Max. range	m	65.6	65.6
	Min. range	m	40.0	40.0
	Azimuth	°	90	90
	Shape parameter	–	1	1

Figures 3.6–3.9 illustrate two realizations and interpolations of the sub-pixel DEMs and their corresponding residual topographies generated with the four benchmarked techniques. Summary statistics for the downscaling results are listed in Table 3.6. Statistical and structural validation metrics for the realizations and interpolations are depicted in Figures 3.10–3.13 and Table 3.7. The empirical CDFs, directional variograms, Euler characteristic, and connectivity curves for the proposed method, area-to-point simulation, and direct sampling algorithm are displayed as min-max envelopes generated from 20 realizations (Figs. 3.10 and 3.11). Statistics and validation metrics calculated from simulated

Table 3.5: Direct sampling algorithm parameters used in the Western Alps and Jura Mountains examples.

Variable	Parameter	Unit	$G = 2$	$G = 4$
	σ_F	m	64	64
	Training image scanning fraction	–	1.0	1.0
Coarse	Normalized acceptance threshold	–	0.005	0.005
	Max. search radius	Number of pixels	5	10
	Max. neighborhood size	Number of pixels	9	21
Fine	Normalized acceptance threshold	–	0.005	0.005
	Max. search radius	Number of pixels	5	10
	Max. neighborhood size	Number of pixels	8	20

realizations consist of the mean values plus or minus one standard deviation.

Statistically, the medium- and fine-resolution DEMs generated with the proposed downscaling algorithm are the closest to the reference data set when compared to the realizations produced by other techniques (Table 3.6). However, a systematic underestimation of the reference standard deviation values is observed. Figure 3.6 illustrates reproduction of low-entropy patterns characterized by the spatial connectivity between high and low residual elevation values. These structures can be observed in the reference fine-resolution residual DEM (Fig. 3.4). The area-to-point simulation realizations overestimate the standard deviation and spread of the reference residual DEMs (Table 3.6). This is likely a consequence of the mismatch between the probability distributions of the fine-scale residuals from the training image and the reference data set. The histogram transformations are based on the empirical CDF of the fine-resolution training image which has a larger range than the fine-scale reference histogram (Table 3.6). As expected, area-to-point simulation realizations have a higher degree of spatial entropy. Simulated textures tend to disconnect high and low residual elevation values (Fig. 3.7). Realizations also exhibit high-frequency structures in areas that are predominantly bland in the reference fine-resolution residual DEM (Figs. 3.4 and 3.7). The direct sampling realizations have slightly lower variance than the results produced by the proposed algorithm. The bicubic interpolation predictions consist of blurred representations of the fine-scale reference DEM (Fig. 3.9). The spatial smoothing caused by the interpolation process is also observed in the summary statistics, characterized by the underestimation of the variance and the sample minimum and maximum (Table 3.6).

On average, the proposed algorithm generates fine-resolution terrain models that are consistent with the coarse-scale conditioning data. The average ME and RMSE between

the reference coarse-resolution DEM and the upscaled realizations are smaller than the
ones produced by the direct sampling and bicubic interpolation (Table 3.7). The area-
to-point simulation realizations have the smallest RMSE for both magnification factors.
However, they produce similar ME values. The scatter plots in Figs. 3.10 and 3.11 reveal
an unbiased dispersion between the reference coarse-resolution residual elevation and the
coarse-scale conditioning error for realizations generated with the proposed algorithm. The
direct sampling error dispersion is somewhat higher. Negative correlation between the refer-
ence residual elevation and the conditioning errors for the upper and lower ends is observed
(Figs. 3.10 and 3.11). By contrast, area-to-point simulations provide precise reproduction
of intermediate coarse-resolution measurements but they generate a positive correlation
towards low and high values. The bicubic interpolation results clearly show a negative
correlation between the conditioning errors and the coarse residual elevation (Figs. 3.9 and
3.10).

Structural validation metrics reveal that the proposed downscaling method is more
effective at reproducing the reference fine-scale variability and sub-pixel structures. This is
reflected in the agreement between the simulations and the reference data in the directional
variograms, Euler characteristic, and probability of connection plots (Figs. 3.10 and 3.11).
Area-to-point simulations generate more variability and are unable to reproduce the spatial
connectivity of fine-scale residuals. It is also evident that the bicubic interpolation method
underestimates the sub-pixel variability and does not reproduce the topology and the con-
nectivity of the reference residual DEMs. The direct sampling realizations tend to generate
less variability when compared to the proposed algorithm and have issues for reproducing
the Euler characteristic curves for residual elevation values within the interval between -10
and 10 m for $G = 4$. However, it is worth noting that the proposed algorithm seems to
underestimate the reference negative Euler number values for residual elevation thresholds
within the interval from -10 to 10 m (Figs. 3.9 and 3.10). In addition, similarly to the
other stochastic techniques, simulated realizations tend to produce erratic fluctuations in
the probability of connection for residual elevation values under -15 m and over 15 m for
$G = 4$ (Fig. 3.10). This is most likely to be due to random noise inherent to the simula-
tion process and its respective propagation across scales (i.e. in the following iterations).
As a result, the structural accuracy of the realizations is expected to deteriorate at higher
magnification factors.

The bicubic interpolation estimates have the highest mean SSIM for both the medium-
and fine-resolution predictions whereas the area-to-point simulated realizations display the
smallest scores (Table 3.7). Stochastic methods will generally yield lower SSIM as they

do not aim to minimize the local variance of the predictions. The bicubic interpolation produces smooth surfaces devoid from noise. Withal, the resulting textures are deprived from the sub-pixel patterns imported from the dual-resolution training image. Figures 3.12 and 3.13 show the mean absolute error (MAE) between the simulated and the reference sub-pixel residual elevation third- and fourth-order cumulant maps. The spatial templates used for computing the experimental cumulants are displayed next to the maps. As expected, the MPS-based approaches outperform the other two methods. The MAE generated at short lags configurations by both MPS methods are approximately one order of magnitude smaller than the MAE produced by area-to-point simulation and bicubic interpolation. The proposed approach tends generate larger small-scale errors in the third-order cumulant map compared to the direct sampling algorithm. This is likely caused by edge artifacts between adjacent simulated patches. Nevertheless, the scenario is reversed in the fourth-order cumulant MAE map.

Table 3.6: Summary statistics of the downscaled DEMs from the Western Alps example.

	G	Mean	SD	Min.	Max.
Training	2	-0.12	8.99	-63.69	72.44
Reference	2	-0.45	6.83	-40.54	37.37
Proposed method	2	-0.44 ± 0.00	6.67 ± 0.01	-40.08 ± 1.16	37.35 ± 1.69
Area-to-point	2	-0.44 ± 0.00	7.10 ± 0.01	-54.63 ± 2.89	55.96 ± 3.20
Direct sampling	2	-0.45 ± 0.00	6.57 ± 0.02	-39.32 ± 2.01	38.74 ± 2.92
Bicubic	2	-0.45	6.19	-34.62	31.48
Training	4	-0.11	8.89	-63.33	85.03
Reference	4	-0.41	6.76	-41.43	37.36
Proposed method	4	-0.41 ± 0.00	6.55 ± 0.02	-42.07 ± 1.98	40.07 ± 2.38
Area-to-point	4	-0.41 ± 0.00	7.06 ± 0.02	-57.93 ± 2.84	60.96 ± 3.80
Direct sampling	4	-0.42 ± 0.00	6.42 ± 0.01	-43.59 ± 1.52	40.39 ± 1.90
Bicubic	4	-0.42	5.95	-35.23	31.38

Numbers represent average statistics plus or minus one standard deviation over 20 realizations. Values are in residual elevation (in m)

Table 3.7: Validation of the Western Alps example.

	G	ME[1](cm)	RMSE[2](cm)	SSIM[3]
Proposed method	2	0.90 ± 0.76	58.62 ± 1.17	0.914 ± 0.001
Area-to-point	2	-1.24 ± 0.37	40.63 ± 0.94	0.883 ± 0.003
Direct sampling	2	1.50 ± 0.82	86.43 ± 1.50	0.893 ± 0.002
Bicubic	2	1.33	68.05	0.932
Proposed method	4	1.13 ± 0.80	60.15 ± 1.00	0.877 ± 0.002
Area-to-point	4	-1.44 ± 0.58	46.98 ± 1.18	0.832 ± 0.002
Direct sampling	4	1.24 ± 0.66	67.17 ± 1.20	0.875 ± 0.001
Bicubic	4	1.68	79.45	0.897

[1] mean error; [2] root-mean-square error; [3] structural similarity; Values represent average statistics plus or minus one standard deviation over 20 realizations
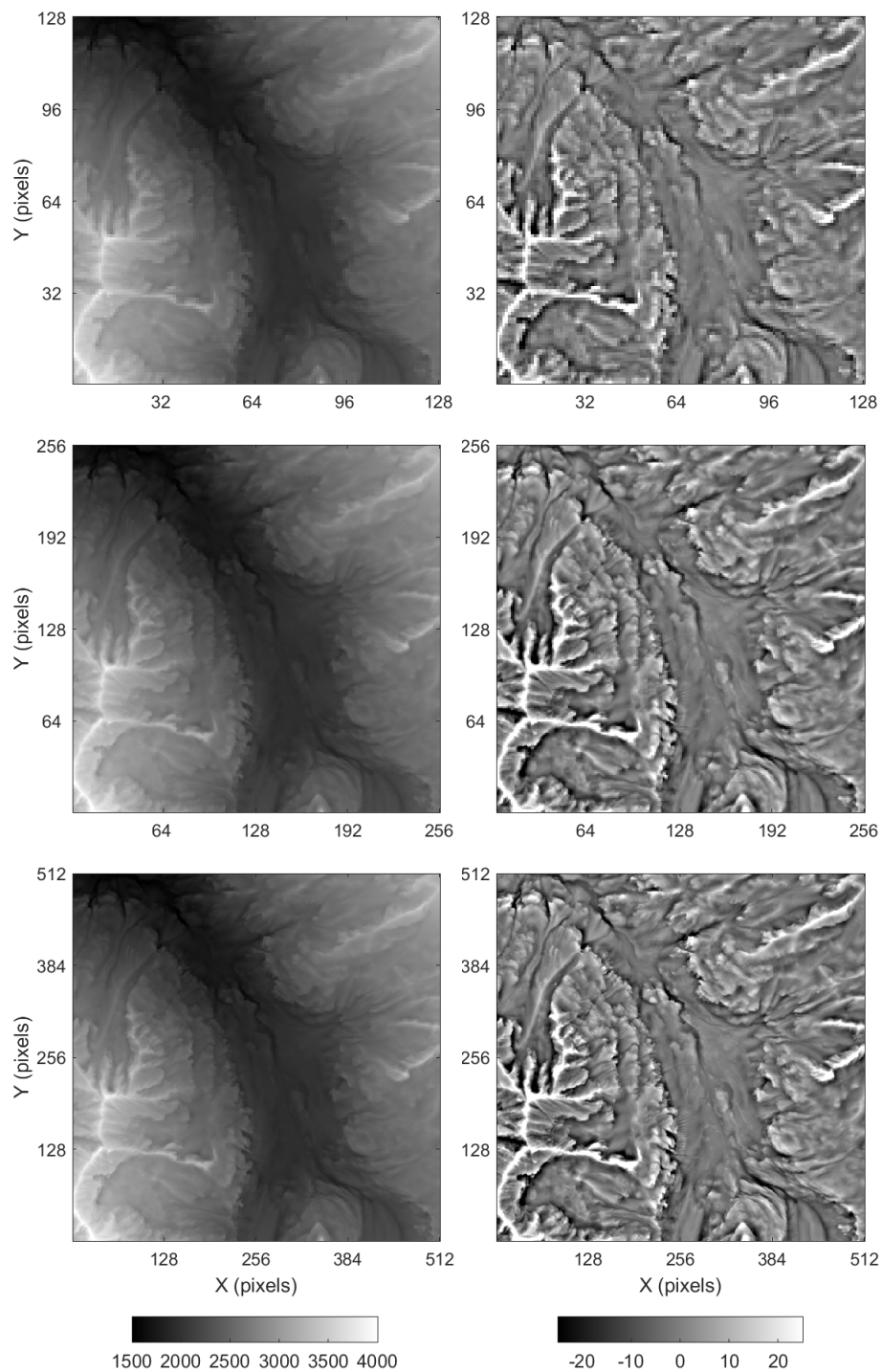
Figure 3.5: The Western Alps training DEMs. *Top left*: coarse-resolution DEM. *Top right*: coarse-resolution residual DEM. *Middle left*: medium-resolution DEM. *Middle right*: medium-resolution residual DEM. *Bottom left*: fine-resolution DEM. *Bottom right*: fine-resolution residual DEM. The residual component of the trended DEMs has a vertical exaggeration factor of $8\times$. Colorbars' unit is m.
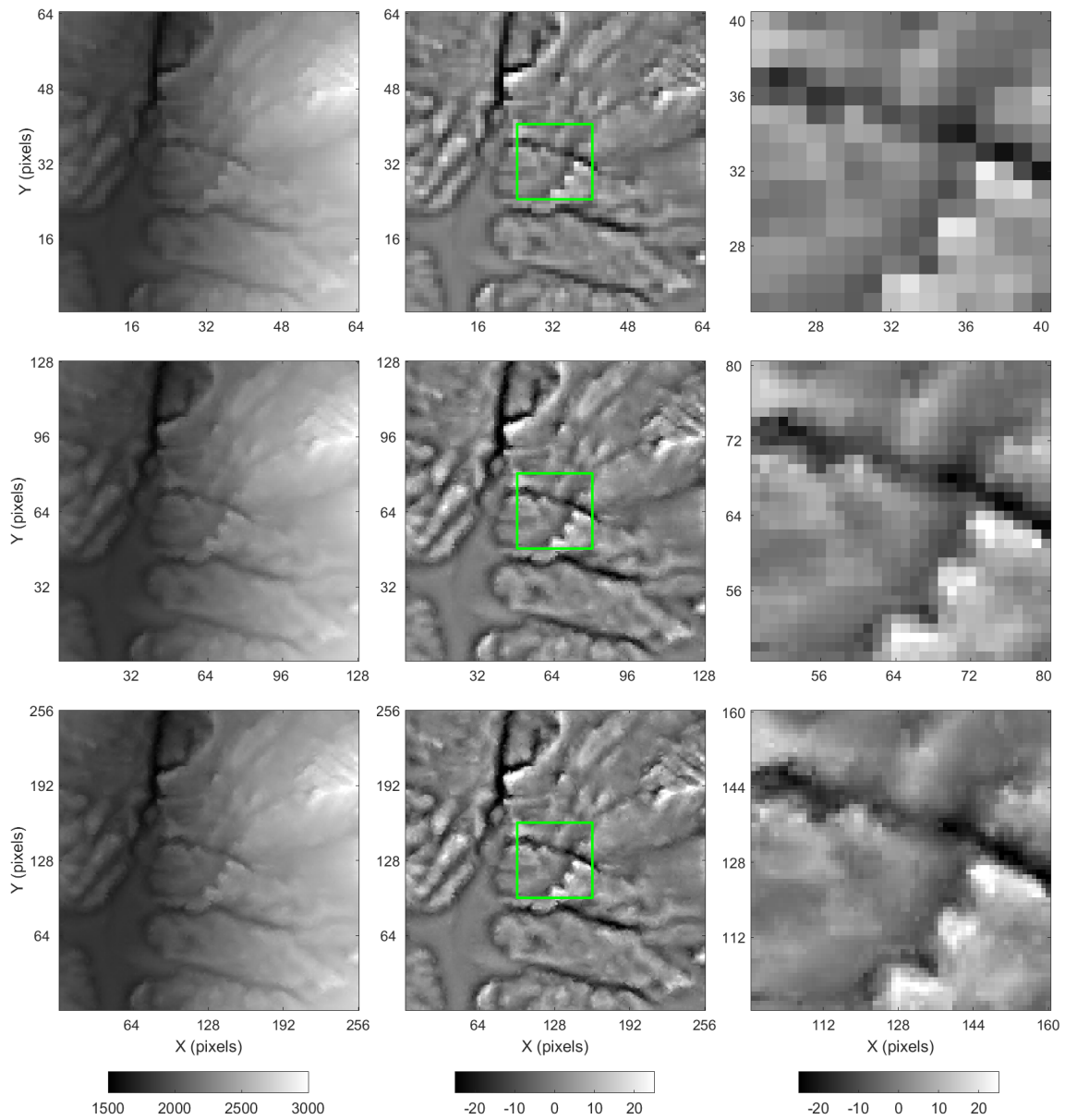
Figure 3.6: The Western Alps downscaled DEMs produced with the proposed algorithm. *Top left*: coarse-resolution DEM. *Top center*: coarse-resolution residual DEM. *Top right*: coarse-resolution zoom. *Middle left*: simulated medium-resolution DEM. *Middle center*: simulated medium-resolution residual DEM. *Middle right*: medium-resolution zoom. *Bottom left*: simulated fine-resolution DEM. *Bottom center*: simulated fine-resolution residual DEM. *Bottom right*: fine-resolution zoom. The residual component of the trended DEMs has a vertical exaggeration factor of 8×. Green boxes highlight the magnified area. Colorbars' unit is m.
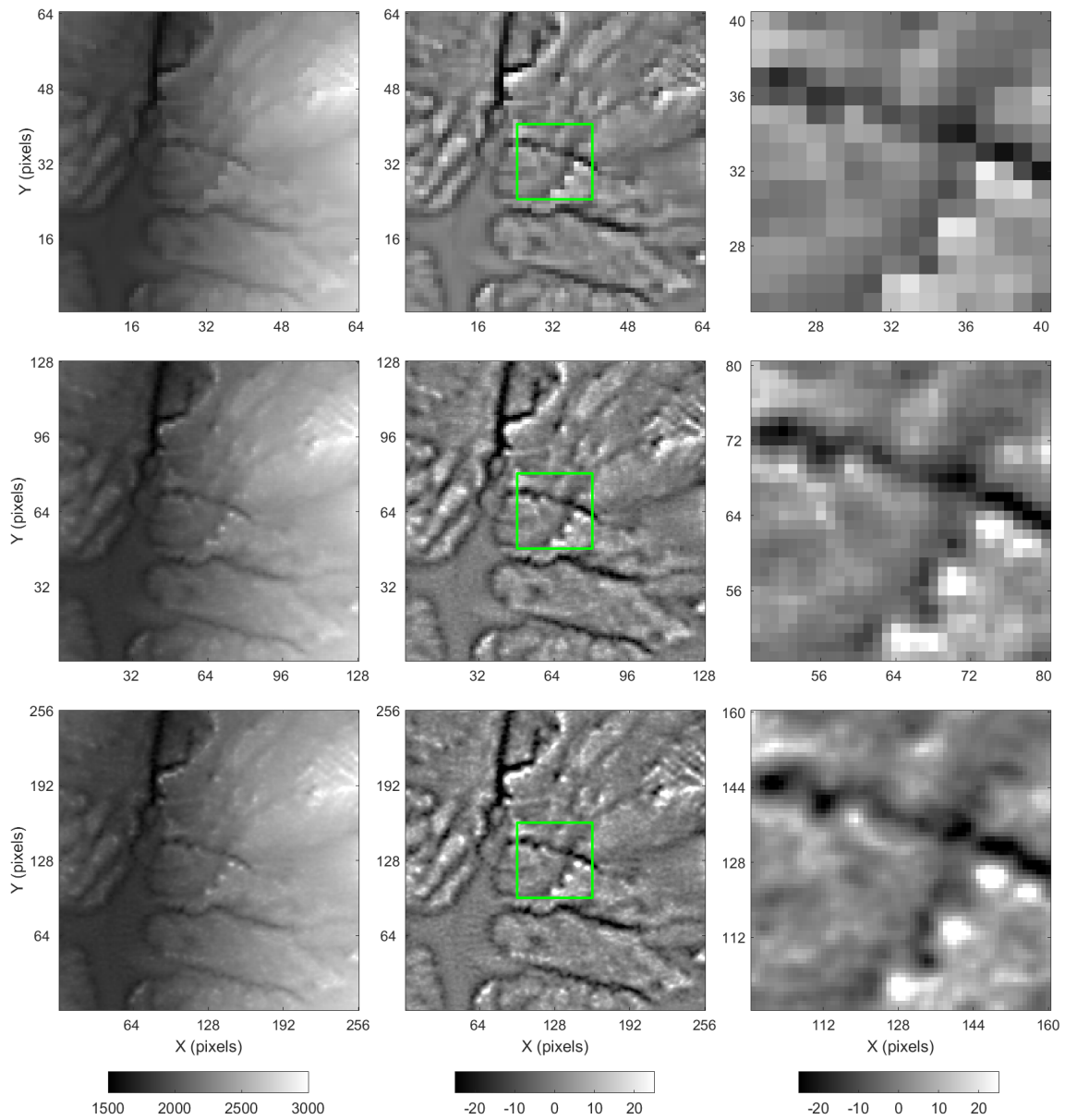
Figure 3.7: The Western Alps downscaled DEMs produced with area-to-point simulation. *Top left*: coarse-resolution DEM. *Top center*: coarse-resolution residual DEM. *Top right*: coarse-resolution zoom. *Middle left*: simulated medium-resolution DEM. *Middle center*: simulated medium-resolution residual DEM. *Middle right*: medium-resolution zoom. *Bottom left*: simulated fine-resolution DEM. *Bottom center*: simulated fine-resolution residual DEM. *Bottom right*: fine-resolution zoom. The residual component of the trended DEMs has a vertical exaggeration factor of 8×. Green boxes highlight the magnified area. Colorbars' unit is m.
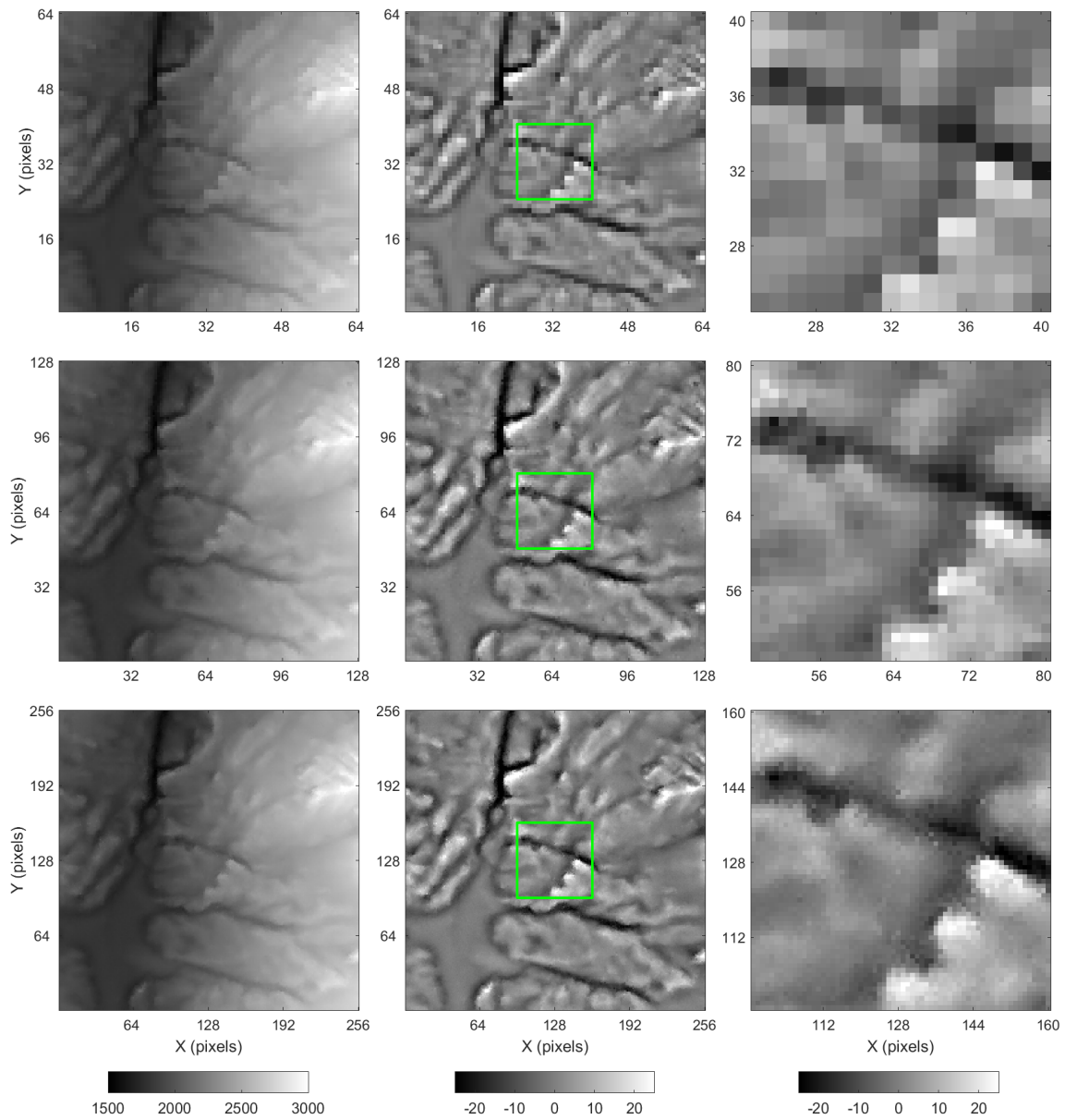
Figure 3.8: The Western Alps downscaled DEMs produced with direct sampling. *Top left*: coarse-resolution DEM. *Top center*: coarse-resolution residual DEM. *Top right*: coarse-resolution zoom. *Middle left*: simulated medium-resolution DEM. *Middle center*: simulated medium-resolution residual DEM. *Middle right*: medium-resolution zoom. *Bottom left*: simulated fine-resolution DEM. *Bottom center*: simulated fine-resolution residual DEM. *Bottom right*: fine-resolution zoom. The residual component of the trended DEMs has a vertical exaggeration factor of $8\times$. Green boxes highlight the magnified area. Colorbars' unit is m.
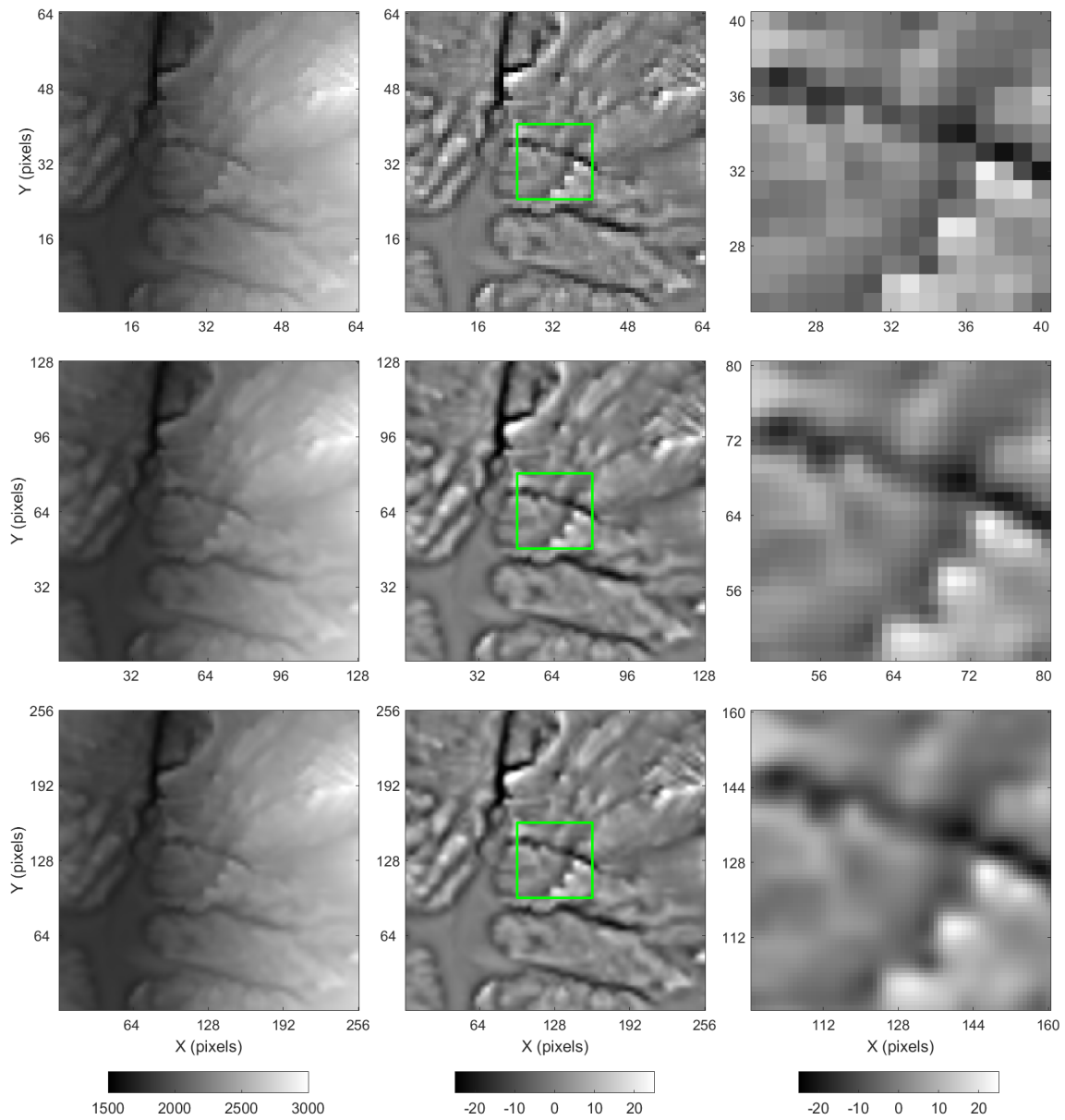
Figure 3.9: The Western Alps downscaled DEMs produced with bicubic interpolation. *Top left*: coarse-resolution DEM. *Top center*: coarse-resolution residual DEM. *Top right*: coarse-resolution zoom. *Middle left*: interpolated medium-resolution DEM. *Middle center*: interpolated medium-resolution residual DEM. *Middle right*: medium-resolution zoom. *Bottom left*: interpolated fine-resolution DEM. *Bottom center*: interpolated fine-resolution residual DEM. *Bottom right*: fine-resolution zoom. The residual component of the trended DEMs has a vertical exaggeration factor of 8×. Green boxes highlight the magnified area. Colorbars' unit is m.
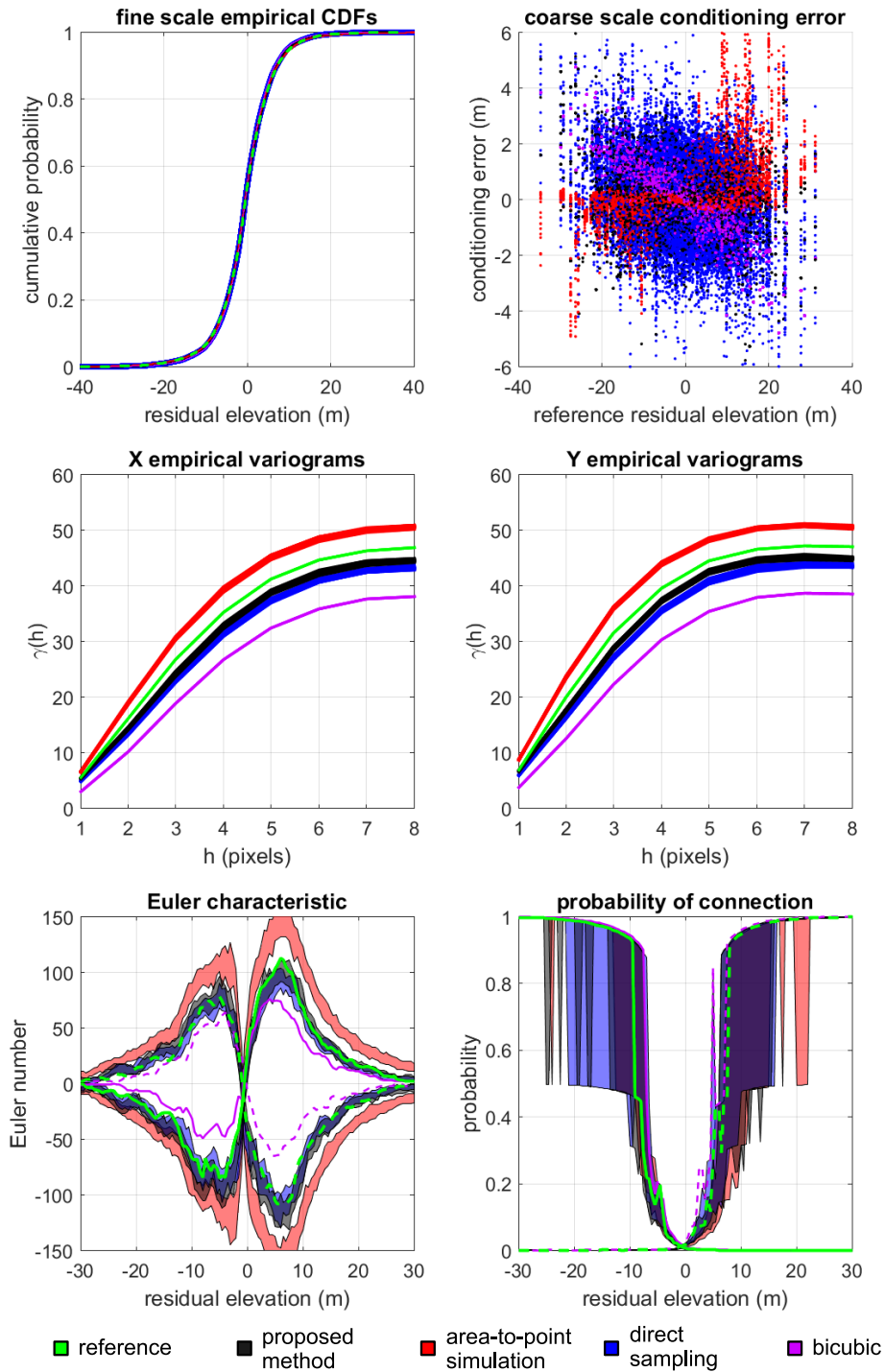
Figure 3.10: Validation of the Western Alps example ($G = 2$). *Top left*: sub-pixel empirical CDFs. *Top right*: scatter plots between reference coarse residual elevation and conditioning error. *Middle left*: sub-pixel empirical variograms along the X axis. *Middle right*: sub-pixel empirical variograms along the Y axis. *Bottom left*: fine-scale Euler characteristic. *Bottom right*: fine-scale probability of connection.
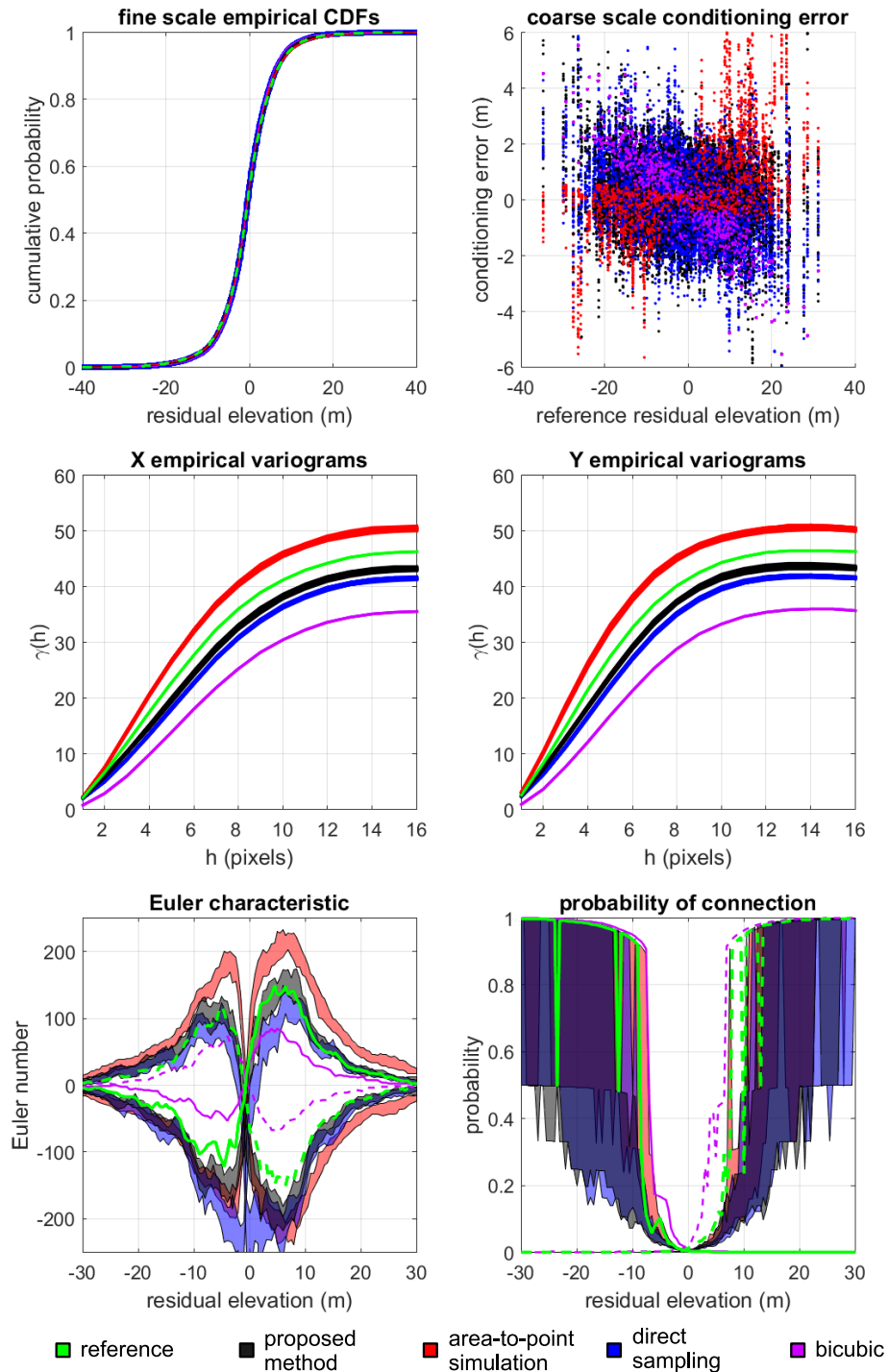
Figure 3.11: Validation of the Western Alps example ($G = 4$). *Top left*: sub-pixel empirical CDFs. *Top right*: scatter plots between reference coarse residual elevation and conditioning error. *Middle left*: sub-pixel empirical variograms along the X axis. *Middle right*: sub-pixel empirical variograms along the Y axis. *Bottom left*: fine-scale Euler characteristic. *Bottom right*: fine-scale probability of connection.
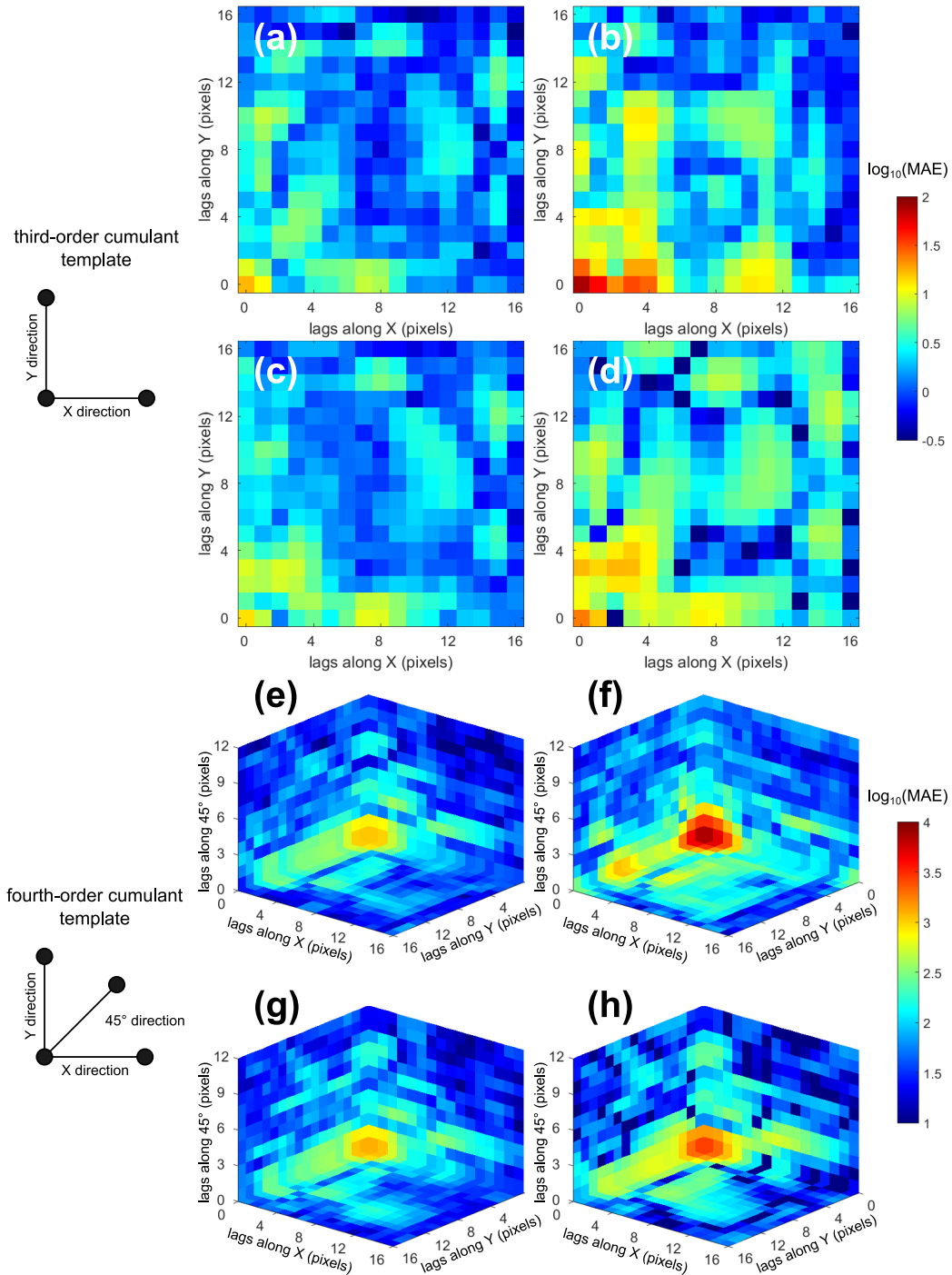
Figure 3.12: MAE between simulated and reference third- and fourth-order cumulant maps from the Western Alps example ($G = 2$). *Top*: third-order cumulant MAE maps for **a** proposed method, **b** area-to-point simulation, **c** direct sampling, and **d** bicubic interpolation. Colorbar unit is m^3. *Bottom*: fourth-order cumulant MAE maps for **e** proposed method, **f** area-to-point simulation, **g** direct sampling, and **h** bicubic interpolation. Colorbar unit is m^4.
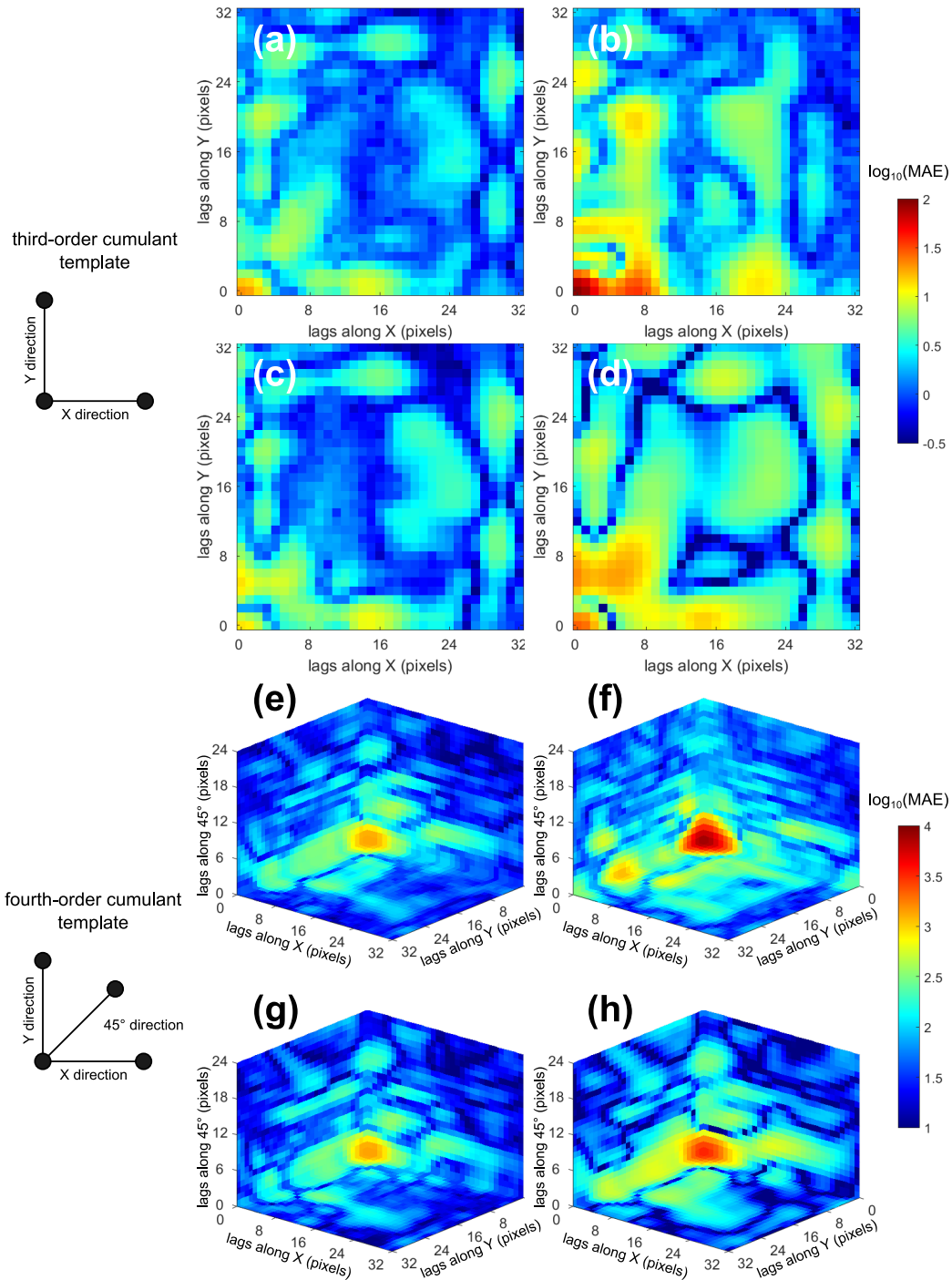
Figure 3.13: MAE between simulated and reference third- and fourth-order cumulant maps from the Western Alps example ($G = 4$). *Top*: third-order cumulant MAE maps for **a** proposed method, **b** area-to-point simulation, **c** direct sampling, and **d** bicubic interpolation. Colorbar unit is m^3. *Bottom*: fourth-order cumulant MAE maps for **e** proposed method, **f** area-to-point simulation, **g** direct sampling, and **h** bicubic interpolation. Colorbar unit is m^4.

3.4.5   The Jura Mountains example

The second case study uses DEMs from a subset of the Jura Mountains. This sub-alpine mountain range is characterized by karst topography and relative low-gradient landforms when compared to the Western Alps example. Figure 3.14 illustrates the reference DEMs and the residual terrain elevation models. The training trended and residual DEMs from a neighboring analog area are depicted in Figure 3.15. The spatial low-pass filter configuration for obtaining the residuals, the DEMs dimensions, pixel sizes, footprints are identical to the ones presented in Subsection 3.4.4.

A set of 20 conditional simulations was generated using the same multi-scale iterative downscaling approach and parameters setup used in the Western Alps case study (Table 3.3). The area-to-point simulation and the direct sampling algorithm parameters used for this example are listed in Tables 3.4 and 3.5, respectively. Simulated realizations and estimates are shown in Figures 3.16–3.19. Summary statistics are listed in Table 3.8. The statistical validation metrics are depicted in Table 3.9 and Figures 3.20–3.23.

The results for the Jura Mountains example confirm the ones from the Western Alps case study. The proposed MPS algorithm outperforms the other techniques for the majority of validation metrics. The method is able to reproduce relatively well the fine-scale terrain elevation probability distributions for both magnification factors (Table 3.8 and Figs. 3.20, 3.21). The area-to-point simulated realizations generate more variability than the reference data set. Similarly to the previous example, this is most likely caused by the reliance on the training image fine-scale empirical CDF for the histogram transform. The conditioning ME, RMSE in Table 3.9 and the error dispersions displayed in the scatter plots for both medium-(Fig. 3.20) and fine-resolution (Fig. 3.21) predictions are akin to the results presented in Subsection 3.4.4, although the magnitude of the errors is significantly smaller. The proposed approach generates the smallest ME for both magnification factors, and the highest SSIM values among the stochastic simulation methods (Table 3.9).

The structural accuracy of the downscaled DEMs produced by the different techniques are also akin to the Western Alps case study. Notwithstanding, the loss of fine-scale variability is significantly less pronounced in this example. The relative differences between the standard deviations of the reference and simulated DEMs is approximately halved (Table 3.8). This can also be observed in the improved match between the empirical variograms (Figs. 3.20 and 3.21). The Euler characteristic and probability of connection plots indicate

that the proposed algorithm generates less random noise. Underestimation of negative Euler numbers within the range of -5 to 5 m is evident after two iterations of the algorithm. However, the erratic fluctuations in the connectivity curves for small and large residual elevations are much less pronounced (Fig. 3.21). The noise reduction might be related to the fact that the topography in this region is not as rugged as in the Western Alps. The spatial patterns in the training DEMs are generally smoother and, consequently, less noise is propagated throughout the simulation process. The area-to-point simulation and the bicubic interpolation method are unable to the reproduce the fine-scale variability present in the reference data, and cannot adequately mimic the topology and the spatial connectivity of the sub-pixel residual variable (Figs. 3.20 and 3.21). The proposed algorithm and the direct sampling realizations tend to produce similar Euler characteristic and connectivity curves for $G = 2$ (Figs. 3.20). However, these curves start to differentiate themselves when $G = 4$. The proposed algorithm managed to outperform all the other methods in the reproduction of high-order statistics. Figures 3.22 and 3.23 reveal that the approach generates the smallest MAE between the simulated and the reference third- and fourth-order cumulant maps for both magnification factors. Fine-scale errors in the third- and fourth-order cumulant maps are roughly one order of magnitude lower than the ones produced by other techniques.

Table 3.8: Summary statistics of the downscaled DEMs from the Jura Mountains example.

	G	Mean	SD	Min.	Max.
Training	2	-0.04	4.93	-21.57	34.30
Reference	2	-0.06	3.25	-18.09	15.88
Proposed method	2	-0.06 ± 0.00	3.20 ± 0.00	-17.64 ± 0.65	15.93 ± 0.70
Area-to-point	2	-0.06 ± 0.00	3.42 ± 0.01	-17.87 ± 0.38	17.33 ± 0.73
Direct sampling	2	-0.06 ± 0.00	3.16 ± 0.00	-16.68 ± 0.25	16.59 ± 0.90
Bicubic	2	-0.06	3.05	-14.54	14.65
Training	4	-0.04	4.76	-21.65	38.56
Reference	4	-0.05	3.16	-19.22	16.21
Proposed method	4	-0.05 ± 0.00	3.10 ± 0.00	-18.13 ± 0.84	16.97 ± 0.83
Area-to-point	4	-0.05 ± 0.00	3.34 ± 0.01	-18.18 ± 0.37	18.10 ± 1.11
Direct sampling	4	-0.05 ± 0.00	3.06 ± 0.00	-17.69 ± 0.25	16.86 ± 1.00
Bicubic	4	-0.05	2.91	-15.00	14.26

Numbers represent average statistics plus or minus one standard deviation over 20 realizations. Values are in residual elevation (in m)

Table 3.9: Validation of the Jura Mountains example.

	G	ME[1](cm)	RMSE[2](cm)	SSIM[3]
Proposed method	2	-0.07 ± 0.20	21.75 ± 0.39	0.936 ± 0.001
Area-to-point	2	0.66 ± 0.24	18.32 ± 0.59	0.840 ± 0.003
Direct sampling	2	-0.42 ± 0.37	29.86 ± 0.66	0.914 ± 0.002
Bicubic	2	0.19	25.42	0.946
Proposed method	4	0.00 ± 0.21	22.04 ± 0.43	0.906 ± 0.001
Area-to-point	4	0.62 ± 0.25	19.72 ± 0.58	0.803 ± 0.003
Direct sampling	4	-0.59 ± 0.25	23.73 ± 0.27	0.893 ± 0.001
Bicubic	4	0.24	29.94	0.917

[1] mean error; [2] root-mean-square error; [3] structural similarity; Values represent average statistics plus or minus one standard deviation over 20 realizations
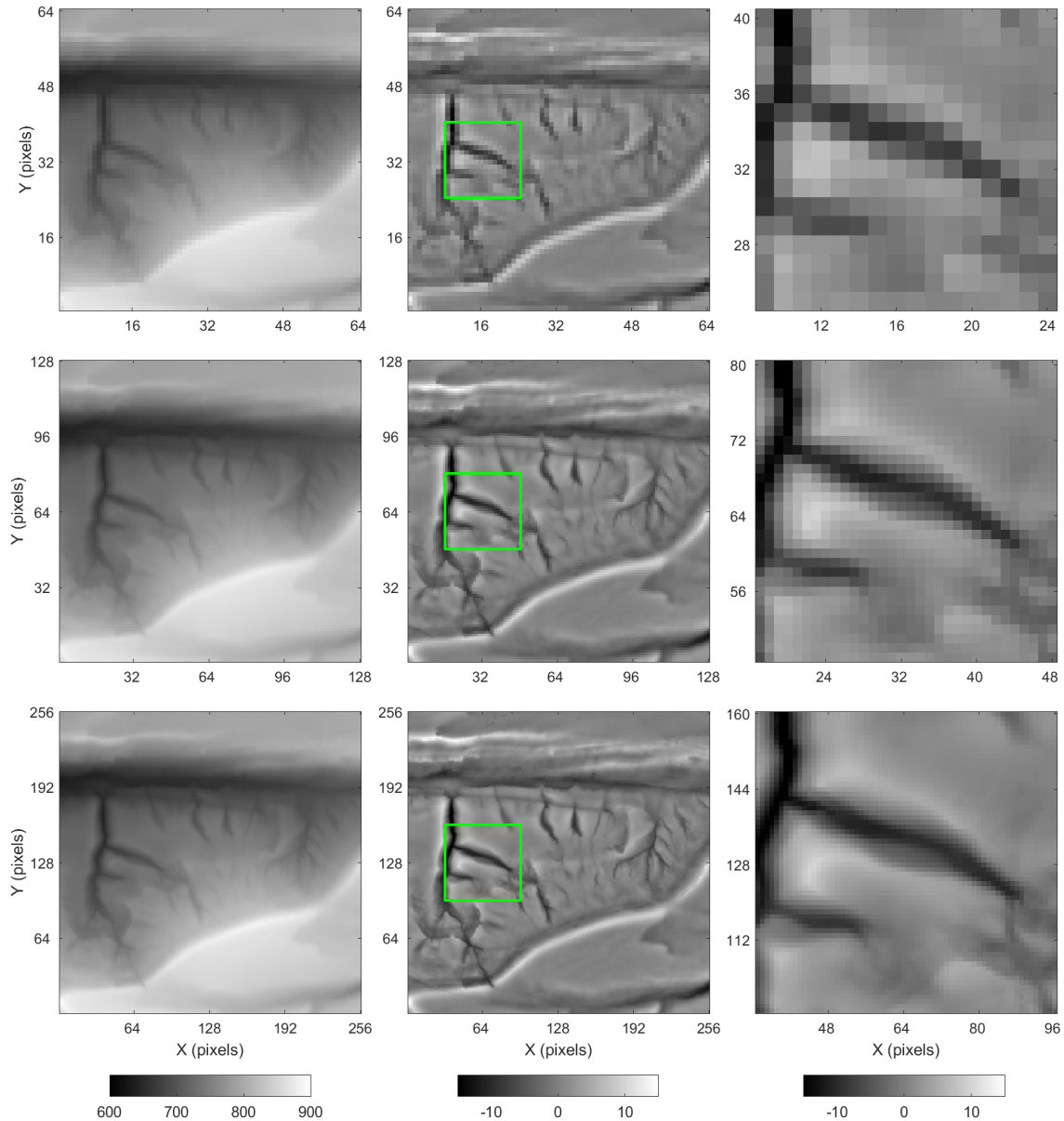
Figure 3.14: The Jura Mountains reference DEMs. *Top left*: coarse-resolution DEM. *Top center*: coarse-resolution residual DEM. *Top right*: coarse-resolution zoom. *Middle left*: medium-resolution DEM. *Middle center*: medium-resolution residual DEM. *Middle right*: medium-resolution zoom. *Bottom left*: fine-resolution DEM. *Bottom center*: fine-resolution residual DEM. *Bottom right*: fine-resolution zoom. The residual component of the trended DEMs has a vertical exaggeration factor of $2\times$. Green boxes highlight the magnified area. Colorbars' unit is m.
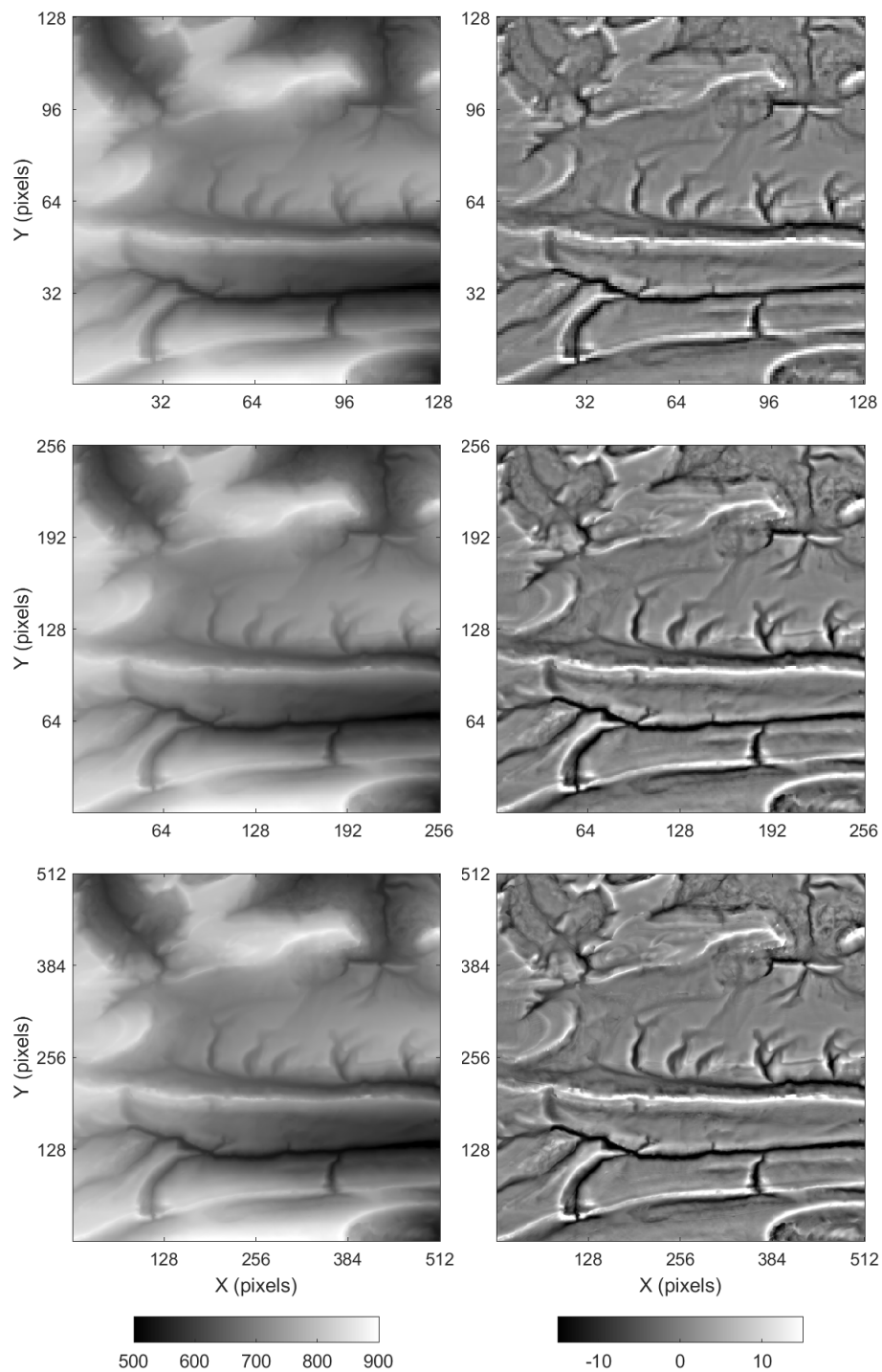
Figure 3.15: The Jura Mountains training DEMs. *Top left*: coarse-resolution DEM with trend. *Top right*: coarse-resolution residual DEM. *Middle left*: medium-resolution DEM with trend. *Middle right*: medium-resolution residual DEM. *Bottom left*: fine-resolution DEM with trend. *Bottom right*: fine-resolution residual DEM. The residual component of the trended DEMs has a vertical exaggeration factor of $2\times$. Colorbars' unit is m.
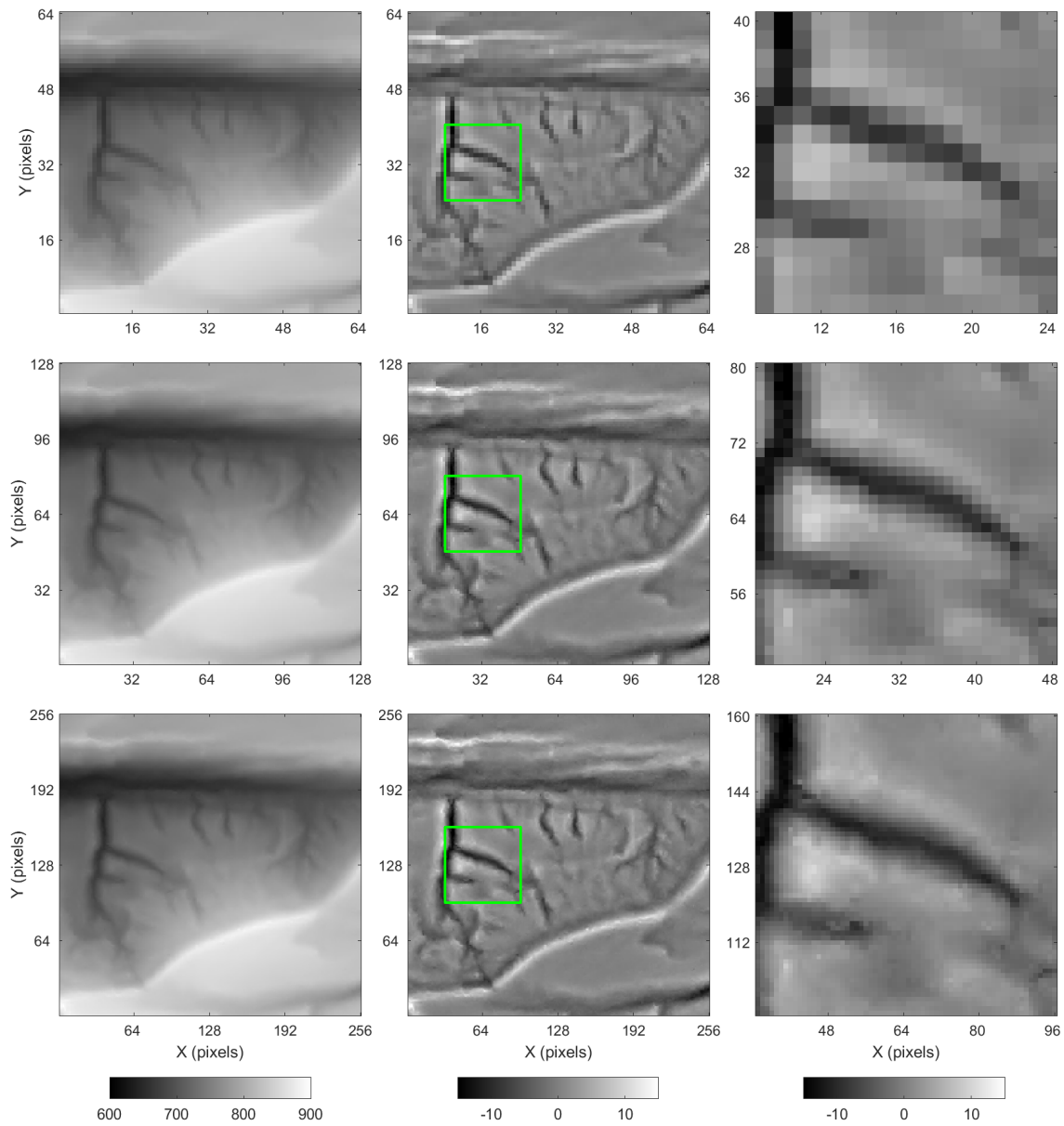
Figure 3.16: The Jura Mountains downscaled DEMs produced with the proposed algorithm. *Top left*: coarse-resolution DEM. *Top center*: coarse-resolution residual DEM. *Top right*: coarse-resolution zoom. *Middle left*: simulated medium-resolution DEM. *Middle center*: simulated medium-resolution residual DEM. *Middle right*: medium-resolution zoom. *Bottom left*: simulated fine-resolution DEM. *Bottom center*: simulated fine-resolution residual DEM. *Bottom right*: fine-resolution zoom. The residual component of the trended DEMs has a vertical exaggeration factor of 2×. Green boxes highlight the magnified area. Colorbars' unit is m.
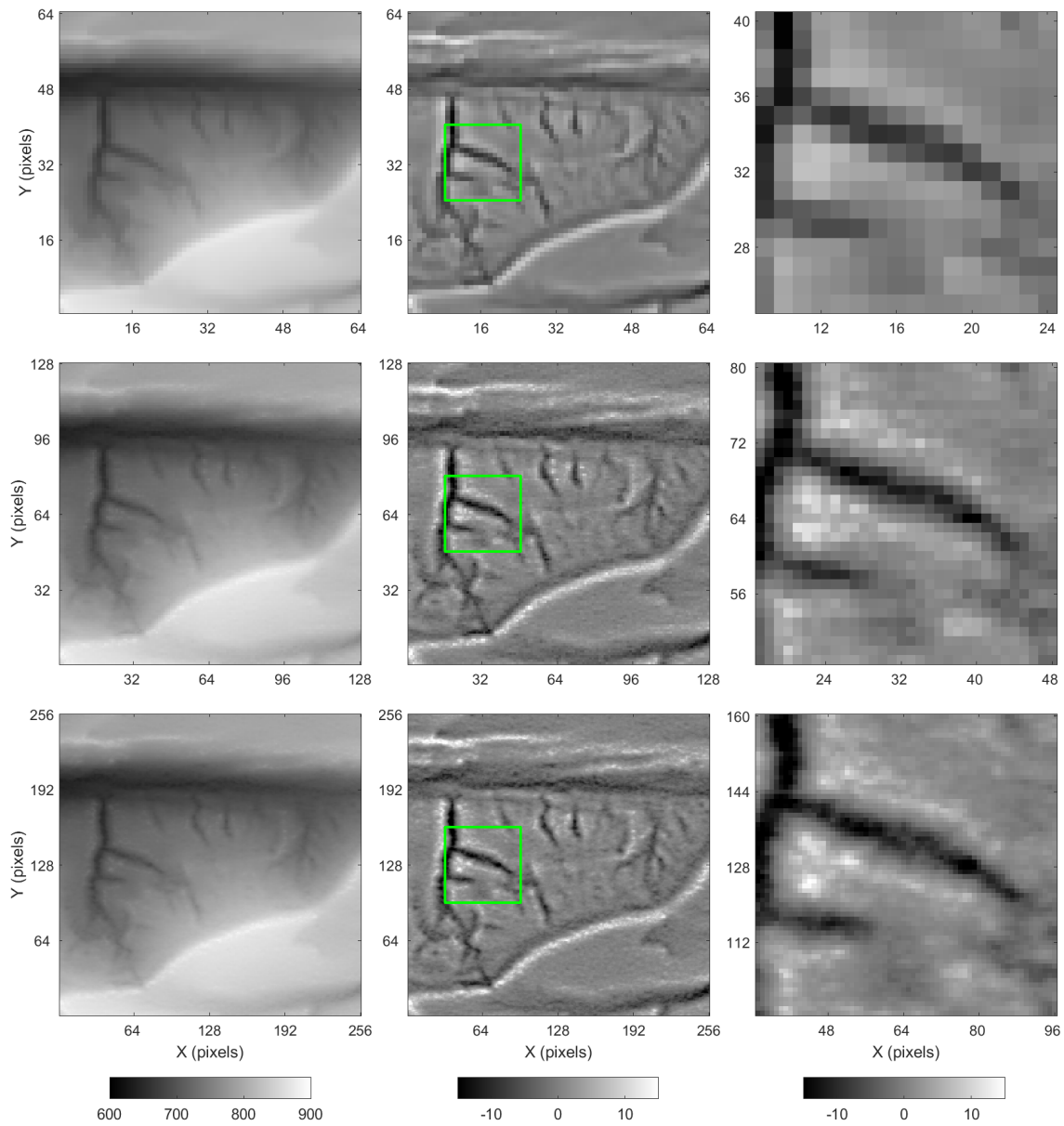
Figure 3.17: The Jura Mountains downscaled DEMs produced with area-to-point simulation. *Top left*: coarse-resolution DEM. *Top center*: coarse-resolution residual DEM. *Top right*: coarse-resolution zoom. *Middle left*: simulated medium-resolution DEM. *Middle center*: simulated medium-resolution residual DEM. *Middle right*: medium-resolution zoom. *Bottom left*: simulated fine-resolution DEM. *Bottom center*: simulated fine-resolution residual DEM. *Bottom right*: fine-resolution zoom. The residual component of the trended DEMs has a vertical exaggeration factor of $2\times$. Green boxes highlight the magnified area. Colorbars' unit is m.
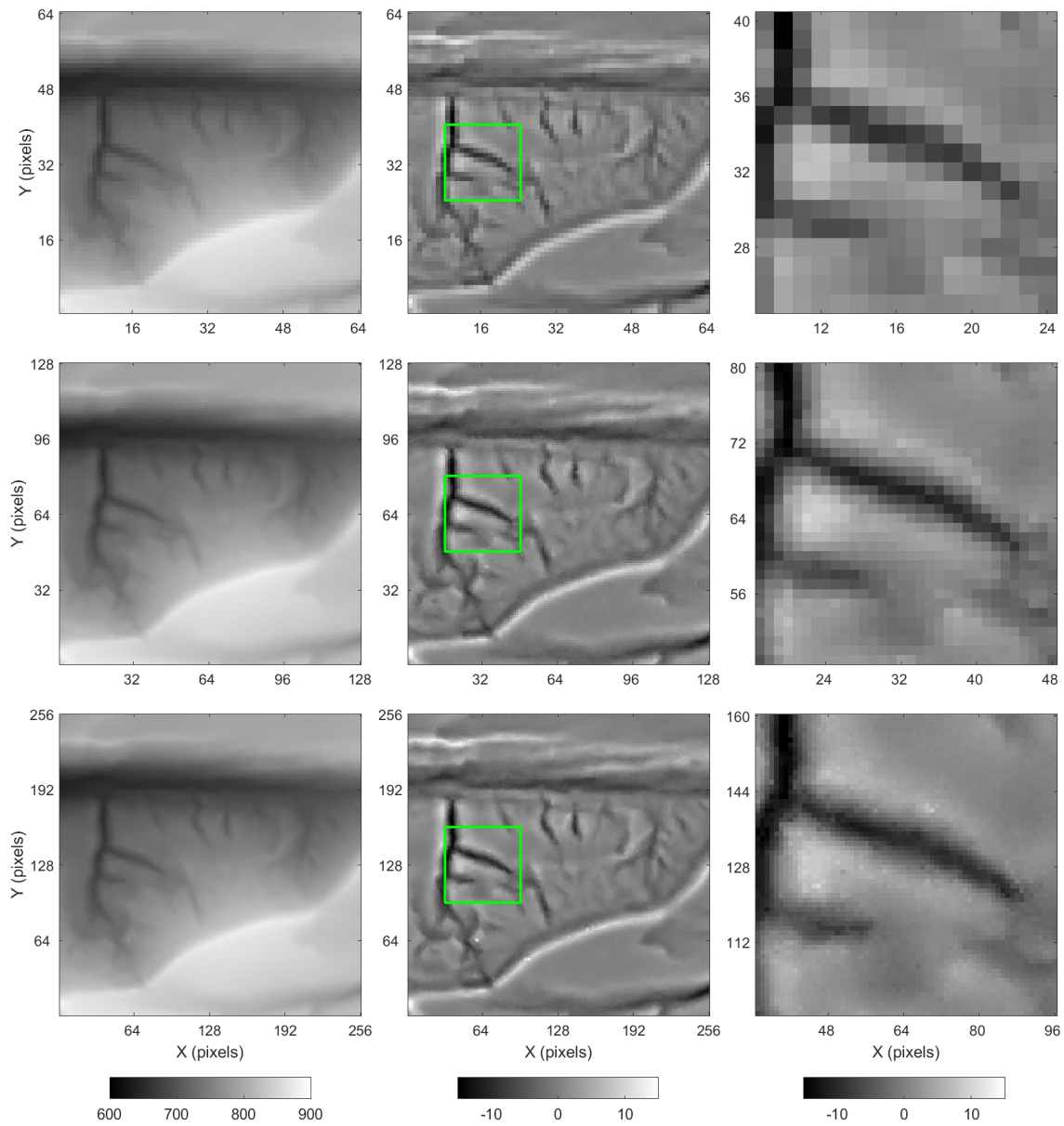
Figure 3.18: The Jura Mountains downscaled DEMs produced with direct sampling. *Top left*: coarse-resolution DEM. *Top center*: coarse-resolution residual DEM. *Top right*: coarse-resolution zoom. *Middle left*: simulated medium-resolution DEM. *Middle center*: simulated medium-resolution residual DEM. *Middle right*: medium-resolution zoom. *Bottom left*: simulated fine-resolution DEM. *Bottom center*: simulated fine-resolution residual DEM. *Bottom right*: fine-resolution zoom. The residual component of the trended DEMs has a vertical exaggeration factor of 2×. Green boxes highlight the magnified area. Colorbars' unit is m.
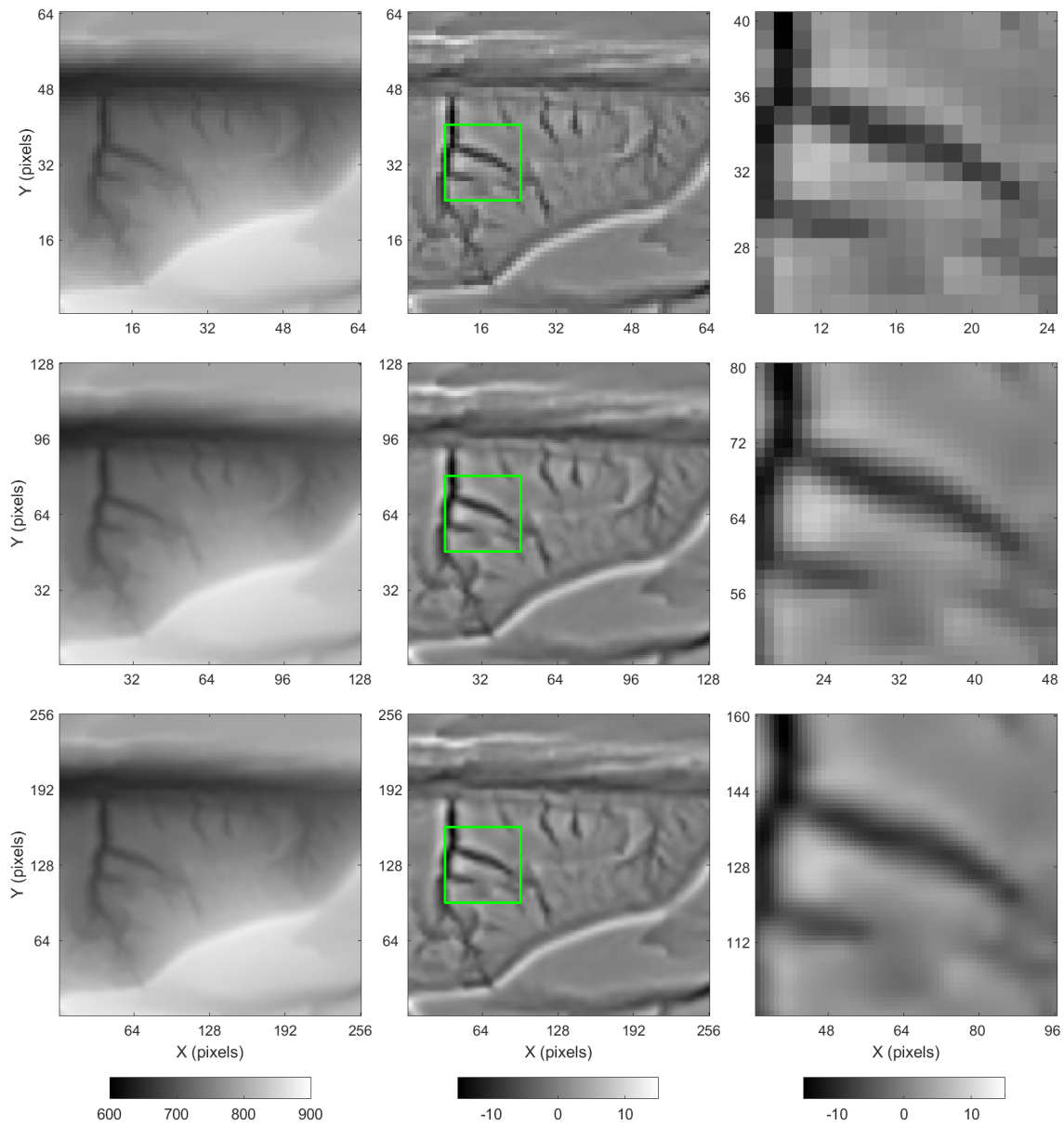
Figure 3.19: The Jura Mountains downscaled DEMs produced with bicubic interpolation. *Top left*: coarse-resolution DEM. *Top center*: coarse-resolution residual DEM. *Top right*: coarse-resolution zoom. *Middle left*: interpolated medium-resolution DEM. *Middle center*: interpolated medium-resolution residual DEM. *Middle right*: medium-resolution zoom. *Bottom left*: interpolated fine-resolution DEM. *Bottom center*: interpolated fine-resolution residual DEM. *Bottom right*: fine-resolution zoom. The residual component of the trended DEMs has a vertical exaggeration factor of $2\times$. Green boxes highlight the magnified area. Colorbars' unit is m.
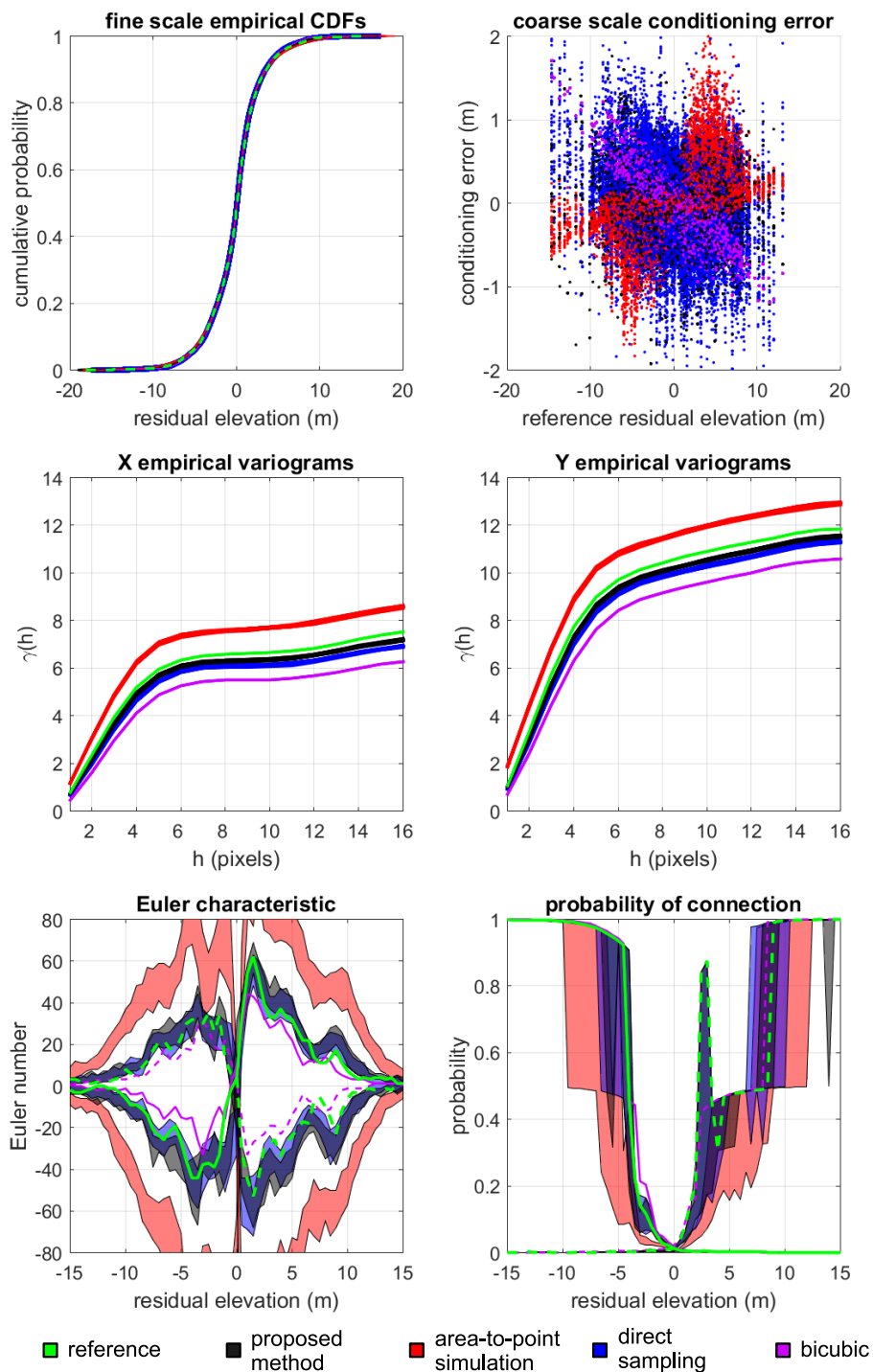
Figure 3.20: Validation of the Jura Mountains example ($G = 2$). *Top left*: sub-pixel empirical CDFs. *Top right*: scatter plots between reference coarse residual elevation and conditioning error. *Middle left*: sub-pixel empirical variograms along the X axis. *Middle right*: sub-pixel empirical variograms along the Y axis. *Bottom left*: fine-scale Euler characteristic. *Bottom right*: fine-scale probability of connection.
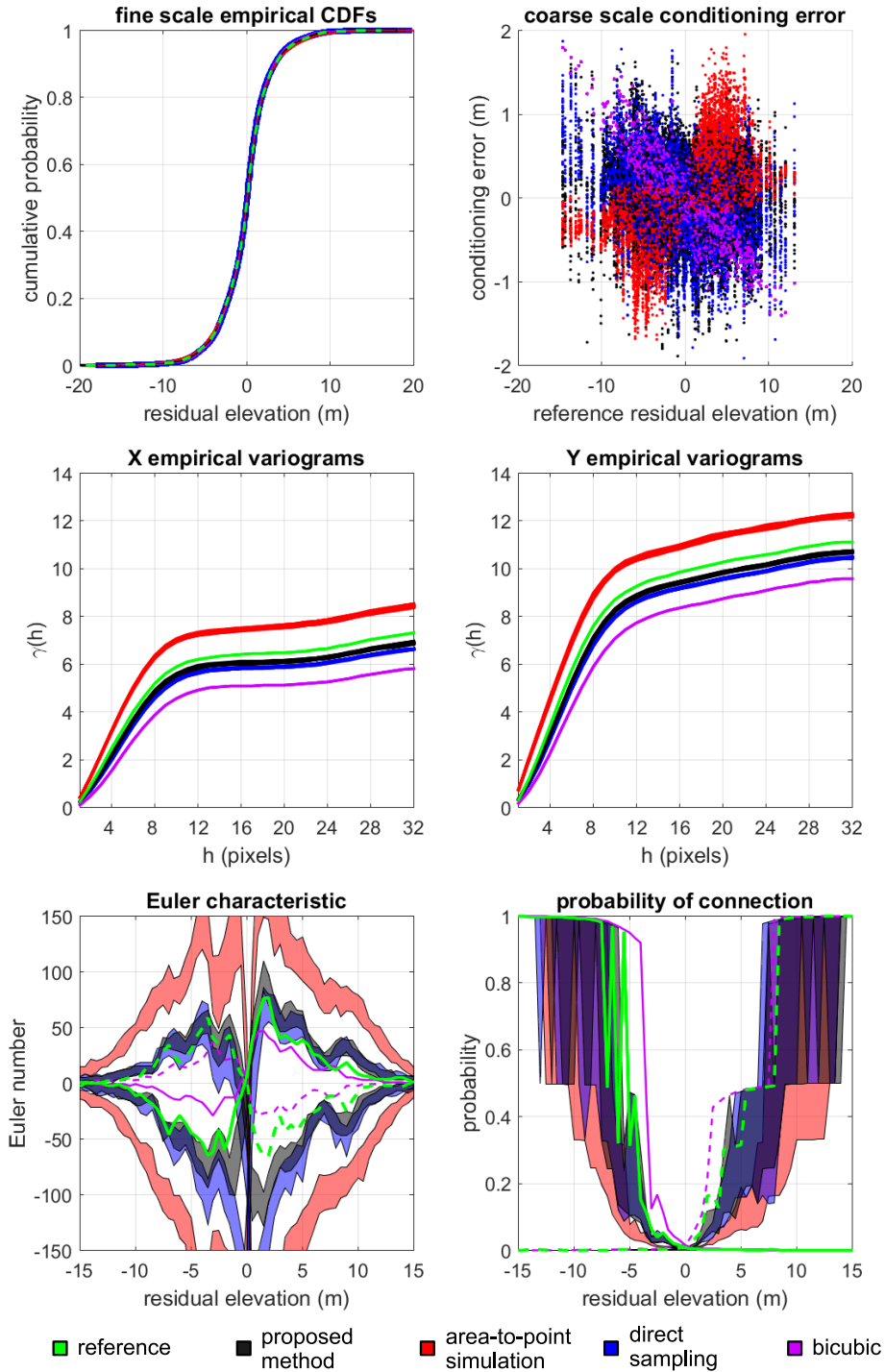
Figure 3.21: Validation of the Jura Mountains example ($G = 4$). *Top left*: sub-pixel empirical CDFs. *Top right*: scatter plots between reference coarse residual elevation and conditioning error. *Middle left*: sub-pixel empirical variograms along the X axis. *Middle right*: sub-pixel empirical variograms along the Y axis. *Bottom left*: fine-scale Euler characteristic. *Bottom right*: fine-scale probability of connection.
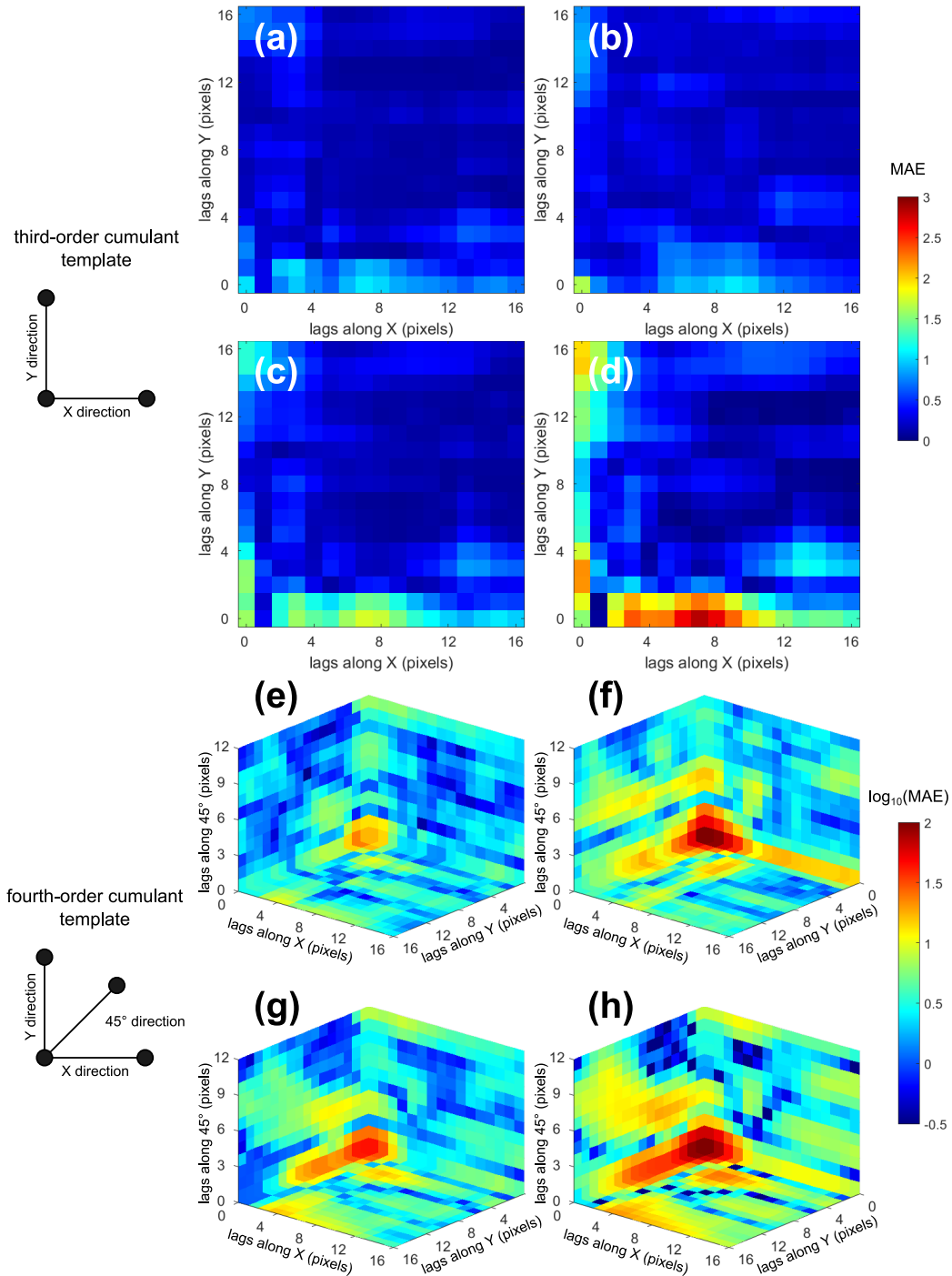
Figure 3.22: MAE between simulated and reference third- and fourth-order cumulant maps from the Jura Mountains example ($G = 2$). *Top*: third-order cumulant MAE maps for **a** proposed method, **b** area-to-point simulation, **c** direct sampling, and **d** bicubic interpolation. Colorbar unit is m^3. *Bottom*: fourth-order cumulant MAE maps for **e** proposed method, **f** area-to-point simulation, **g** direct sampling, and **h** bicubic interpolation. Colorbar unit is m^4.
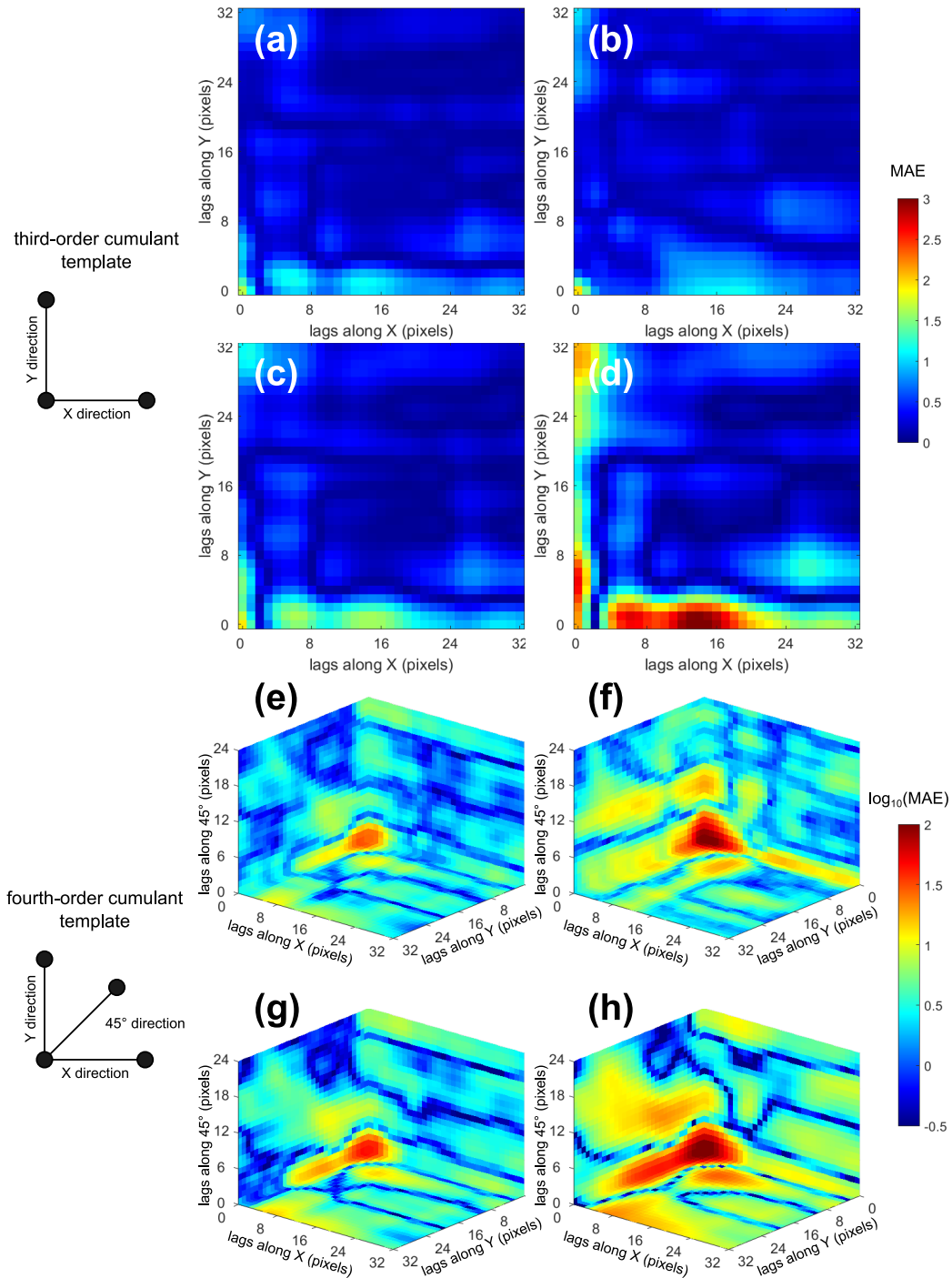
Figure 3.23: MAE between simulated and reference third- and fourth-order cumulant maps from the Jura Mountains example ($G = 4$). *Top*: third-order cumulant MAE maps for **a** proposed method, **b** area-to-point simulation, **c** direct sampling, and **d** bicubic interpolation. Colorbar unit is m^3. *Bottom*: fourth-order cumulant MAE maps for **e** proposed method, **f** area-to-point simulation, **g** direct sampling, and **h** bicubic interpolation. Colorbar unit is m^4.

3.5   Discussion

Results demonstrate that the proposed method is able to downscale coarse images with trends and reproduce target fine-scale statistics. Simulations in both case studies are unbiased regarding conditioning to coarse-resolution measurements. Fine-scale topological properties such as the Euler characteristic and the probability of connection curves are also relatively well reproduced. Results also indicate good reproduction of second-, third-, and fourth-order statistics.

The exhaustive scanning of the training image for the K best training data events allows the proposed framework to handle non-stationary data sets. This is often the case when one has to deal with non-constructed training images or simulate non-repetitive structures. The distance-to-probability transformation function improves the reproduction of less frequent spatial structures and values by assigning higher conditional probabilities to the training data events that are more compatible with the local conditioning data. At the same time, it also allows the algorithm to generate variability on output realizations whenever multiple compatible data events are available in the training image. Building each local CPDF based upon the distance-to-probability transformation function is particularly important within the proposed iterative downscaling framework. Since fine-scale features are conditionally simulated based on previously simulated data, the propagation of errors across scales can potentially compromise the simulation of finer resolution features. The framework is also particularly suitable for simulating textures that might contain both repetitive and non-repetitive structures. Conversely, traditional two-point statistics simulation methods infer the variogram model and histogram transformations using all available data. Therefore, they have trouble reproducing location-specific patterns and statistics. This also extends to MPS simulation algorithms which compute conditional probabilities based upon the entire training image.

Although the realizations globally honor the statistics and structural properties of the reference data, not all fine-scale features can be recovered on the downscaled DEMs. Visually, it is noticeable that the texture of the realizations (Figs. 3.6 and 3.16) tends to be less sharp than the corresponding textures found on the reference fine-resolution DEMs (Figs. 3.4 and 3.14). While the algorithm is to be able to generate realizations that depict the same type of variogram structures present in the reference fine-resolution DEMs, simulations tend to underestimate the variability of the reference data. This is a common problem for conditional MPS simulations. Straubhaar et al. (2016) reported the same phenomenon while running simulations constrained to block data, and Oriani et al. (2017)

experienced a similar effect when simulating rainfall fields conditioned to weather state variables and DEMs. In our experiments, this effect is more evident when downscaling high-complexity terrains, such as the Western Alps example. One possible reason for this variance underestimation is that many of the structures to be recovered are significantly smaller than the pixel size of the coarse-resolution image. In the super-resolution mapping literature, such scenario is classified as an L-resolution type problem (Atkinson, 2009). Results indicate that some of these structures cannot be properly simulated when relying solely on coarse-scale observations and previously simulated data. Imposed local conditioning constrains combined with the finite size of the training image may also play a role in preventing proper reproduction of such features. The addition of auxiliary fine-scale covariates (e.g. high-resolution remote sensing imagery) might improve the simulation of these sub-pixel features. Further work is required to determine the magnification factor limits for different types of terrain and data sets.

3.6 Conclusions

This contribution presents a novel MPS simulation algorithm for downscaling images with trends. The method is illustrated with examples using DEMs from two geomorphologically distinct mountain ranges in Switzerland. Results show that the method is capable of generating fine-resolution realizations that honor the input coarse-resolution image and reproduce key structural properties and statistics.

To address the presence of trends in the data sets, the target variable is decomposed into a trend and a residual component at multiple scales. The trend component is downscaled with a deterministic interpolation method. The sub-pixel residual variable is simulated with a multi-scale sequential simulation framework. In order to improve the conditioning to coarse-scale data, we propose the adoption of kernel weighting when computing the distances between target and training data events.

We have introduced a new approach for integrating different support data in the context of distance-based MPS simulation. The proposed framework is well-suited for simulating images with non-repetitive structures, such as DEMs. The generality of the framework also offers the possibility to streamline the integration of other types of covariates. The transformation of distances between multivariate data events (with possibly different units or orders of magnitude) into probabilities facilitates the integration of multi-sensor data. The proposed scheme also eases the implementation of error/bias control systems (e.g. servo

systems) (Remy et al., 2009) through direct manipulation of conditional probabilities.

Future work will explore the conflation of auxiliary variables to improve the quality and reduce the uncertainty associated with the downscaling process. The development of strategies to mitigate the generation of random noise on simulated realizations without causing loss of variability has particular importance for applications where the spatial structure of the downscaled image has an effect on the transfer function response. Particular effort will be put also on the development of an automated calibration procedure of the algorithm parameters based on a given training image. Additional research topics that should be investigated are the formulation of a quantitative criterion for selecting the training image, the evaluation of different distance-to-probability transformation functions and their impact on the structural quality and variability of simulated realizations, and the adaptation of the algorithm for supporting tridimensional data sets.

Chapter 4

An automation framework for downscaling of digital elevation models with multiple-point statistics simulation

MPS simulation algorithms are notably difficult to parameterize, often requiring manual parameter tuning and laborious sensitivity analyses. Automation of these algorithms is of central importance for the design and operation of efficient, low-cost alternatives for fine-resolution probabilistic terrain mapping. This chapter addresses the second objective of this thesis: ii. automation of the downscaling process.

In this chapter, an automation framework for MPS-driven downscaling algorithms is proposed. The approach is demonstrated with the algorithm introduced in Chapter 3. An automation routine based on simulated annealing and cross-validation techniques is used to infer optimal algorithm parameters by framing the parameter calibration task as an optimization problem. The approach relies on the training data set for automatic calibration of the algorithm parameters prior to the downscaling of the coarse-resolution target DEM.

This chapter will be submitted to Mathematical Geosciences as an original research article. Therefore, readers must be aware of potential differences between the future publication and this chapter.

4.1 Introduction

Fine-resolution digital elevation models (DEMs) are essential for the study of Earth's surface processes. A compilation of studies on the effect of DEM spatial resolution and its impact on a wide range of hydrologic derivatives can be found in Wechsler (2007). Fine-resolution DEMs are more appropriate for landscape representation and hydrological simulations (Zhang and Montgomery, 1994). The spatial resolution of DEMs also plays a significant role in hydraulic modeling for flood warning systems (Lamichhane and Sharma, 2018) and urban flood assessment (Leitão and de Sousa, 2018). The extraction of drainage networks (McMaster, 2002), terrain derivatives (Kienzle, 2003), topographic indexes (Vaze et al., 2010; Mukherjee et al., 2013), analysis of surface texture (Trevisani et al., 2012), spatial patterns of saturated areas (Hoang et al., 2018), and the accuracy of snow estimates (Sohrabi et al., 2019) are also affected by the spatial resolution of the input DEM. Nevertheless, most of Earth's topography is mapped at relatively coarse spatial and temporal resolutions (Yamazaki et al., 2017). Spaceborne DEMs (Wilson, 2012) are one of the most common data sources for characterizing Earth's relief structures. Although useful for large-scale terrain analysis, satellite-derived DEMs are often not suitable for modeling fine-scale phenomena.

Statistical downscaling is one of the main approaches for enhancing the spatial resolution of digital images. An overview of different techniques in the field of remote sensing can be found in Atkinson (2013). Being an ill-posed problem, downscaling can be adequately addressed with stochastic methods (Bertero and Boccacci, 1998). Geostatistical simulation-based techniques (Goovaerts, 1997) are of special interest owing to their conditioning capabilities and relatively short processing time. By generating multiple scenarios, one can assess the uncertainty associated with the predictions and propagate it throughout subsequent models (e.g. transfer functions). Traditional two-point statistics techniques characterize spatial heterogeneity through covariance function models (Kyriakidis and Yoo, 2005; Boucher and Kyriakidis, 2007; Liu and Journel, 2009). These methods have been applied for conflation of terrain elevation data (Kyriakidis et al., 1999) and downscaling of coarse-resolution DEMs with auxiliary maps (Hengl et al., 2008). The main issue associated with their application for modeling terrain elevation data is the limited ability of the variogram to describe non-stationary and low-entropy textures. Multiple-point statistics (MPS) (Remy et al., 2009) consists of a branch of geostatistics concerned with the characterization and simulation of such types of structures. MPS algorithms describe the spatial variability

through the usage of an analog data set known as a training image. Realizations of random fields are generated as a stochastic imaging process. An algorithm is used to identify and transfer similar spatial features from the training image based on template matching. This enables a better description and simulation of complex textures. Examples of MPS-driven downscaling methods are the approches developed by Boucher (2009), Mariethoz et al. (2011), Straubhaar et al. (2016) and (Rasera et al., 2020b,a). Applications of MPS in geomorphometry include the simulation of braided river DEM time series (Pirot et al., 2014), terrain elevation data fusion (Tang et al., 2015), and downscaling of coarse-resolution DEMs (Rasera et al., 2020b,a).

One of the main challenges for practical application of MPS simulation methods is their parametrization. MPS algorithm parameters are often non-intuitive and cumbersome to set up. Parameters are algorithm-specific and their calibration is data dependent. As a result, extensive sensitivity analyses are often employed (Liu, 2006; Meerschman et al., 2013). In addition, parameters must be re-calibrated if either the conditioning or training data are updated. Nonlinear programming provides a potential framework for automatizing the calibration of MPS algorithms. Baninajar et al. (2019) proposed the application of stochastic optimization for automatic parameter calibration based on a sub-sampling cross-validation setting. Multiple gaps are randomly placed in the training image and subsequently simulated using the remaining parts of the image as training data. The algorithm parameters are optimized using the simultaneous perturbation gradient approximation method (Spall, 1992) by minimizing the mean-squared error between the realizations and the original reference data in the gaps. Dagasan et al. (2018) applied the simulated annealing algorithm (Kirkpatrick et al., 1983) for calibration of MPS simulation parameters. The approach aims at minimizing the dissimilarity between pattern statistics from the conditioning data and the simulated realizations. The objective function used in the study was the Jensen-Shannon divergence between multiple-point histograms (Boisvert et al., 2010) using the smooth histogram method (Melnikova et al., 2015).

The two aforementioned schemes provide a mathematical framework for the determination of algorithm parameters and efficient alternatives for parameter calibration tasks. Yet, there are several issues associated with both approaches. The framework proposed by Baninajar et al. (2019) is grounded on sub-sampling cross-validation, which means that not all available data are used for both training and validation. This strategy might be inappropriate if the training image is non-stationary, as not all relevant spatial structures may be used for cross-validation. In addition, defining the dimensions, placement, and number of gaps in the training image can be challenging. The approach presented by Dagasan et al.

(2018) relies solely on the conditioning data for calibrating parameters. This may lead to biased pattern reproduction due to sample spacing, uneven sample density, and preferential sampling. If the sampling grid is sparse relative to the patterns' spatial variation, the reproduction of textural features finer than the sample spacing is not explicitly taken into account in the optimization process. In order to control the reproduction of fine-scale structures, external prior information must be injected in the form of a finer-resolution training image or expert knowledge.

In this contribution, an automatic calibration framework for MPS-based downscaling is proposed and presented in the context of geomorphometric applications. The developed approach addresses the main shortcomings of the aforementioned parameter calibration strategies by providing a robust alternative for handling of non-stationary data sets, and an explicit control over the reproduction of spatial structures finer than the sampling grid size. The procedure is illustrated with an updated version of the stochastic downscaling algorithm developed by Rasera et al. (2020b,a). The algorithm parameters are inferred from the training data using cross-validation. An optimization process combines the simulated annealing algorithm (Kirkpatrick et al., 1983) and the K-fold cross-validation technique (Hastie et al., 2009; Pohjankukka et al., 2017) for estimating the set of downscaling parameters that minimizes an objective (or energy) function. This function evaluates the statistical and structural accuracy of the simulated realizations. It is defined as a dissimilarity measure between the reference spatial features in the training data and those of the realizations. The minimization of the system's energy ultimately results in the maximization of the structural similarity between the downscaling realizations and the fine-resolution training data. Guidelines for the formulation of the objective function are discussed. The proposed framework is demonstrated by case studies using DEMs from the Alaska Range, the Appalachian Mountains, and the Central Lowlands in South Australia.

This chapter is organized as follows. In Section 4.2, we introduce an updated version of the MPS-driven downscaling algorithm originally developed by (Rasera et al., 2020b,a) and its associated parameters. Section 4.3 reviews the K-fold cross-validation and the simulated annealing techniques, and discusses the proposed automatic parametrization framework. Section 4.4 documents the algorithm parametrization and the downscaling results for the three case studies. Finally, in Section 4.5, we conclude the chapter by summarizing the framework and outlining future research topics.

4.2 Stochastic downscaling of digital elevation models with multiple-point statistics

This section introduces the stochastic framework for representing terrain elevation data and the MPS algorithm developed by Rasera et al. (2020b,a) for downscaling of images with trends. Subsection 4.2.1 introduces the modeling of digital terrain elevation data as a stochastic spatial signal. The MPS simulation algorithm for downscaling DEMs is described in Subsection 4.2.2. Novel functionalities of the algorithm are also discussed. For more information about the method the reader is referred to Rasera et al. (2020b,a).

4.2.1 Stochastic representation of terrain elevation data

In this work, elevation data in raster-type DEMs are represented as a stochastic spatial signal. This signal can be decomposed into two variables: a deterministic low-frequency trend, and a stochastic higher-frequency residual. The trend component encompasses large-scale topographic structures, such as mountains and valleys, whereas the residual represents small-scale geomorphic features like ridgelines and drainage networks.

Let z_V denote a coarse-resolution target DEM, with $z_V(\mathbf{u})$ being the terrain elevation at the coarse pixel V centered at the location $\mathbf{u}$, where $\mathbf{u} = [x, y]$ corresponds to a two-dimensional position vector in a projected Cartesian coordinate system. In addition, let $z_v(\mathbf{u})$ be the fine-resolution elevation measurement assigned to a fine-resolution pixel v in a co-registered fine-resolution DEM represented by z_v. The coarse-to-fine resolution ratio between z_V and z_v is defined as $G = \sqrt{|V|/|v|}$, where $|V|$ and $|v|$ are the areas of the coarse and fine-resolution pixels, respectively.

In a geostatiscal framework, the measurements $z_V(\mathbf{u})$ and $z_v(\mathbf{u})$ are interpreted as realizations of the continuous random variable $Z(\mathbf{u})$

$$Z(\mathbf{u}) = m(\mathbf{u}) + R(\mathbf{u}), \tag{4.1}$$

where $Z(\mathbf{u})$ denotes either coarse or fine random variables $Z_V(\mathbf{u})$ and $Z_v(\mathbf{u})$; $m(\mathbf{u})$ is its deterministic trend component; and $R(\mathbf{u})$ is its associated complementary stochastic residual component.

In practice, $Z(\mathbf{u})$ also has an intrinsic measurement error component $\epsilon(\mathbf{u})$. This term

represents errors related to the remote sensing acquisition method, local terrain surface properties, and the DEM generation process itself. In most cases, $\epsilon(\mathbf{u})$ can only be assessed by validation against a more accurate data set (Kolecka and Kozak, 2014; Mukul et al., 2017). For simplification purposes, we assume that the contribution of the error component is negligible (i.e. $\epsilon(\mathbf{u}) \approx 0$). An overview of the different types of measurement errors found in spaceborne DEMs and error filtering techniques is provided by Yamazaki et al. (2017).

The trend $m(\mathbf{u})$ is estimated by applying an appropriate spatial low-pass filter on $z(\mathbf{u})$. The estimator $\hat{m}(\mathbf{u})$ is defined as a weighted linear combination of $z(\mathbf{u})$ and its neighboring data $\{z(\mathbf{u} + \mathbf{h}_j), j = 1, \ldots, n\}$ lying within a search radius ρ

$$\hat{m}(\mathbf{u}) = \sum_{j=0}^{n} \lambda(\mathbf{h}_j)\, z(\mathbf{u} + \mathbf{h}_j) \quad \text{with} \quad \sum_{j=0}^{n} \lambda(\mathbf{h}_j) = 1, \tag{4.2}$$

where $\mathbf{h}_j$ corresponds to the set of $n + 1$ coordinates lag vectors that radiate from $\mathbf{u}$, with $z(\mathbf{u}) = z(\mathbf{u} + \mathbf{h}_0)$, and $\lambda(\mathbf{h}_j)$ are weights given by a kernel function. A realization of $R(\mathbf{u})$, represented by $r(\mathbf{u})$, is the complement of $\hat{m}(\mathbf{u})$.

The weights $\lambda(\mathbf{h}_j)$ of the spatial low-pass filter are computed using a Gaussian radial basis function kernel

$$\lambda(\mathbf{h}_j) = \frac{1}{2\pi\sigma^2\beta} \exp\left(-\frac{\|\mathbf{h}_j - \mathbf{h}_0\|_2^2}{2\sigma^2} \right), \tag{4.3}$$

where $\sigma > 0$ is the kernel shape parameter, and $\beta > 0$ is the normalizing constant, which corresponds to the sum of all kernel weights.

4.2.2 Downscaling terrain elevation with multiple-point statistics simulation

A new version of the MPS downscaling algorithm developed by Rasera et al. (2020b,a) is applied for enhancing the spatial resolution of DEMs. The updated algorithm offers additional functionalities for scanning the training data set, parametrizing the distance functions, and customizing the integration of coarse- and fine-scale data. The algorithm relies on a pair of co-registered coarse- and fine-resolution training DEMs from an analog to construct a dual-resolution training data set. This data structure describes the correspondence between

coarse- and fine-scale topographic patterns. The target DEM spatial resolution is gradually magnified by a series of conditional iterations of the algorithm. In the first iteration, realizations are conditioned to the coarse-resolution target DEM, whereas in the subsequent iterations, they are conditioned to previous iteration outputs. The simulation of sub-pixel features is conducted by direct transfer of fine-scale information from the dual-resolution training data to the target DEM.

Fundamentally, the goal is to predict the fine-scale variables $\hat{m}_v(\mathbf{u})$ and $R_v(\mathbf{u})$, so that $Z_v(\mathbf{u})$ may be reconstructed with Equation (4.1). As $\hat{m}_v(\mathbf{u})$ and $R_v(\mathbf{u})$ cannot be directly computed, their inference is based on an interpolated version of $\hat{m}_V$ and prior information in the dual-resolution training data. The downscaling of $\hat{m}_V(\mathbf{u})$ is performed with the bicubic interpolation method (Keys, 1981), thus allowing to obtain its fine-scale counterpart $\hat{m}_v(\mathbf{u})$. The residual variable $R_V(\mathbf{u})$ is downscaled with a quasi-pixel-based simulation scheme (Rasera et al., 2020b,a). The MPS simulation algorithm $F(\cdot)$ is used to generate S conditional simulated realizations of the fine-resolution multivariate random variable $\mathbf{R}_v(\mathbf{u})$, denoted as $\mathbf{r}_v^{(s)}(\mathbf{u}), s = 1 \ldots, S$

$$\mathbf{R}_v(\mathbf{u}) = F(\boldsymbol{\theta}, \Psi \mid \Omega) \mapsto \{\mathbf{r}_v^{(s)}(\mathbf{u}), s = 1, \ldots, S\}, \tag{4.4}$$

where $\boldsymbol{\theta}$ is the $(L \times 1)$ vector of algorithmic parameters associated with $F(\cdot)$, Ψ is the dual-resolution training data built from $z_V^{(t)}$ and $z_v^{(t)}$, $\mid \Omega$ denotes the conditioning to available coarse information and previously simulated fine-resolution data, and $\mathbf{r}_v^{(s)}(\mathbf{u})$ consists of a fine-resolution simulated residual patch (i.e. a square array of residual elevation values). This contribution focuses on developing an automatic framework for inferring $\boldsymbol{\theta}$.

The flowchart in Figure 4.1 illustrates the DEM downscaling algorithm. The parametrization of the spatial low-pass filters and the bicubic interpolation processes is identical so that compatible terrain elevation data can be compared and transferred to the target DEM. Under the assumptions that $\epsilon(\mathbf{u}) \approx 0$ and $Z(\mathbf{u})$ corresponds to the average sensor response over its associated pixel, an artificial coarse-resolution training DEM may be constructed by linear upscaling of the input fine-resolution training DEM. The residual variables derived from the training DEMs are used to assemble the dual-resolution training data set.

The simulation of sub-pixel topographic structures that are consistent with both coarse-resolution conditioning data and training data is attained through a template matching framework. Residual spatial patterns are represented as data events. A data event comprises a set of spatially arranged residual elevation values centered at a reference location $\mathbf{u}$.
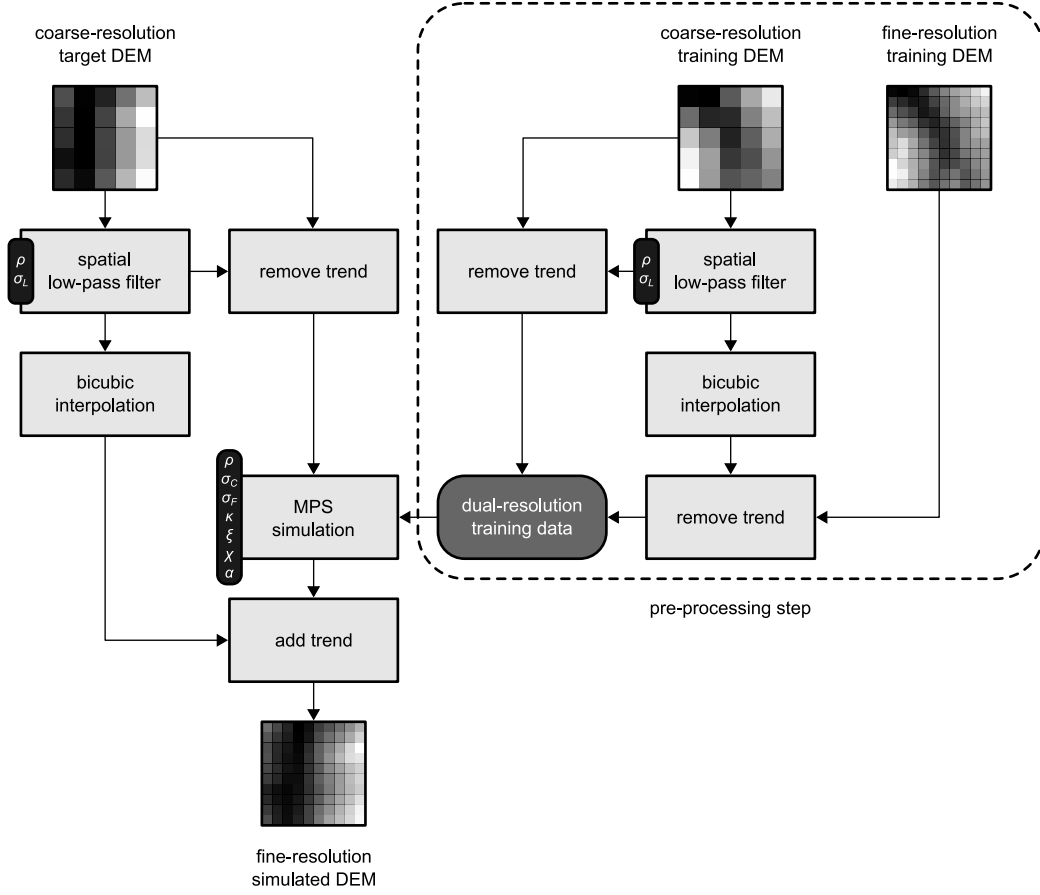
Figure 4.1: Downscaling algorithm flowchart (modified from Rasera et al. (2020b,a)). Processes are represented as gray rectangles. Intermediate data structures are depicted as rounded dark gray rectangles. Column-shaped black polygons on the left edge of processes boxes indicate the required input parameters.

Coarse-resolution data events are denoted as $d_V(\mathbf{u}_i) = \{r_V(\mathbf{u}_i + \mathbf{h}_j), j = 0, \ldots, n_V\}$, $i = 1, \ldots, N$, where N is the number of pixels in r_V. For each extracted conditioning data event, a search procedure for the κ-most similar training data events is carried out, where κ is a pre-specified parameter.

Local conditioning to coarse-resolution information is performed by restrictive sampling of training data events that minimize the coarse-scale distance function

$$D(d_V(\mathbf{u}_i), d_V^{(t)}(\mathbf{u})) = \left(\sum_{j=0}^{n_V} \lambda(\mathbf{h}_j) \left[r_V(\mathbf{u}_i + \mathbf{h}_j) - r_V^{(t)}(\mathbf{u} + \mathbf{h}_j) \right]^2 \right)^{1/2}, \qquad (4.5)$$

where $\lambda(\mathbf{h}_j)$ are kernel weights calculated with Equation (4.3), and $d_V^{(t)}(\mathbf{u}) = \{r_V^{(t)}(\mathbf{u} +$

$\mathbf{h}_j), j = 0, \ldots, n_V\}$ is a given coarse-resolution training data event. The number of pixels stored in the data events is defined based on the search radius ρ.

To impose control on the reproduction of sub-pixel features extracted from the dual-resolution training DEM, an additional distance function is computed. This function enforces the preferential sampling of compatible fine-scale training data events by taking into account previously simulated data $d_v(\mathbf{u}_i) = \{r_v^{(s)}(\mathbf{u}_i + \mathbf{h}_j), j = 1, \ldots, n_v(\mathbf{u}_i)\}$

$$D(d_v(\mathbf{u}_i), d_v^{(t)}(\mathbf{u})) = \left(\sum_{j=1}^{n_v(\mathbf{u}_i)} \lambda(\mathbf{h}_j) \Big[r_v^{(s)}(\mathbf{u}_i + \mathbf{h}_j) - r_v^{(t)}(\mathbf{u} + \mathbf{h}_j) \Big]^2 \right)^{1/2}, \qquad (4.6)$$

where $d_v^{(t)}(\mathbf{u})$ corresponds to a fine-resolution training data event. Equations (4.5) and (4.6) can be efficiently computed over the entire dual-resolution training data by performing convolutions in the frequency domain using the fast Fourier transform (FFT) algorithm (Kwatra et al., 2003).

The search for training data events is initially determined by coarse-resolution data as they are exhaustively known in r_V. As a result, the retrieval of fine-scale training data events is conditioned to the set of κ candidate coarse-resolution training data events. As the simulation progresses, $r_v^{(s)}$ becomes increasingly populated with previously simulated data. This information may turn useful for prediction due to its higher spatial resolution. For each coarse pixel visited along the sequential simulation path, the data stored in its co-registered fine-resolution conditioning data event are analyzed. At this point, the algorithm may switch the hierarchy of the training data events search procedure. The alteration is contingent to the quantity of data and their positioning relative to the pixel to be downscaled. If the scanning process is swapped favoring fine-scale information, the selection of co-registered pairs of coarse- and fine-scale training data events is primarily controlled by previously simulated data instead. The scanning process is altered if

$$\alpha_i = \sum_{j=1}^{n_v(\mathbf{u}_i)} \lambda(\mathbf{h}_j) \geq \xi, \qquad (4.7)$$

where $0 \leq \xi \leq 1$ is a control parameter.

Information derived from Equations (4.5) and (4.6) is integrated by converting the

distances between data events into local conditional probabilities through a distance-to-probability transformation function $\Phi(\cdot)$ (Rasera et al., 2020b,a; Hoffimann et al., 2017). The local coarse-scale derived conditioning probability is expressed as

$$\Pr\{\mathbf{R}_v(\mathbf{u}_i) = \mathbf{r}_v \mid d_V(\mathbf{u}_i)\} \propto \Phi(\mathbf{D}_V), \tag{4.8}$$

where $\mathbf{D}_V$ is a $(\kappa \times 1)$ vector which stores the coarse-scale distance function outputs associated with $d_V(\mathbf{u}_i)$. Fine-scale conditional probabilities are computed in a similar fashion. The formulation of $\Phi(\cdot)$ is described in Rasera et al. (2020b,a).

Fine-resolution data are simulated by sampling local conditional probability distribution functions (CPDFs). Probabilities derived from coarse- and fine-scale data are aggregated with the log-linear pooling operator (Allard et al., 2012). The local probability aggregation weight for fine-resolution data, denoted by α_i, can be either dynamic (i.e. defined as a function of the kernel weights associated with the neighboring informed fine pixels) or static (i.e. set to a constant value α, $\forall i = 1, \ldots, N$) based on a second control variable χ

$$\alpha_i = \begin{cases} \sum_{j=1}^{n_v(\mathbf{u}_i)} \lambda(\mathbf{h}_j), & \text{if } \chi = \text{true} \\ \alpha, & \text{otherwise} \end{cases} \tag{4.9}$$

consequently, the weight for coarse-scale data is calculated as $1 - \alpha_i$. Note that the dynamic weighting scheme implies that the probability aggregation weights are modulated by the fine-resolution kernel and the sequential simulation path.

Table 4.1 summarizes the algorithm parameters and typical values for their lower and upper bounds when downscaling DEMs with nominal pixel size of 30×30 m. The search radius ρ used to retrieve data events is shared by the spatial low-pass filter and the two distance functions. The next three parameters, denoted by σ_L, σ_C, σ_F, correspond to the kernel shape parameter in Equation (4.3), which is used by the spatial low-pass filter, and both coarse- and fine-resolution distance functions (Eqs. (4.5) and (4.6)), respectively.

Table 4.1: Parameters of the downscaling algorithm.

$\boldsymbol{\theta}$	Bounds	Description
ρ	[30, 109]	Search radius for retrieving data events (m)
σ_L	[4, 1024]	Spatial low-pass filter kernel parameter (m)
σ_C	[4, 1024]	Coarse-scale distance function kernel parameter (m)
σ_F	[4, 1024]	Fine-scale distance function kernel parameter (m)
κ	[2, 64]	Number of candidate training data events
ξ	[0, 1]	Threshold for switching training data events search
χ	Boolean	Dynamic probability aggregation weights
α	[0, 1]	Fine-scale probability aggregation weight (if $\chi = $ false)

4.3 Automatic calibration of downscaling parameters with K-fold cross-validation and optimization by simulated annealing

This section presents the framework developed for automatic calibration of the downscaling algorithm parameters as a function of the dual-resolution training data. The approach relies on the combined application of a spatial variant of the K-fold cross-validation technique and the simulated annealing algorithm. A key aspect of the methodology is the formulation of the objective function for evaluating the statistical and structural quality of the downscaled DEMs. Subsection 4.3.1 provides an introduction to the K-fold cross-validation approach, and explains it usefulness for assessing the predictive performance of spatial simulation techniques. The formulation of the objective function is discussed in Subsection 4.3.2. An algorithm inspired by the work of Deutsch and Cockerham (1994) for calibrating the weights of multiple-component objective functions is presented in Subsection 4.3.3. Subsection 4.3.4 provides an overview of the simulated annealing technique. In Subsection 4.3.5, we describe the application of the simulated annealing algorithm for the optimization of the downscaling parameters using the K-fold cross-validation framework.

4.3.1 The K-fold cross-validation approach

Cross-validation comprises a group techniques used for assessing the accuracy and precision of predictive models. The objective of cross-validation is to evaluate the predictive performance of a model or algorithm when dealing with external data (i.e. data not used to calibrate it). It is also useful for identifying problems such as overfitting and estimation

bias (Cawley and Talbot, 2010). Cross-validation methods may be employed for selecting predictor variables, model parameters, and parameter calibration tasks. Poorly calibrated spatial simulation algorithms, for example, can lead to systematic over- or underestimation of target statistics and biased textural reproduction. Within a cross-validation setting, the calibration is performed based on conditioning data, or an external data set, when the former is not available or is only sparsely informed. The data set is divided in two parts: the training set and the validation set. The training set is used to train the predictive model or algorithm, whereas the validation set serves to assess its performance.

In this contribution, we explore the application of a non-exhaustive cross-validation technique known as K-fold cross-validation (Hastie et al., 2009). This method is of particular interest due to the way it divides the training data set. Geographical variables are often spatially auto-correlated. As a result, when dealing with such data sets, standard cross-validation methods will produce optimistically biased prediction performance estimates (Pohjankukka et al., 2017). Exhaustive cross-validation techniques, such as the leave-one-out method (Hastie et al., 2009), excel at calibration for local prediction (e.g. least-squares estimation), but are not well-suited for evaluating textural reproduction if the spatial resolution of the conditioning data or the sampling grid is coarser than the support of the simulated realizations. Moreover, cross-validating a single simulated value at a time does not account for the reproduction of the joint spatial relationship between neighboring simulated data (i.e. image texture).

In K-fold cross-validation, the training data set is segmented into K subsamples of equal size named folds. A given target fold (i.e. the validation set) is temporarily removed, and the remaining $K - 1$ folds (i.e. the training set) are used to train the algorithm. The algorithm is executed in the target fold and the predictions are subsequently evaluated by comparison against the validation set. The process is repeated for the remaining folds. Each fold consists of a continuous subset of the input data set. This is critical for spatial modeling as structural properties, such as spatial variability and connectivity, often have to be evaluated over large domains and at different scales. Additionally, unlike sub-sampling cross-validation methods, all available data are systematically used for training and validation. This is particularly valuable for obtaining robust prediction performance estimates when dealing with non-stationary data sets.

The training and validation sets, denoted as $\tau = \{\tau_k, k = 1, \dots, K\}$ and $\upsilon = \{\upsilon_k, k = 1, \dots, K\}$, respectively, are generated with intersection and set difference operators between the coarse- and fine-resolution training DEMs and a K-fold cross-validation template. The

template $f = \{f_k, k = 1, \ldots, K\}$ defines the layout and geometry of the folds. The k-th validation set v_k is defined as

$$v_k = \{z_V^{(t)}, z_v^{(t)}\} \cap f_k, \quad k = 1, \ldots, K \tag{4.10}$$

where f_k denotes the k-th target fold. The corresponding training set τ_k is given by

$$\tau_k = v_k^c = \{z_V^{(t)}, z_v^{(t)}\} \setminus v_k, \tag{4.11}$$

where $\setminus$ is the difference operator.

Figure 4.2 illustrates a 4-fold cross-validation setup. The template is constructed based on a quadrant partitioning scheme. For all four configurations, the training data set is composed by co-registered coarse- and fine-resolution information from three different folds. The coarse-scale data in the validation set condition the downscaling. The fine-resolution data are only used to evaluate the structural quality of the simulated realizations.

Whenever determining a value for K it is important to consider the resulting dimensions of the folds with regard to the scale of the spatial structures being modeled. For unconditional simulation, the folds should be at least equal or larger in size than the biggest structures to be simulated. Otherwise, the reproduction of long-range spatial correlations will not be explicitly evaluated. For conditional simulation with an exhaustive secondary variable, this is less severe because covariates will generally describe the large-scale spatial structures. Consequently, farther data will be less informative for prediction. In downscaling, we are mostly concerned with resolving the missing fine-scale features. Therefore, the size of the folds might not be equally important as the coarse-resolution variable is typically known over the entire simulation domain. A basic guideline, for example, would be to use a spatial correlation function, such as the range of the empirical variogram, or connectivity function, as a reference metric to define an appropriate minimum fold size.
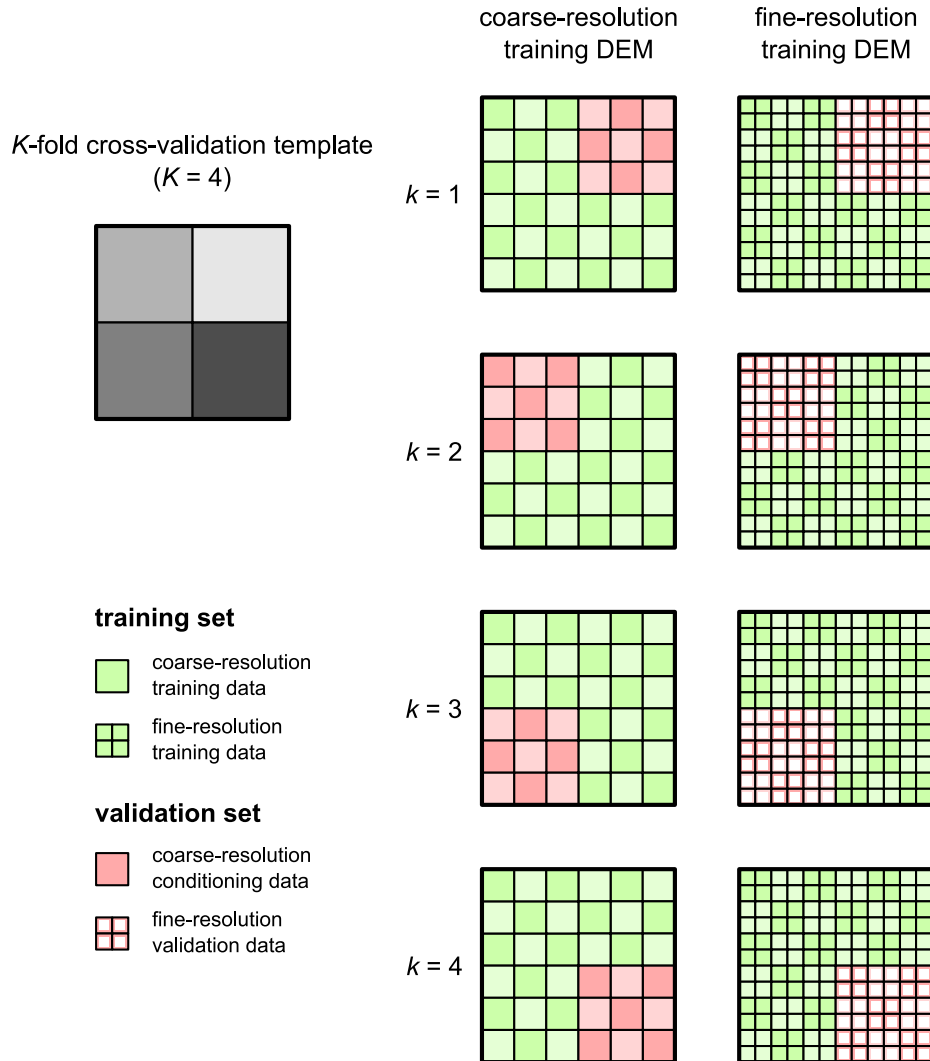
Figure 4.2: Illustrative example of a 4-fold cross-validation setup.

4.3.2 Formulating the multiple-component objective function

The calibration of the downscaling algorithm with optimization by simulated annealing requires the formulation of an objective function. This function measures the similarity between realizations and the validation data set. The objective function aims at describing key statistical and structural properties sought in the output realizations. These attributes may be numerically described by a single or multiple metrics. Often numerical models must meet several specifications for a target application, including consistency with various types of conditioning data and additional prior information. Statistical downscaling algorithms have to achieve at least two basic requirements: i. generate fine-resolution images that honor the coarse-resolution data, and ii. reproduce a given prior fine-scale structural model. In

the presented MPS-driven downscaling framework, the dual-resolution training data is the structural model itself.

The simulation of fine-resolution DEMs that are both consistent with available coarse-scale measurements and exhibit the small-scale topographic features found in the training data entails the formulation of a multiple-component objective function as these conditions can seldom be evaluated by a single metric. Two fundamental concepts for describing spatial heterogeneity are spatial variability and connectivity. Spatial variability is commonly characterized with two-point statistics, such as covariance functions, variograms (Marcotte, 1996), or spatial entropy (Renard and Allard, 2013). Two-point statistics describe the probability of having a given value at a certain position as a function of a known value at another position. This metric can be used to describe terrain roughness and the preferential anisotropy of geomorphic features.

Curvilinear structures, such as drainage networks, are better characterized with spatial connectivity metrics. Connectivity is usually measured with multiple-point statistics, static connectivity functions, and topological properties. Multiple-point statistics, such as multiple-point histograms (Boisvert et al., 2010) and high-order spatial cumulants (Dimitrakopoulos et al., 2010), compute conditional probabilities based on the analysis of the joint spatial relationship between multiple values. These statistics require the definition of spatial templates for analyzing different data configurations. Static connectivity (Renard and Allard, 2013) refers to the probability of having at least two pixels with identical values adjacent to each other. Renard and Allard (2013) proposed an adaptation of this metric for evaluating continuous random fields. In this approach, the continuous image is segmented into a series of binary images based on thresholding operations. The probability of having connected pixels is computed for each individual binary image and represented as a function of the truncation thresholds. Another important metric is the Euler number (Pratt, 1991). It consists of a topological invariant used to describe the shape or structure of a topological space. In two-dimensional binary images, the Euler number corresponds to the total number of objects in an image minus the number of holes in these objects. This property can be used to characterize continuous images by applying a series of thresholding operations in similar fashion to the static connectivity function (Renard and Allard, 2013).

In this work, we formulate a multiple-component objective function based on four metrics deemed important for DEM spatial analysis. The component objective functions associated with these criteria are described below. A multiple-component objective function O can be expressed as a linear combination of C component objective functions

$$O = \sum_{c=1}^{C} w_c\, O_c, \quad c = 1, \ldots, C \tag{4.12}$$

where O_c is the component objective function of the c-th component, and w_c is its corresponding weight.

Conditioning realizations to coarse-scale observations ensures that the simulated sub-pixel DEMs are coherent with the target DEM. Therefore, the first component objective function consists of the root-mean-square error (RMSE) between upscaled realizations and the residual coarse-resolution target DEM

$$O_1 = \left(\frac{1}{N} \sum_{i=1}^{N} \left[r_V^{(s)}(\mathbf{u}_i) - r_V(\mathbf{u}_i) \right]^2 \right)^{1/2}, \quad \forall\, i = 1, \ldots, N \tag{4.13}$$

where $r_V^{(s)}(\mathbf{u}_i)$ for $i = 1, \ldots, N$ is the upscaled simulated terrain elevation, and $r_V(\mathbf{u}_i)$ is the reference coarse-resolution elevation. If the upscaling function is not explicitly defined, the relationship between the coarse- and fine-scales is implicitly borrowed from the dual-resolution training data. In this case, $r_V^{(s)}(\mathbf{u}_i)$ corresponds to the central pixel value of its source coarse-resolution training data event.

Short-range empirical variogram maps (Marcotte, 1996) are employed to describe fine-scale topographic roughness and preferential anisotropy. The second component objective function is a weighted RMSE between the fine-scale variogram maps of the residual elevation simulations and the validation set

$$O_2 = \left(\sum_{j=0}^{J} \lambda(\mathbf{h}_j) \left[\frac{\hat{\gamma}_v^{(s)}(\mathbf{h}_j) - \hat{\gamma}_v(\mathbf{h}_j)}{\hat{\gamma}_v(\mathbf{h}_j)} \right]^2 \right)^{1/2}, \tag{4.14}$$

where $\hat{\gamma}_v^{(s)}(\mathbf{h}_j)$ and $\hat{\gamma}_v(\mathbf{h}_j)$ denote the simulated and validation empirical variograms, respectively, for the coordinates lag vector $\mathbf{h}_j, j = 0, \ldots, J$, and $\lambda(\mathbf{h}_j)$ is the weight associated with $\mathbf{h}_j$. Typically, $\lambda(\mathbf{h}_j) = \|\mathbf{h}_j - \mathbf{h}_0\|_2^{-2}$. Larger weights are commonly given to short lags as they are associated with small-scale features of the residual component. The normalization by $\hat{\gamma}_v(\mathbf{h}_j)$ makes the objective function consider only relative errors between the two maps. This is necessary as the residual-to-trend amplitude ratio depends on the low-pass filter kernel shape parameter.

The reproduction of complex residual features in the simulated realizations, such as channelized systems, is evaluated with two connectivity metrics. Proper reproduction of these structures is critical because they exert direct control on surface processes. The third component objective function is based on the RMSE between the simulated and the validation fine-resolution connectivity functions

$$O_3 = \left[\frac{1}{2Q} \sum_{q=1}^{Q} \left(\left[\Gamma(\iota_q^{(s)}) - \Gamma(\iota_q) \right]^2 + \left[\Gamma^c(\iota_q^{(s)}) - \Gamma^c(\iota_q) \right]^2 \right) \right]^{1/2}, \qquad (4.15)$$

where $\Gamma(\iota_q^{(s)})$ and $\Gamma(\iota_q)$ are the probabilities of connection computed from the fine-resolution simulated and reference binary indicator maps $\iota_q^{(s)}$ and ι_q, respectively, associated with the residual elevation threshold r_q; with $\Gamma^c(\iota_q^{(s)})$ and $\Gamma^c(\iota_q)$ being the probabilities calculated based on the complement of the indicator maps.

The indicator transform for generating the binary maps is defined as

$$\iota_q(\mathbf{u}, r_q) = \begin{cases} 1, & \text{if } r_v(\mathbf{u}) \geq r_q \\ 0, & \text{otherwise} \end{cases} \qquad q = 1, \ldots, Q \qquad (4.16)$$

where $r_q, q = 1, \ldots, Q$ are the different thresholds applied to the residual. The threshold values are selected based on quantiles from the validation set fine-resolution empirical cumulative distribution function (CDF).

The fourth component objective function consists of the RMSE between sub-pixel Euler characteristic curves of the simulated and the validation residuals

$$O_4 = \left[\frac{1}{2Q} \sum_{t=1}^{Q} \left([\phi(\iota_q^{(s)}) - \phi(\iota_q)]^2 + [\phi^c(\iota_q^{(s)}) - \phi^c(\iota_q)]^2 \right) \right]^{1/2}, \qquad (4.17)$$

where $\phi(\iota_q^{(s)})$ and $\phi(\iota_q)$ correspond to the simulated and the reference Euler numbers, respectively, and $\phi^c(\iota_q^{(s)})$ and $\phi^c(\iota_q)$ are their associated values computed from the complementary maps. As with the previous component objective function, thresholds are extracted from the quantiles of the validation set fine-resolution empirical CDF.

4.3.3 Weighting the component objective functions

The component objective functions can be potentially measuring metrics with different units or orders of magnitude. As a result, the calibration of the weights $w_c, c = 1, \ldots, C$ often demands extensive sensitivity analyses. Ideally, the weights should ensure that each component objective function receives equal importance in the decision making process. However, predefined weights may be assigned to each component based on a priori criteria.

To address this issue, we propose an adaptation of the perturbation mechanism introduced by Deutsch and Cockerham (1994) for automatic adjustment of the weights in Equation (4.12). The concept resides in estimating $w_c, c = 1, \ldots, C$ so that, in average, each component objective function has approximately equal contribution in the global objective function output. The rationale is to adjust the weights such that they are inversely proportional to the expected variability of their associated component objective functions. Therefore, calibrated weights should attenuate the impact of components with greater variability, and amplify the effect of small changes in less variable component objective functions.

In practice, the statistical dispersion of each component objective function cannot be calculated analytically, but it may be numerically approximated by performing a large number (e.g. 10^3) of independent stochastic perturbations. For each p-th perturbation, the downscaling algorithm is executed using a random set of parameters $\boldsymbol{\theta}^{(p)}$, and all C component objective functions are subsequently evaluated with K-fold cross-validation. The variability of each component is computed as

$$\text{var}(O_c) = \left(\frac{1}{P} \sum_{p=1}^{P} \left| O_c^{(p)} - \bar{O}_c \right|^{\nu} \right)^{1/\nu}, \quad c = 1, \ldots, C \tag{4.18}$$

where $O_c^{(p)}$ is the component objective function of the p-th perturbation, $\bar{O}_c$ is the mean component objective function computed over all P perturbations, and ν is an exponent parameter.

The contribution of each component is equalized by making the weights inversely proportional to the output of Equation (4.18)

$$w_c = \frac{\lambda_c}{\text{var}(O_c)}, \quad c = 1, \ldots, C \quad \text{with} \quad \sum_{c=1}^{C} \lambda_c = 1, \tag{4.19}$$

where λ_c controls relative importance of the c-th component.

Algorithm 3 summarizes the weight calibration process. We seek a representative estimate of the variability of each component objective function by drawing a random ensemble of parameter vectors $\boldsymbol{\theta}^{(p)}, p = 1 \ldots, P$ with Latin hypercube sampling (McKay et al., 1979). To reduce computational cost, as MPS simulation runs are fairly expensive, at each perturbation, the downscaling algorithm is executed for only one of the K cross-validation configurations selected at random (lines 3 and 4 of Algorithm 3). For reproducibility, an initial seed may be provided to the pseudo-random number generator.

Algorithm 3 Calibration of the objective function weights

    input: the training set τ, the validation set v, the multiple-component objective function O, the number of perturbations P, the exponent ν

    output: the calibrated weights $w_c, c = 1, \ldots, C$

 1: Draw the set of parameters $\boldsymbol{\theta}^{(p)}, p = 1, \ldots, P$ with Latin hypercube sampling

 2: **for** each p-th perturbation **do**

 3:      Select one of the K folds at random

 4:      Execute the downscaling algorithm $F(\boldsymbol{\theta}^{(p)}, \tau_k \mid v_k)$

 5:      Compute the component objective functions $O_c^{(p)}, c = 1, \ldots, C$

 6: **end for**

 7: Compute $\text{var}(O_c), c = 1, \ldots, C$

 8: Compute $w_c, c = 1, \ldots, C$

 9: **return** the calibrated weights $w_c, c = 1, \ldots, C$

4.3.4 The simulated annealing technique

In this work, the downscaling parameters are optimized with simulated annealing (Kirkpatrick et al., 1983). The simulated annealing technique is a metaheuristic designed to approximate the global optimum (i.e. minimum or maximum) of an objective function. Metaheuristics are particularly suited for providing approximate solutions to complex global optimization problems, especially when dealing with incomplete or uncertain information (Bianchi et al., 2009). Furthermore, these methods do not make any assumptions about the objective function response surface. Gradient-based optimization techniques, for example, require that the objective function is differentiable. In addition, many of these algorithms are prone to be trapped in local minima. In that regard, metaheuristics are more robust.

However, there is no guarantee that the global optimum may ever be found. Typically, multiple runs are performed to ensure a sufficiently good approximation.

The simulated annealing algorithm is based on an analogy with a heat treatment used in metallurgy and materials science. Annealing refers to the process in which a solid material undergoes heating without changing its phase so that its molecules can reorder into a lower energy crystalline structure. The probability that any two molecules may swap positions follows the Boltzmann distribution. Technically, the name simulated annealing only applies when the acceptance probably is based on this distribution (Kirkpatrick et al., 1983). Over time, however, the term has become used to describe a wider group of methods grounded on the principle of stochastic relaxation (Deutsch and Cockerham, 1994). This concept is explored in simulated annealing as a prescription for accepting or rejecting a target perturbation (thermal vibration). The most common acceptance criterion is the one used by the Metropolis algorithm (Metropolis et al., 1953), wherein a perturbation is accepted if the energy is decreased. Otherwise, it is accepted with a certain probability. The acceptance probability distribution is given by

$$\Pr\{accept \mid \Delta O, T\} = \begin{cases} 1, & \text{if } \Delta O \leq 0 \\ \exp\left(-\Delta O / T\right), & \text{otherwise} \end{cases} \tag{4.20}$$

with $\Delta O = O' - O$, where O corresponds to the current energy, O' is a candidate solution, and T is the temperature.

A fundamental aspect of simulated annealing is the cooling schedule. It defines how T decreases as a function of time (i.e. time steps or cycles). At high temperatures, any solution, regardless of its quality, can be potentially accepted. This results in the exploration of the objective function response surface. As T decreases, the likelihood of accepting worse solutions lessens (Eq. (4.20)). In this phase, the algorithm focuses on refining the search for the global minimum until a ground state is reached. Several cooling strategies have been proposed (Nourani and Andresen, 1998). In practice, monotonically decreasing functions are more commonly used owing to their lower computational cost. In a geometric cooling schedule, the temperature $T(t)$ for a given cycle t is calculated as

$$T(t) = T_0\, \zeta^t \quad \text{with} \quad 0 < \zeta < 1, \tag{4.21}$$

where T_0 is the initial temperature, and ζ is the reduction factor.

The temperature T decreases once a number of accepted target perturbations P_{accept} is reached. To avoid very slow cooling rates, at any given temperature, a maximum number of perturbations per cycle $P_{max} > P_{accept}$ is set. The algorithm is terminated if either a convergence criterion is met, say a low $|\Delta O|$, or the efforts to reduce the energy become discouraging. Other simulated annealing hyperparameters may include the number of neighboring states, the candidate generation function (also known as perturbation scheme), and additional convergence criteria, such as a minimum global objective function, a global maximum number of perturbations, and a target proportion of accepted perturbations (Goovaerts, 1997). Restart procedures are generally implemented. In restarting, the simulated annealing algorithm is allowed to move back to a solution that was significantly better than the current state. The process can be triggered by several criteria. The cooling schedule may also be re-initiated.

4.3.5   Parameter optimization by simulated annealing

In this subsection, the algorithm for calibrating the downscaling parameters with simulated annealing and K-fold cross-validation is presented. The main assumption of the proposed scheme is that the downscaling parameters can be inferred from the training DEMs, and subsequently used to enhance the target DEM spatial resolution. The downscaling algorithm is trained using the dual-resolution training data as it contains information at both scales. The procedure enables the algorithm to find an optimal parameter setup as fine-resolution training data can be used to assess the quality of simulated realizations.

The flowchart in Figure 4.3 depicts the automatic parameter calibration process. The input data comprise the coarse- and fine-resolution training DEMs, the K-fold cross-validation template, and the multiple-component objective function. The training and validation sets are generated in a pre-processing phase with intersection and difference operations between the template and the training DEMs. The downscaling algorithm is executed in cross-validation mode, and its outputs are systematically evaluated with the multiple-component objective function. The optimization is terminated when any of the stopping criteria are met.

The parameter optimization process consists of a nonlinear multivariate problem. To address that, the K-fold cross-validation method is adapted such that the optimization of the multiple-component objective function is not performed on each fold individually, but rather on all the K folds as a whole. By relying on the entire the dual-resolution training data, a more robust estimate of $\boldsymbol{\theta}$ can be obtained. To this end, Equation (4.12) is modified

as follows

$$\bar{O} = \sum_{k=1}^{K} \sum_{c=1}^{C} a_k \, w_c \, O_c^{(k)}, \tag{4.22}$$

where $\bar{O}$ represents the averaged global objective function, $O_c^{(k)}$ is c-th component objective function associated with the k-th fold, and a_k is a weight linked to the k-th fold cross-validation setup enabling the algorithm to accommodate irregular-sized folds.

A dimensionless cooling schedule (i.e. $T_0 = 1$) is adopted by re-scaling Equation (4.22) based on its initial evaluation

$$\bar{O} = \frac{1}{\bar{O}^{(0)}} \sum_{k=1}^{K} \sum_{c=1}^{C} a_k \, w_c \, O_c^{(k)}, \tag{4.23}$$

where $\bar{O}^{(0)}$ is the initial averaged objective function output.

A pseudocode for the optimization by simulated annealing is presented in Algorithm 4. The simulated annealing hyperparameters, denoted by $\boldsymbol{\eta}$, are summarized in Table 4.2. For reproducibility, an initial seed may be prescribed. The sequential simulation path fed to the downscaling algorithm is randomized after each realization to avoid overfitting $\boldsymbol{\theta}$ for a given path (lines 4 and 10 of Algorithm 4). Faster cooling schedules may be used by employing perturbation schemes based on specific probability distribution functions (PDFs). In the proposed approach, the perturbation scheme responsible for proposing neighboring states $\boldsymbol{\theta}'$ comprises a series of L one-dimensional PDFs (one per parameter) which vary as a function of T (line 19 of Algorithm 4). The probability of assigning a parameter proposal $\theta_l^{(p)}$ as a candidate θ_l' is computed with the Cauchy PDF

$$\Pr\{\theta_l' \leftarrow \theta_l^{(p)} \mid \theta_l, T\} = \frac{1}{\pi \gamma \beta} \left[\frac{\gamma^2}{\left(\theta_l^{(p)} - \theta_l\right)^2 + \gamma^2} \right], \quad l = 1, \ldots, L \tag{4.24}$$

where $\theta_l \in \boldsymbol{\theta}$, $\gamma = T \times \max(\theta_l) > 0$ is the scale parameter, with $\max(\theta_l)$ denoting the upper bound of the l-th parameter, and $\beta > 0$ is a normalizing constant. The Cauchy PDF its particularly useful because of its fat tails, which facilitate escaping from local minima (Szu and Hartley, 1987).

During the early stages of the optimization, the algorithm explores large-scale structures in the objective function response surface as the perturbation PDFs are stretched. As T decreases, the PDFs narrow down, and the focus shifts towards surveying local fine-scale features. At this point, candidate solutions neighboring the current state $\boldsymbol{\theta}$ are more likely to be sampled. $U \sim U[0,1]$ denotes a random number drawn from a uniform distribution bounded between 0 and 1. The optimization is executed with a single neighboring state. The stopping criteria consist of a maximum number of attempted perturbations

$$P_{attempt} = N_{stop} \times P_{max},\tag{4.25}$$

where N_{stop} is the stopping number (usually set at 2 or 3), or if the following convergence criterion is satisfied

$$|\Delta \bar{O}| \leq \delta,\tag{4.26}$$

where δ is the convergence constant.

Restart procedures are based on several criteria, which may include a fixed number of perturbations, or whether the current energy $\bar{O}$ is too high compared to the best solution recorded so far. In the proposed algorithm, the simulated annealing is restarted if the former type of condition holds

$$P(t) = P_{max},\tag{4.27}$$

where $P(t)$ is the current number of attempted perturbations at the t-th cycle.

Table 4.2: Simulated annealing hyperparameters.

$\boldsymbol{\eta}$	Description
T_0	Initial temperature
ζ	Reduction factor
P_{accept}	Number of accepted target perturbations
P_{max}	Maximum number of perturbations
N_{stop}	Stopping number
δ	Convergence constant

Algorithm 4 Parameter optimization by simulated annealing

---

    input: the training set τ, the validation set υ, the objective function O, the perturbation PDFs, the simulated annealing hyperparameters $\boldsymbol{\eta}$

    output: the calibrated downscaling parameters $\boldsymbol{\theta}$

  1: Let $T \leftarrow T_0$ and $\bar{O} \leftarrow +\infty$

  2: Sample $\boldsymbol{\theta}$ in the parameter space at random

  3: **for** each k-th fold, $k = 1, \ldots, K$ **do**

  4:      Execute the downscaling algorithm $F(\boldsymbol{\theta}, \tau_k \mid \upsilon_k)$

  5: **end for**

  6: Compute the initial averaged objective function $\bar{O}^{(0)}$

  7: **while** stopping criteria have not been met **do**

  8:      Sample $\boldsymbol{\theta}'$ with the perturbation PDFs

  9:      **for** each k-th fold, $k = 1, \ldots, K$ **do**

10:          Execute the downscaling algorithm $F(\boldsymbol{\theta}', \tau_k \mid \upsilon_k)$

11:      **end for**

12:      Compute the averaged objective function $\bar{O}'$

13:      Draw $U \sim U[0, 1]$

14:      **if** $\Pr\{\Delta\bar{O}, T\} \geq U$ **then**

15:          Let $\boldsymbol{\theta} \leftarrow \boldsymbol{\theta}'$ and $\bar{O} \leftarrow \bar{O}'$

16:      **end if**

17:      **if** P_{accept} **or** P_{max} is reached **then**

18:          Reduce T according to the cooling schedule

19:          Update the perturbation PDFs

20:          Reset perturbation counters

21:      **end if**

22: **end while**

23: **return** the calibrated downscaling parameters $\boldsymbol{\theta}$
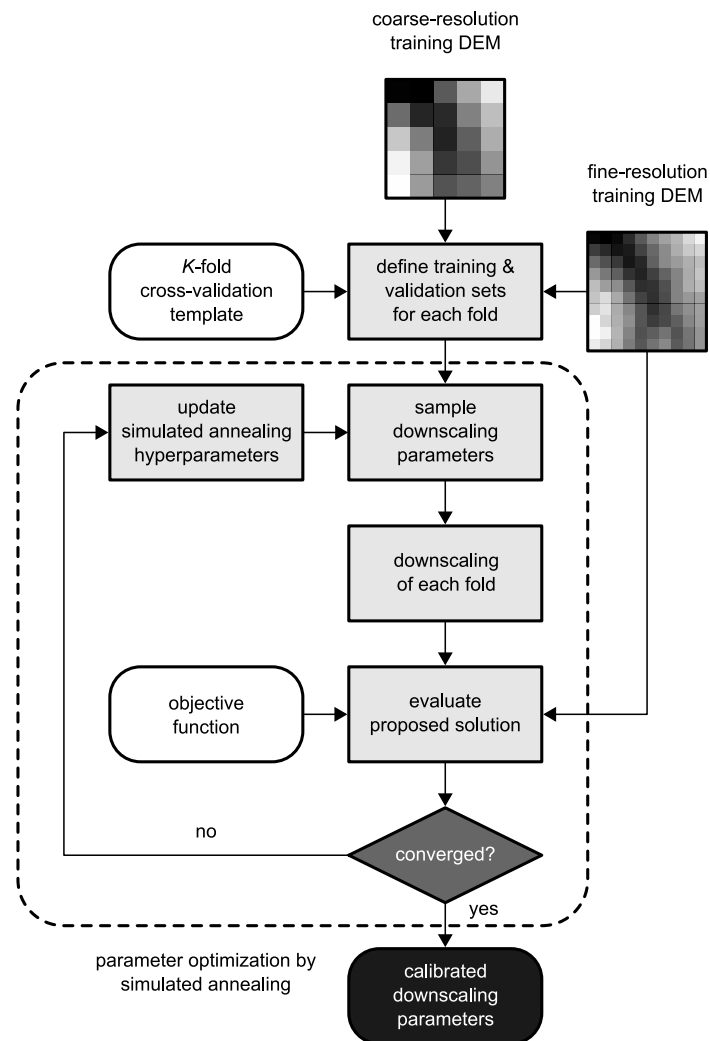
Figure 4.3: Automatic parameter calibration flowchart. Rounded white rectangles indicate input data and functions. Processes are represented as light gray rectangles. The dark gray diamond indicates a conditional decision operation. The calibrated downscaling parameters are indicated by the rounded black rectangle.

4.4 Case studies

In this section, we demonstrate the automatic parameter calibration framework with illustrative examples of DEMs from three distinct topographic settings: The Alaska Range, in the south-central Alaska; the Central Appalachians, in eastern North America; and the Central Lowlands, in South Australia. Subsection 4.4.1 presents the target and training DEMs. Subsection 4.4.2 shows the calibration of the weights of the multiple-component objective function. Subsection 4.4.3 illustrates the optimization of the downscaling algorithm parameters for each data set. In Subsection 4.4.4, we perform the downscaling of the coarse-resolution target DEMs using the parameters inferred from the training data, and validate the results with statistical and structural metrics.

4.4.1 Target and training data sets

The proposed framework is demonstrated with freely available DEMs. The target and training data sets comprise coarsened versions of three fine-resolution source DEMs: the Polar Geospatial Center at the University of Minnesota ArcticDEM (Porter et al., 2018), Geoscience Australia's Australian 5 m DEM (Geoscience Australia, 2015), and the USGS National Map 3DEP 1 m DEM (Sugarbaker et al., 2017). Table 4.3 lists the DEMs used in each illustrative example. A summary of the acquisition periods, sensing techniques used to produce the DEMs, and spatial resolution of the aforementioned products is provided.

Table 4.3: Source DEM products.

Example	Source product	Sensing year(s)	Sensor type	Nominal pixel size (m)
Alaska Range	ArcticDEM	2015-2016	Optical	2×2
Appalachians	3DEP 1 m DEM	2016-2023	LiDAR	1×1
Central Lowlands	Australian 5 m DEM	2001-2015	LiDAR	5×5

The approach is illustrated with artificial coarse-resolution target DEMs in order to eliminate the effect of measurement errors into the downscaling process. Numerical experiments based on non-artificial target DEMs are presented in Appendix A.1. The non-artificial target data sets include a corrected version of the 1-arc second near-global DEM from the U.S. National Geospatial-Intelligence Agency (NGA) and NASA's Shuttle Radar Topography Mission (SRTM30) (Farr et al., 2007; Geoscience Australia, 2015), JAXA's Earth

Observatory Research Center (EORC) 1-arc second global digital surface model ALOS World 3D-30m (AW3D30) (Tadono et al., 2016), and the USGS National Map 3D Elevation Program (3DEP) 1-arc second DEM (Sugarbaker et al., 2017).

The target, training, and reference DEMs are generated by linear upscaling of the source finer-resolution DEMs (Table 4.3). The downscaling is conditioned to the coarse-resolution target DEMs. The reference DEMs are only used for validation. The dimensions and nominal pixel sizes of the coarse-, medium-, and fine-resolution data sets are listed in Table 4.4. The footprints of the target/reference and training DEMs are approximately 3.69 and 14.75 km^2, respectively.

Table 4.4: Coarse-, medium-, and fine-resolution DEMs.

Data set	Spatial resolution	Dimensions (pixels)	Nominal pixel size (m)
Target	Coarse	64×64	30×30
Reference	Medium	128×128	15×15
	Fine	256×256	7.5×7.5
Training	Coarse	128×128	30×30
	Medium	256×256	15×15
	Fine	512×512	7.5×7.5

Figures 4.4–4.6 display the target and training DEMs for the Alaska Range, the Appalachian Mountains, and the Australian Central Lowlands case studies. Only the coarse-resolution target DEMs and the fine-resolution training DEMs are shown. The training DEMs are selected from neighboring sites with similar geomorphic features to their respective target data sets. The residual DEMs are computed based on a spatial low-pass filter with $\rho = 90$ m and $\sigma_L = 600$ m (Figs. 4.4–4.6). Positive structures in the residual represent ridgelines and crags in the landscape, whereas negative features denote rivers and gully networks. A brief description of the geomorphological settings of the three illustrative examples is provided below.

The Alaska Range is a relatively narrow mountain range located in south-central Alaska. The range is part of the American Cordillera, and extends for 650 km in an east-west direction, from Lake Clark at west, to the White River in Canada's Yukon Territory at its easternmost end. The regional climate is characterized by heavy snowfalls that feed a number of glaciers. The terrain is marked by glacial valleys and steep natural slopes. The Appalachians are an ancient mountain range in eastern North America formed almost a

half-billion years ago. The range is 160 to 480 km wide and runs 2,400 km southwestward from the island of Newfoundland, in southeastern Canada, to the U.S. state of Alabama. Over time, the mountain range experienced significant natural erosion. In the present day, the topography is characterized by a series of alternating ridgelines and fluvial valleys. The Central Lowlands cover one-fourth of mainland Australia, stretching south-northward from the Murray-Darling basin to the Gulf of Carpentaria. The landscape features extremely flat, low-lying plains of sedimentary rock, large deserts, and salt pans. The region is home to the lowest landforms in Australia, with an average height of less than 200 m.

The three case studies represent distinct geomorphic scenarios. The DEMs of the Alaska Range and Appalachian Mountains examples feature high-amplitude trend components with peak-to-peak amplitudes of approximately 700 and 250 m in the target data sets, and 1 km and 400 m in the training data, respectively (Figs. 4.4 and 4.5). By contrast, the trend in the Central Lowlands DEMs has a peak-to-peak amplitude of only 50 m (Fig. 4.6). Summary statistics of the coarse-resolution residual DEMs are listed in Table 4.5. Residuals have mean values of approximately zero, and their variability is somewhat proportional to the amplitude of their associated trend components. Two out of the tree training data sets have higher standard deviation (SD) and range values than their corresponding target data sets. This is an important aspect to be considered when choosing the training DEMs, as MPS algorithms are unable to generate simulated values outside the range of the fine-resolution training data empirical PDF. Only the Central Lowlands example does not abide to this guideline. The MPS-driven downscaling algorithm herein used is especially robust to this type of scenarios owing to its inbuilt capabilities for handling non-stationary data sets.

Table 4.5: Summary statistics of the coarse-resolution DEMs from the Alaska Range, the Appalachians, and the Central Lowlands examples.

Example	Data set	Mean	SD	Min.	Max.
Alaska Range	Training	0.04	6.76	−34.77	40.43
	Target	−0.37	5.61	−20.99	32.86
Appalachians	Training	0.08	3.52	−16.29	18.01
	Target	0.03	2.77	−9.45	15.46
Central Lowlands	Training	−0.02	2.11	−5.96	11.44
	Target	−0.02	3.26	−7.68	11.79

Values are in residual elevation (in m)
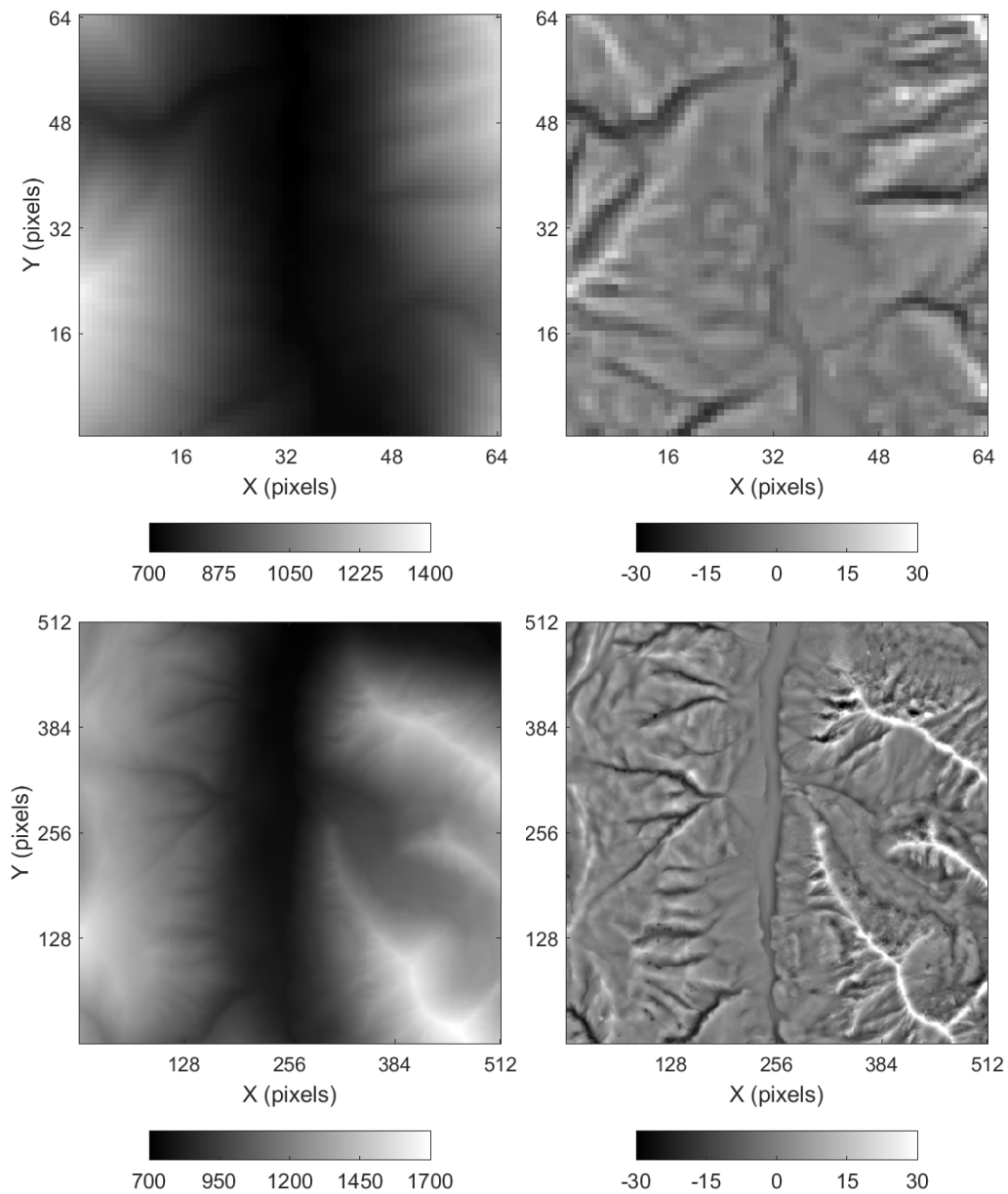
Figure 4.4: The Alaska Range example target and training DEMs. *Top left*: coarse-resolution target DEM. *Top right*: coarse-resolution target residual DEM. *Bottom left*: fine-resolution training DEM. *Bottom right*: fine-resolution training residual DEM. Colorbars' unit is m.
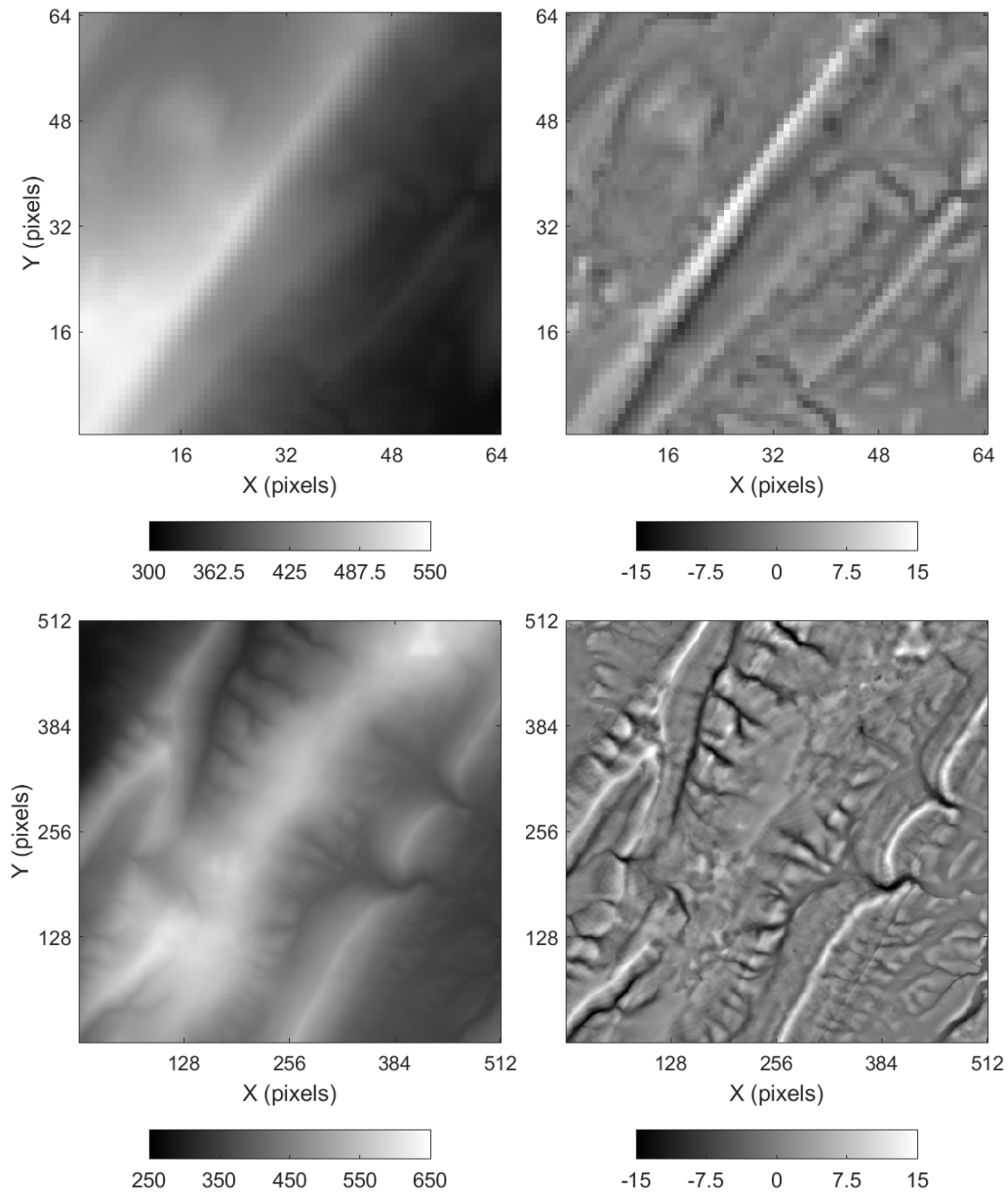
Figure 4.5: The Appalachians example target and training DEMs. *Top left*: coarse-resolution target DEM. *Top right*: coarse-resolution target residual DEM. *Bottom left*: fine-resolution training DEM. *Bottom right*: fine-resolution training residual DEM. Color-bars' unit is m.
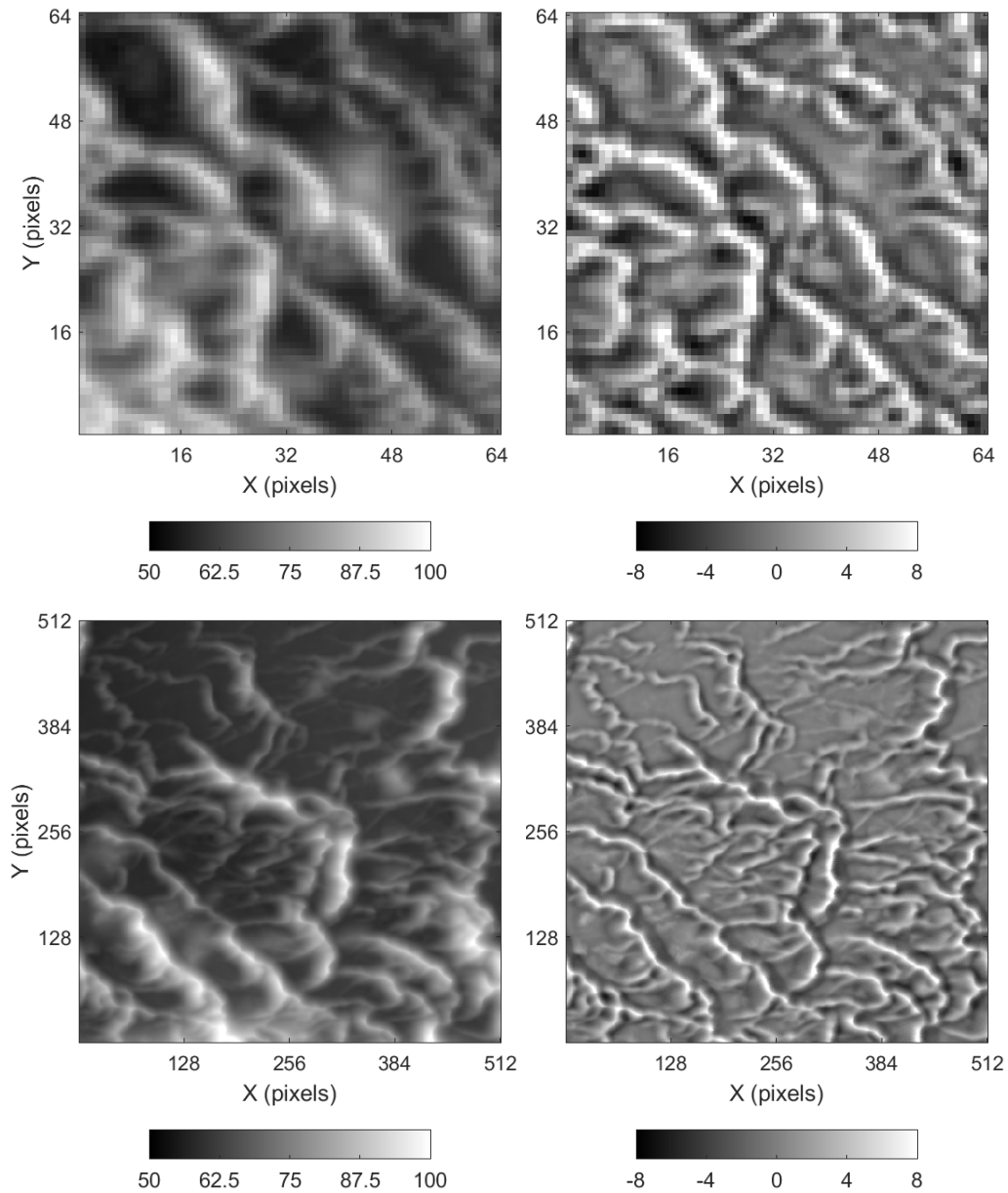
Figure 4.6: The Central Lowlands example target and training DEMs. *Top left*: coarse-resolution target DEM. *Top right*: coarse-resolution target residual DEM. *Bottom left*: fine-resolution training DEM. *Bottom right*: fine-resolution training residual DEM. Colorbars' unit is m.

4.4.2 Calibration of the component objective function weights

The multiple-component objective function presented in Subsection 4.3.2 is employed in all three examples. The component objective functions weights are calibrated with Algorithm 3. The stochastic perturbation hyperparameters for the magnification factors of $2\times$ and $4\times$ are listed in Table 4.6. For all three case studies, we define a 16- and a 64-fold cross-validation setup for $G = 2$ and $G = 4$, respectively. The K-fold cross-validation templates are generated using a quadrant-recursive partitioning scheme. The component objective function weights need to be calibrated at each magnification as the sub-pixel structures to be resolved have different scales.

Table 4.6: Stochastic perturbation hyperparameters.

η	$G = 2$	$G = 4$
K	16	64
P	4×10^3	4×10^3
ν	1	1

Figure 4.7 presents the convergence curves associated with the calibration of the component objective functions weights for the three case studies. The plots display the evolution of the component weights estimates as a function of the number of perturbations. Values are normalized to facilitate comparison among the components. In general, the data sets exhibit similar convergence patterns. Estimates tend to wildly fluctuate during the initial perturbations but as the number of perturbations increases they gradually stabilize (roughly after 3×10^3 perturbations).

The calibrated component objective functions weights are listed in Table 4.7. A uniform distribution is assumed for the prior weights λ_c. In the three examples, the third component objective function, which is associated with the connectivity function, was granted the highest weights for both magnification factors. This component has the smallest response dispersion, thus, it receives larger weights to compensate for its lesser variability. By contrast, the fourth component objective function received the smallest weights due to the large variations in the RMSE between the simulated and reference Euler characteristic curves. The mean absolute deviations of the first and second component objective functions lie somewhere between the third and fourth components. Note that the relative contribution of each component to the total sum of weights varies per magnification factor (Table 4.7).

Table 4.7: Calibrated component objective function weights.

Example	G	w_1	w_2	w_3	w_4
Alaska Range	2	0.2007 (3)	1.6552 (22)	5.7346 (75)	0.0235 (<1)
	4	1.0717 (13)	0.4042 (5)	6.4955 (81)	0.0113 (<1)
Appalachians	2	0.4179 (5)	1.9792 (23)	6.3329 (72)	0.0230 (<1)
	4	2.6775 (26)	1.0027 (10)	6.7586 (65)	0.0120 (<1)
Central Lowlands	2	0.6586 (7)	2.1155 (22)	7.0144 (71)	0.0304 (<1)
	4	5.4776 (44)	1.0097 (8)	5.9399 (48)	0.0152 (<1)

Values in parentheses give the approximate percentage of the contribution of each component to the total sum of weights
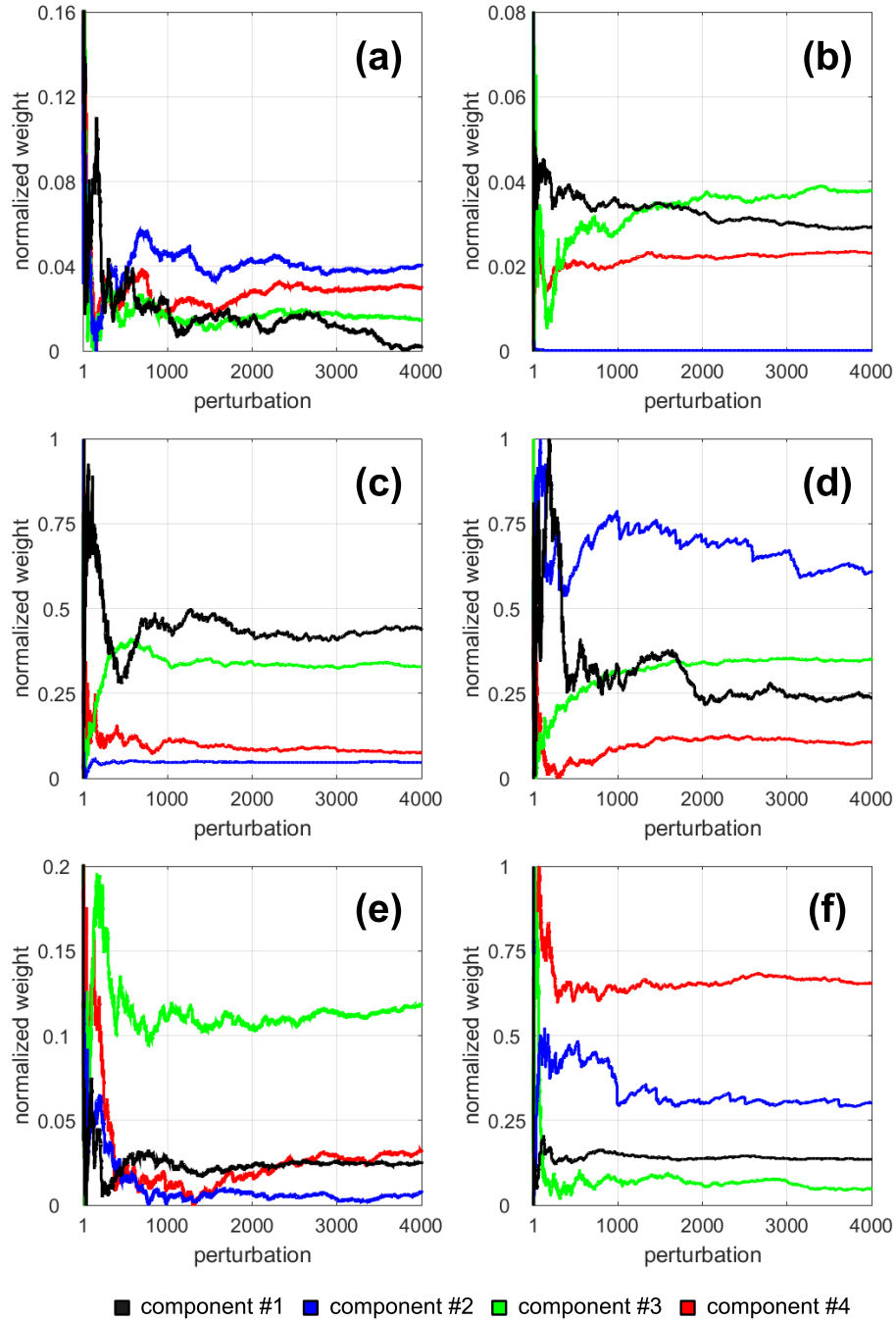
Figure 4.7: Calibration of the component objective functions weights. **a** the Alaska Range example ($G = 2$), **b** the Alaska Range example ($G = 4$), **c** the Appalachians example ($G = 2$), **d** the Appalachians example ($G = 4$), **e** the Central Lowlands example ($G = 2$), **f** the Central Lowlands example ($G = 4$). Components: #1 – coarse-scale conditioning; #2 – empirical variogram map; #3 – probability of connection; #4 – Euler characteristic.

4.4.3 Optimization of the downscaling algorithm parameters

The quality of the approximation to the objective function's global minimum is proportional to the optimization run-time. Therefore, slower cooling schedules are expected to give better approximations than faster cooling strategies as they allow the algorithm more time to explore the solution space. The drawback is that they entail a larger number of perturbations. This is notably critical to MPS simulation algorithms because of their high computational cost.

In order to accelerate the optimization process, we create a bounded discrete parameter space. To further reduce the optimization run-time, this space is unevenly sampled for specific algorithm parameters. The reason is that the structural quality of the simulations does not vary significantly when some parameters lie at certain ranges of the parameter space. This applies to all kernel shape parameters (i.e. $\sigma_L, \sigma_C, \sigma_F$) and the number of candidate training data events κ. Assigning different large values to the kernel shape parameter does not visibly affect the simulated realizations due to limited length of the search radius ρ (Table 4.1). Typically, ρ is much smaller than the target DEM dimensions (Table 4.4). A similar effect is observed if κ is set as a large number. For the sizes of the DEMs presented in the case studies, differences between small values (e.g. $\kappa < 10$) may heavily impact the structural quality of the simulations, but for larger values (e.g. $\kappa > 100$), they do not. Hence, these parameters can be densely sampled around their lower bounds, and sparsely sampled towards their upper bounds. The remaining algorithm parameters are sampled uniformly.

To handle the preferential sampling of certain dimensions of the parameter space, the term $\left(\theta_l^{(p)} - \theta_l\right)^2$ in the denominator of Equation (4.24) is modified. Rather than computing it in the original parameter units, computations are executed based on the indexes of the elements within the vector discretizing a given dimension. This enables the algorithm to safely explore the objective function response surface at low temperatures by minimizing the risk of accidentally getting trapped at a sparsely sampled sector in the parameter space. The Cauchy PDF scale parameter γ is also made proportional to the length of the vector instead of being based on the parameter upper bound value (Eq. (4.24)).

The optimization of the downscaling parameters is performed with Algorithm 4. The K-fold cross-validation templates used in Subsection 4.4.2 are also employed in the optimization process. Table 4.8 lists the simulated annealing hyperparameters used in the three illustrative examples. Figure 4.8 displays the convergence curves of the multiple-component

objective functions and the simulated annealing cooling schedules. The approximated global minima and restarts are indicated in the plots. The optimization processes took roughly 900 to 1,100 perturbations to terminate given the pre-specified hyperparameters configuration (Table 4.8). The optimizations related to the first iteration of the algorithm required less perturbations than the ones for the second iteration. Each process restarted at least once, except the first magnification of the Central Lowlands example. This optimization process was interrupted relatively earlier since it managed to reach the convergence criterion around the 400th perturbation.

Table 4.8: Simulated annealing hyperparameters.

η	$G = 2$	$G = 4$
K	16	64
T_0	1	1
ζ	0.9	0.9
P_{accept}	10	10
P_{max}	100	100
N_{stop}	3	3
δ	1×10^{-4}	1×10^{-4}

Table 4.9 lists the optimized downscaling parameters for each case study and magnification factor. The calibrated parameters appear to cluster around an optimal setup but also reveal several differences among data sets and scales. The parameter configurations are primarily characterized by a search radius ρ with length ranging from 2 to 4 coarse pixels. The spatial low-pass filter's shape parameter σ_L is set to fairly high values, which yields nearly flat kernels. These kernels produce highly auto-correlated residual components that appear to enhance the structural accuracy of the simulated realizations. The kernels associated with the coarse-scale distance functions have their centroids concentrating at least half of the sum of the weights. However, striking differences are observed between the kernels of the coarse- and fine-resolution distance functions based on the magnification factor. The parameter configurations associated with $G = 2$ gravitate towards setups where $\sigma_C > \sigma_F$, whereas $G = 4$ favors configurations with $\sigma_C < \sigma_F$. Results suggest that the optimal number of candidate training data events κ is both data- and scale-dependent. For $G = 2$, the optimal setup is $\kappa \leq 12$, but for $G = 4$, κ is significantly larger. This parameter is notably sensitive to the non-stationarity of the residual and the size of the training data set. At the second iteration, the sheer number of training data events rises, hence the number of potential replicates for any given data event is expected to increase. Ultimately, this allows the algorithm to relax the value for κ. Although a direct function of the distance function

kernel, the scanning hierarchy control variable ξ appears to systematically assume values larger than 0.6. This result suggests that at any given scale, the coarse-resolution data will more often dictate the retrieval and simulation of fine-scale data. This is rather logical if one considers that the coarse-resolution residual comprises the only source of co-registered information available at every uniformed fine-resolution pixel. Finally, the choice of either a static or a dynamic weighting scheme, and the probability aggregation weight for the fine-scale data, which are controlled by χ and α, respectively, appear to be data dependent.

Table 4.9: Optimized downscaling algorithm parameters.

Example	G	ρ	σ_L	σ_C	σ_F	κ	ξ	χ	α
Alaska Range	2	90	446	11	6	12	0.78	false	0.95
	4	55	69	14	137	56	0.93	true	-
Appalachians	2	109	388	16	11	4	0.65	true	-
	4	30	194	7	37	34	0.80	true	-
Central Lowlands	2	68	832	17	6	5	0.81	false	0.85
	4	45	169	8	16	23	0.98	false	0.39
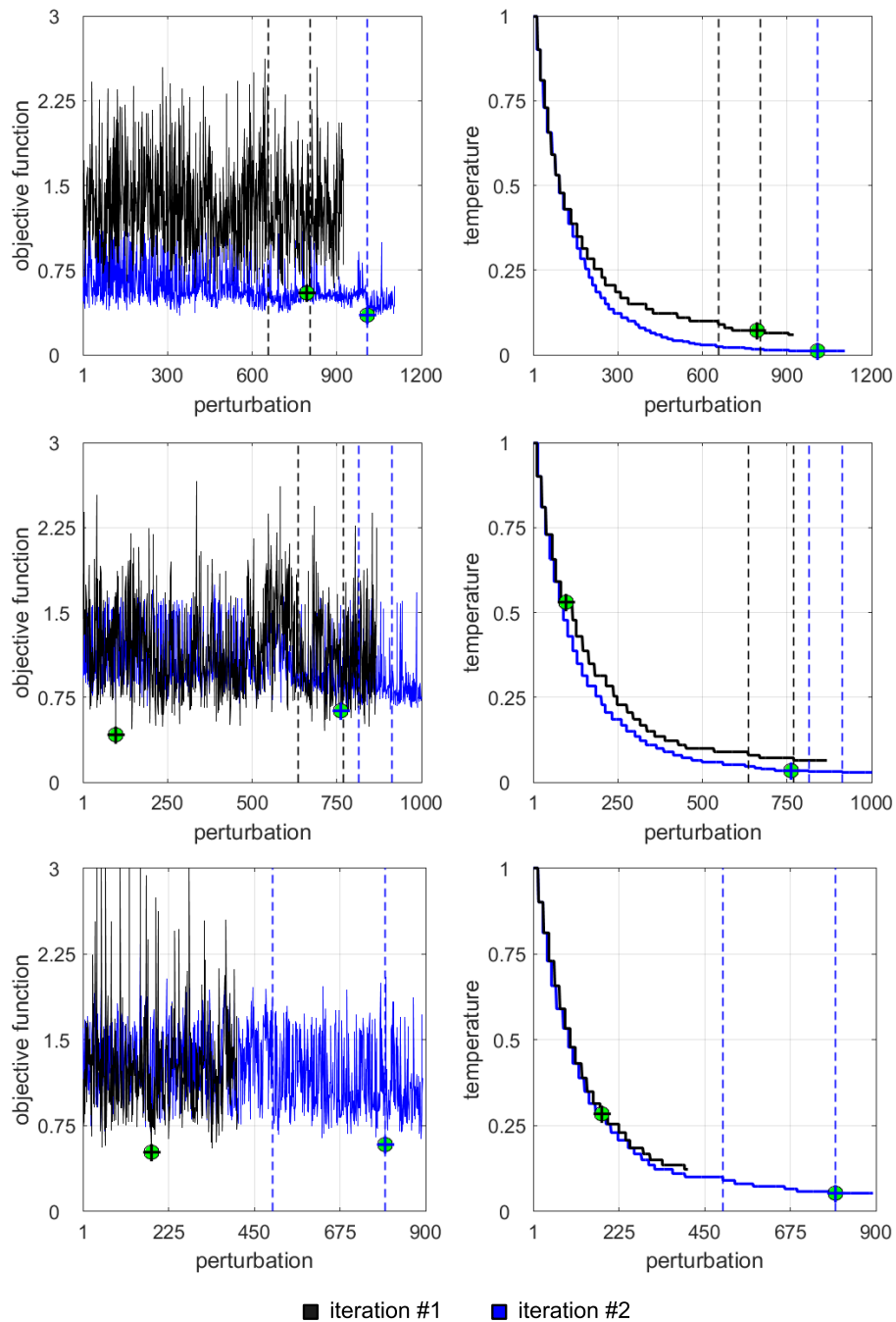
Figure 4.8: Objective functions and simulated annealing cooling schedules. *Top row*: the Alaska Range example. *Middle row*: the Appalachians example. *Bottom row*: the Central Lowlands example. Approximated global minima are indicated by the green circles with a cross. Vertical dashed lines denote restarts.

4.4.4 Simulation and validation

Figures 4.9–4.14 illustrate the reference DEMs and sample downscaling realizations of the three case studies. Both trended and residual versions of the DEMs are displayed. The residual DEMs are computed with the same spatial low-pass filter used in Figures 4.4–4.6. The DEMs are shown in three different spatial resolutions (Table 4.4). Detailed views of the terrain features are given by zooms of selected areas in the residual DEMs. The green boxes highlight the magnified areas (Figures 4.9–4.14).

Table 4.10 lists the statistics describing the conditioning quality of simulated realizations to the coarse-resolution target residual DEMs. Statistics characterize both systematic and random errors. Random errors (i.e. precision related) are described with the standard deviation of error (SDE) and the Pearson's linear correlation coefficient (r). Systematic errors (i.e. accuracy related) are characterized using the mean error (ME), and the slope of the regression line (m) calculated based on the reduced major axis (RMA) regression model. The RMA regression is preferred over the ordinary least squares model because it assumes that "m" is independent of "r", thus making it a true estimate of bias. Statistics are computed based upon the upscaled simulated realizations and the coarse-resolution target residual DEMs. The conditioning MEs and SDEs associated with each realization are computed by accumulating at each iteration the mismatch between the centroids of the target data events and their corresponding source data events in the training data. Table 4.10 statistics represent average values plus or minus one standard deviation over 20 realizations. Results show that the downscaling outputs adequately honor the target residual DEMs. Average MEs are close to zero, and the mean SDEs do not exceed 1 m. As expected, the second magnification ($G = 4$) systematically produces higher SDEs because of the propagation of errors across iterations. Slight underpredicion (m > 1) and deterioration in the reproduction of the coarse-resolution residual data (r < 1) are observed.

Summary statistics of the medium- and fine-resolution reference and simulated residual DEMs are listed in Table 4.11. The sub-pixel residual DEMs are computed with the same spatial low-pass filter used in Subsection 4.4.1. In general, realizations reproduce fairly well both medium- and fine-resolution reference statistics for all three examples. The standard deviations of the simulated realizations are underestimated by a narrow margin of only 1 to 2%. The reference minima and maxima are reasonably well reproduced, except for the second iteration of the Alaska Range example, which reveals slight underestimation, and for realizations of the Central Lowlands examples, that underestimate the reference minima (Table 4.11).

Table 4.10: Conditioning to coarse-resolution residual data.

Example	G	ME[1](cm)	SDE[2](cm)	m[3]	r[4]
Alaska Range	2	-0.15 ± 0.33	17.28 ± 15.17	1.00 ± 0.00	1.00 ± 0.00
	4	0.26 ± 1.60	79.81 ± 64.00	1.05 ± 0.00	0.93 ± 0.01
Appalachians	2	0.04 ± 0.23	11.91 ± 9.01	1.01 ± 0.00	1.00 ± 0.00
	4	-0.02 ± 0.54	28.42 ± 18.90	1.03 ± 0.00	0.79 ± 0.04
Central Lowlands	2	-0.49 ± 0.34	31.96 ± 20.65	1.02 ± 0.00	1.00 ± 0.00
	4	-1.02 ± 0.45	65.14 ± 28.78	1.01 ± 0.00	0.95 ± 0.01

[1] mean error;   [2] standard deviation of error;   [3] RMA regression slope;
[4] Pearson's linear correlation coefficient; Values represent average statistics plus or minus one standard deviation over 20 realizations

Figures 4.15–4.17 illustrate the structural validation of the downscaled DEMs. The validation metrics comprise spatial statistics employed by the second, third, and fourth component objective functions. These include directional variograms, Euler characteristic curves, and connectivity functions. Results are displayed for the two magnification factors. All spatial statistics refer exclusively to the residual DEMs to filter out the effect of large-scale structures present in the trend components. Green curves denote the reference data, whereas simulated realizations are indicated in black. The envelopes represent the range covered by 20 simulated realizations.

The reference structural statistics are well reproduced for the three data sets and both magnification factors. However, systematic underestimation of the contributions of the reference empirical variograms, and issues in the reproduction of high-amplitude spikes in the reference Euler characteristic curves, notably for the Alaska Range and the Appalachians examples, are observed (Figs. 4.15 and 4.16). Accurate reproduction of the reference connectivity functions at low and high residual values appears to be particularly challenging. Optimization of the weighting schemes associated with the component objective functions could further enhance the reproduction of these statistics. Realizations of the Central Lowlands example replicate extremely well the reference Euler characteristic curves, but underestimate to a larger extent the contribution of the empirical variograms for $G = 2$ compared to the other two examples (Fig. 4.17). This might indicate a potential conflict between accurate reproduction of two-point and high-order statistics.

Results suggest that an exact reproduction of the reference spatial statistics becomes harder at higher magnification factors. The relative terrain spatial complexity may play a significant role in the structural accuracy of the downscaling process. Rough and steep

terrains, such as the Alaska Range example and, to a lesser degree, the Appalachians, are comparatively more difficult to downscale than areas of smooth topography, such as the Central Lowlands example. In addition, the Central Lowlands case study, in particular, demonstrates that the approach is capable of handling scenarios in which the training data may have smaller dispersion than that of the target DEM.
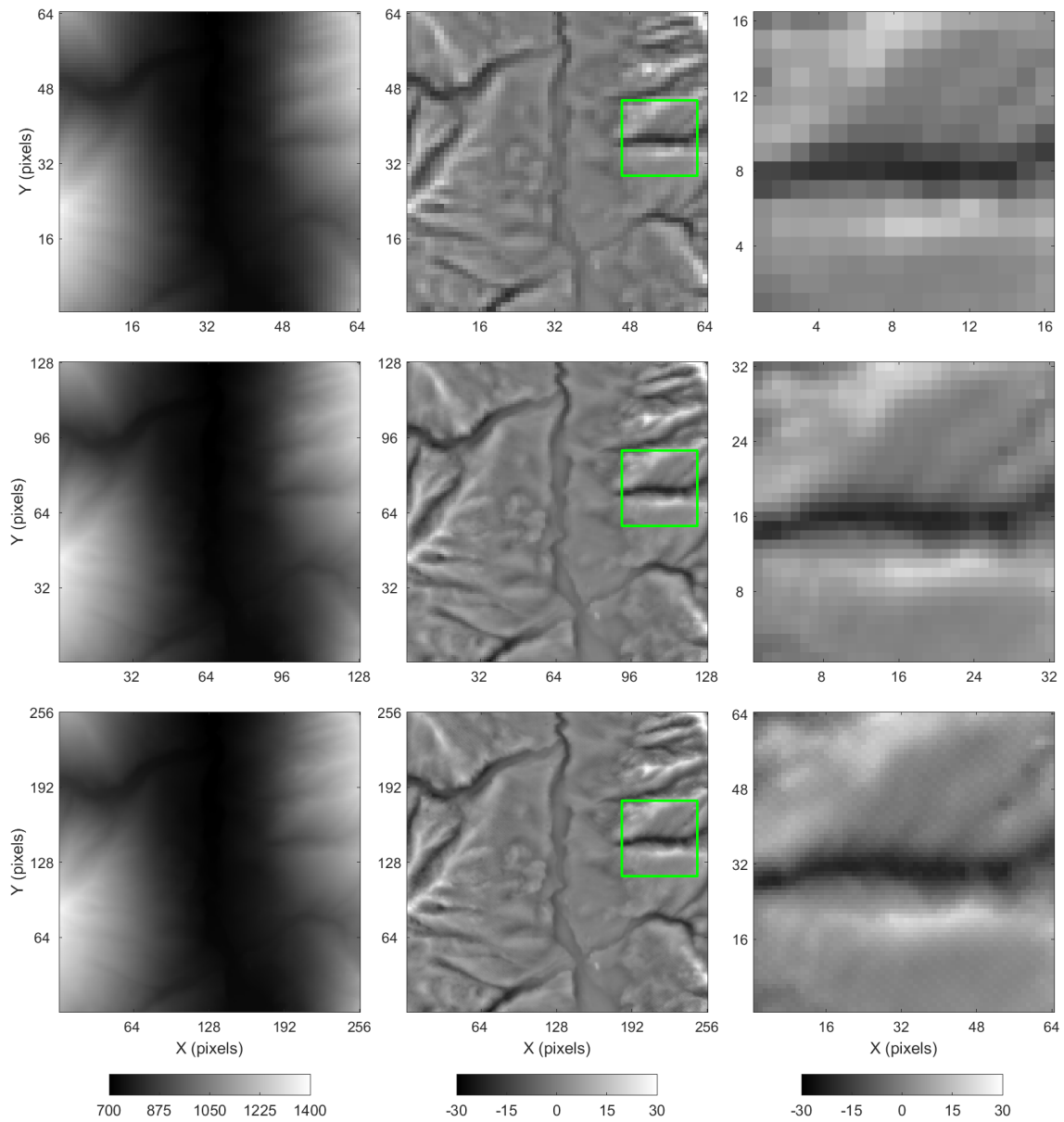
Figure 4.9: The Alaska Range example reference DEMs. *Top left*: coarse-resolution DEM. *Top center*: coarse-resolution residual DEM. *Top right*: coarse-resolution zoom. *Middle left*: medium-resolution DEM. *Middle center*: medium-resolution residual DEM. *Middle right*: medium-resolution zoom. *Bottom left*: fine-resolution DEM. *Bottom center*: fine-resolution residual DEM. *Bottom right*: fine-resolution zoom. Green boxes highlight the magnified area. Colorbars' unit is m.
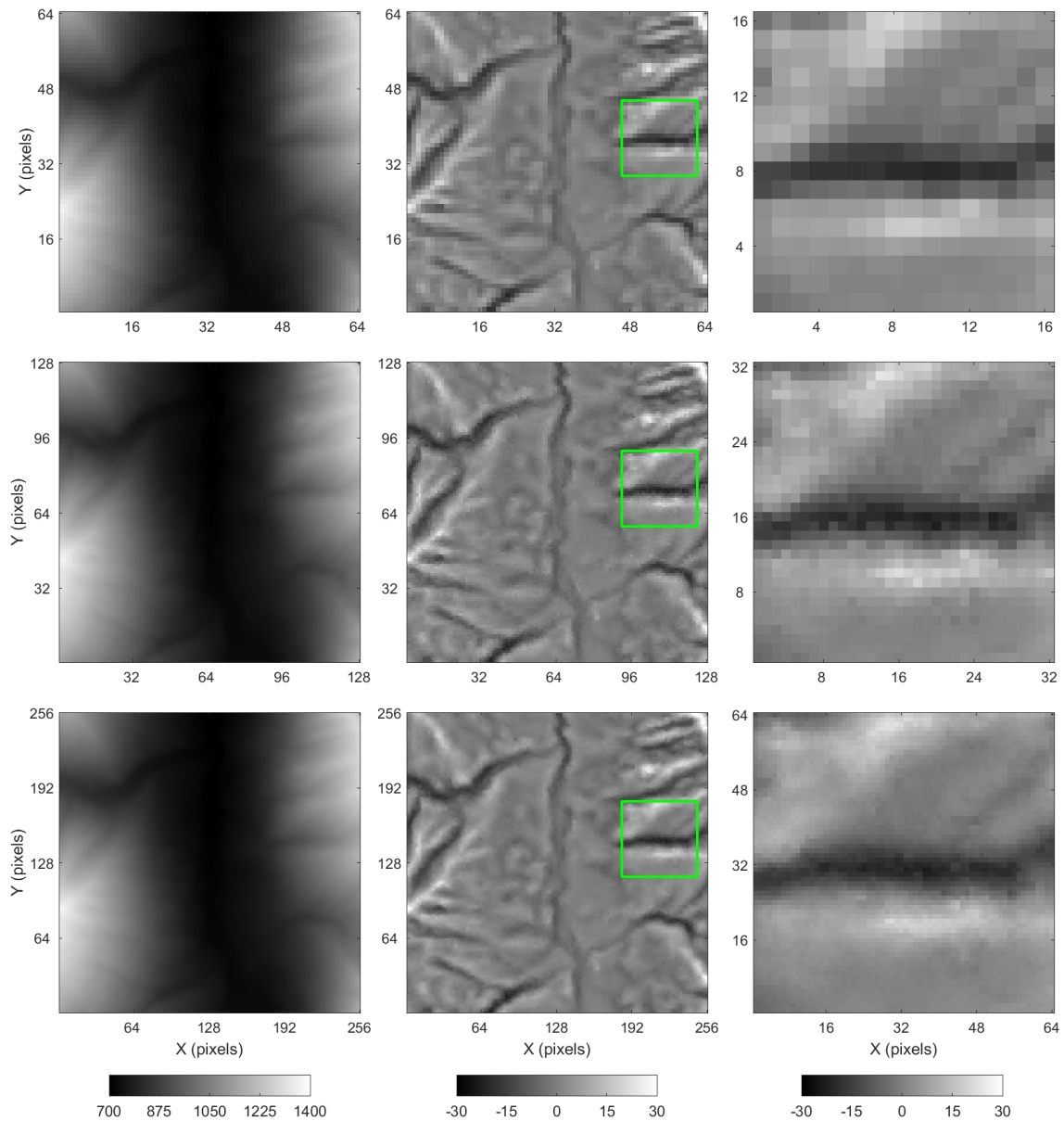
Figure 4.10: The Alaska Range example downscaled DEMs. *Top left*: coarse-resolution DEM. *Top center*: coarse-resolution residual DEM. *Top right*: coarse-resolution zoom. *Middle left*: medium-resolution DEM. *Middle center*: medium-resolution residual DEM. *Middle right*: medium-resolution zoom. *Bottom left*: fine-resolution DEM. *Bottom center*: fine-resolution residual DEM. *Bottom right*: fine-resolution zoom. Green boxes highlight the magnified area. Colorbars' unit is m.
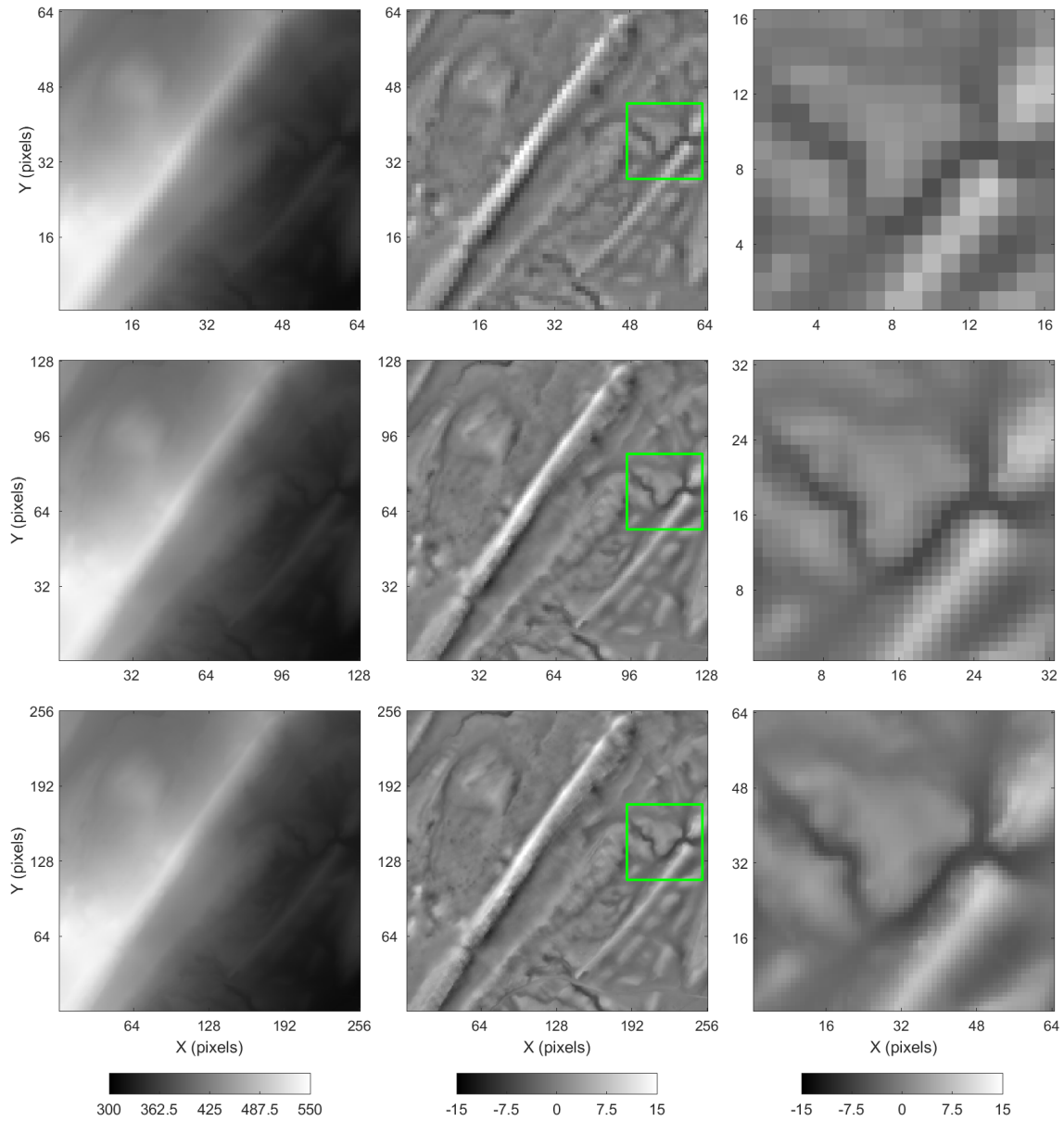
Figure 4.11: The Appalachians example reference DEMs. *Top left*: coarse-resolution DEM. *Top center*: coarse-resolution residual DEM. *Top right*: coarse-resolution zoom. *Middle left*: medium-resolution DEM. *Middle center*: medium-resolution residual DEM. *Middle right*: medium-resolution zoom. *Bottom left*: fine-resolution DEM. *Bottom center*: fine-resolution residual DEM. *Bottom right*: fine-resolution zoom. Green boxes highlight the magnified area. Colorbars' unit is m.
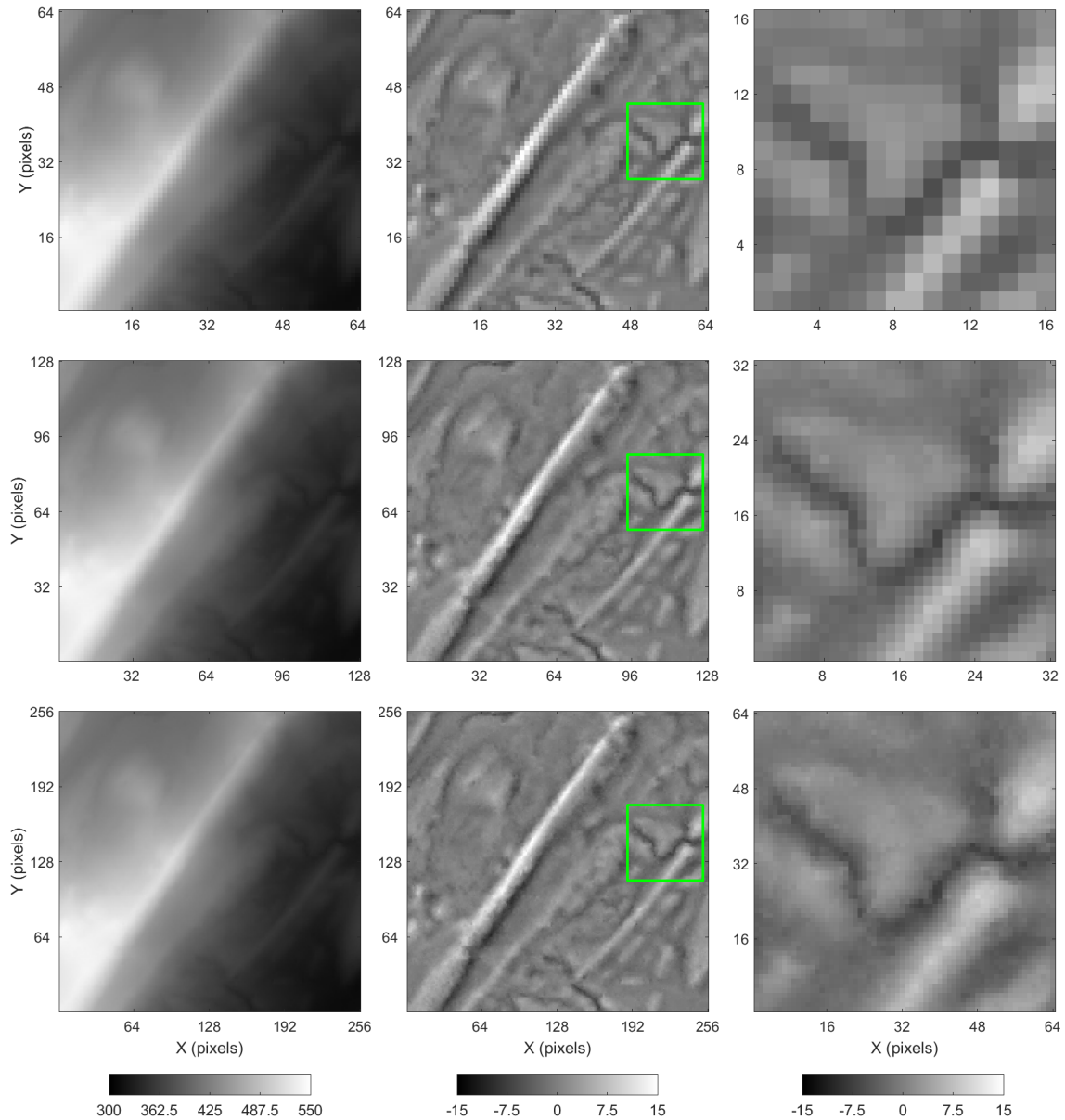
Figure 4.12: The Appalachians example downscaled DEMs. *Top left*: coarse-resolution DEM. *Top center*: coarse-resolution residual DEM. *Top right*: coarse-resolution zoom. *Middle left*: medium-resolution DEM. *Middle center*: medium-resolution residual DEM. *Middle right*: medium-resolution zoom. *Bottom left*: fine-resolution DEM. *Bottom center*: fine-resolution residual DEM. *Bottom right*: fine-resolution zoom. Green boxes highlight the magnified area. Colorbars' unit is m.
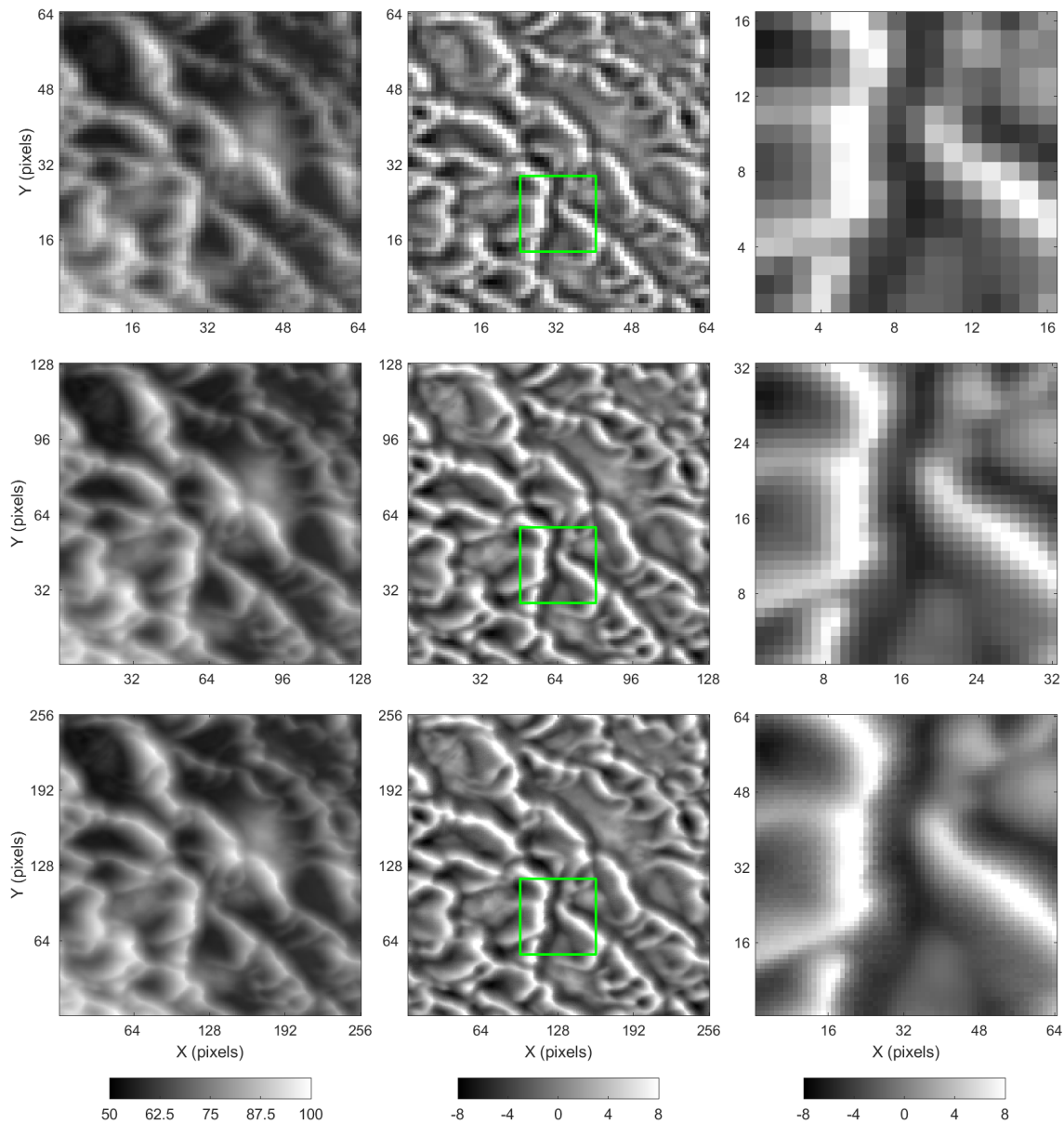
Figure 4.13: The Central Lowlands example reference DEMs. *Top left*: coarse-resolution DEM. *Top center*: coarse-resolution residual DEM. *Top right*: coarse-resolution zoom. *Middle left*: medium-resolution DEM. *Middle center*: medium-resolution residual DEM. *Middle right*: medium-resolution zoom. *Bottom left*: fine-resolution DEM. *Bottom center*: fine-resolution residual DEM. *Bottom right*: fine-resolution zoom. Green boxes highlight the magnified area. Colorbars' unit is m.
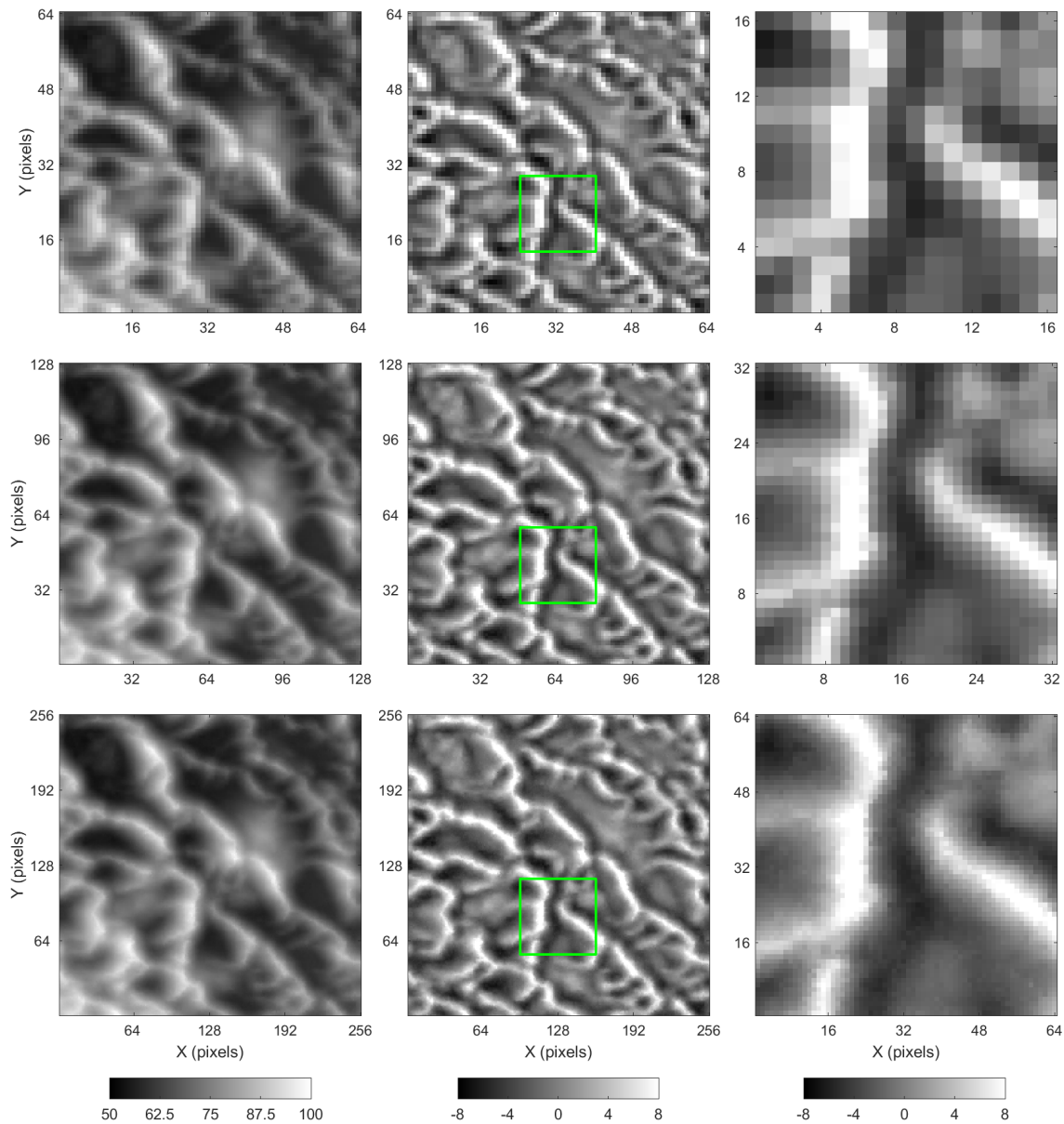
Figure 4.14: The Central Lowlands example downscaled DEMs. *Top left*: coarse-resolution DEM. *Top center*: coarse-resolution residual DEM. *Top right*: coarse-resolution zoom. *Middle left*: medium-resolution DEM. *Middle center*: medium-resolution residual DEM. *Middle right*: medium-resolution zoom. *Bottom left*: fine-resolution DEM. *Bottom center*: fine-resolution residual DEM. *Bottom right*: fine-resolution zoom. Green boxes highlight the magnified area. Colorbars' unit is m.

Table 4.11: Summary statistics of the medium- and fine-resolution reference and downscaled DEMs from the Alaska Range, the Appalachians, and the Central Lowlands examples.

Example	Data set	G	Mean	SD	Min.	Max.
Alaska Range	Reference	2	−0.36	5.75	−24.44	36.58
		4	−0.35	5.75	−26.16	40.77
	Simulation	2	−0.36 ± 0.00	5.72 ± 0.00	−24.68 ± 0.81	37.34 ± 1.01
		4	−0.35 ± 0.00	5.60 ± 0.01	−23.79 ± 0.79	37.70 ± 1.17
Appalachians	Reference	2	0.03	2.79	−10.45	16.85
		4	0.03	2.79	−10.78	17.34
	Simulation	2	0.03 ± 0.00	2.75 ± 0.00	−10.63 ± 0.41	16.08 ± 0.37
		4	0.03 ± 0.00	2.73 ± 0.00	−10.94 ± 0.35	16.43 ± 0.39
Central Lowlands	Reference	2	−0.02	3.33	−7.79	12.77
		4	−0.02	3.32	−7.89	13.89
	Simulation	2	−0.02 ± 0.00	3.26 ± 0.00	−7.06 ± 0.06	12.49 ± 0.04
		4	−0.02 ± 0.00	3.25 ± 0.00	−7.11 ± 0.10	12.94 ± 0.24

Numbers represent average statistics plus or minus one standard deviation over 20 realizations. Values are in residual elevation (in m)
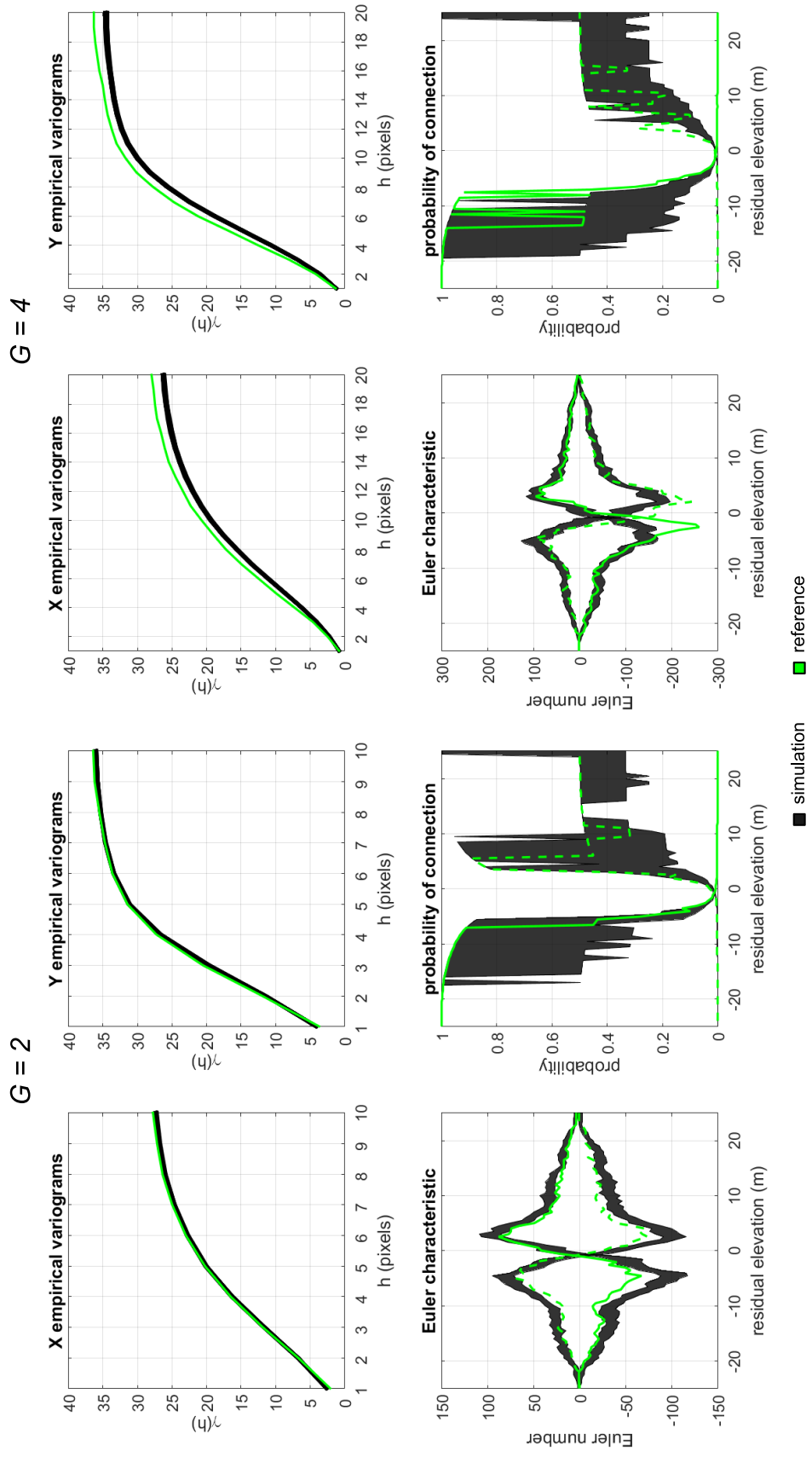
Figure 4.15: The Alaska Range example structural statistics.
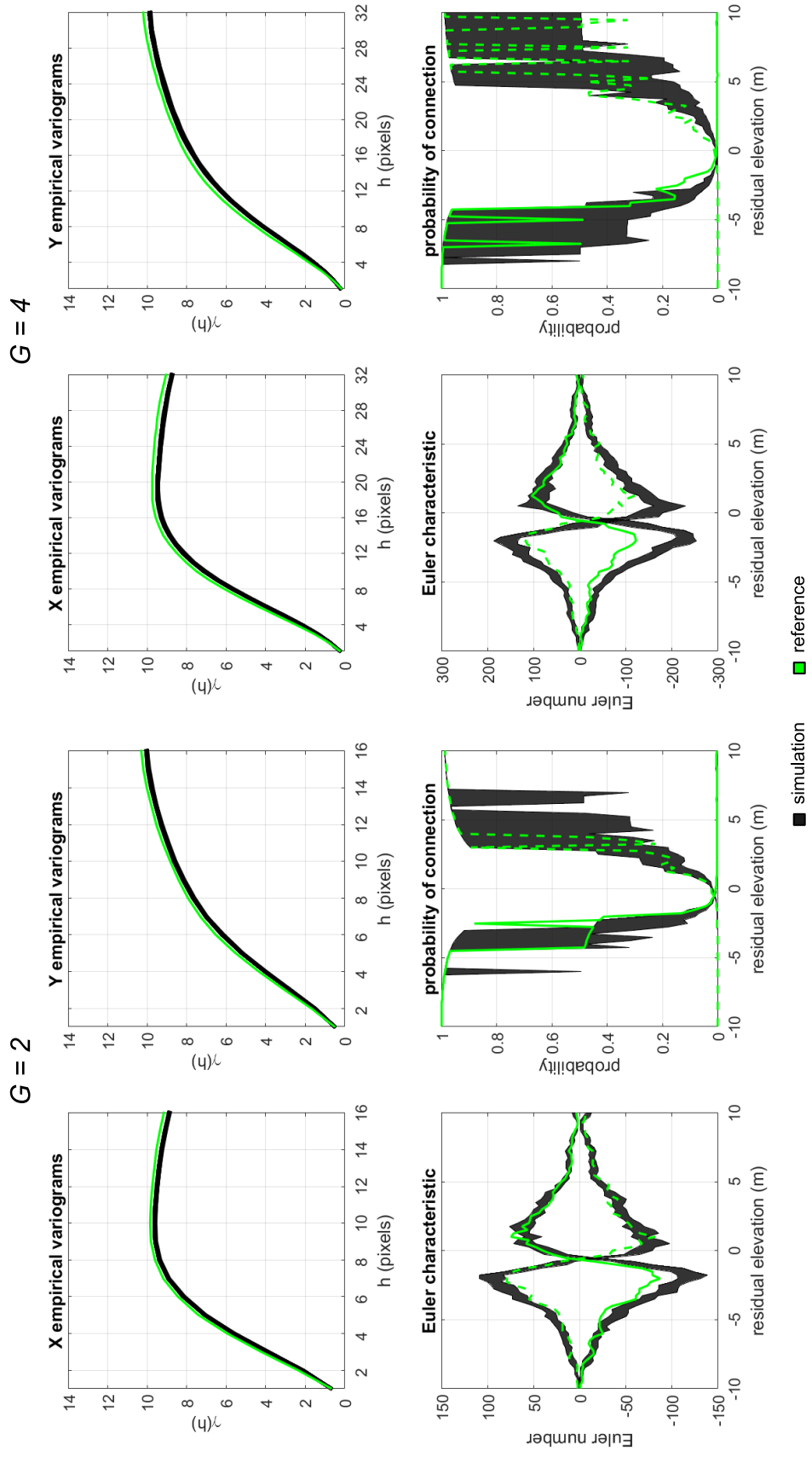
Figure 4.16: The Appalachians example structural statistics.
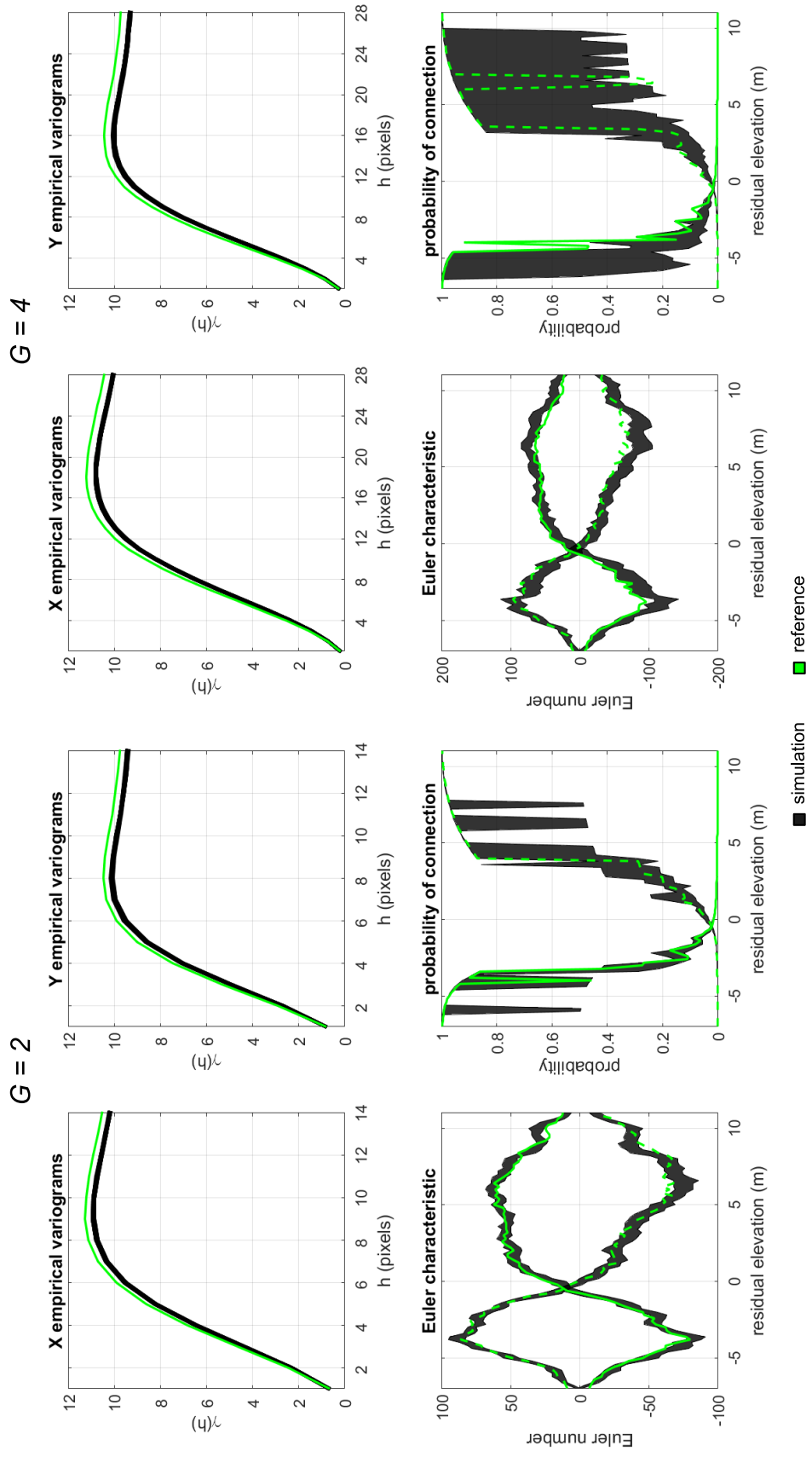
Figure 4.17: The Central Lowlands example structural statistics.

4.5   Conclusions

MPS simulation has proven to be an effective tool for statistical downscaling of DEMs. However, one of the main issues hindering a more widespread application of MPS simulation algorithms is the difficulty linked to their parametrization. To address that, we developed an automated framework for calibrating MPS-driven algorithms with specific focus on DEM downscaling. In the proposed approach, the K-fold cross-validation and simulated annealing techniques are used for optimizing a set of algorithm parameters based on a dual-resolution training data set. The parameter calibration process is framed as an optimization problem, where the goal consists of minimizing an objective function which evaluates the dissimilarity between simulations and the fine-resolution training data. The framework is demonstrated with an updated version of the downscaling algorithm originally proposed by Rasera et al. (2020b,a). Three case studies with different DEM products illustrate the method.

In the initial part of this contribution, we introduced two novel functionalities of the downscaling algorithm. These functionalities include: i. the customization of the training data events search procedure; and ii. the customization of the weighing scheme for integrating coarse- and fine-resolution data. In addition, the new version of the algorithm enables the parametrization of the coarse- and fine-scale distance functions with independent kernels. Another minor upgrade is the definition of a single search radius to parametrize both the trend filtering and the retrieval of data events operations.

The reliance on the K-fold cross-validation technique makes the proposed parameter calibration framework notably suited for handling non-stationary and spatially auto-correlated data sets, such as DEMs. The approach also allows systematic use of the entire training data set for both training and validation, which provides a more accurate prediction performance estimate. The simulated annealing technique is particularly useful as it enables tackling non-differentiable objective functions that might contain multiple local minima. Although prior configuration of the optimization hyperparameters is required, this task is significantly easier and less sensitive than the calibration of the simulation algorithm itself.

An essential aspect of the framework is the formulation of the objective function. The objective function serves to evaluate statistical and textural properties deemed important for a given application. In this work, the inherent complexity of topographic patterns calls for the formulation of a multiple-component objective function. This allows considering different complementary spatial statistics to more accurately characterize such textures. It

is important to note that the "optimal" parameter setup is entirely subject to the chosen objective function. Therefore, the choice of different objective functions implies distinct optimal parameter configurations.

Results demonstrate that the automation algorithm is capable of determining an optimal parameter setup for a given data set. Numerical experiments reveal that the calibrated parameters enable to generate statistically accurate fine-resolution realizations provided that the quality of the coarse-resolution target DEM has not been severely compromised by measurement errors. Please refer to Appendix A.1 for an analysis of the impact of measurement errors in the target DEM into the downscaling process.

In our opinion, the benefits offered by the automation framework far outweight the computational burden associated with running MPS simulations within an optimization setting. In most cases, the approach provides a more efficient alternative than having to perform extensive sensitivity analyses. We strategically reduce the optimization run-time by implementation of a temperature-dynamic simulated annealing perturbation scheme and a uneven discretization of the parameter space. Once the calibration process is finalized, the optimized parameters can be reused for downscaling multiple DEMs, as long as the target and training data sets are believed to share similar sub-pixel topographic patterns.

Future work should focus on refining and further develop the proposed framework using different component objective functions and optimization algorithms. Additional experiments with different folding strategies, and other cross-validation techniques must be carried out. The determination of the algorithm's hyperparameters is a subject not addressed in this contribution. Hyperparameter optimization (Claesen and Moor, 2015) is fundamental for the development of fully-automated, self-tuning algorithms. Future research should also analyze the effect of different hyperparameter configurations on the quality of the approximation of global minima.

Data and code availability

The ArcticDEM was provided by the Polar Geospatial Center at the University of Minnesota under NSF-OPP awards 1043681, 1559691, and 1542736. The 3DEP 1 m DEM is made available by the U.S. Geological Survey. All 3DEP products are public domain. The Australian 5 m DEM is made available by Geoscience Australia under the Creative Commons Attribution 4.0 International Licence. MATLAB codes and data sets used in the case

studies will be provided on GitHub (https://github.com/lgrasera).

Chapter 5

Integrating fine-resolution satellite imagery into the downscaling of digital elevation models

Data integration methods combine disparate data sources to produce more accurate predictions and data-consistent models. Available fine-resolution MSI may be used as secondary information to enhance the structural quality and limit the inherent uncertainty of the stochastic downscaling of coarse-resolution DEMs. This chapter develops the third objective of this thesis: iii. integration of finer-resolution secondary data in the form of MSI into the downscaling.

In this chapter, a probabilistic data integration framework is proposed and illustrated by building upon the MPS-driven downscaling algorithm proposed in Chapter 3. The automation framework introduced in Chapter 4 is used to perform the calibration of algorithm parameters and integration of multiple data sources. The approach provides an efficient alternative for integration of different types of remote sensing data with varying spatial resolution.

This chapter will be submitted to Earth and Space Science as an original research article. Therefore, readers must be aware of potential differences between the future publication and this chapter.

5.1 Introduction

Most of the Earth's terrain features are mapped at relatively coarse spatial and temporal resolutions (Yamazaki et al., 2017). Spaceborne DEMs (Wilson, 2012) comprise the main, and in many cases, the only available data products in remote regions across the planet. Although useful for the analysis of large-scale structures, spaceborne DEMs are unsuited for small-scale landscape representation and hydrological simulations (Zhang and Montgomery, 1994). Wechsler (2007) showed that the spatial resolution of DEMs has a significant impact on multiple hydrologic derivatives. The spatial resolution of DEMs also plays a critical role in hydraulic modeling for flood warning systems (Lamichhane and Sharma, 2018) and urban flood assessment (Leitão and de Sousa, 2018). Small-scale surface processes are more appropriately modeled with ground- and unmanned aerial vehicle-derived fine-resolution DEMs (Wilson, 2012). The spatial resolution of these products enables a more accurate extraction of drainage networks (McMaster, 2002), terrain derivatives (Kienzle, 2003), and topographic indexes (Vaze et al., 2010; Mukherjee et al., 2013). Other applications for fine-resolution DEMs include the analysis of surface texture (Trevisani et al., 2012), spatial patterns of saturated areas (Hoang et al., 2018), and snow estimates (Sohrabi et al., 2019). Nevertheless, fine-resolution DEMs are relatively sparse and unevenly distributed across the planet.

Statistical downscaling is one of the most prominent approaches for enhancing the spatial resolution of remote sensing data (Atkinson, 2013). Geostatistical simulation methods (Goovaerts, 1997; Remy et al., 2009) are widely used, in particular, because of their data conditioning capabilities, relatively low computational cost, and most importantly, their ability to provide uncertainty estimates for the spatial predictions. Being an ill-posed problem, any solution to downscaling calls for prior information, in the form of extant data, or as a model of sub-pixel texture, in order to minimize the problem underdetermination (Bertero and Boccacci, 1998; Boucher and Kyriakidis, 2007). Two-point statistics methods rely on spatial covariance function models to generate simulated realizations of random fields (Kyriakidis and Yoo, 2005; Boucher and Kyriakidis, 2007; Liu and Journel, 2009). These techniques have found application in conflation of terrain elevation measurements and different types of auxiliary data (Kyriakidis et al., 1999; Hengl et al., 2008). Although useful, these methods are not entirely appropriate for modeling the non-stationary low-entropy textures often present in DEMs (Rasera et al., 2020b,a) because of the limited capacity of the variogram to capture higher-order statistics (Dimitrakopoulos et al., 2010). Multiple-point statistics (MPS) (Remy et al., 2009) comprise an alternative group

of geostatistical algorithms specifically designed for simulating such type of textures. MPS algorithms simulate spatial features by resampling replicates from a better-informed analog training data set through a template matching framework. Simulated realizations are generated following either a sequential simulation formalism (Strebelle, 2002) or an optimization process (Deutsch and Cockerham, 1994). Examples of MPS-driven downscaling methods include Boucher (2009), Mariethoz et al. (2011), Straubhaar et al. (2016) and Rasera et al. (2020b,a). Applications in the field of geomorphometry include the simulation of braided river DEM time series (Pirot et al., 2014), terrain elevation data fusion (Tang et al., 2015), and downscaling of coarse-resolution DEMs (Rasera et al., 2020b,a).

Available fine-resolution hard and soft data may be also integrated into the downscaling process. Examples relevant to remote sensing and geomorphometry include the integration of fine-scale geographical information systems data (e.g. delineated water bodies, road networks, previously mapped impervious surfaces) in super-resolution land cover mapping (Boucher and Kyriakidis, 2007; Boucher, 2009), multipectral image sharpening by cokriging (Pardo-Igúzquiza et al., 2006; Atkinson et al., 2008; Pardo-Igúzquiza et al., 2011), downscaling of DEMs based on auxiliary maps with regression kriging (Hengl et al., 2008), and the integration of point- and block-support data in two-point statistics simulation and estimation (Liu and Journel, 2009; Zagayevskiy and Deutsch, 2015). In the last decade, fine-resolution multispectral satellite imagery (MSI) have become widely available, providing extensive information for monitoring the Earth's surface (Gorelick et al., 2017). Despite rendering no elevation information, fine-resolution satellite images can be potentially used as a proxy for resolving sub-pixel terrain features on coarse-resolution DEMs. The concept shares similarities with pan-sharpening algorithms (Du et al., 2007; Thomas et al., 2008; Yokoya et al., 2017). Pan-sharpening methods create a more informative product by combining the small-scale spatial information from a fine-resolution panchromatic band with the spectral information content of coarser-resolution multispectral bands. However, unlike pan-sharpening, the fusion of DEM and MSI data differs substantially because the textural information in an optical image is not easily translatable into terrain elevation measurements due to the complex non-linear relationship between both variables.

In this contribution, we investigate the possibility of integrating fine-resolution MSI to enhance the statistical downscaling of coarse-resolution DEMs. In the presented data integration framework, fine-resolution satellite imagery is incorporated as soft data for resolving sub-pixel terrain features in a coarse-resolution target DEM. The approach contrasts with subsurface geology data integration methods (Deutsch and Wen, 2000), where the spatial

resolution of the soft data (e.g. geophysical imagery) is typically much coarser than the resolution of the hard data (e.g. core samples) and the numerical model itself (i.e. geological model). The proposed framework is illustrated with the MPS downscaling algorithm developed by Rasera et al. (2020b,a,c). Rather than formulating a geostatistical model to describe the correspondence between the coarse- and fine-scale structures, an MPS simulation algorithm is used for resampling similar structures from on a fully-informed training data set that contains co-registered terrain and imagery data at multiple scales. The training data set is ultimately used for optimizing the algorithm parameters, and subsequent downscaling of a coarse-resolution target DEM which also has co-registered fine-resolution imagery data. Information derived from the DEMs and MSI is integrated using the log-linear pooling operator (Allard et al., 2012). The parametrization of the downscaling algorithm and the data integration are carried out using the automation framework developed by Rasera et al. (2020c). The method is illustrated by two case studies in the Western United States (the Colorado Plateau and the San Gabriel Mountains) using the USGS National Map 3D Elevation Program (3DEP) 1 m DEM (Sugarbaker et al., 2017), and the EU Copernicus Programme/European Space Agency (ESA) 10 m resolution Sentinel-2 MSI Level-2A data products (Sudmanns et al., 2019).

The chapter is structured as follows. Section 5.2 provides an overview of the MPS-driven downscaling algorithm proposed by Rasera et al. (2020b,a). Section 5.3 addresses the integration of terrain elevation and satellite imagery data based on a probability aggregation framework. In Section 5.4, we illustrate the algorithm with two case studies. Lastly, Section 5.5 summarizes the results and concludes the chapter with general thoughts on alternative data integration methodologies.

5.2 Downscaling digital elevation models with multiple-point statistics simulation

The following section presents the building blocks of the MPS-driven downscaling algorithm developed by Rasera et al. (2020b,a). Subsection 5.2.1 introduces the concept of representing terrain elevation data as a stochastic spatial signal. Subsection 5.2.2 frames the downscaling problem using the sequential simulation formalism. In Subsection 5.2.3, we describe an approach for computing local conditional probabilities from distances between data events through a distance-to-probability transformation function.

5.2.1 Stochastic representation of terrain elevation data

Let $z_V(\mathbf{u})$ be the terrain elevation measurement assigned to a coarse-resolution pixel V centered at the location $\mathbf{u}$ on coarse-resolution DEM indicated by z_V, where $\mathbf{u} = [x, y]$ corresponds to a position vector in a projected Cartesian coordinate system. In addition, let $z_v(\mathbf{u})$ denote the terrain elevation on a fine-resolution pixel v indexed on a co-registered fine-resolution DEM z_v. The coarse-to-fine resolution ratio between z_V and z_v is expressed as $G = \sqrt{|V|/|v|}$, where $|V|$ and $|v|$ indicate the surface areas of the pixels. The notation is presented in Table 5.1.

The terrain elevation on gridded DEMs can be modeled as a stochastic spatial signal. In this framework, $z_V(\mathbf{u})$ and $z_v(\mathbf{u})$ are interpreted as realizations of the continuous random variables $Z_V(\mathbf{u})$ and $Z_v(\mathbf{u})$

$$Z(\mathbf{u}) = m(\mathbf{u}) + R(\mathbf{u}) + \epsilon(\mathbf{u}), \tag{5.1}$$

where $Z(\mathbf{u})$ denotes either $Z_V(\mathbf{u})$ or $Z_v(\mathbf{u})$; $m(\mathbf{u})$ is a deterministic low-frequency trend component; $R(\mathbf{u})$ is its associated stochastic high-frequency residual; and $\epsilon(\mathbf{u})$ is an intrinsic measurement error component.

The spatial frequency is interpreted as the inverse of the scale of features on the DEM. The trend accounts for large-scale topographic structures, whereas the residual encompasses small-scale features. The term $\epsilon(\mathbf{u})$ comprises local errors associated with the remote sensing acquisition method, georeferencing, terrain properties, and the DEM generation process itself. Typically, $\epsilon(\mathbf{u})$ can only be estimated by validation against a more accurate data set (Kolecka and Kozak, 2014; Mukul et al., 2017). For simplification purposes, we assume that the contribution of $\epsilon(\mathbf{u})$ is negligible (i.e. $\epsilon(\mathbf{u}) \approx 0$). Yamazaki et al. (2017) provides an overview on the different types of measurement errors present on spaceborne DEMs and related error filtering techniques.

The trend $m(\mathbf{u})$ is estimated by applying an appropriate spatial low-pass filter on $z(\mathbf{u})$. The estimator $\hat{m}(\mathbf{u})$ is defined as a weighted linear combination of $z(\mathbf{u})$ and its neighboring data $\{z(\mathbf{u} + \mathbf{h}_j), j = 1, \ldots, n\}$ located within a search radius ρ

$$\hat{m}(\mathbf{u}) = \sum_{j=0}^{n} \lambda_L(\mathbf{h}_j) \, z(\mathbf{u} + \mathbf{h}_j) \quad \text{with} \quad \sum_{j=0}^{n} \lambda_L(\mathbf{h}_j) = 1, \tag{5.2}$$

Table 5.1: Notation.

Notation	Description
β	kernel weights normalizing constant
$\epsilon(\mathbf{u})$	measurement error centered at $\mathbf{u}$
$\lambda(\mathbf{h}_j)$	kernel weight as a function of $\mathbf{h}_j$
σ	kernel shape parameter
$\phi(\cdot)$	distance-to-probability transformation function
Ψ	dual-resolution training data
Ω	conditioning data
$\boldsymbol{\theta}$	vector of algorithm parameters
$\boldsymbol{\Psi}$	multi-resolution training data
$\mathbf{h}_j$	coordinates offset of the j-th node from $\mathbf{u}$
$\mathbf{D}(\mathbf{u})$	local distance vector centered at $\mathbf{u}$
$\mathbf{d}(\mathbf{u})$	data event centered at $\mathbf{u}$
$\mathbf{R}_v(\mathbf{u})$	multivariate fine residual random variable centered at $\mathbf{u}$
$\mathbf{r}_v(\mathbf{u})$	fine residual patch centered at $\mathbf{u}$
$\mathbf{u}$	data location
$\mathbf{w}$	vector of probability aggregation weights
$\mathbf{z}_v(\mathbf{u})$	fine elevation patch centered at $\mathbf{u}$
A	generic event
B	spectral band random variable
d	generic data source
$D(\cdot)$	distance function
$F(\cdot)$	MPS simulation algorithm
G	coarse-to-fine resolution ratio
$m(\mathbf{u})$	trend value centered at $\mathbf{u}$
m	trend component
N	number of pixels on z_V and r_V
$n(\mathbf{u})$	number of pixels in the search neighborhood centered at $\mathbf{u}$
$P(\cdot)$	pooling operator
$R(\mathbf{u})$	residual random variable centered at $\mathbf{u}$
$r(\mathbf{u})$	residual value centered at $\mathbf{u}$
r	residual component
(s)	superscript indicating simulated data
(t)	superscript indicating training data
V	subscript indicating coarse-scale data
v	subscript indicating fine-scale data
w	generic weight
$Z(\mathbf{u})$	elevation random variable centered at $\mathbf{u}$
$z(\mathbf{u})$	elevation value centered at $\mathbf{u}$
z	elevation signal
$\hat{}$	operator indicating estimated data

where $\mathbf{h}_j$ is the set of $n+1$ coordinates lag vectors that radiate from $\mathbf{u}$, with $z(\mathbf{u}) = z(\mathbf{u}+\mathbf{h}_0)$, and $\lambda_L(\mathbf{h}_j)$ are the weights given by a kernel function. The datum $r(\mathbf{u})$ is interpreted as a realization of $R(\mathbf{u})$, and corresponds to the complement of $\hat{m}(\mathbf{u})$ (Eq. (5.1)) .

5.2.2   Downscaling with sequential simulation

The objective is to generate predictions of the fine-resolution variables $\hat{m}_v(\mathbf{u})$ and $R_v(\mathbf{u})$, so that $Z_v(\mathbf{u})$ can be restored with Equation (5.1). Unfortunately, $\hat{m}_v(\mathbf{u})$ and $R_v(\mathbf{u})$ cannot be directly computed as $Z_v(\mathbf{u})$ is unknown. To limit the problem underdetermination, we resort on estimating both variables indirectly based on the interpolation of $\hat{m}_V$ and by providing a prior sub-pixel textural model in the form of a finer-resolution training DEM. Under the assumption that the fine-scale trend is a smooth surface, $\hat{m}_v$ is estimated by resampling $\hat{m}_V(\mathbf{u})$ at a finer resolution with the bicubic interpolation method (Keys, 1981). The residual $R_v(\mathbf{u})$ is simulated by downscaling $R_V(\mathbf{u})$ with a quasi-pixel-based simulation approach (Rasera et al., 2020b,a). An MPS algorithm $F(\cdot)$ is used to generate conditional simulated realizations of the fine-resolution multivariate random variable $\mathbf{R}_v(\mathbf{u})$ co-located with $r_V(\mathbf{u})$, denoted as $\{\mathbf{r}_v^{(s)}(\mathbf{u}), s = 1\dots,S\}$

$$\mathbf{R}_v(\mathbf{u}) = F(\boldsymbol{\theta}, \Psi \mid \Omega) \mapsto \{\mathbf{r}_v^{(s)}(\mathbf{u}), s = 1,\ldots,S\}, \qquad (5.3)$$

where $\boldsymbol{\theta}$ is the vector of algorithmic parameters associated with $F(\cdot)$; Ψ is the dual-resolution training data assembled from two co-registered training DEMs denoted by $z_V^{(t)}$ and $z_v^{(t)}$; $\mid \Omega$ denotes the conditioning to the original coarse and previously simulated fine-resolution data; and $\mathbf{r}_v^{(s)}(\mathbf{u})$ consists of a $(G \times G)$ fine-resolution simulated residual patch.

The spatial resolution of R_v is gradually magnified following a series of conditional iterations of the algorithm in a pyramid-based fashion (Burt and Adelson, 1983). Simulated realizations of $\mathbf{R}_v(\mathbf{u}_i)$ are generated based on a sequential simulation framework (Goovaerts, 1997). The multivariate conditional probability $\Pr\{\mathbf{R}_v(\mathbf{u}_i) = \mathbf{r}_v \mid \Omega_{i-1}\}$ for $i = 1,\ldots,N$ is given by the recursive Bayes relation

$$\Pr\{\mathbf{R}_v(\mathbf{u}_1) = \mathbf{r}_v,\ldots,\mathbf{R}_v(\mathbf{u}_N) = \mathbf{r}_v \mid \Omega_N\} \qquad (5.4)$$
$$= \Pr\{\mathbf{R}_v(\mathbf{u}_1) = \mathbf{r}_v \mid \Omega_0\} \cdot \prod_{i=2}^{N-1} \Pr\{\mathbf{R}_v(\mathbf{u}_i) = \mathbf{r}_v \mid \Omega_{i-1}\},$$

where $\mid \Omega_0$ refers to the conditioning of the downscaling to the input coarse-scale data, and $\mid \Omega_{i-1}$ to the conditioning of the i-th iteration to the $i - 1$ previously simulated fine-resolution residual patches and the original coarse-resolution data. The index sequence $i = 1, \ldots, N$ defines the simulation path. The conditional probability $\Pr\{\mathbf{R}_v(\mathbf{u}_i) = \mathbf{r}_v \mid \Omega_{i-1}\}$ is approximated based on $F(\cdot)$ and the dual-resolution training data Ψ.

5.2.3 Computing local conditional probabilities

The simulation of sub-pixel residual features is achieved by direct transferring of fine-resolution patches from training data set to the target DEM. The conditioning to coarse- and fine-scale data events, denoted by $\mathbf{d}_e(\mathbf{u}_i) = \{d_e(\mathbf{u}_i + \mathbf{h}_j), j = 1, \ldots, J_e(\mathbf{u}_i)\}$, where $d_e(\mathbf{u}_i + \mathbf{h}_j)$ indicates a data value associated with a generic variable e, is performed by preferential sampling of candidate training data events $\mathbf{d}_e^{(t)}(\mathbf{u})$ that minimize a pattern dissimilarity metric (i.e. a distance function)

$$D(\mathbf{d}_e(\mathbf{u}_i), \mathbf{d}_e^{(t)}(\mathbf{u})) = \left(\sum_{\forall j \text{ if } \|\mathbf{h}_j - \mathbf{h}_0\|_2^2 \leq \rho} \lambda_e(\mathbf{h}_j) \left[d_e(\mathbf{u}_i + \mathbf{h}_j) - d_e^{(t)}(\mathbf{u} + \mathbf{h}_j) \right]^2 \right)^{1/2}, \quad (5.5)$$

where $\lambda_e(\mathbf{h}_j)$ are weights given by a kernel function associated with the variable e, with $\sum_j \lambda_e(\mathbf{h}_j) = 1$. Note that the number of pixels retained within a data event is a function of the search radius ρ and the spatial resolution of the input variable. Equation (5.5) can be efficiently computed for all data events stored in Ψ by performing convolutions in the frequency domain using the fast Fourier transform (FFT) algorithm (Kwatra et al., 2003).

In order to integrate information derived from multiple variables, Hoffimann et al. (2017) and Rasera et al. (2020b,a) proposed, in the context of MPS simulation, the conversion of distances between data events into conditional probabilities based upon an empirical transformation function. The rationale is to define local probabilities for sampling each training data event as a function of its distance to a reference target data event. The structural accuracy of simulated realizations is maximized by the formulation of a transformation function $\phi(\cdot)$ which grants higher probabilities to training data events that minimize Equation (5.5). In this study, we employ the transformation function introduced by Rasera et al. (2020b,a), which enables computing conditional probabilities as follows

$$\Pr\{\mathbf{R}_v(\mathbf{u}_i) = \mathbf{r}_v \mid \Omega_{i-1}^{(e)}\} \approx \Pr\{\mathbf{R}_v(\mathbf{u}_i) = \mathbf{r}_v^{(t)}(\mathbf{u}_k) \mid \mathbf{d}_e(\mathbf{u}_i)\} \propto \phi\left(\mathbf{D}_e(\mathbf{u}_i)\right), \qquad (5.6)$$

where $\mathbf{r}_v^{(t)}(\mathbf{u}_k)$ corresponds to the central patch of the fine-resolution residual data event $\mathbf{d}_{R_v}^{(t)}(\mathbf{u}_k)$, $\Omega_{i-1}^{(e)}$ is the conditioning data associated with the variable e, and $\mathbf{D}_e(\mathbf{u}_i)$ is a $(K \times 1)$ vector storing the distances between the local conditioning data and the set of training data events $\{\mathbf{d}_e^{(t)}(\mathbf{u}_k), k = 1, \dots, K\}$, with K being a user-defined parameter.

5.3 Integrating fine-resolution satellite imagery data into the downscaling

This section discusses the merging of conditional probabilities derived from the coarse- and fine-resolution residual DEMs and MSI data into the downscaling process. Subsection 5.3.1 introduces the framework for data integration based on probability aggregation operators. The conditioning of the simulated realizations to fine-resolution satellite imagery as soft data is described in Subsection 5.3.2. Subsection 5.3.3 provides a summary of the algorithm.

5.3.1 Data integration with probability aggregation operators

Probability aggregation methods (Clemen and Winkler, 1999; Allard et al., 2012) provide a general framework for combining multiple estimates of an event A obtained from different data sources $\{d_e, e = 1, \dots, E\}$ with unknown dependences. A pooling operator denoted by $P(\cdot)$ is used to approximate the conditional probability $\Pr\{A \mid d_1, \dots, d_E\}$ based on several individual conditional probabilities $\Pr\{A \mid d_e\}$

$$\Pr\{A \mid d_1, \dots, d_E\} \approx P(\Pr\{A\}, \Pr\{A \mid d_1\}, \dots, \Pr\{A \mid d_E\}), \qquad (5.7)$$

where $\Pr\{A\}$ is the prior probability.

An overview of different pooling operators can be found in Allard et al. (2012). Among the available methods, the log-linear pooling operator stands out as being one of the most popular approaches. This operator is based on the multiplication of probabilities

$$\Pr\{A \mid d_1, \ldots, d_E\} \propto \Pr\{A\}^{1-\sum_{e=1}^{E} w_e} \prod_{e=1}^{E} \Pr\{A \mid d_e\}^{w_e}, \tag{5.8}$$

Allard et al. (2012) demonstrate that the log-linear pooling decomposition is exact if there is one weight w_e per combination $\{A \mid d_1, \ldots, d_E\}$. The weights w_e are computed as follows

$$w_e = \frac{\ln \Pr\{d_e \mid A, \Omega_{e-1}\}}{\ln \Pr\{d_e \mid A\}}, \tag{5.9}$$

where $\Omega_{e-1} = \{d_1 \cap \cdots \cap d_{e-1}\}$.

Yet, in most cases, the denominator in Equation (5.9) is unknown, therefore, the weights have to be approximated. If $w_e = 1$, the numerator and denominator of Equation (5.9) become equal, and the data $\{d_e, e = 1, \ldots, E\}$ are assumed independent conditionally to A. When $\sum_{e=1}^{E} w_e = 1$ the prior distribution $\Pr\{A\}$ in Equation (5.8) vanishes and the pooling preserves the unanimity property. This implies that, if all individual conditional probabilities are equal, the pooling aggregation results in the same probability.

5.3.2 Integrating hard and soft data into the downscaling

Available fine-resolution data may be also integrated in the downscaling process. This enables generating alternative scenarios that are consistent with both coarse-scale measurements and any additional, or previously mapped, fine-scale data. Such data can be obtained via direct surveys, archival data, or by another finer-resolution imaging technique. These measurements may consist of either "hard" or "soft" data. Hard (or primary) data comprise direct measurements of the target variable at the exact sample locations. Conversely, soft (or secondary) data encompass any type of indirect, and often less precise, measurement of the primary variable. Disparate data sets are generally integrated following a probabilistic framework (Journel, 2002; Remy et al., 2009; Allard et al., 2012). Probabilities provide a unit-free, standardized, coding of information, which facilitates the task of integrating data.

Let $\Omega_{i-1}^{\mathrm{hd}}$ denote the available conditioning hard data (i.e. coarse- and fine-resolution residuals) at the i-th iteration of the sequential simulation. In addition, let Ω^{sd} indicate a co-registered multivariate soft data set represented by a fine-resolution orthorectified MSI. In the algorithm, the distinction between hard and soft data is solely based on a hierarchical

criterion for sampling the training data set. Coarse- and fine-resolution hard data events offer direct and reliable information about terrain features, therefore they are used to control the retrieval of training data events. Consequently, the MSI serves only as an auxiliary source of textural information for resolving sub-pixel structures. If the satellite imagery proves to be informative (i.e. enhances the structural accuracy of simulated realizations), the retrieval of data events is relaxed by the algorithm self-calibration process, and allows considering a larger number of candidate training data events K.

The log-linear pooling operator is used to merge the conditional probabilities derived from the coarse- and fine-scale residual variables and the spectral bands B_l to estimate the posterior probability $\Pr\{A_i \mid \Omega_{i-1}^{\mathrm{hd}}, \Omega^{\mathrm{sd}}\}$, with $A_i = \{\mathbf{R}_v(\mathbf{u}_i) = \mathbf{r}_v^{(t)}(\mathbf{u}_k)\}$, through the use of the vector of aggregation weights $\mathbf{w} = [w_{R_V}, w_{R_v}, \{w_{B_l}, l = 1, \ldots, L\}]$

$$\Pr\{A_i \mid \Omega_{i-1}^{\mathrm{hd}}, \Omega^{\mathrm{sd}}\} \propto \prod_{i=1}^{N} \left\{ \Pr\{A_i \mid \mathbf{d}_{R_V}(\mathbf{u}_i)\}^{w_{R_V}} \cdot \Pr\{A_i \mid \mathbf{d}_{R_v}(\mathbf{u}_i)\}^{w_{R_v}} \cdot \right. \tag{5.10}$$
$$\left. \prod_{l=1}^{L} \Pr\{A_i \mid \mathbf{d}_{B_l}(\mathbf{u}_i)\}^{w_{B_l}} \right\},$$

Note that we eliminate the prior probability $\Pr\{A_i\}$ by imposing the following constrain on the aggregation weights $w_{R_V} + w_{R_v} + \sum_{l=1}^{L} w_{B_l} = 1$. This is equivalent to assuming a uniform prior distribution, which has no influence on the aggregation process.

In our implementation, $\mathbf{w}$ can be either static or dynamic. In a static setting, the weights are fixed throughout the progress of the simulation. By contrast, if the weighting scheme is set to dynamic, $\mathbf{w}(\mathbf{u}_i)$ is allowed to vary as a function of the data surrounding the location $\mathbf{u}_i$. This accounts for the varying amount of information available for the residual variable throughout the sequential simulation. If a dynamic weighting scheme is chosen, w_{R_v} becomes a function of the fine-resolution residual kernel weights $\{\lambda_{R_v}(\mathbf{h}_j), j = 1, \ldots, n(\mathbf{u}_i)\}$

$$w_{R_v}(\mathbf{u}_i) = \sum_{j=1}^{n(\mathbf{u}_i)} \lambda_{R_v}(\mathbf{h}_j), \tag{5.11}$$

where $n(\mathbf{u}_i)$ denotes the local number of informed fine-scale residual pixels. The remaining elements in $\mathbf{w}(\mathbf{u}_i)$ are re-scaled accordingly.

5.3.3 Algorithm

The flowchart in Figure 5.1 illustrates the main processes included in the downscaling and data integration framework. The residuals extracted from the training DEMs and the spectral bands from the fine-resolution MSI are used to construct the dual-resolution training data set. The spatial low-pass filters applied to the target and training DEMs have the same parametrization so that compatible residual data can be compared and transferred to the target DEM.

Algorithm 5 shows a pseudocode for the data integration framework. The retrieval of training data events is regulated by either the coarse- or fine-resolution residual based on the search control parameter $\xi \in [0,1]$ (line 8 of Algorithm 5). If $w_{R_v}(\mathbf{u}_i) \geq \xi$, the conditioning fine-resolution residual data event has enough information to lead the retrieval of training data events. Otherwise, the training data events are selected based on the coarse-resolution residual. If the algorithm calibration process reveals that a dynamic probability aggregation scheme enhances the statistical quality of the downscaling outputs, the Boolean control variable χ is used to activate the local updating of $\mathbf{w}(\mathbf{u}_i)$ (line 16 of Algorithm 5). After the simulation process is terminated, $z_v^{(s)}$ is restored with Equation (5.1) (line 23 of Algorithm 5). For reproducibility, an initial seed may be specified to initialize the pseudo-random number generator which defines the simulation path and the sampling of the local conditional probability distribution functions (CPDFs). For further magnification, one can iterate Algorithm 5 using the fine-resolution output of the previous iteration as input for the following iteration (i.e. $z_V \leftarrow z_v^{(s)}$). Note that this entails replacing Ψ by a vector of dual-resolution training data sets. We recommend performing iterations with $G \leq 3$, otherwise artifacts might appear in the realizations.

Table 5.2 provides a list with all the algorithm parameters and their typical lower and upper bounds for downscaling a target DEM with nominal pixel size of 30×30 m. The search radius ρ is shared by the spatial low-pass filter and all distance functions. The effective search radius can be potentially modulated by the kernel function. In this study, the kernel parameter associated with the spatial low-pass filter and distance functions corresponds to the standard deviation of a normalized Gaussian radial basis function

$$\lambda(\mathbf{h}_j) = \frac{1}{2\pi\sigma^2\beta} \exp\left(-\frac{\|\mathbf{h}_j - \mathbf{h}_0\|_2^2}{2\sigma^2}\right), \tag{5.12}$$

where $\sigma > 0$ is the shape parameter, and $\beta > 0$ is the normalizing constant (i.e. the sum of

---

Algorithm 5 Downscaling and data integration with sequential simulation

---

     input: the initial hard data Ω_0^{hd}, the soft data Ω^{sd}, a vector of algorithmic parameters $\boldsymbol{\theta}$, and a dual-resolution multivariate training data set Ψ

     output: a conditional simulated realization $z_v^{(s)}$

  1: Compute r_V and $\hat{m}_v$

  2: Generate a path visiting $r_V(\mathbf{u}_i), i = 1, \ldots, N$

  3: **for** each $r_V(\mathbf{u}_i), i = 1, \ldots, N$ along the path **do**

  4:     **for** each e-th variable, $e = 1, \ldots, E$ **do**

  5:         Retrieve the local conditioning data event $\mathbf{d}_e(\mathbf{u}_i)$

  6:         Compute $D(\mathbf{d}_e(\mathbf{u}_i), \mathbf{d}_e^{(t)}(\mathbf{u}))$ for all training data events in Ψ

  7:     **end for**

  8:     **if** $w_{R_v}(\mathbf{u}_i) \geq \xi$ **then**

  9:         Retrieve the K-best fine-resolution residual training data events

10:     **else**

11:         Retrieve the K-best coarse-resolution residual training data events

12:     **end if**

13:     **for** each of the remaining $E - 1$ variables **do**

14:         Retrieve the K co-registered training data events

15:     **end for**

16:     **if** $\chi = \text{true}$ **then**

17:         Compute the probability aggregation weights $\mathbf{w}(\mathbf{u}_i)$

18:     **end if**

19:     Estimate $\Pr\{\mathbf{R}_v(\mathbf{u}_i) = \mathbf{r}_v^{(t)}(\mathbf{u}_k) \mid \Omega_{i-1}^{\mathrm{hd}}, \Omega^{\mathrm{sd}}\}, k = 1, \ldots, K$

20:     Draw a simulated patch $\mathbf{r}_v^{(s)}(\mathbf{u}_i)$ from the local CPDF

21:     Add $\mathbf{r}_v^{(s)}(\mathbf{u}_i)$ to $r_v^{(s)}$

22: **end for**

23: $z_v^{(s)} \leftarrow \hat{m}_v + r_v^{(s)}$

24: **return** the conditional simulated realization $z_v^{(s)}$

---

all kernel weights).

Table 5.2: Algorithm parameters.

$\boldsymbol{\theta}$	Bounds	Description
ρ	[30, 109]	Search radius for retrieving data events (m)
σ_L	[4, 1024]	Spatial low-pass filter kernel parameter (m)
σ_{R_V}	[4, 1024]	Coarse residual distance function kernel parameter (m)
σ_{R_v}	[4, 1024]	Fine residual distance function kernel parameter (m)
σ_B	[4, 1024]	Spectral band distance function kernel parameter (m)
K	[2, 64]	Number of candidate training data events
ξ	[0, 1]	Threshold for switching training data events search
χ	Boolean	Dynamic probability aggregation weights
w_{R_V}	[0, 1]	Coarse residual probability aggregation weight
w_{R_v}	[0, 1]	Fine residual probability aggregation weight
w_B	[0, 1]	Spectral band probability aggregation weight
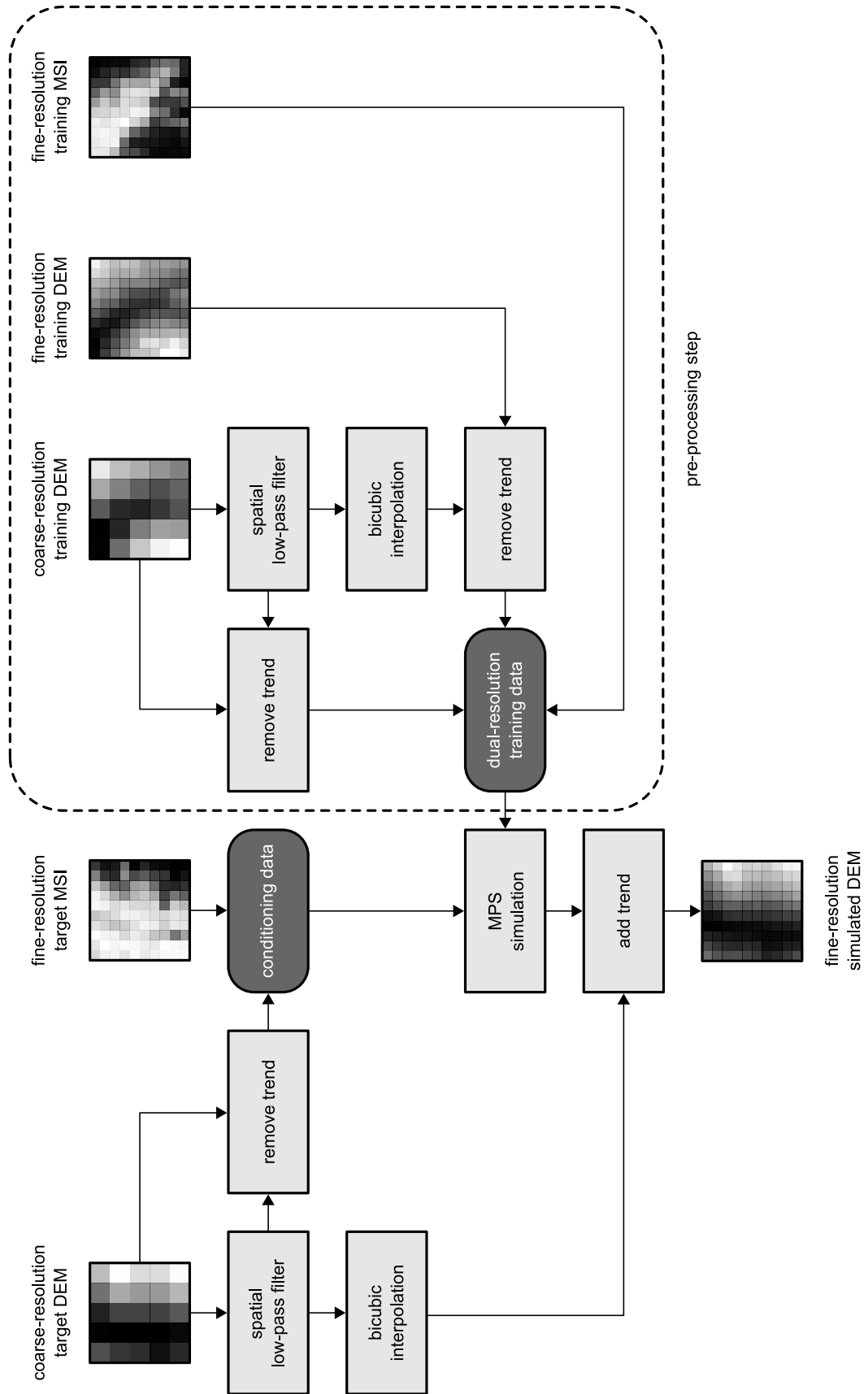
Figure 5.1: Downscaling and data integration algorithm flowchart (modified from Rasera et al. (2020b,a,c)). Processes are represented as gray rectangles. Intermediate data structures are depicted as rounded dark gray rectangles.

5.4 Case studies

In the following section, we demonstrate the algorithm by two case studies. The advantages offered by the integration of fine-resolution secondary information into the downscaling are investigated by conducting numerical experiments with and without MSI data. Subsection 5.4.1 presents the target and training data sets. Subsection 5.4.2 details the parametrization of the algorithm. The downscaling results and their statistical validation are presented in Subsection 5.4.3.

5.4.1 Target and training data sets

The proposed data integration framework is illustrated with two freely available data products: the USGS National Map 3DEP 1 m DEMs (Sugarbaker et al., 2017), and the EU Copernicus Programme/ESA 10 m resolution Sentinel-2 Level-2A multispectral imagery (Sudmanns et al., 2019). The Level-2A products correspond to bottom of atmosphere (BOA) reflectance orthoimages derived from the associated Level-1C top of atmosphere reflectance data sets. To minimize the propagation of measurement errors, often present in spaceborne DEMs (Yamazaki et al., 2017), into the downscaling, we demonstrate the approach with artificial coarse-resolution target DEMs generated by linear upscaling of the 3DEP 1 m DEMs. Table 5.3 provides additional information on the aforementioned data products. Appendix A.1 illustrates the framework using the 3DEP 1-arc second DEM (Sugarbaker et al., 2017) as coarse-resolution target DEM.

Table 5.3: Data products.

Product	Sensing years	Data type	Sensor type	Nominal pixel size (m)
3DEP 1 m	2016-2023	DEM	LiDAR	1×1
Sentinel-2 Level-2A	2017-2024	MSI	Optical	10×10

The method is demonstrated by executing two iterations of the algorithm. Under the assumptions that $\epsilon(\mathbf{u}) \approx 0$ and the data in the DEMs correspond the average sensor response over their associated pixels, artificial training and reference DEMs with different spatial resolutions are constructed by linear upscaling of the original 3DEP 1 m DEMs. Both target and training MSI derive from Sentinel-2 Level-2A data products. The dimensions and nominal pixel sizes of the coarse-, medium-, and fine-resolution DEMs and MSI

are listed in Table 5.4. The medium-resolution MSI data sets are produced by linear up-scaling of the original Sentinel-2 imagery, whereas the fine-resolution MSI are resampled with bicubic interpolation. The medium- and fine-resolution reference DEMs serve to validate the downscaling outputs. The footprints of the target/reference and training DEMs correspond to 3.69 and 14.75 km^2, respectively.

Table 5.4: Coarse-, medium-, and fine-resolution DEMs and MSI.

Data set	Spatial resolution	Data type(s)	Dimensions (pixels)	Nominal pixel size (m)
Target	Coarse	DEM	64×64	30×30
Target/Reference	Medium	DEM/MSI	128×128	15×15
	Fine	DEM/MSI	256×256	7.5×7.5
Training	Coarse	DEM	128×128	30×30
	Medium	DEM/MSI	256×256	15×15
	Fine	DEM/MSI	512×512	7.5×7.5

The MSI consists of composites assembled by merging of spatially overlapping images acquired between the years of 2017 and 2019. The downscaling is conditioned to information derived from the spectral bands 4 and 8. The two bands correspond to the red and near-infrared (NIR) wavelengths, centered at 664.6 and 832.8 nm, and with bandwidths of 31 and 106 nm, respectively. Four additional bands are generated and added to each data set by computing the normalized difference vegetation index (NDVI) and applying the Sobel–Feldman operator on all three bands. The Sobel–Feldman operator is used to remove trends and highlight high-frequency features in the optical imagery. Table 5.5 provides a summary of the variables considered in the study.

Table 5.5: Hard and soft variables.

Variable	Type	Description
R_V	Hard	Coarse-scale residual elevation (m)
R_v		Fine-scale residual elevation (m)
B_1	Soft	BOA reflectance – Red
B_2		BOA reflectance – NIR
B_3		NDVI
B_4		BOA reflectance – Red (Sobel–Feldman filtered)
B_5		BOA reflectance – NIR (Sobel–Feldman filtered)
B_6		NDVI (Sobel–Feldman filtered)

In this contribution, directional effects in the MSI due to surface reflectance anisotropy (Hügli and Frei, 1983; Feingersh et al., 2010; Wen et al., 2018) and changes in the solar and viewing geometry are ignored. Reflectance intensity values in satellite imagery can vary as a function of the spatial anisotropy of the target of interest and the angular geometry of the illumination source and observation at the time of the measurements, hence intensity values will depend on the position of the target within the swath of the sensor and the time of passage of the satellite over the imaged area. Moreover, light-occlusion effects caused by mountainous terrain (e.g. shadows casted by mountains) have a substantial impact on reflectance values. The usage of composite images and spectral band ratios attenuates these effects to some degree, but does not eliminate them as this form of anisotropy is also often spectrally dependent.

The method is illustrated by two case studies in the Western United States, including terrain and imagery data from the Colorado Plateau, in Western Colorado, and the San Gabriel Mountains, in Southern California. Figures 5.2–5.5 show the target and training DEMs, and two of their associated fine-resolution composite images (Red and NIR bands). Only the coarse-resolution target DEMs and fine-resolution training DEMs are displayed. The target and training data sets are extracted from neighboring sites which exhibit similar geomorphic features. Brief descriptions of the geological and geomorphological settings for both study areas are provided below.

The Colorado Plateau is one of the constituents of the Intermontane Plateaus located in the Western United States, and it is roughly centered on the Four Corners region. It is predominately made up of a high desert characterized by the presence of buttes, gorges, and deeply incised meandering rivers. The San Gabriel Mountains are part of the Transverse Ranges, and lie between the Los Angeles Basin and the Mojave Desert. The mountain range was originally a large fault block that was uplifted and later dissected by various rivers and washes. The present-day topography is characterized by rolling peaks and rugged mountainous terrains, which includes a large number of canyons.

The residual DEMs are computed using a spatial low-pass filter with $\rho = 90$ m and $\sigma_L = 600$ m. Positive features of the residual variable indicate crags and ridgelines, while negative structures represent rivers and gully networks. The examples present two disparate scenarios for the downscaling algorithm. The Colorado Plateau example residual DEMs are primarily characterized by relatively smooth textures and localized sharp curvilinear gradients. Several of the main features in the landscape, such as the meanders, are substantially larger than the target DEM pixel size. The peak-to-peak amplitude of the trend component

for both target and training data sets does not exceed 300 m. By contrast, the San Gabriel Mountains example residual DEMs display rough textures, predominately dominated by dendritic drainage patterns and ridgeline structures. Many of these features tend to be finer than, or equal to, the spatial resolution of the target DEM. The peak-to-peak amplitudes of the target and training data sets surpass 0.5 and 1 km, respectively. Descriptive statistics of the coarse-resolution residual DEMs are given in Table 5.6.

Table 5.6: Summary statistics of the coarse-resolution DEMs from the Colorado Plateau and the San Gabriel Mountains examples.

Example	Data set	Mean	SD	Min.	Max.
Colorado Plateau	Training	0.00	8.25	−30.54	65.25
	Target	−0.48	7.14	−26.03	27.97
San Gabriel Mountains	Training	0.02	10.06	−40.52	34.47
	Target	0.26	10.60	−27.54	28.63

Values are in residual elevation (in m)
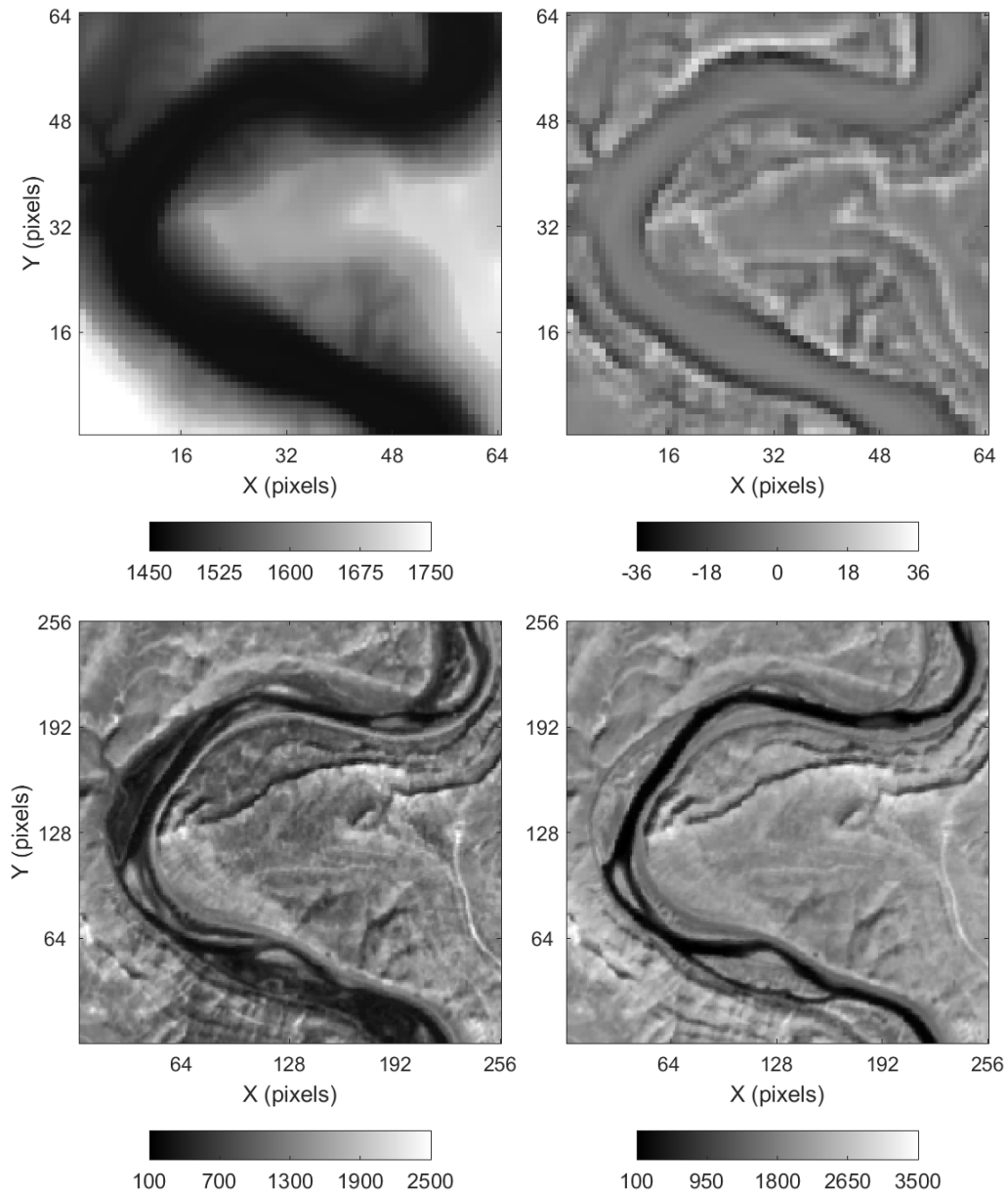
Figure 5.2: The Colorado Plateau example coarse-resolution target DEM and fine-resolution MSI. *Top left*: coarse-resolution DEM. *Top right*: coarse-resolution residual DEM. *Bottom left*: fine-resolution BOA reflectance orthoimage (Red). *Bottom right*: fine-resolution BOA reflectance orthoimage (NIR). DEM colorbars' unit is m. MSI colorbars' unit is digital number.
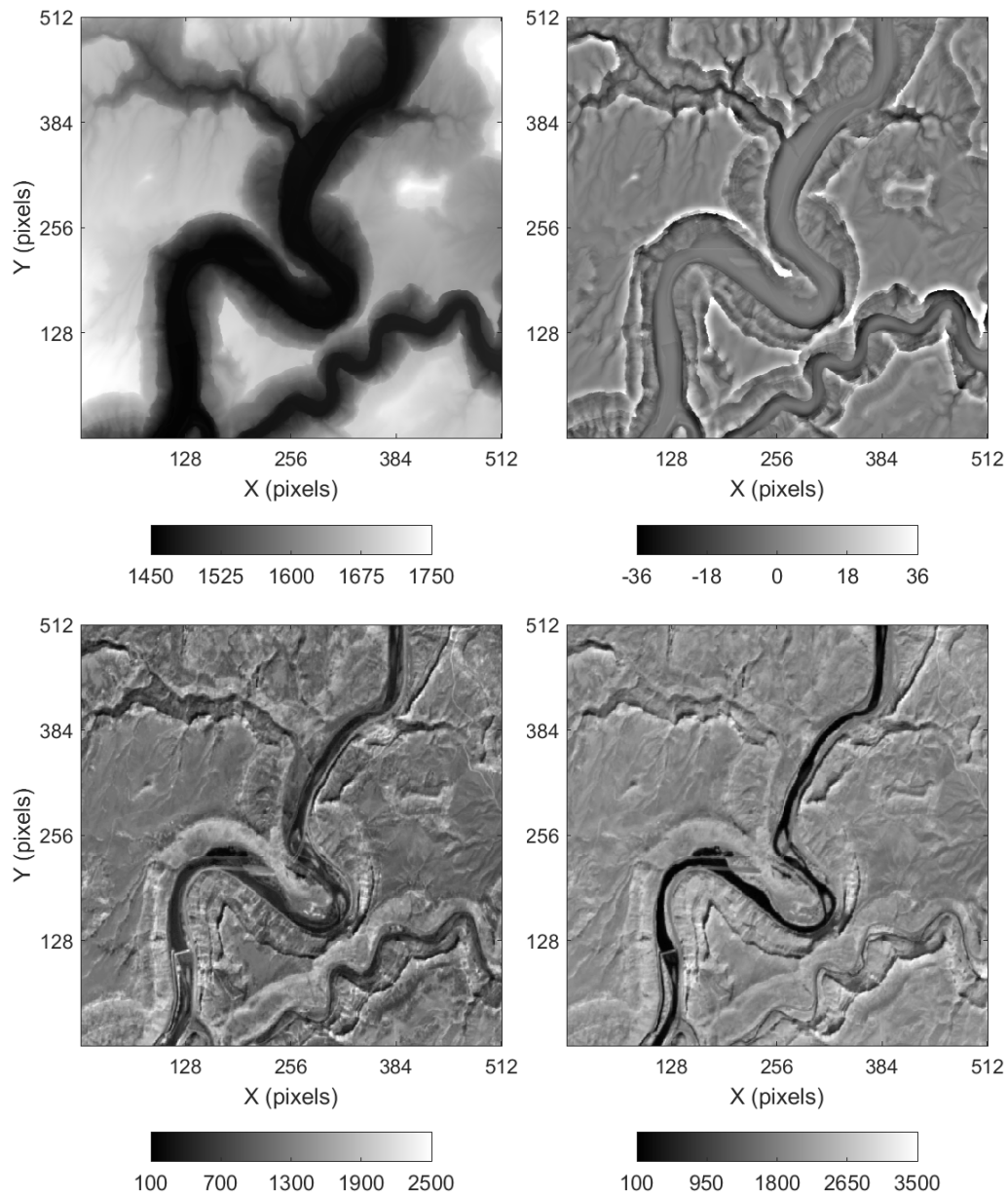
Figure 5.3: The Colorado Plateau example fine-resolution training DEM and MSI. *Top left*: fine-resolution DEM. *Top right*: fine-resolution residual DEM. *Bottom left*: fine-resolution BOA reflectance orthoimage (Red). *Bottom right*: fine-resolution BOA reflectance orthoimage (NIR). DEM colorbars' unit is m. MSI colorbars' unit is digital number.
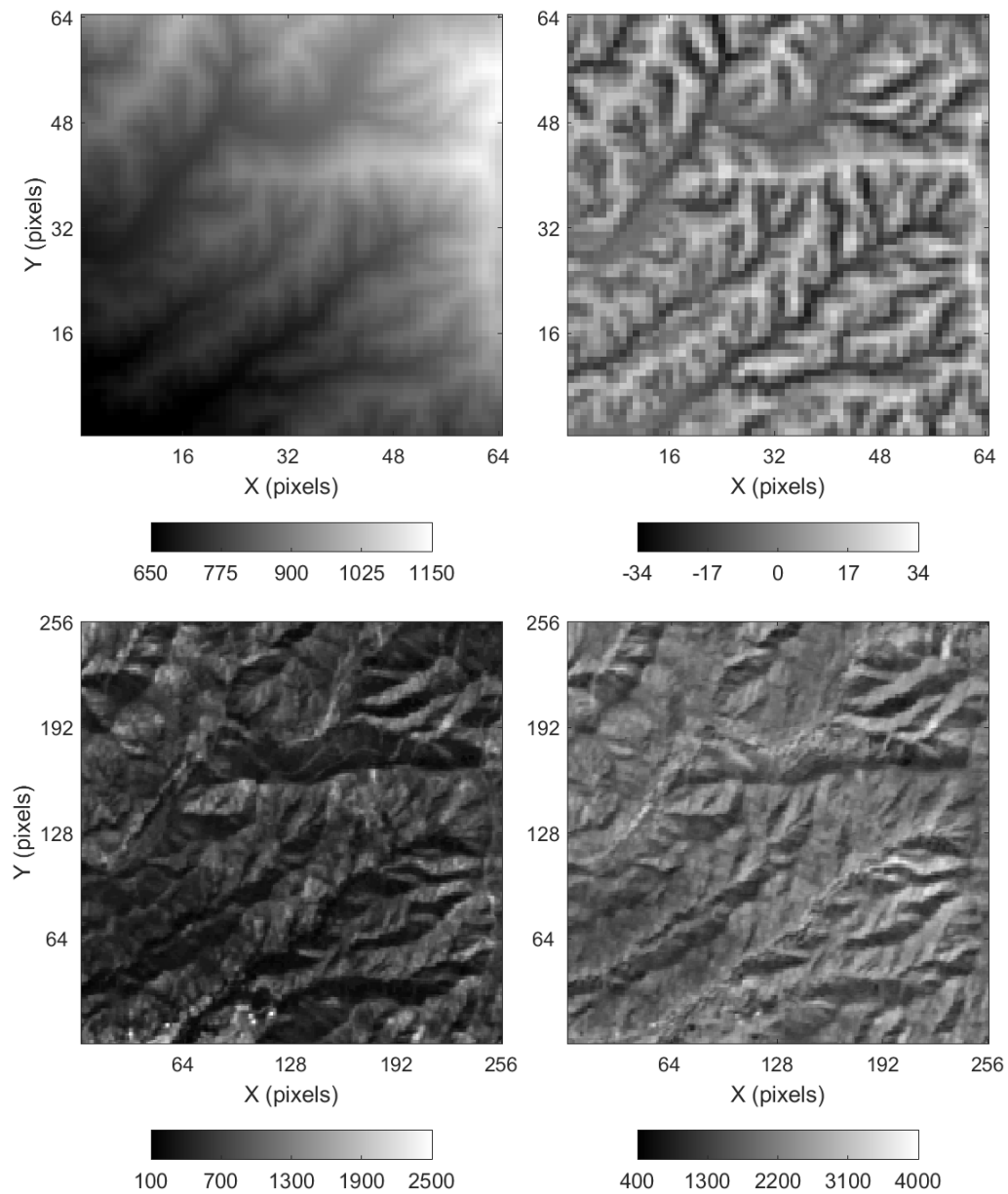
Figure 5.4: The San Gabriel Mountains example coarse-resolution target DEM and fine-resolution MSI. *Top left*: coarse-resolution DEM. *Top right*: coarse-resolution residual DEM. *Bottom left*: fine-resolution BOA reflectance orthoimage (Red). *Bottom right*: fine-resolution BOA reflectance orthoimage (NIR). DEM colorbars' unit is m. MSI colorbars' unit is digital number.

Figure 5.5: The San Gabriel Mountains example fine-resolution training DEM and MSI. *Top left*: fine-resolution DEM. *Top right*: fine-resolution residual DEM. *Bottom left*: fine-resolution BOA reflectance orthoimage (Red). *Bottom right*: fine-resolution BOA reflectance orthoimage (NIR). DEM colorbars' unit is m. MSI colorbars' unit is digital number.
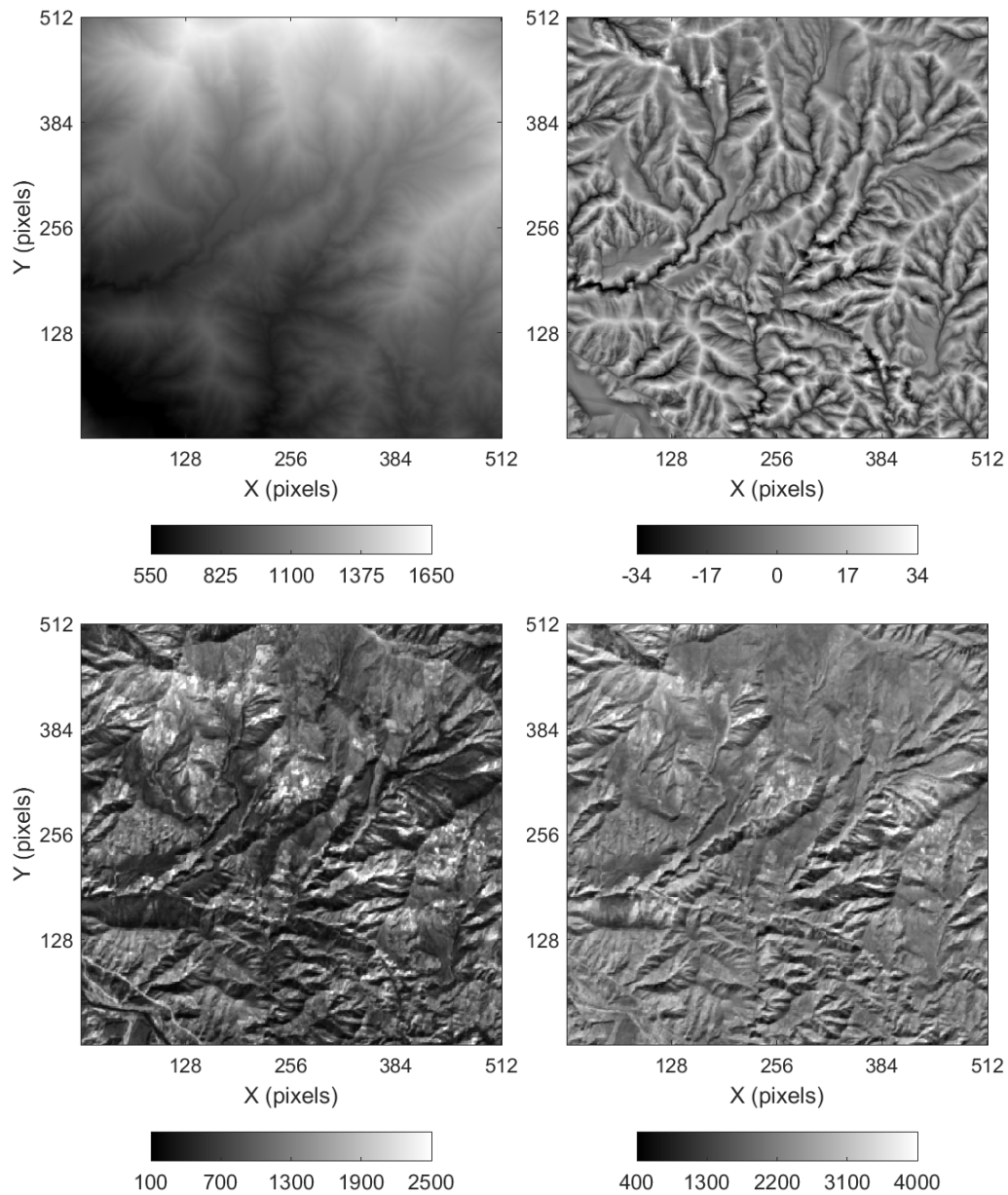
5.4.2   Algorithm parametrization

All input parameters required by the downscaling algorithm and data integration process are automatically inferred from the training data using the calibration framework proposed by Rasera et al. (2020c). The approach relies on the coalescence of the K-fold cross-validation (Hastie et al., 2009; Pohjankukka et al., 2017) and simulated annealing techniques (Kirkpatrick et al., 1983) for optimizing the algorithm parameters. As all variables are exhaustively known over the training data set, this information can be used within a cross-validation setting to calibrate the parameters by minimization of an objective function. The objective function measures the structural dissimilarity between simulated realizations and the validation data in the training data set.

The structural quality of the simulated fine-resolution residual component cannot be accurately assessed based on a single statistic due to the inherent complexity of topographic patterns. Therefore, several complementary statistics are used to improve the characterization of simulated sub-pixel textures during cross-validation. In this work, we employ the multiple-component objective function introduced by Rasera et al. (2020c). The function measures the local and structural accuracy of the simulated residual component based on four component objective functions, which include: i. the root-mean-square error (RMSE) between the upscaled realizations and the coarse-resolution validation data, ii. the weighted RMSE between fine-scale empirical variogram maps (Marcotte, 1996), and iii. the RMSE between fine-resolution connectivity and iv. Euler characteristic curves (Renard and Allard, 2013) between realizations and the validation set. The first component objective function evaluates whether simulations are coherent with the input coarse-resolution residual data (i.e. local accuracy). The remaining objective functions measure the dissimilarity between textural properties of the realizations and the validation data (i.e. structural accuracy). The global objective function is formulated as a linear combination of the four components. The contribution of the weights associated with each component is numerically estimated using a stochastic perturbation algorithm inspired by the approach proposed by Deutsch and Cockerham (1994). The rationale consists of equalizing the contribution of the components by making their weights inversely proportional to the statistical dispersion of their corresponding objective functions. A detailed description on the objective function components and the weight equalization process is provided by Rasera et al. (2020c).

Table 5.7 lists the calibrated weights of the component objective functions for the two illustrative examples. The equalization process consisted of executing a total of 4×10^3 independent perturbations per iteration, using 16- and 64-fold cross-validation setups for $G = 2$

and $G = 4$, respectively. Results reveal similar weight distributions among components objective functions for the two conditioning data configurations (i.e. downscaling with and without MSI data). However, the relative distribution of weights among components varies significantly according to the data set and magnification factor.

Table 5.7: Calibrated component objective function weights.

Example	Data	G	w_1	w_2	w_3	w_4
Colorado	DEM	2	0.1495 (2)	1.4486 (23)	4.7742 (75)	0.0239 (<1)
Plateau		4	0.5998 (9)	0.0835 (1)	5.6776 (89)	0.0104 (<1)
	DEM/MSI	2	0.1454 (2)	1.4396 (23)	4.7797 (75)	0.0231 (<1)
		4	0.5606 (9)	0.0873 (1)	5.8773 (90)	0.0104 (<1)
San Gabriel	DEM	2	0.1204 (2)	1.8394 (26)	5.0493 (72)	0.0208 (<1)
Mountains		4	0.5609 (6)	1.2787 (14)	7.4343 (80)	0.0103 (<1)
	DEM/MSI	2	0.1177 (2)	1.8665 (26)	5.2002 (72)	0.0202 (<1)
		4	0.5329 (6)	1.4106 (15)	7.3925 (79)	0.0104 (<1)

Values in parentheses give the approximate percentage of the contribution of each component to the total sum of weights

The proposal mechanism for generating candidate weights **w** is based on a uniform sampling of a probability simplex (Rubin, 1981). The parameter optimization process, however, requires the candidate generation mechanism to take into account a temperature-dynamic simulated annealing perturbation scheme, which is used to speed up the optimization. To this end, at each perturbation, the probabilities for sampling randomly generated candidate weights **w** are computed based on a target probability distribution function (PDF) whose shape (i.e. spread) is a function of the temperature. Individual probabilities are set as a function of the distance between a given candidate **w** and the current state weight vector.

The configurations of the parameter optimization process for the two iterations are listed in Table 5.8. The same cross-validation templates used in the calibration of the component objective functions' weights are employed for both magnification factors. The simulated annealing is executed using a dimensionless geometric cooling schedule with a temperature reduction factor of 0.9. The temperature is reduced if either a predefined number target perturbations is accepted, or a maximum number of attempted perturbations is reached. When the latter condition is triggered, the simulated annealing is restarted, but the cooling schedule is not re-initiated. The optimization is terminated if either a maximum number of restarts has been reached (i.e. stopping number) or the objective function satisfies the convergence criterion (i.e. the absolute energy difference between the last two perturbations is less than or equal to the convergence constant). The perturbation scheme

is based on the Cauchy PDF. Figures 5.6 and 5.7 display the objective function convergence curves and cooling schedules for the two illustrative examples. The approximated global minima and simulated annealing restarts are indicated in the plots by the green circles with a cross and the vertical dashed lines, respectively.

Table 5.8: Configuration of the parameter optimization by simulated annealing.

Hyperparameter	$G = 2$	$G = 4$
Number of folds	16	64
Initial temperature	1	1
Cooling schedule function	Geometric	Geometric
Reduction factor	0.9	0.9
Number of accepted target perturbations	10	10
Maximum number of perturbations	100	100
Stopping number	3	3
Convergence constant	1×10^{-4}	1×10^{-4}

Table 5.9 lists the optimized downscaling and data integration parameters for each case study and conditioning data configuration. The parameter setups are linked to the global minima shown in Figures 5.6 and 5.7. Overall, specific patterns can be observed in the calibrated parameter setups. The search radius ρ appears to be proportional to the target scale. The spatial low-pass filter's shape parameter σ_L is often substantially larger than ρ. This configuration yields essentially flat kernels, which favors the generation of highly spatially auto-correlated residuals. This underlines the importance of spatial information for accurate reproduction of the target sub-pixel structures in the downscaling outputs. For $G = 2$, the coarse-scale distance function's kernels attribute more than half of the sum of the weights to their centroids. For $G = 4$, however, these kernels are significantly flatter. A similar pattern is observed for the fine-scale distance function's kernels, but those systematically display higher standard deviations than their coarse counterparts. The number of candidate training data events K reveals a scale-dependent behavior, as the algorithm tends to relax its value at higher magnification factors. Nonetheless, such behavior is not observed for the second magnification of the Colorado Plateau example with MSI data. The control variable ξ gravitates towards values above 0.7. This indicates that the coarse-scale residual most often dictates the training data event retrieval process. The choice of either a static or a dynamic probability aggregation weighting scheme, represented by χ, does not show a clear pattern. The probability aggregation weights assigned to each variable appear data- and scale-dependent. The weights given to the orthoimages associated with the red and NIR bands suggest that they may provide valuable textural

information for the first and second iterations of the algorithm, respectively. The Sobel–Feldman filtered NDVI orthoimage for the Colorado Plateau example, in particular, is likely an informative secondary data source owing to its substantial contribution in the probability aggregation process. Finally, the distance functions' kernel shape parameters associated with the different bands appear to be proportional to the scale being simulated.

Table 5.9: Optimized downscaling and data integration parameters.

$\boldsymbol{\theta}$	Colorado Plateau				San Gabriel Mountains			
	DEM		DEM/MSI		DEM		DEM/MSI	
	$G=2$	$G=4$	$G=2$	$G=4$	$G=2$	$G=4$	$G=2$	$G=4$
ρ	90	34	68	43	68	45	68	48
σ_L	194	18	256	416	776	256	111	274
σ_{R_V}	11	7	12	12	11	10	13	10
σ_{R_v}	14	79	17	13	16	17	74	60
σ_{B_1}	–	–	776	128	–	–	30	49
σ_{B_2}	–	–	832	274	–	–	15	111
σ_{B_3}	–	–	158	39	–	–	955	147
σ_{B_4}	–	–	256	104	–	–	45	6
σ_{B_5}	–	–	158	28	–	–	891	223
σ_{B_6}	–	–	74	21	–	–	42	194
K	5	42	5	4	8	17	3	26
ξ	0.85	0.95	0.98	0.88	1.00	0.75	0.96	0.93
χ	false	true	true	true	true	false	false	true
w_{R_V}	0.36	–	0.17	0.10	–	0.00	0.15	0.25
w_{R_v}	0.64	–	0.13	0.06	–	1.00	0.10	0.04
w_{B_1}	–	–	0.20	0.05	–	–	0.26	0.04
w_{B_2}	–	–	0.05	0.47	–	–	0.16	0.28
w_{B_3}	–	–	0.00	0.10	–	–	0.05	0.19
w_{B_4}	–	–	0.08	0.07	–	–	0.16	0.06
w_{B_5}	–	–	0.04	0.05	–	–	0.07	0.06
w_{B_6}	–	–	0.33	0.10	–	–	0.05	0.08

Figure 5.6: Objective functions and simulated annealing cooling schedules of the Colorado Plateau example. *Top row*: Optimization without MSI data. *Bottom row*: Optimization with MSI data. Approximated global minima are indicated by the green circles with a cross. Vertical dashed lines denote restarts.
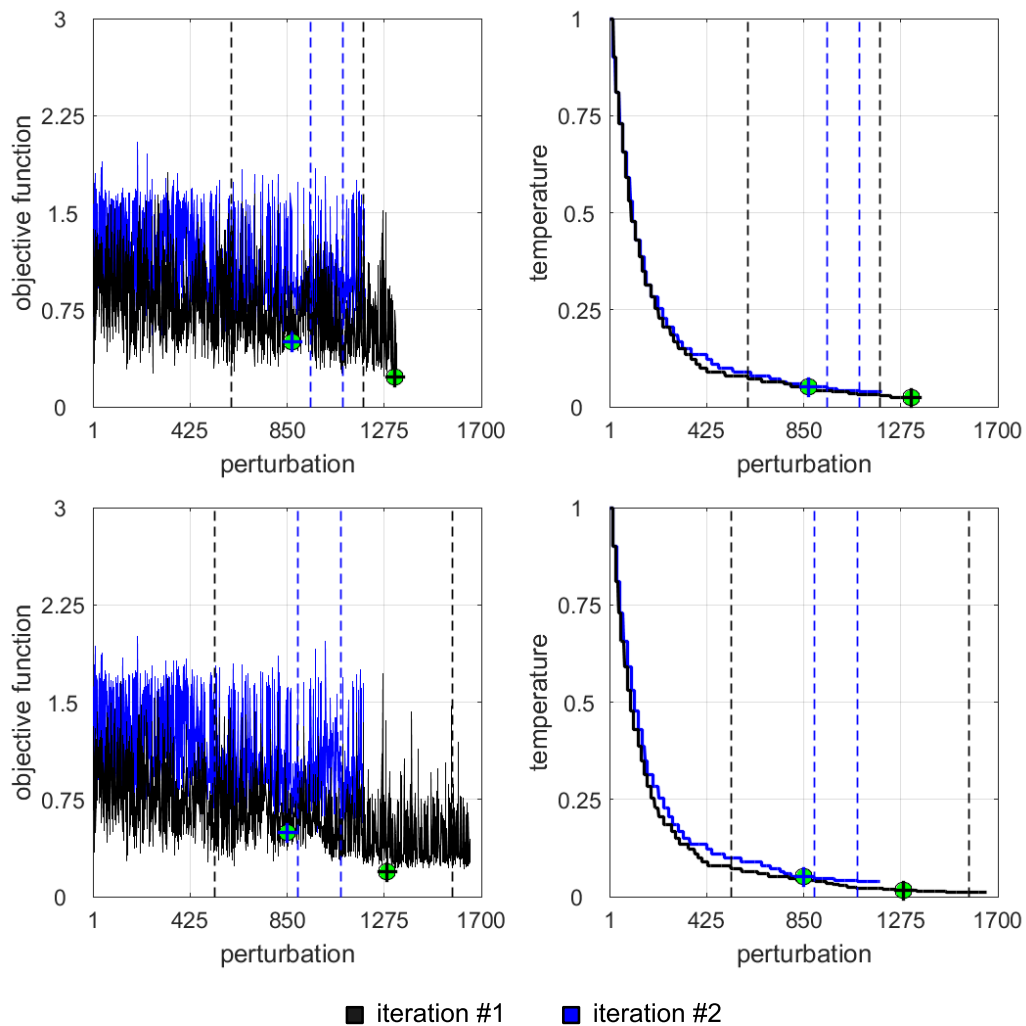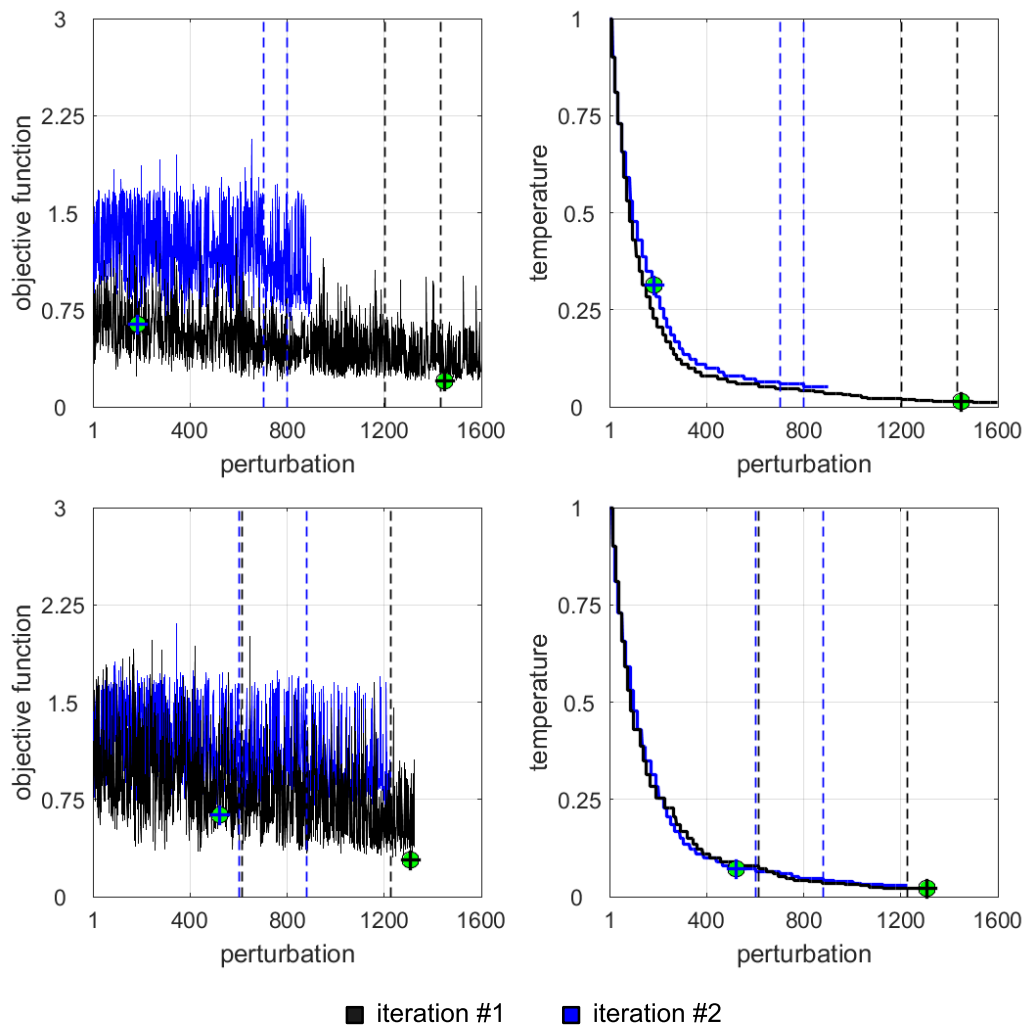
Figure 5.7: Objective functions and simulated annealing cooling schedules of the San Gabriel Mountains example. *Top row*: Optimization without MSI data. *Bottom row*: Optimization with MSI data. Approximated global minima are indicated by the green circles with a cross. Vertical dashed lines denote restarts.

5.4.3   Simulation and validation

Figures 5.8–5.10 and 5.12–5.14 display the reference and downscaled DEMs for the Colorado Plateau and the San Gabriel Mountains examples. Figures illustrate the DEMs at three different spatial resolutions. First-row subplots show the coarse-resolution target DEMs. The second- and third-row subplots display their corresponding medium- and fine-resolution reference and simulated residual DEMs. Zooms of specific areas in the residual DEMs are placed on the third column of each figure. Magnified areas are indicated in the residual DEMs by the green boxes. Figures 5.11 and 5.15 place the medium- and fine-resolution magnified areas in the residual DEMs and the co-registered fine-resolution target MSI (Red and NIR bands) side-by-side. Visual validation of the sample realizations from the Colorado Plateau example (Figs. 5.9–5.11) suggests that the integration of fine-resolution MSI into the downscaling process seems to enhance the reproduction of sub-pixel features on the simulated DEMs. Resolved textures of realizations constrained to MSI data exhibit comparatively sharper gradients and less unstructured noise than the ones generated without secondary data. The advantages offered by the integration of MSI into the downscaling are less evident for the San Gabriel Mountains example (Figs. 5.13–5.15). Nonetheless, simulated drainage networks appear slightly more defined in the realizations conditioned to the secondary data.

Table 5.10 lists statistics describing the conditioning quality of simulated realizations to the coarse-resolution target residual DEMs. Statistics represent average values plus or minus one standard deviation over 20 realizations, and outline random and systematic errors related to discrepancies between the upscaled simulated realizations and the coarse-resolution target residual DEMs. Random errors (i.e. precision related) are described with the standard deviation of error (SDE) and the Pearson's linear correlation coefficient (r). Systematic errors (i.e. accuracy related) are characterized using the mean error (ME), and the slope of the regression line (m) calculated based on the reduced major axis regression model. The ME and SDE of each realization are calculated by accumulating the mismatch between the centroids of the target data events and their corresponding source data events in the training data at each iteration. Results demonstrate that simulated realizations adequately honor the target residual DEMs. However, conditioning errors tend to increase at higher magnification factors due to error propagation effects. For $G = 4$, simulations not constrained to MSI underestimate the input coarse-resolution data, whereas realizations conditioned to secondary data are prone to produce slight overestimation. Although the integration of fine-resolution MSI into the downscaling process appears to induce a small positive coarse-scale conditioning bias for $G = 4$, statistics also reveal that it might improve

the precision of the conditioning. Realizations not constrained to MSI, and previous experiments with different DEMs (Rasera et al., 2020c), suggest that the algorithm has a natural tendency to underestimate the coarse-scale target data.

Table 5.10: Conditioning to coarse-resolution residual data.

Example	Data	G	ME[1](cm)	SDE[2](cm)	m[3]	r[4]
Colorado Plateau	DEM	2	-0.16 ± 0.28	17.20 ± 10.76	1.00 ± 0.00	1.00 ± 0.00
		4	0.65 ± 0.81	53.36 ± 38.44	1.02 ± 0.01	0.75 ± 0.06
	DEM/MSI	2	-0.43 ± 0.00	27.60 ± 0.00	1.00 ± 0.00	1.00 ± 0.00
		4	-4.00 ± 0.23	255.65 ± 14.86	0.97 ± 0.00	0.88 ± 0.02
San Gabriel Mountains	DEM	2	0.06 ± 0.33	16.02 ± 14.21	1.00 ± 0.00	1.00 ± 0.00
		4	1.96 ± 2.92	193.45 ± 110.51	1.03 ± 0.00	0.89 ± 0.02
	DEM/MSI	2	1.04 ± 0.00	66.49 ± 0.00	1.00 ± 0.00	1.00 ± 0.00
		4	0.15 ± 0.34	19.73 ± 12.21	0.98 ± 0.00	0.94 ± 0.01

[1] mean error;   [2] standard deviation of error;
[3] RMA regression slope;   [4] Pearson's linear correlation coefficient; Values represent average statistics plus or minus one standard deviation over 20 realizations

Summary statistics for the medium- and fine-resolution simulated DEMs are presented in Table 5.11. Numerical experiments show that the simulated realizations accurately reproduce the medium- and fine-resolution empirical PDFs. Realizations underestimated the reference standard deviations by a very small margin. Although fine-scale variance underestimation is a known problem of MPS-driven downscaling methods (Straubhaar et al., 2016; Rasera et al., 2020b,a), inconsistencies between the simulation and reference statistics could be related, at least in part, to the limited size of the training data set.

Figures 5.16 and 5.17 illustrate the structural validation of the downscaled DEMs. The validation metrics comprise the same spatial statistics employed in the multiple-component objective function used for the parameter optimization and data integration process. Statistics include directional variograms, Euler characteristic, and connectivity functions. All statistics are computed on the residual component in order to filter out large-scale trends. Results are displayed for the two magnification factors. Green curves denote the reference data. Simulated realizations with and without MSI data are indicated by the black and blue curves, respectively. The envelopes represent the range covered by 20 realizations. Results suggest that the integration of finer-resolution MSI enhances the structural accuracy of downscaling outputs, as seen by the improvement in the reproduction of Euler characteristic and probability of connection curves for both examples. Nevertheless, for $G = 4$,

empirical variograms associated with the realizations conditioned to secondary information reveal that the long-range variability is comparatively lower than for those not conditioned to the MSI. This suggest that the additional constrain imposed by secondary data might favor the reproduction of higher-order statistics over two-point statistics.

The integration of fine-resolution MSI can potentially limit the inherent indetermination of the downscaling because it may provide indirect information about the underlying fine-scale topography. This uncertainty is intrinsically associated with the downscaling process due to the lack of information at the target scale. Note that it does not account for another source of uncertainty related to the choice of the prior sub-pixel structural model (i.e. the training data set). Figures 5.18 and 5.19 display medium- and fine-resolution post-processing maps with the pixel-wise mean (known as E-type) and standard deviation (referred as SD-type) of 20 realizations, for the two illustrative examples and data configurations. E-type maps provide estimates of the local expected value of residual PDF associated with each pixel, and SD-type maps enable visualization of the spread of those PDFs. Table 5.12 lists summary statistics of the SD-type maps for the two examples and data configurations. Statistics comprise the mean and the standard deviation of each SD-type map, as well as their relative changes induced by the integration of MSI into the downscaling process.

Results indicate that the assimilation of MSI into the downscaling reduces the uncertainty of sub-pixel predictions, which is observed by the negative change in the SD-type mean. Differences are more evident for the San Gabriel Mountains example (Fig. 5.19 and Table 5.12), where many of the residual structures to be determined are finer than the target DEM pixel size. Uncertain areas appear to be primarily associated with steep changes in the gradient of the residual component. The reduction of sub-pixel uncertainty in the Colorado Plateau example is subtle, becoming more apparent in the second magnification (Fig. 5.18 and Table 5.12). By contrast, in the San Gabriel Mountains example it reveals a more heterogeneous pattern (Fig. 5.19), which is expressed as a positive change in the spread of both medium- and fine-resolution SD-type maps (Table 5.12). The reduced uncertainty observed in the SD-type maps from realizations conditioned to the MSI indicates that the secondary information constrains the sampling of the local CPDFs (line 20 of Algorithm 5) by narrowing down the local pool of candidate training data events.
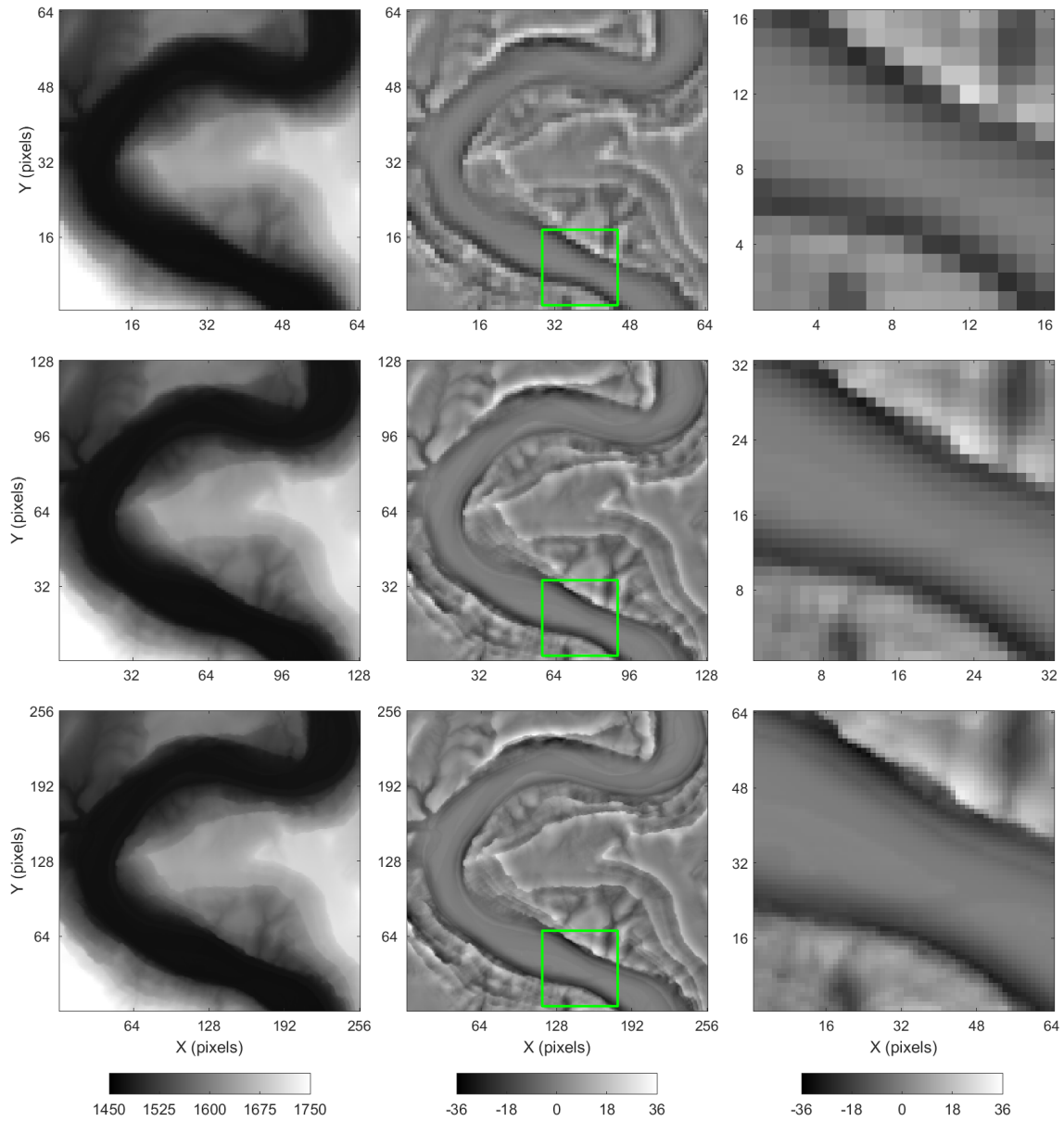
Figure 5.8: The Colorado Plateau example reference DEMs. *Top left*: coarse-resolution DEM. *Top center*: coarse-resolution residual DEM. *Top right*: coarse-resolution zoom. *Middle left*: medium-resolution DEM. *Middle center*: medium-resolution residual DEM. *Middle right*: medium-resolution zoom. *Bottom left*: fine-resolution DEM. *Bottom center*: fine-resolution residual DEM. *Bottom right*: fine-resolution zoom. Green boxes highlight the magnified area. Colorbars' unit is m.
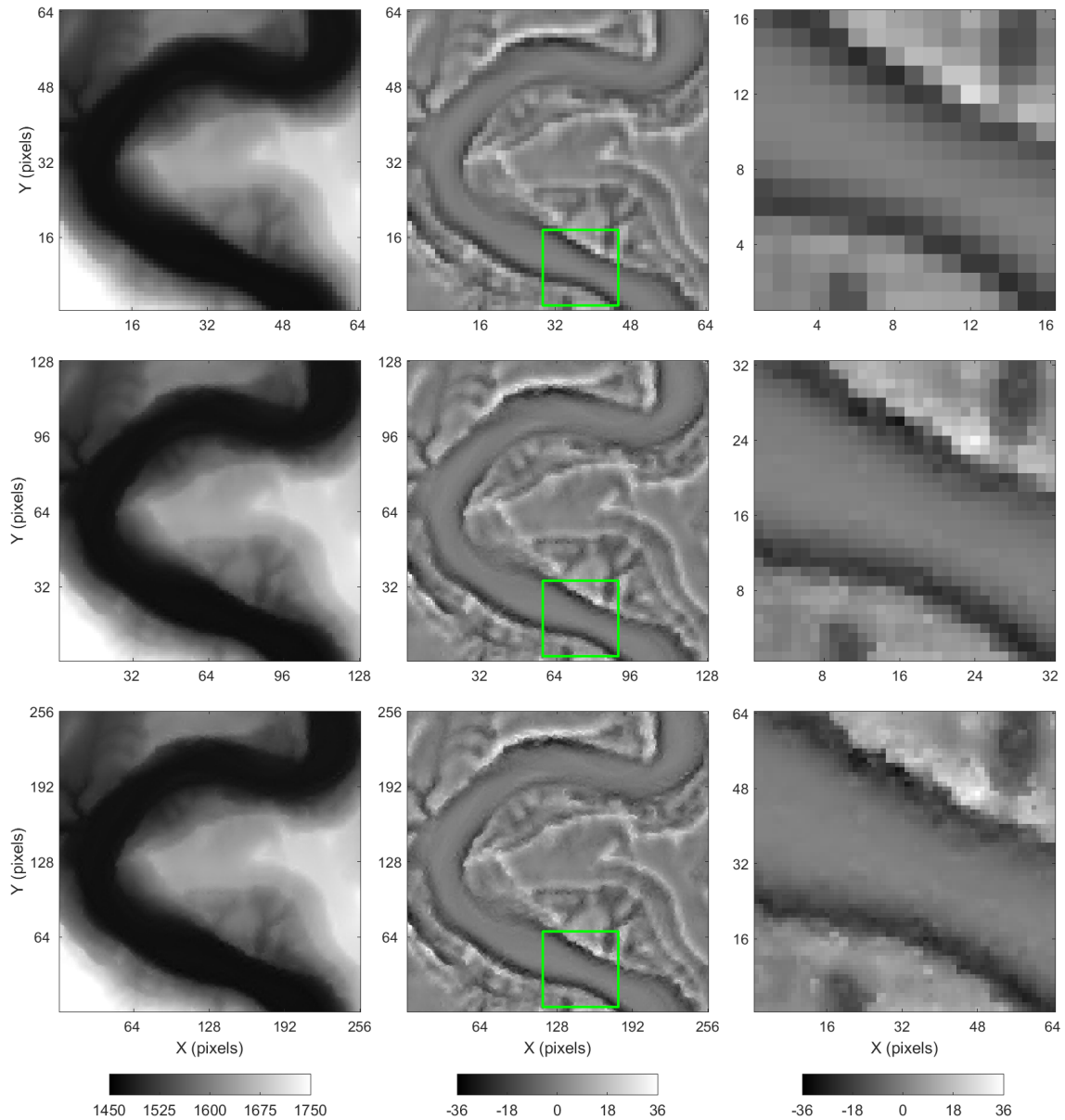
Figure 5.9: The Colorado Plateau example downscaled DEMs (without MSI data). *Top left*: coarse-resolution DEM. *Top center*: coarse-resolution residual DEM. *Top right*: coarse-resolution zoom. *Middle left*: medium-resolution DEM. *Middle center*: medium-resolution residual DEM. *Middle right*: medium-resolution zoom. *Bottom left*: fine-resolution DEM. *Bottom center*: fine-resolution residual DEM. *Bottom right*: fine-resolution zoom. Green boxes highlight the magnified area. Colorbars' unit is m.

Figure 5.10: The Colorado Plateau example downscaled DEMs (with MSI data). *Top left*: coarse-resolution DEM. *Top center*: coarse-resolution residual DEM. *Top right*: coarse-resolution zoom. *Middle left*: medium-resolution DEM. *Middle center*: medium-resolution residual DEM. *Middle right*: medium-resolution zoom. *Bottom left*: fine-resolution DEM. *Bottom center*: fine-resolution residual DEM. *Bottom right*: fine-resolution zoom. Green boxes highlight the magnified area. Colorbars' unit is m.

Figure 5.11: Medium- and fine-resolution magnified areas of the Colorado Plateau example. Colorbar unit is m.
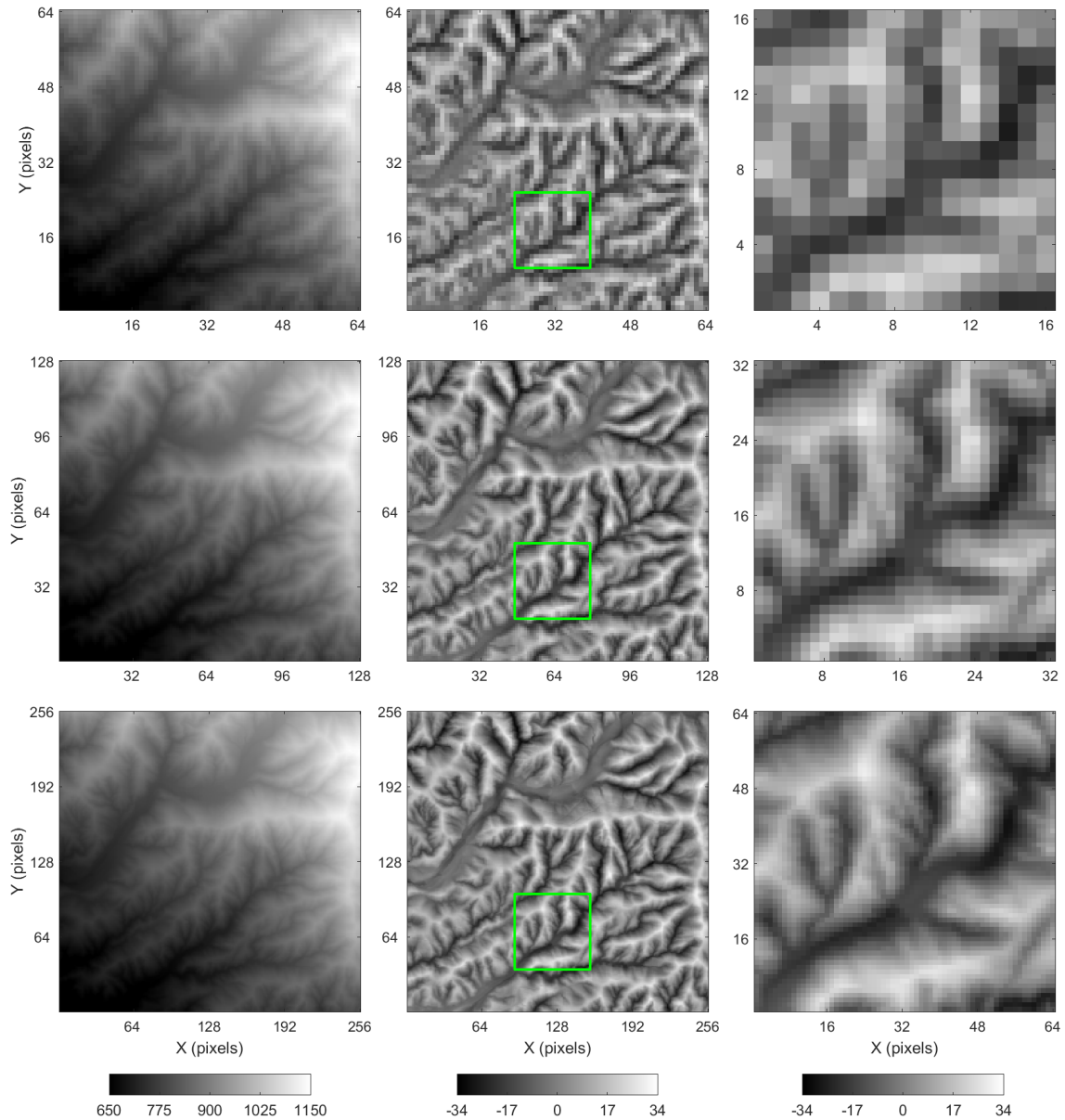
Figure 5.12: The San Gabriel Mountains example reference DEMs.   *Top left*: coarse-resolution DEM. *Top center*: coarse-resolution residual DEM. *Top right*: coarse-resolution zoom. *Middle left*: medium-resolution DEM. *Middle center*: medium-resolution residual DEM. *Middle right*: medium-resolution zoom. *Bottom left*: fine-resolution DEM. *Bottom center*: fine-resolution residual DEM. *Bottom right*: fine-resolution zoom. Green boxes highlight the magnified area. Colorbars' unit is m.
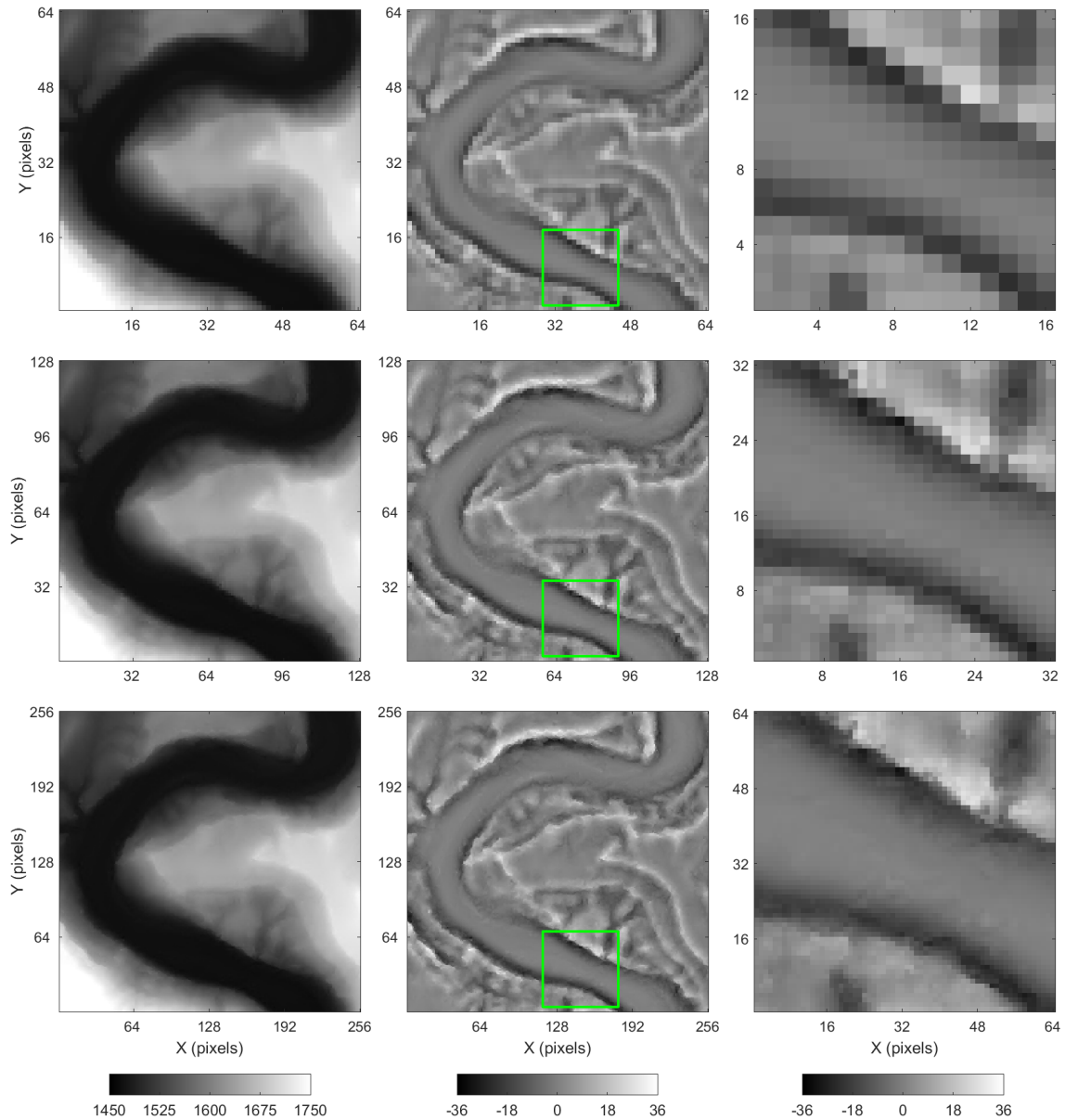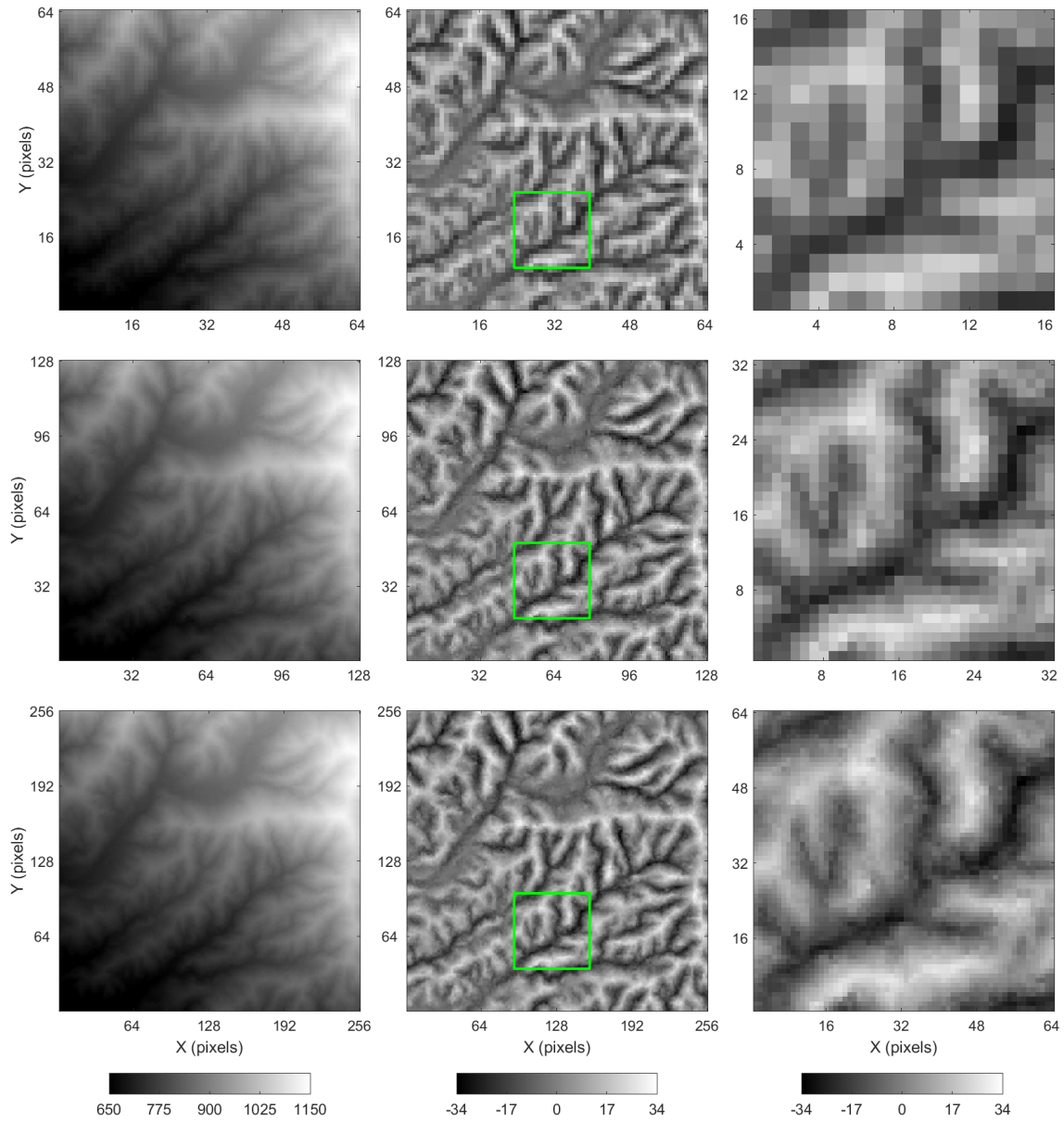
Figure 5.13: The San Gabriel Mountains example downscaled DEMs (without MSI data). *Top left*: coarse-resolution DEM. *Top center*: coarse-resolution residual DEM. *Top right*: coarse-resolution zoom. *Middle left*: medium-resolution DEM. *Middle center*: medium-resolution residual DEM. *Middle right*: medium-resolution zoom. *Bottom left*: fine-resolution DEM. *Bottom center*: fine-resolution residual DEM. *Bottom right*: fine-resolution zoom. Green boxes highlight the magnified area. Colorbars' unit is m.
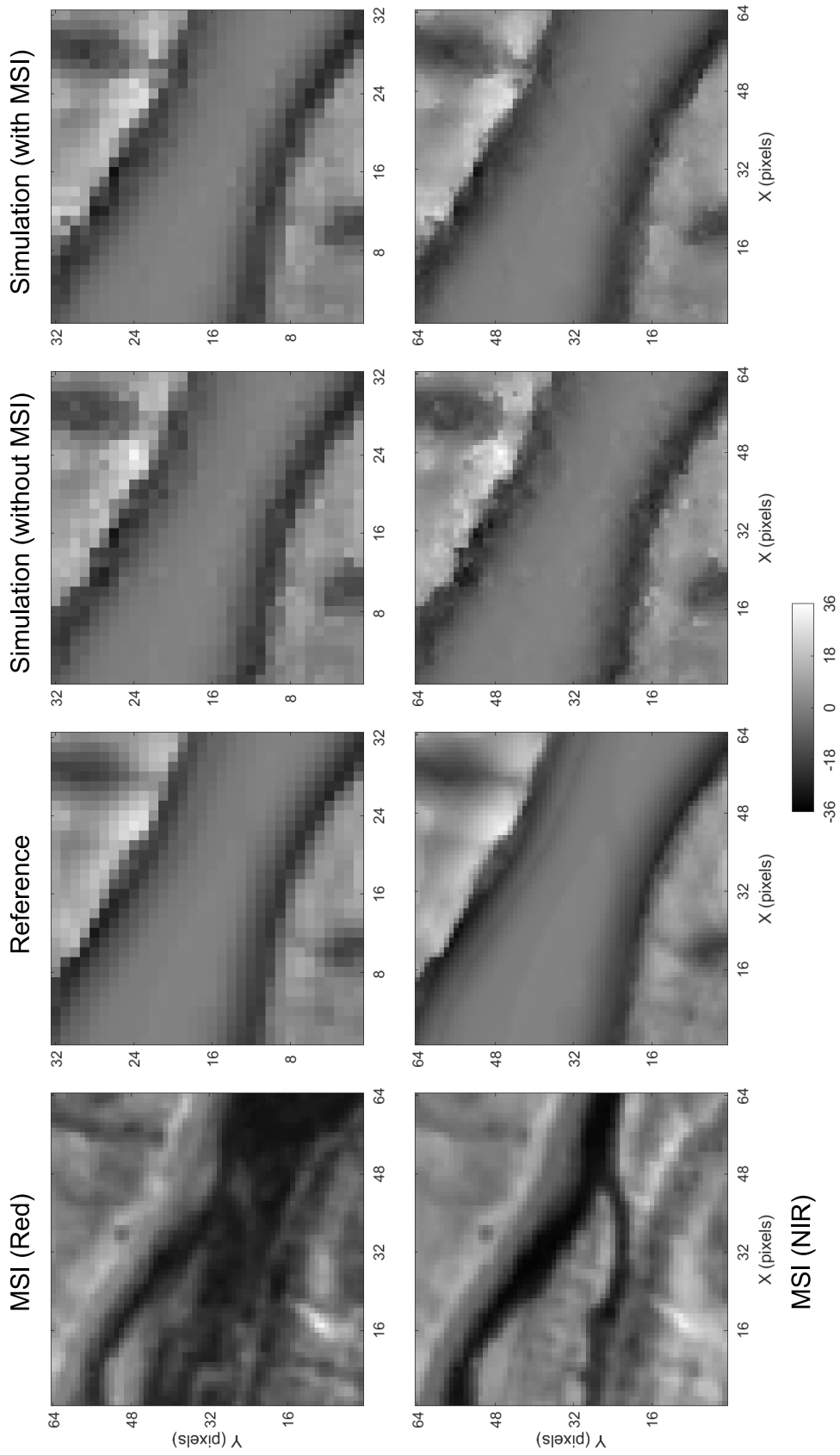
Figure 5.14: The San Gabriel Mountains example downscaled DEMs (with MSI data). *Top left*: coarse-resolution DEM. *Top center*: coarse-resolution residual DEM. *Top right*: coarse-resolution zoom. *Middle left*: medium-resolution DEM. *Middle center*: medium-resolution residual DEM. *Middle right*: medium-resolution zoom. *Bottom left*: fine-resolution DEM. *Bottom center*: fine-resolution residual DEM. *Bottom right*: fine-resolution zoom. Green boxes highlight the magnified area. Colorbars' unit is m.
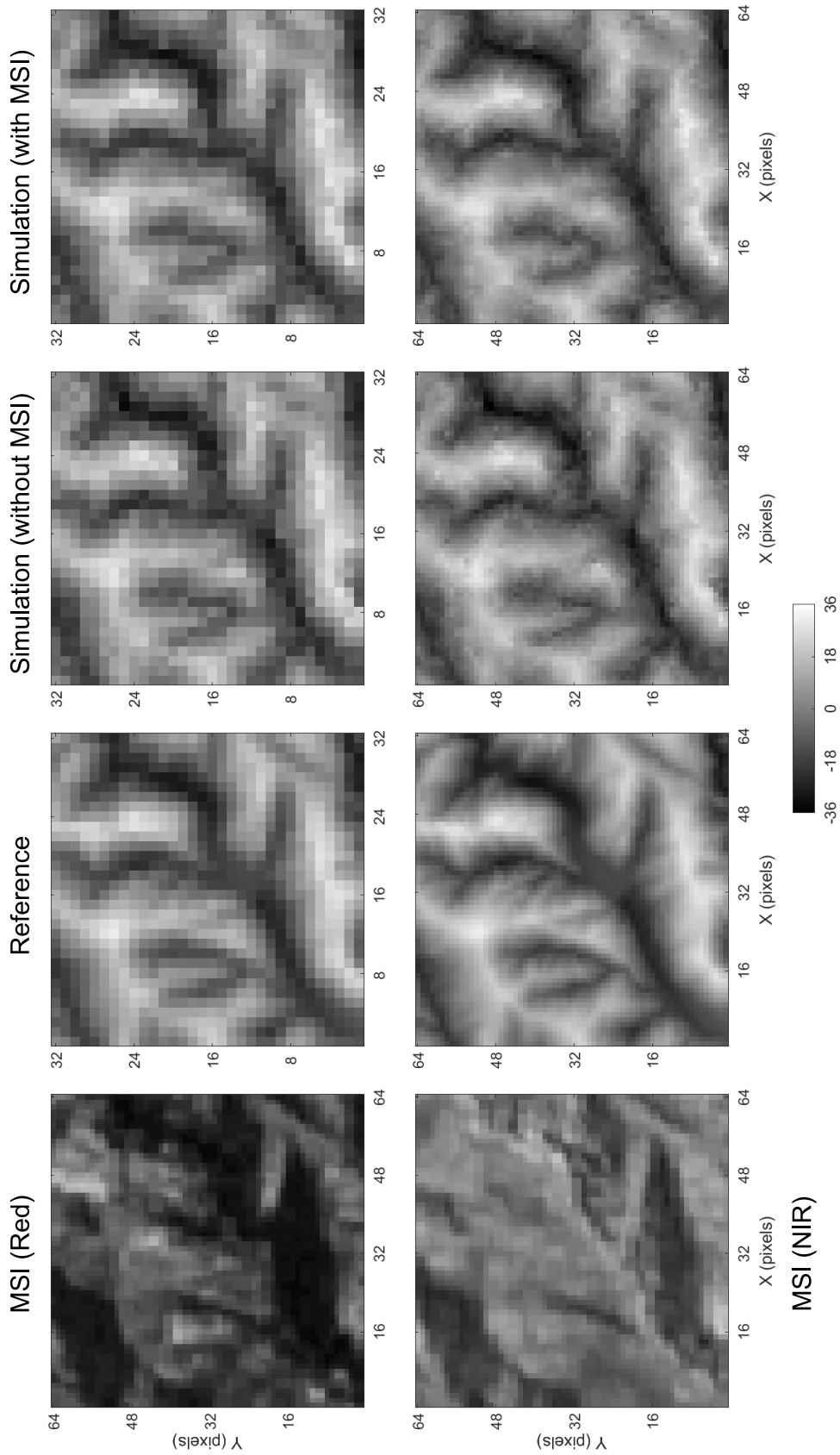
Figure 5.15: Medium- and fine-resolution magnified areas of the San Gabriel Mountains example. Colorbar unit is m.
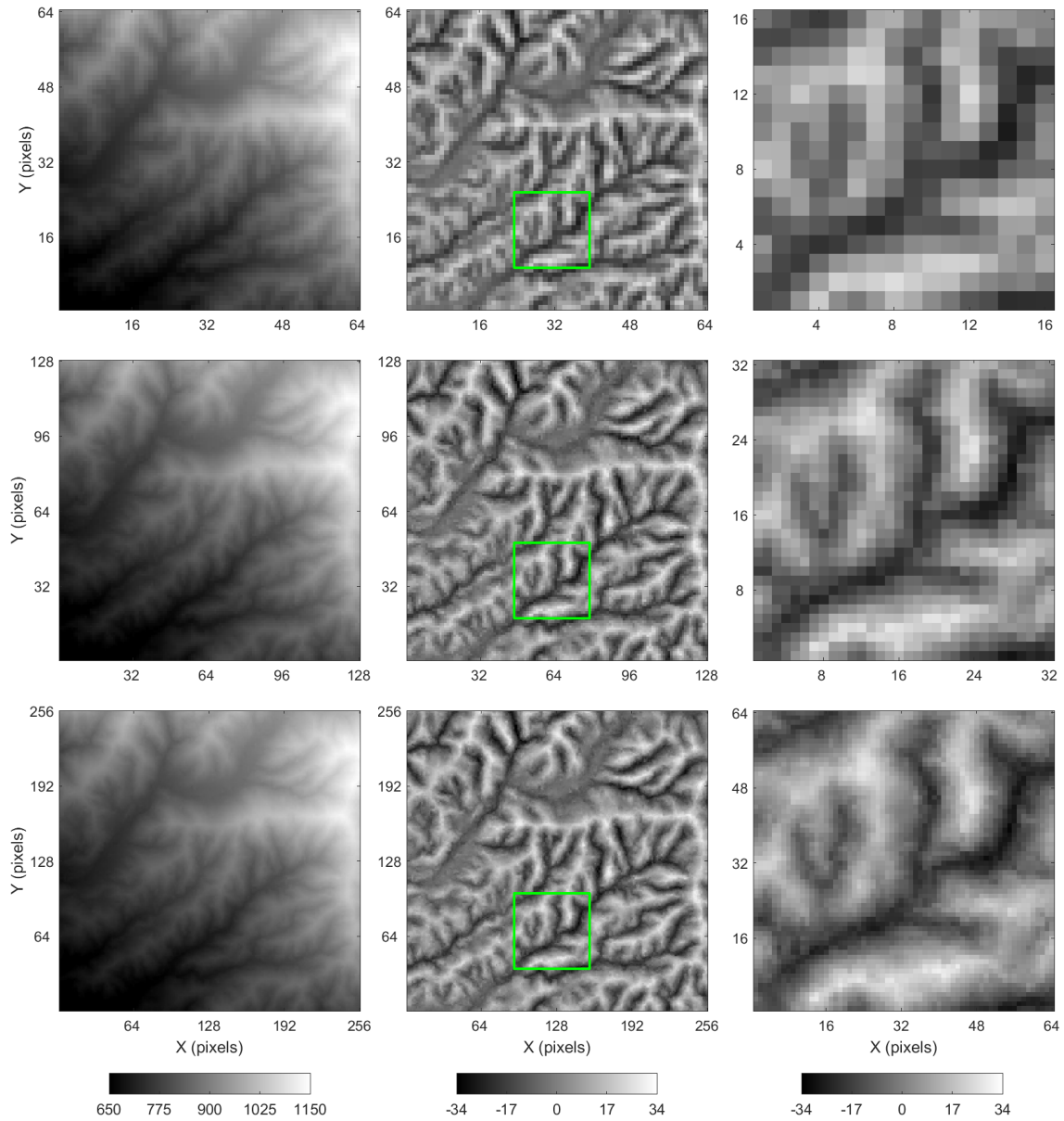
Table 5.11: Summary statistics of the medium- and fine-resolution reference and downscaled DEMs from the Colorado Plateau and the San Gabriel Mountains examples.

Example	Data	G	Mean	SD	Min.	Max.
Colorado Plateau	Reference	2	-0.47	7.43	-30.44	33.10
		4	-0.45	7.50	-33.39	36.86
	DEM	2	-0.47 ± 0.00	7.37 ± 0.01	-30.46 ± 0.94	35.32 ± 2.95
		4	-0.45 ± 0.00	7.40 ± 0.01	-34.64 ± 3.24	40.28 ± 2.93
	DEM/MSI	2	-0.47 ± 0.00	7.37 ± 0.01	-30.80 ± 1.73	39.99 ± 5.69
		4	-0.45 ± 0.00	7.37 ± 0.01	-34.59 ± 2.87	43.20 ± 5.06
San Gabriel Mountains	Reference	2	0.25	11.09	-30.99	31.15
		4	0.25	11.18	-34.19	32.69
	DEM	2	0.25 ± 0.00	11.03 ± 0.01	-34.84 ± 1.22	32.83 ± 1.04
		4	0.25 ± 0.00	11.01 ± 0.01	-36.13 ± 1.31	33.71 ± 1.33
	DEM/MSI	2	0.25 ± 0.00	11.01 ± 0.01	-34.70 ± 1.72	32.07 ± 0.70
		4	0.25 ± 0.00	10.98 ± 0.01	-35.78 ± 1.50	33.04 ± 1.33

Numbers represent average statistics plus or minus one standard deviation over 20 realizations. Values are in residual elevation (in m)
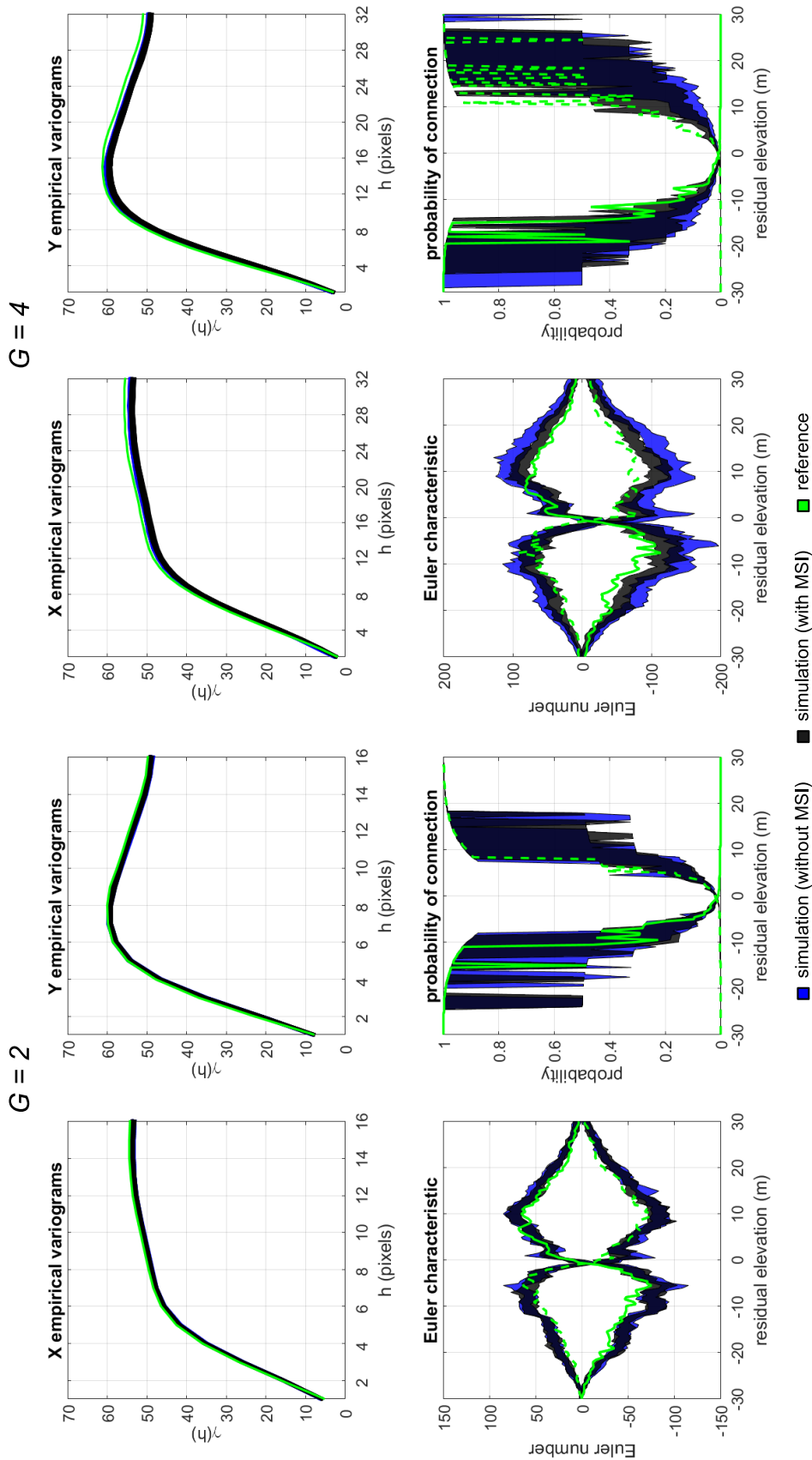
Figure 5.16: The Colorado Plateau example structural statistics.
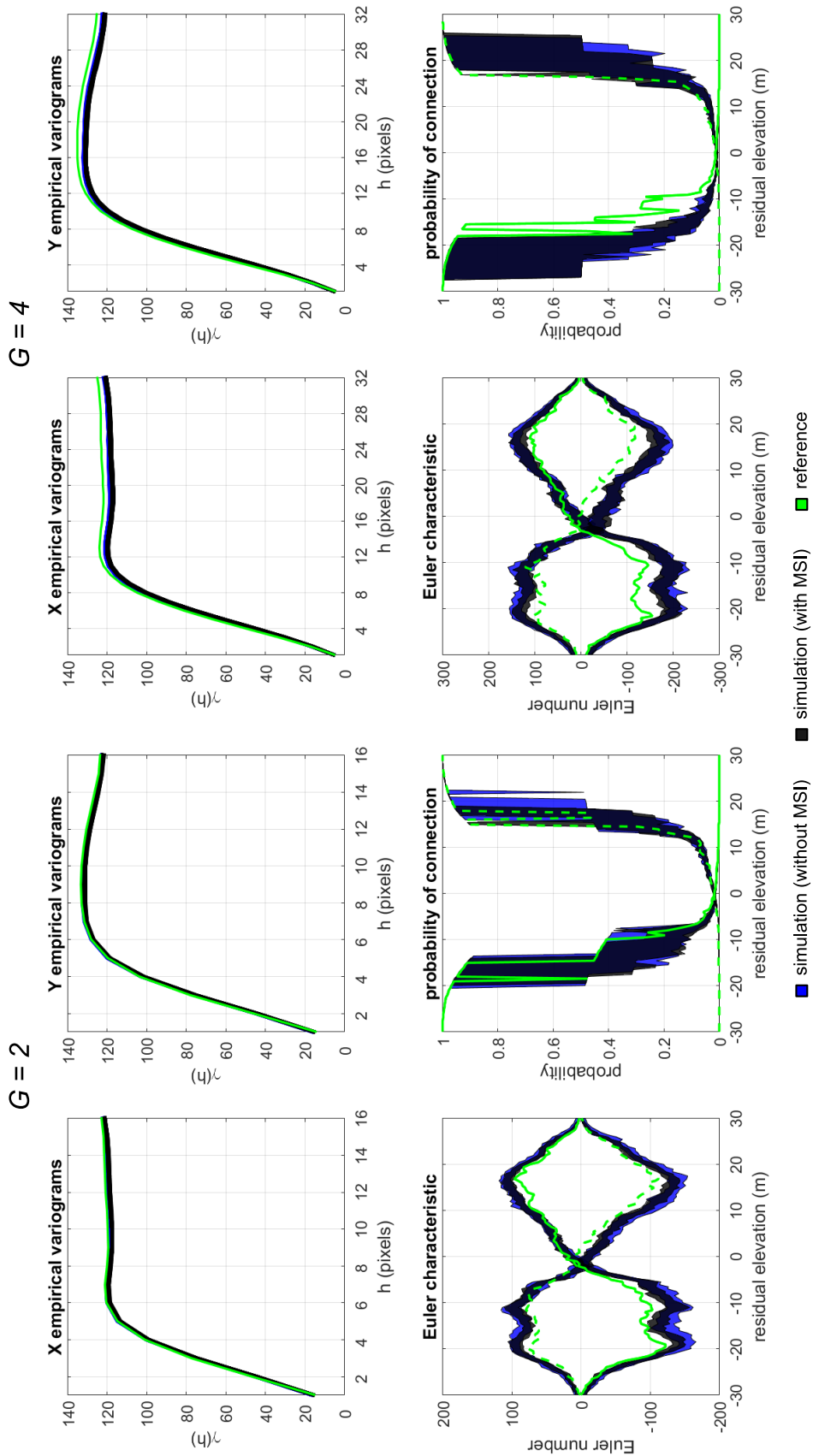
Figure 5.17: The San Gabriel Mountains example structural statistics.
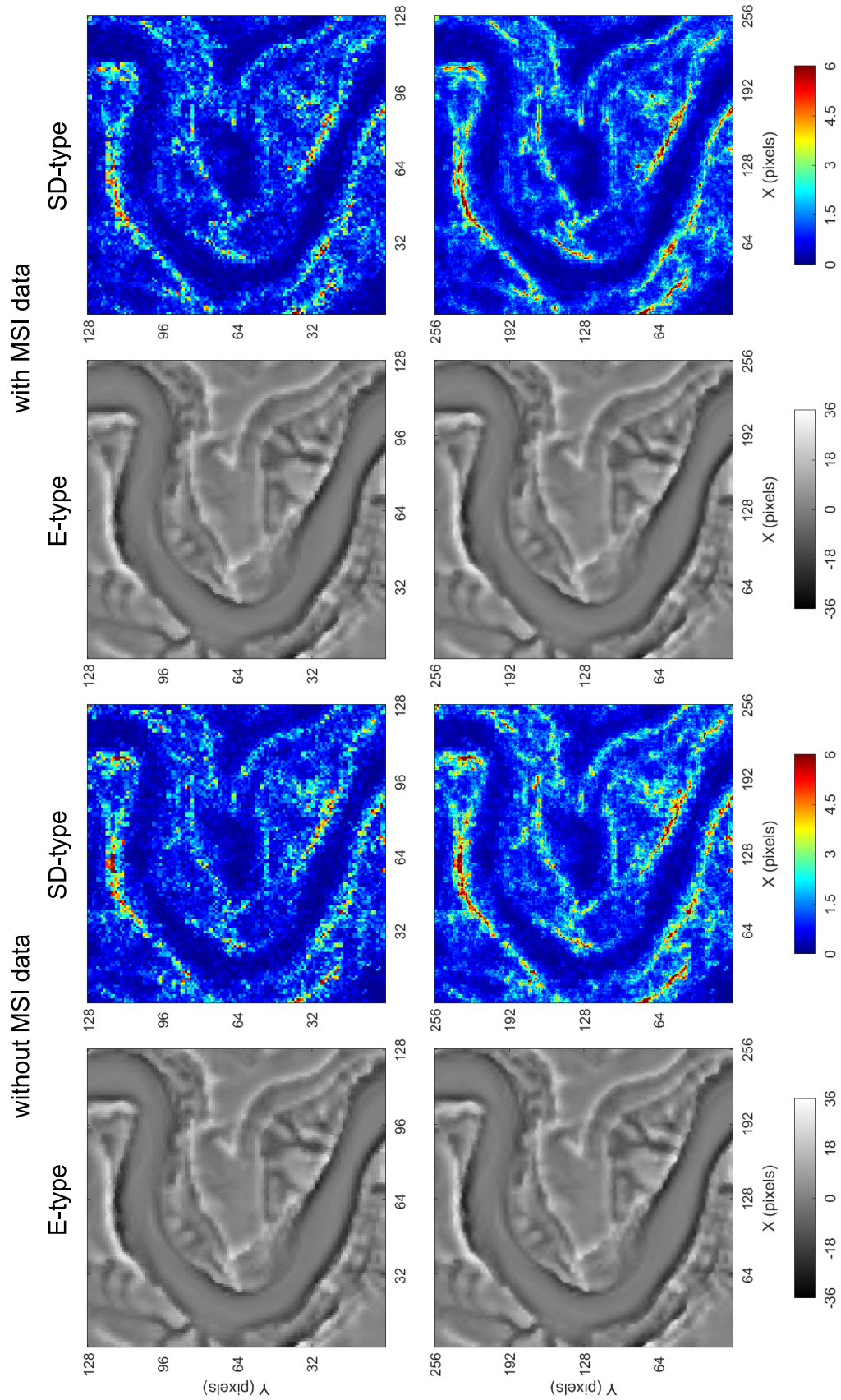
Figure 5.18: Post-processing of simulated realizations from the Colorado Plateau example. Values are in residual elevation (in m).
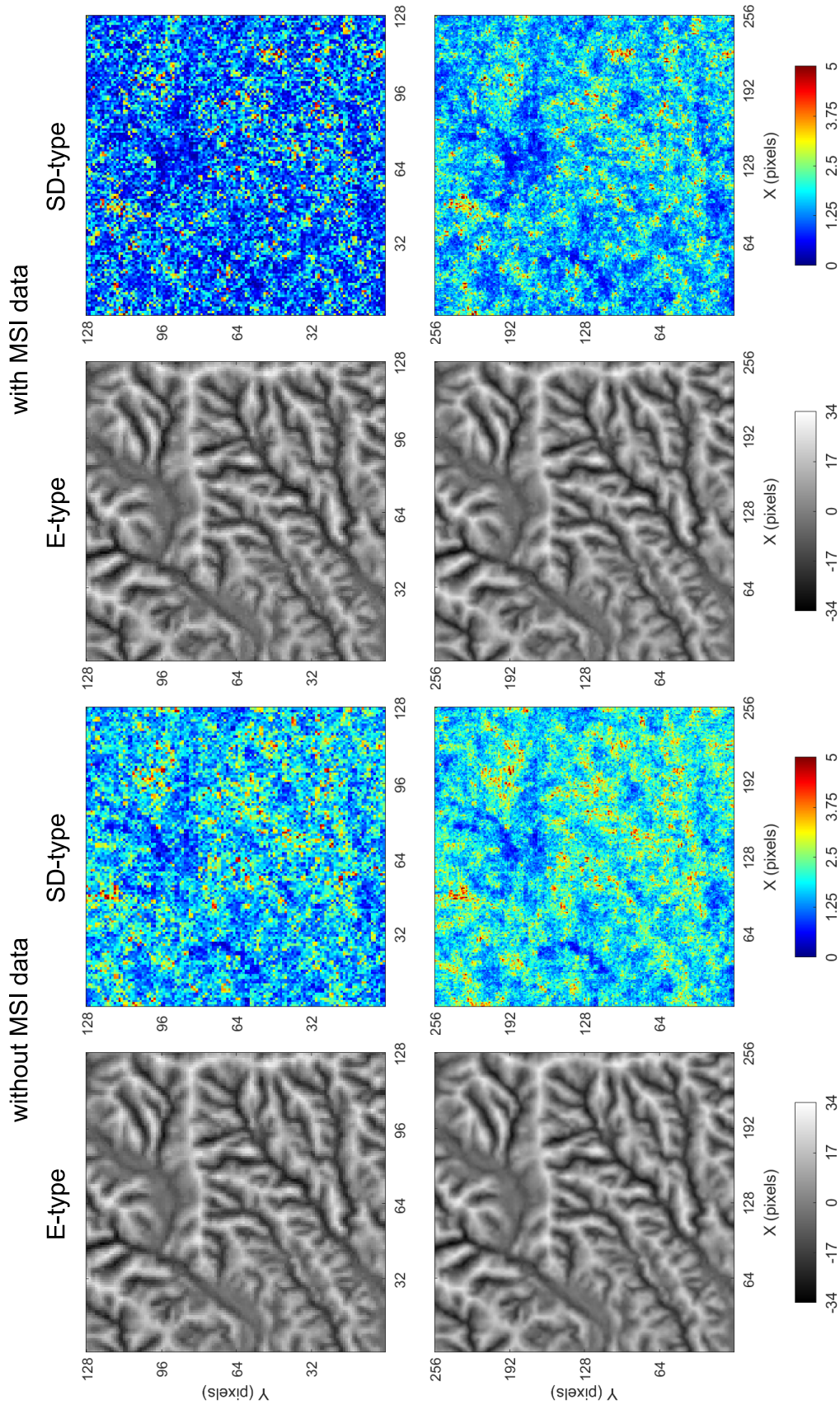
Figure 5.19: Post-processing of simulated realizations from the San Gabriel Mountains example. Values are in residual elevation (in m).

Table 5.12: SD-type statistics.

Example	Data	G	Mean	SD	Change (%)	
			(m)	(m)	Mean	SD
Colorado	DEM	2	0.91	0.86	–	–
Plateau		4	1.15	1.01	–	–
	DEM/MSI	2	0.88	0.82	−3.39	−5.12
		4	1.03	0.91	−11.08	−9.18
San Gabriel	DEM	2	1.71	0.71	–	–
Mountains		4	1.94	0.63	–	–
	DEM/MSI	2	1.30	0.81	−24.04	+14.48
		4	1.68	0.65	−13.26	+3.79

5.5 Conclusions

Satellite MSI provides extensive information of Earth's surface features at relatively fine spatial resolution. In this contribution, we investigate the possibility of enhancing the structural accuracy of the downscaling of spaceborne coarse-resolution DEMs by integration of finer-resolution co-registered MSI data. The data integration framework is demonstrated using the MPS-driven downscaling algorithm developed by Rasera et al. (2020b,a). MSI is integrated as secondary data following a probabilistic framework. All data integration and downscaling parameters are inferred from a dual-resolution training data set based on the automation framework proposed by Rasera et al. (2020c). The approach is demonstrated by two cases studies in the Western United States using the USGS 3DEP 1 m DEM and the EU/ESA Sentinel-2 MSI Level-2A data products.

Results suggest that the assimilation of fine-resolution MSI into the downscaling improves the structural accuracy of simulated realizations and the precision of their conditioning to coarse data at higher magnification factors. Post-processing of realizations revealed that the integration of secondary data caused the reduction of the uncertainty related to sub-pixel predictions. The spatial uncertainty at the target scale appears to be primarily associated with changes in the gradient of the residual topography. Improvements in terms of structural accuracy and uncertainty reduction become more evident when the secondary data provides textural information finer than the spatial resolution of the target DEM.

Further experiments with different parameter optimization configurations and data sets must be conducted to more accurately determine the benefits of integrating MSI data into the downscaling process. Determining the extent of the advantages and drawbacks may be strongly case-dependent. Factors such as reflectance anisotropy induced by rough topography and geometric errors in the MSI may compromise its usability. Moreover, optical imagery of forested and urbanized areas, for example, will provide little to no information about the ground surface topography. Vegetation and man-made structures effectively conceal the underlying bare ground surface features and are likely to bring no information to the data integration process.

Future research could focus on the integration of surface reflectance-corrected MSI and fine-scale DEM source data into the downscaling process. Anisotropic reflectance in mountainous terrain optical imagery could be potentially normalized for the training MSI based on the fine-resolution training DEM, information about the orbital characteristics of the sensor platform, and the product metadata properties in a pre-processing step. The

reflection model, or the corrected reflectance patterns in the training data, could be subsequently extrapolated to the target MSI prior to downscaling using some sort of regression or stochastic simulation technique. The integration of textural information from available fine-scale DEM source data can be used for enhancing the structural accuracy of the downscaling. Elevation source data may consist of either raster-type data, such as fine-resolution InSAR imagery (e.g. Sentinel-1 data), or point-support data, such as LiDAR point clouds and spot height measurements.

Data and code availability

The 3DEP 1 m DEM is made available by the USGS. All 3DEP products are public domain. Sentinel-2 Level-2A products are provided by the EU Copernicus Programme/ESA and regulated under EU law. The use of Sentinel data is governed by the Copernicus Sentinel Data Terms and Conditions. MATLAB codes and data sets used in the case studies will be provided on GitHub (https://github.com/lgrasera).

Chapter 6

Concluding remarks

This last chapter summarizes and proposes future developments of the work presented in this thesis. Limitations of the proposed framework are also noted. This thesis makes three main contributions to the fields of applied geostatistics and probabilistic terrain mapping. The algorithms developed in this thesis addressed the problems of: MPS-driven downscaling of coarse-resolution images with trends, the automation of the downscaling process, and the integration of finer-resolution secondary data into the downscaling. Combined, these algorithms provide an efficient, low-cost alternative for fine-resolution stochastic terrain mapping. Section 6.1 recaps the problem and the aim of the thesis. Each of the three primary contributions is subsequently reviewed. Section 6.2 outlines future research ideas.

6.1   Conclusions

Fine-resolution DEMs are essential for quantifying Earth surface processes and for application of Earth system models. Over the past two decades, spaceborne remote sensing missions, such as the NGA and NASA's SRTM (Farr et al., 2007) and JAXA's EORC ALOS World 3D (Tadono et al., 2016), have executed near-global mapping of the topography of the Earth's surface. These missions provided freely available coarse-resolution DEMs that have enabled the study and modeling of large-scale atmospheric, hydrological, and geomorphic processes. However, due to their limited spatial resolution, satellite-derived DEMs are inappropriate for determining small-scale topography and land surface phenomena. To this day, fine-resolution DEMs remain unevenly and sparsely distributed across the planet owing to the technical challenges and elevated financial costs for producing densely sampled

data sets.

This thesis developed a novel MPS-driven data integration framework for downscaling coarse-resolution DEMs based on available finer-resolution analogs. Being an ill-posed problem, downscaling calls for a stochastic approach to resolve its inherent under-determination (i.e. multiple fine-resolution DEMs may correspond to the same coarse-resolution DEM). Geostatistical simulation provides a suitable methodological framework for downscaling as it enables rapid generation of statistically accurate scenarios, and the assessment of the uncertainty associated with the predictions. In practice, downscaling is seldom the end goal per se. Simulated realizations often serve as input to physical and engineering forward models. In most cases, the texture of the simulated scenarios has a critical impact on the forward model response; hence, an accurate reproduction of the fine-scale variability and connectivity is of utmost importance. To limit the problem inherent indetermination, any downscaling technique requires the definition, either explicitly or implicitly, of a prior fine-scale structural model to describe the expected spatial features at the target scale. MPS methods, in particular, excel at simulating complex low-entropy textures that are often found in DEMs. These methods consider the joint spatial correlation between multiple data values, and prior structural information based upon a better-informed analogous training data set. The proposed MPS-driven downscaling and data integration framework was demonstrated by various case studies using DEMs from different geomorphological settings. The following subsections summarize the three main contributions of this thesis.

6.1.1 MPS-driven downscaling of images with trends

Chapter 3 introduced the building blocks of the MPS-driven downscaling method. One of the most challenging aspects for statistical modeling of topographic data is the presence of large-scale trends. Trends in the data violate the stationarity hypothesis of statistical modeling, and entail an explicit decomposition of the target variable into a deterministic low-frequency trend component, and a stochastic higher-frequency residual component. The trend component is downscaled based on a smooth interpolation method, whereas a quasi-pixel-based sequential simulation scheme is used to downscale the residual variable. Such decomposition allows the algorithm to handle the inherent non-stationarity of topography, and more accurately model its spatial structure and variability. The method relies on an iterative pyramid-based framework to gradually enhance the spatial resolution of the target DEM. This ultimately provides a better reproduction of the spatial connectivity at the target scale. The structural model is materialized by a dual-resolution training data set,

which describes the correspondence between the known coarse-scale data (available in the target DEM) and the missing fine-scale features. The method also introduced the application of kernel weighting for computing distances between data events, and the formulation of a probabilistic framework for integrating coarse- and fine-resolution information. The former provides better conditioning to local coarse-resolution data and improves the overall structural accuracy of the downscaling outputs, and the latter eases the task of integrating disparate data sources. The approach was benchmarked against three state-of-the-art methods. Experimental results obtained from two case studies showed that the proposed algorithm outperformed the other methods in most of the validation statistics.

6.1.2 Automation of the downscaling process

Chapter 4 described a framework for automatizing the downscaling of coarse-resolution DEMs in the context of MPS simulation. The technical challenges associated with the calibration of MPS algorithm parameters are one of the main factors hindering a more widespread use of these methods in practical applications. To address this issue, this chapter presented a training data-driven scheme for automatic parameter calibration. The approach frames the calibration task as an optimization problem by combining the K-fold cross-validation and the simulated annealing techniques. A fundamental aspect of the framework is the formulation of the objective function. The objective function defines the sought-after structural properties for the downscaling outputs by measuring the dissimilarity between target statistics from candidate simulated realizations and those of a given validation data set. In this contribution, the objective function was formulated based on local and structural accuracy criteria. Note that such criteria are subjective, and may vary according to the application and the field of study. The application of the K-fold cross-validation technique allows accurate prediction performance estimates during the parameter calibration process and evaluation of the reproduction of non-stationarity structures in the training data. The simulated annealing algorithm offers robustness for optimizing non-differentiable objective functions with multiple local minima. The three illustrative examples of distinct topographic settings and DEM products demonstrated the applicability of the framework.

6.1.3 Integration of fine-resolution secondary data into the downscaling

Finally, Chapter 5 addressed the integration of finer-resolution secondary data into the downscaling process. Finer-resolution MSI is integrated for enhancing the structural accuracy of the downscaling of coarse-resolution DEMs. The objective is to investigate the potential of using the textural information of finer-resolution MSI as a proxy to resolve sub-pixel topographic features in the target coarse DEM. All downscaling and data integration parameters are inferred using the automation routine presented in Chapter 3. The method provides a practical alternative for automatic assimilation of multiple data sources. Disparate data are integrated following a probabilistic framework based on probability aggregation operations. The approach was illustrated by two case studies in the Western United States. Results suggest that the integration of finer-resolution MSI into the downscaling can potentially enhance the structural accuracy of simulated realizations and reduce the uncertainty of sub-pixel predictions. Future research must be conducted in order to refine the data integration process and explore alternative ways of assimilating surface reflectance-corrected MSI and fine-scale DEM source data.

6.2 Future research ideas

In this final section, future research topics that could help to develop further the ideas introduced in this thesis in relation to improving the structural accuracy of the downscaling outputs and strategies for assimilating data with varying quality are outlined. Approaches for generation of data- and application-consistent fine-resolution DEMs (i.e. models that also accurately reproduce the response of a target transfer function) are discussed in comparison.

6.2.1 Accounting for coarse data uncertainty

In this thesis, it is assumed that measurement errors in the coarse-resolution target DEMs are negligible. In practice, such an assumption is unrealistic as all data products contain an intrinsic error component. Spaceborne DEMs, in particular, are significantly affected by measurement errors (Yamazaki et al., 2017). Errors arise from various sources, which may include the data acquisition method, local terrain surface properties, and the DEM generation process itself. Moreover, errors in DEMs are often systematic (i.e. spatially autocorrelated), which complicates their detection and treatment. Effectively, measurement

errors can only be assessed by validation against a more accurate data set (Kolecka and Kozak, 2014; Mukul et al., 2017).

Ideally, the uncertainty arising from errors in the data should be accounted for by the downscaling and data integration process. If possible, one should always attempt to characterize these errors if the quality and amount of data are sufficient for inferring an error model. Systematic errors may be either removed by direct data manipulation using spatial and spectral analysis filters, or explicitly modeled and subsequently attenuated with regression or factorial kriging analyses (de Carvalho et al., 2019). Once systematic errors have been filtered out from data, random errors may be accounted in the downscaling process by setting tolerance intervals for the conditioning to coarse-resolution data based on a parametric (e.g. Gaussian) stochastic error model.

6.2.2   Servo-system for bias correction of coarse data conditioning

One of the limitations of the proposed downscaling method is the limited accuracy of conditioning of simulated realizations to the input coarse-resolution data. Resampling methods, such as MPS simulation algorithms, are subject to generate biases in data conditioning and reproduction of spatial statistics because of the finite size of the training data set. The dearth of replicates for a given target data event can potentially induce to a bias in the conditioning to the input coarse-resolution target DEM. This bias could be mitigated with either optimization-based post-processing algorithms (Deutsch and Cockerham, 1994), or corrected "on the fly" using a servo-system (Remy et al., 2009).

The developed probabilistic data integration framework is generic enough to easily accommodate a servo-system mechanism. A servo-system consists of an automatic mechanism that uses error-sensing negative feedback to correct the action of a process. In the developed algorithm, such a system can be implemented using the mismatch with respect to some target statistics, such as the RMSE between simulated and conditioning coarse data, to manipulate the local conditional probabilities dynamically so as to sample individual candidate training data events. The system does not necessarily need to be tied to coarse data reproduction, but can be linked to any constraint for which the error can be incrementally computed along the sequential simulation path. The servo-system could be used to improve the reproduction of a target fine-scale empirical variogram or connectivity function, for example. Note that a transformation function for converting errors into probabilities needs to be specified. Since local and structural accuracy are two conflicting goals in spatial interpolation, a potential negative side effect is that the gain in the reproduction of coarse

data can trigger the appearance of artifacts in the simulated realizations, thus undermining their structural accuracy.

6.2.3 Hyperparameter optimization

An important topic of further research is the automatic inference of the algorithm hyperparameters. Hyperparameter optimization is currently a trending topic in the realm of machine learning (Claesen and Moor, 2015), but it is yet an unexplored subject within the geostatistical community. The estimation of hyperparameters is fundamental for the development of fully-automated, self-tuning algorithms and learning strategies. Existing hyperparameter optimization approaches in machine learning and control theory commonly rely on grid or random search methods, as well as heuristics, employed within a cross-validation setting (Bergstra and Bengio, 2012).

6.2.4 Integration of reflectance-corrected MSI and DEM source data

In Chapter 5, surface reflectance anisotropy in the MSI due to irregular topography and the solar and viewing geometry were ignored. Light-occlusion effects caused by mountainous terrain also have a substantial impact on reflectance values. Composite images and spectral band ratios attenuate these effects to some degree but do not eliminate them. Reflectance correction models must be applied to effectively mitigate them (Hügli and Frei, 1983; Feingersh et al., 2010; Wen et al., 2018). However, the application of these models within the proposed framework is challenging. Normalization of anisotropic reflectance requires information on the orbital characteristics of the sensor platform, imagery metadata properties, and most importantly, fine-resolution elevation data. This could be performed directly on the training MSI, but an indirect correction would have to be applied on the target MSI. Regression or stochastic simulation techniques would have to be used to extrapolate the reflection model, or the normalized reflectance patterns from the training data, to the target MSI prior to downscaling. Future experiments with reflectance-corrected MSI are particularly important because they will allow quantification of the impact of reflectance anisotropy in the data integration process.

Case studies were demonstrated with relatively coarse-resolution, freely available imagery data. However, finer-resolution satellite imagery that requires payment has sub-metric spatial resolution and could be used instead. Note that these products must be properly georeferenced, orthorectified, and radiometrically corrected prior to data integration.

Another subject of future research could be integration of available DEM source data into the downscaling process. This additional information can comprise either raster-type data, such as InSAR imagery, or point-support data, such as LiDAR point clouds and spot height measurements. Fine-resolution InSAR imagery (e.g. Sentinel-1 data) may be easily incorporated into the downscaling and can provide additional textural information to enhance the determination of sub-pixel features in the target DEM. Point-support elevation source data comprise very fine-resolution hard data that should be exactly reproduced by the downscaling process. The main challenge for integrating this kind of data sets is the fact that they must be migrated and interpolated into regular grids in order to be assimilated by standard MPS simulation algorithms.

Numerical experiments in this thesis were limited to a maximal magnification factor of $4\times$. Further work needs to be conducted to determine the magnification factor limits for different types of terrain and data sets. The integration of finer-resolution primary and secondary data into the downscaling may push towards higher magnification factors as more information at the target scale will be available.

6.2.5   Transfer function-oriented downscaling

Recall the following paragraph from Section 1.1:

In this thesis, the emphasis is on challenges associated with the automatic integration of different types of remote sensing data for the downscaling of coarse-resolution DEMs. The aim of this thesis is to develop a novel framework for efficient, low-cost generation of statistically accurate fine-resolution digital terrain models from limited information data in the form of coarse-resolution DEMs and fine-resolution MSI. These challenges are tackled from a geostatistical perspective. Numerical experiments illustrated by case studies are validated using well-established and state-of-the-art spatial statistics. An analysis on the impact of the resolved sub-pixel terrain features for modeling Earth surface processes, or land surface parameters, is beyond the scope of this thesis.

The developed framework is a contribution towards more accurate modeling of Earth surface process and risk assessment of natural hazards. The proposed approach is viable for many applications but it is by no means complete or perfect. In this thesis, terrain features are described and modeled based on spatial statistics. These criteria may not be enough for accurate reproduction of other fine-scale spatial properties more relevant to specific Earth surface processes, such as runoff or sediment transport, for example. Future research must

evaluate whether the downscaling outputs reproduce these processes sufficiently in order to be actually useful for particular scientific and engineering problems. These studies would also likely need to post-process realizations to smooth out some of the undesired small-scale variability introduced by the downscaling process.

The physical realism required by certain applications may also entail the formulation of a transfer function-oriented objective function. In this case, statistics associated with land surface parameters (e.g. flow accumulation, wetness index, sediment connectivity), which consist of proxies to specific surface processes, could be included in the objective function in order to fine-tune the downscaling for a specific problem. In this framework, the algorithm self-calibration process would attempt finding an optimal parameter setup that minimizes the component objective function associated with some dissimilarity metric between the reference and simulated response of a target transfer function. Note that all the aforementioned land surface parameters involve re-trending of the simulated DEMs. Both flow accumulation and the wetness index, for example, would entail specific K-fold cross-validation partitioning schemes. The cross-validation template could be generated by computing the watershed transform on the training DEM so that folds are coherent with the expected geometries of catchments and drainage patterns. The component objective function associated with the transfer function must be carefully designed. The mismatch between the reference and the simulated transfer function empirical CDFs, for example, does not explicitly account for the spatial structure of the transfer function output. In this case, additional statistics describing either the fine-scale residual elevation or the transfer function spatial structure have to be computed.

Appendix A

Numerical experiments with non-artificial coarse-resolution target DEMs

This appendix documents additional numerical experiments related to the illustrative examples presented in Chapters 4 and 5. Supplementary experiments aim to demonstrate the developed downscaling and data integration framework with non-artificial coarse-resolution target DEMs and to evaluate the impact of the measurement errors in the DEMs into the downscaling process.

Section A.1 introduces the DEM products used as target data sets. Section A.2 identifies and describes the measurement errors in the target DEMs. Errors are computed based on artificial coarse-resolution reference DEMs constructed from more accurate finer-resolution products. Results are presented and analyzed in Section A.3.

A.1   DEM products

The coarse-resolution DEM products used as target data include a corrected version of the 1-arc second near-global DEM from the U.S. National Geospatial-Intelligence Agency (NGA) and NASA's Shuttle Radar Topography Mission (SRTM30) (Farr et al., 2007), JAXA's Earth Observatory Research Center (EORC) 1-arc second global digital surface model ALOS World 3D-30m (AW3D30) (Tadono et al., 2016), and the USGS National Map

3D Elevation Program (3DEP) 1-arc second DEM (Sugarbaker et al., 2017). The corrected SRTM30 DEM, entitled DEM-S (Geoscience Australia, 2015), is a post-processed product released by Geoscience Australia. The DEM represents the ground surface topography and is limited to the Australian continent. The product was generated by application of an adaptive smoothing process on the original SRTM30 DEM to reduce noise and improve the representation of surface features. The filtering process was preferentially applied to flat and noisy areas.

The training and reference data sets comprise coarsened versions of three fine-resolution DEMs: the Polar Geospatial Center at the University of Minnesota ArcticDEM (Porter et al., 2018), Geoscience Australia's Australian 5 m DEM (Geoscience Australia, 2015), and the USGS National Map 3DEP 1 m DEM (Sugarbaker et al., 2017). Table A.1 contains a summary of the acquisition periods, sensing techniques used to produce the DEMs, and spatial resolution of the aforementioned products.

Table A.1: DEM products.

DEM product	Sensing year(s)	Sensor type	Nominal pixel size (m)
AW3D30	2006-2011	Optical	30×30
SRTM30 (DEM-S)	2000	Radar	30×30
3DEP 1" DEM	2016-2023	LiDAR	30×30
ArcticDEM	2015-2016	Optical	2×2
Australian 5 m DEM	2001-2015	LiDAR	5×5
3DEP 1 m DEM	2016-2023	LiDAR	1×1

Table A.2 lists the DEMs used as target, training, and reference data in each illustrative example. The coarser-resolution products are used as target DEMs, while the remaining finer-resolution DEMs serve as training data. The reference DEMs are built from the same data products used as training data, but they are only used for validation. The reference and training DEMs are generated by linear upscaling of the source finer-resolution DEMs (Table A.1). The downscaling is conditioned to the coarse-resolution target DEMs. Inconsistencies between target, training and reference DEMs due to different acquisition periods, sensing techniques, and measurement errors are not taken into account in this study. The dimensions and nominal pixel sizes of the coarse-, medium-, and fine-resolution DEMs are identical to the examples presented in Chapters 4 and 5.

Table A.2: Target, training, and reference data sets.

Example	Target	Training/Reference
Alaska Range	AW3D30	ArcticDEM
Appalachians	3DEP 1" DEM	3DEP 1 m DEM
Central Lowlands	SRTM30 (DEM-S)	Australian 5 m DEM
Colorado Plateau	3DEP 1" DEM	3DEP 1 m DEM
San Gabriel Mountains	3DEP 1" DEM	3DEP 1 m DEM

Figures A.1–A.3 display the target DEMs for the Alaska Range, the Appalachian Mountains, and the Australian Central Lowlands case studies. Figures A.4 and A.5 show the coarse-resolution target DEM and fine-resolution MSI of the Colorado Plateau and the San Gabriel Mountains examples. The training DEMs and target/training MSI correspond to the data sets used in the case studies of Chapters 4 and 5. The residual DEMs are computed based on a spatial low-pass filter with $\rho = 90$ m and $\sigma_L = 600$ m (Figs. A.1–A.5). Summary statistics of the coarse-resolution residual DEMs are listed in Table A.3.
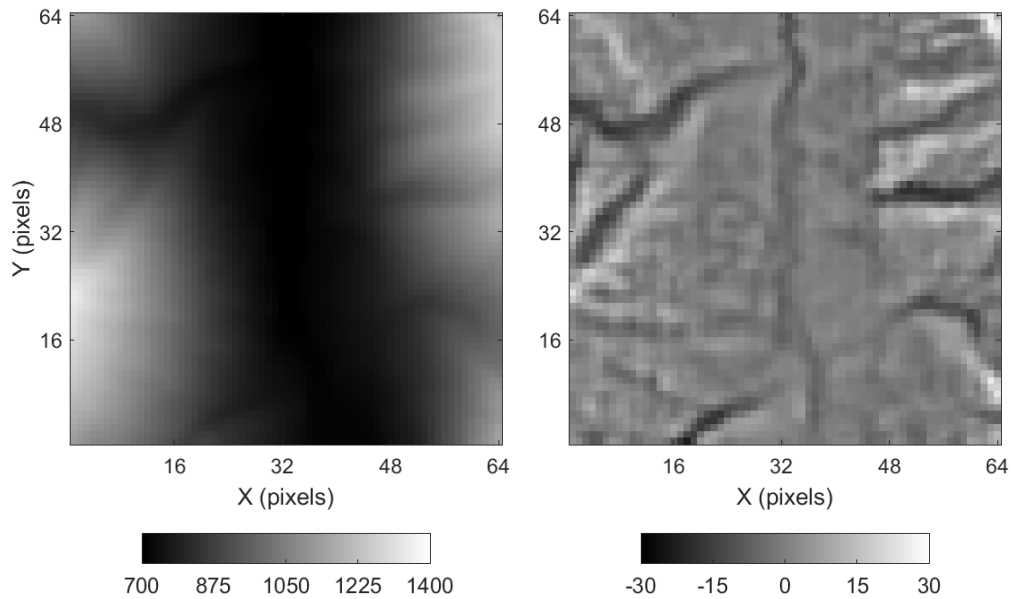

Figure A.1: The Alaska Range example target DEM. *Left*: coarse-resolution target DEM. *Right*: coarse-resolution target residual DEM. Colorbars' unit is m.
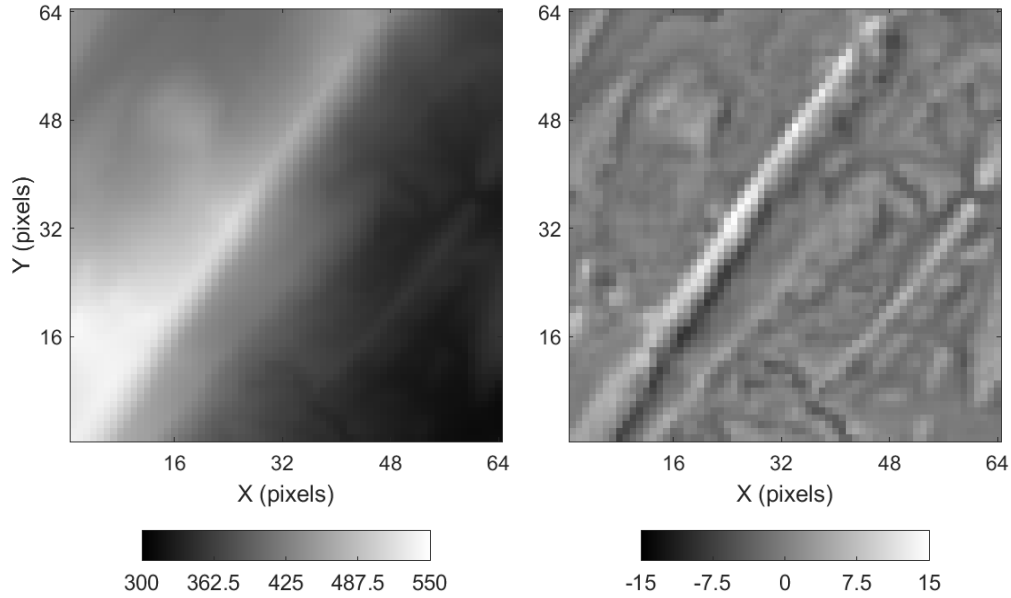
Figure A.2: The Appalachians example target DEM. *Left*: coarse-resolution target DEM. *Right*: coarse-resolution target residual DEM. Colorbars' unit is m.

Table A.3: Summary statistics of the coarse-resolution DEMs.

Example	Data set	Mean	SD	Min.	Max.
Alaska Range	Training	0.04	6.76	−34.77	40.43
	Target	−0.38	5.36	−23.34	27.04
	Reference	−0.37	5.61	−20.99	32.86
Appalachians	Training	0.08	3.52	−16.29	18.01
	Target	0.03	2.71	−9.13	14.54
	Reference	0.03	2.77	−9.45	15.46
Central Lowlands	Training	−0.02	2.11	−5.96	11.44
	Target	−0.02	1.50	−4.20	5.25
	Reference	−0.02	3.26	−7.68	11.79
Colorado Plateau	Training	0.00	8.25	−30.54	65.25
	Target	−0.49	7.06	−26.60	30.40
	Reference	−0.48	7.14	−26.03	27.97
San Gabriel Mountains	Training	0.02	10.06	−40.52	34.47
	Target	0.24	10.09	−26.63	27.10
	Reference	0.26	10.60	−27.54	28.63

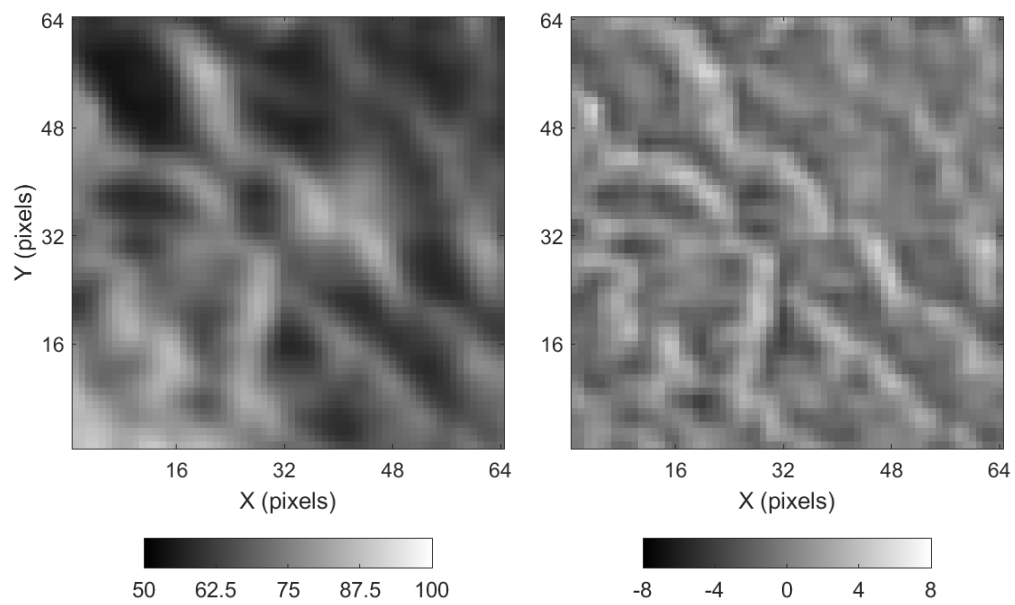Values are in residual elevation (in m)

Figure A.3: The Central Lowlands example target DEM. *Left*: coarse-resolution target DEM. *Right*: coarse-resolution target residual DEM. Colorbars' unit is m.
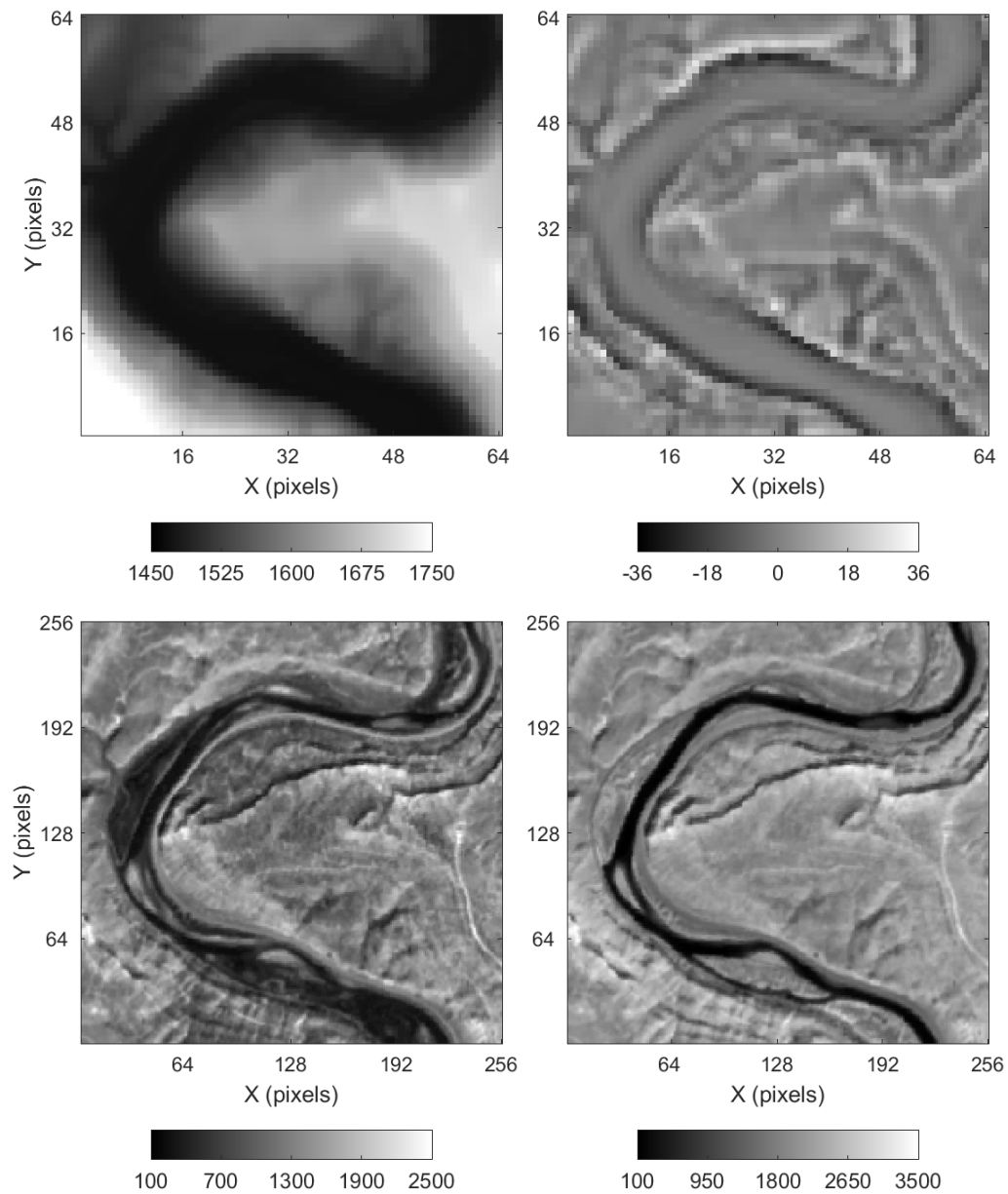
Figure A.4: The Colorado Plateau example coarse-resolution target DEM and fine-resolution MSI. *Top left*: coarse-resolution DEM. *Top right*: coarse-resolution residual DEM. *Bottom left*: fine-resolution BOA reflectance orthoimage (Red). *Bottom right*: fine-resolution BOA reflectance orthoimage (NIR). DEM colorbars' unit is m. MSI colorbars' unit is digital number.

Figure A.5: The San Gabriel Mountains example coarse-resolution target DEM and fine-resolution MSI. *Top left*: coarse-resolution DEM. *Top right*: coarse-resolution residual DEM. *Bottom left*: fine-resolution BOA reflectance orthoimage (Red). *Bottom right*: fine-resolution BOA reflectance orthoimage (NIR). DEM colorbars' unit is m. MSI colorbars' unit is digital number.
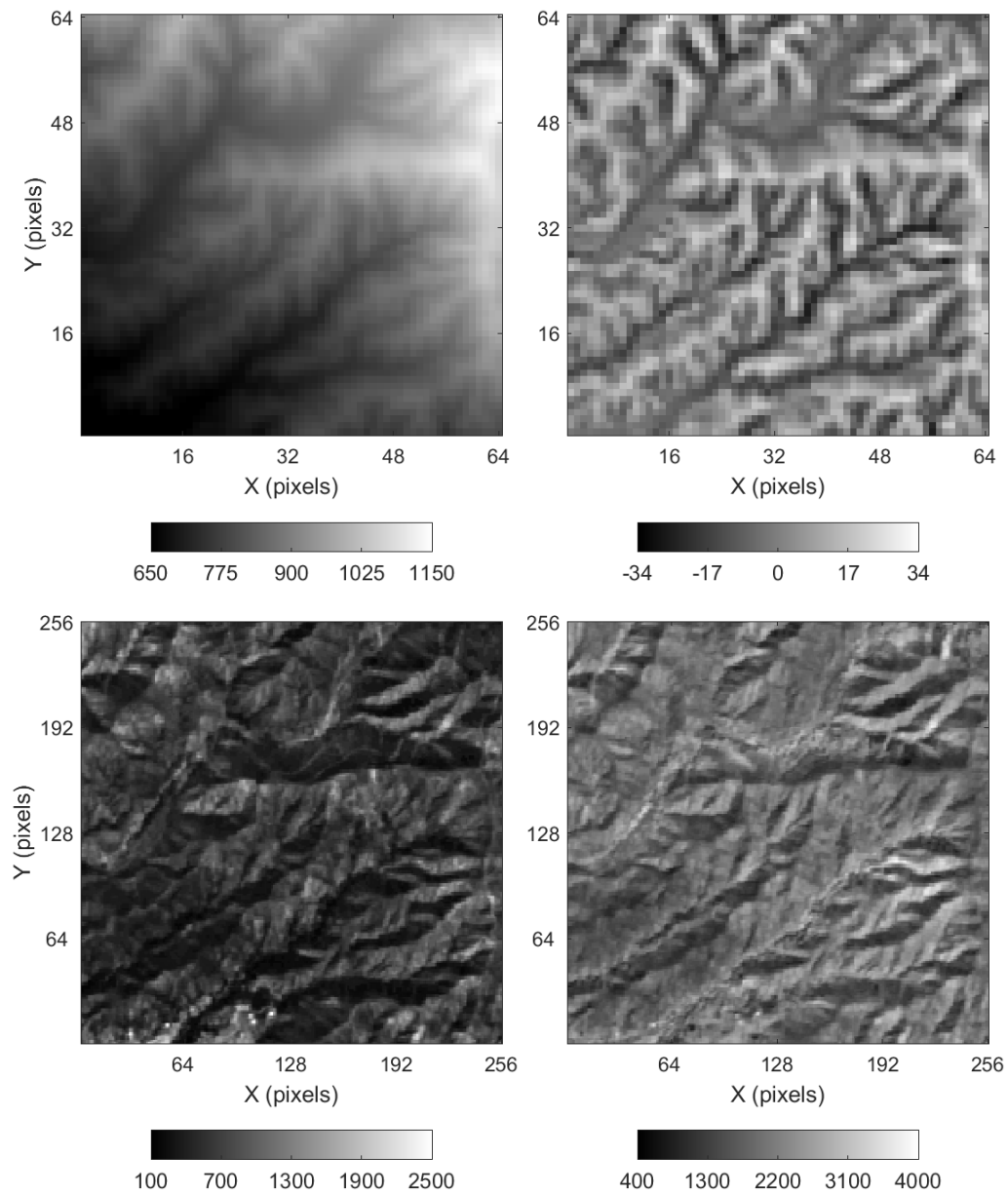
A.2 Characterization of measurement errors

Figures A.6 and A.7 reveal the discrepancies between the coarse-resolution target and reference DEMs. The maps display the relative errors (with the trend) and the absolute residual errors (without the trend) for the five data sets. Errors are computed based on the reference DEMs. The reference data sets provide a more accurate representation of the underlying "true" topography, and therefore are used for identifying errors and validating the downscaling outputs. Figures A.6 and A.7 evidentiate substantial spatial auto-correlation of the error components. Artifacts originating from either the data acquisition process, or the DEM interpolation procedure, are also noticeable. Tables A.4 and A.5 summarize statistics of the errors in both trended and residual versions of the coarse-resolution target DEMs.

The target data sets based on the 3DEP 1-arc second DEM, used in the Appalachians, the Colorado Plateau, and San Gabriel Mountains examples, are the most accurate among the five products as they contain the lowest systematic bias and highest precision for both trended and residual DEMs (Tables A.4 and A.5). Nonetheless, the magnitude of the errors in the residual component appears to be positively correlated with its variability (Table A.3) and the relative terrain complexity (Figs. A.6 and A.7). The Appalachians example target DEM, in particular, displays acquisition artifacts in the form of horizontal and vertical stripes arranged in a semi-regular pattern (Fig. A.6). A subtle quasi-horizontal stripes pattern can also be observed in the San Gabriel Mountains target DEM (Fig. A.7).

The Alaska Range example target DEM exhibits significant negative offset bias (Fig. A.6 and Table A.4), with ME of -1.75% and relative errors reaching up to -4%, respectively. Its corresponding residual DEM displays underestimation bias and lower precision (Table A.5). Absolute errors can reach up to 15 m, which corresponds to almost 50% of the peak amplitude of its residual component (Table A.5, Figs. A.1 and A.6). The target DEM also reveals acquisition artifacts in the form of a gridding pattern, which is more visible in the rugged parts of the terrain.

The Central Lowlands example target DEM is by far the worst product in terms of quality (Tables A.4 and A.5). This is quite apparent by visual inspection of Figures A.3 and A.6. Relative errors in the data may reach up to $\pm14\%$, with absolute errors in the residual component ranging from -100 to $+50\%$ of the target peak amplitude (Table A.5, Figs. A.3 and A.6).

All target DEMs display a systematic underestimation bias. Overall, measurement errors appear to be composed by at least three distinct types of systematic errors and an

intrinsic random error component (i.e. speckle noise). The first systematic error component is primarily related to large variations in the terrain gradient. The second component appears to be associated with acquisition artifacts. The third type of systematic error consists of a negative offset bias that is limited to the Alaska Range example target DEM (Fig. A.6). Errors in the coarse-resolution target DEMs are expected to deteriorate the reproduction of the sub-pixel statistics and structural metrics by simulated realizations as they will propagate throughout the downscaling process. The iterative and sequential nature of the algorithm make it especially susceptible to error propagation effects.

Table A.4: Error statistics of the coarse-resolution target trended DEMs.

Example	ME[1](%)	SDE[2](%)	m[3]	r[4]
Alaska Range	-1.75	111.86	1.00	1.00
Appalachians	-0.00	0.03	1.00	1.00
Central Lowlands	-1.25	79.89	1.28	0.96
Colorado Plateau	-0.00	0.17	1.00	1.00
San Gabriel Mountains	0.00	0.17	1.00	1.00

[1] mean error;   [2] standard deviation of error;
[3] RMA regression slope;
[4] Pearson's linear correlation coefficient

Table A.5: Error statistics of the coarse-resolution target residual DEMs.

Example	ME[1](cm)	SDE[2](cm)	m[3]	r[4]
Alaska Range	-0.80	51.21	1.05	0.91
Appalachians	0.02	1.00	1.02	0.99
Central Lowlands	-0.34	21.72	2.17	0.82
Colorado Plateau	-0.17	11.09	1.01	0.98
San Gabriel Mountains	-2.11	135.26	1.05	0.98

[1] mean error;   [2] standard deviation of error;
[3] RMA regression slope;
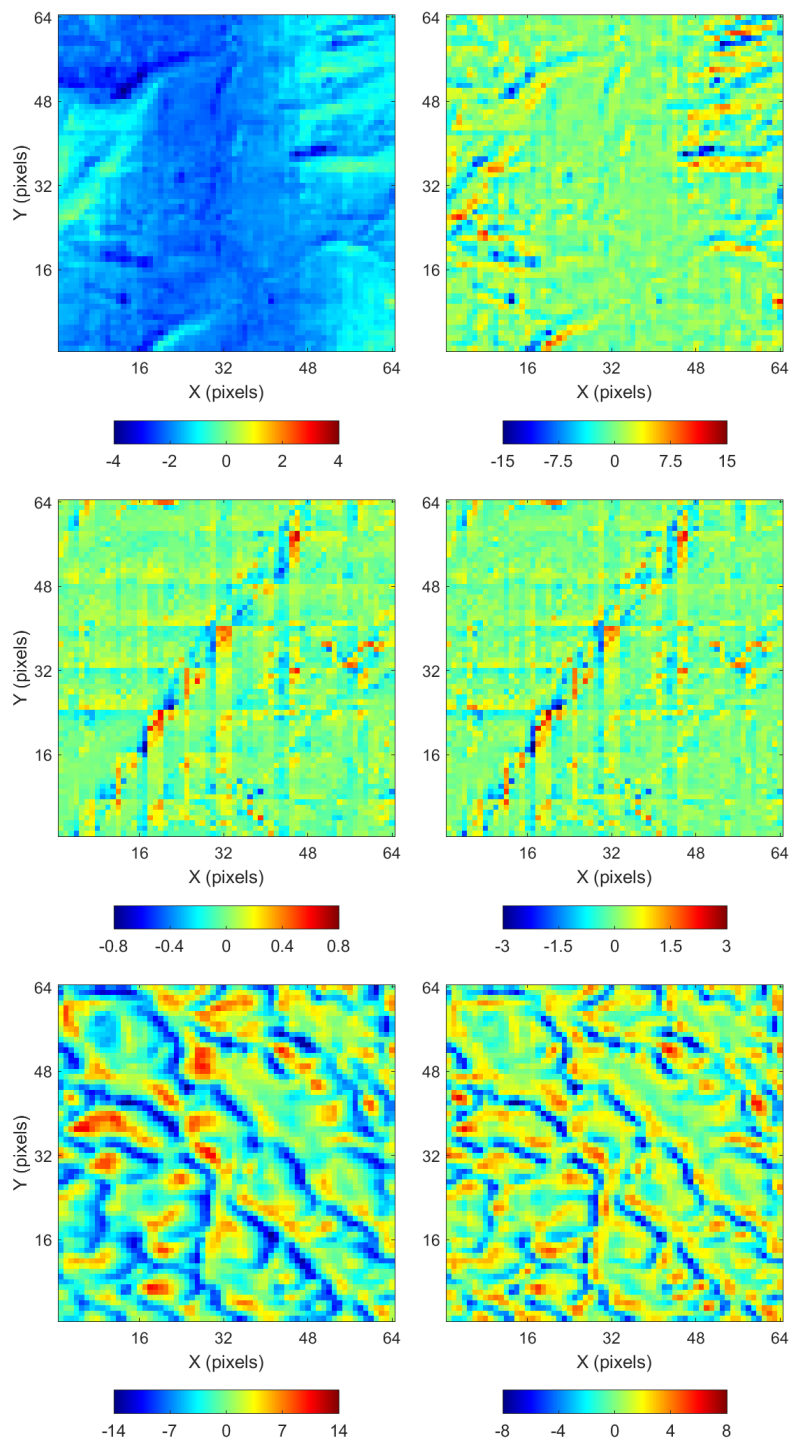[4] Pearson's linear correlation coefficient

Figure A.6: Errors in the coarse-resolution target DEMs. *Top row*: relative error (%) and absolute residual error (m) in the Alaska Range example DEM. *Middle row*: relative error (%) and absolute residual error (m) in the Appalachians example DEM. *Bottom row*: relative error (%) and absolute residual error (m) in the Central Lowlands example DEM.
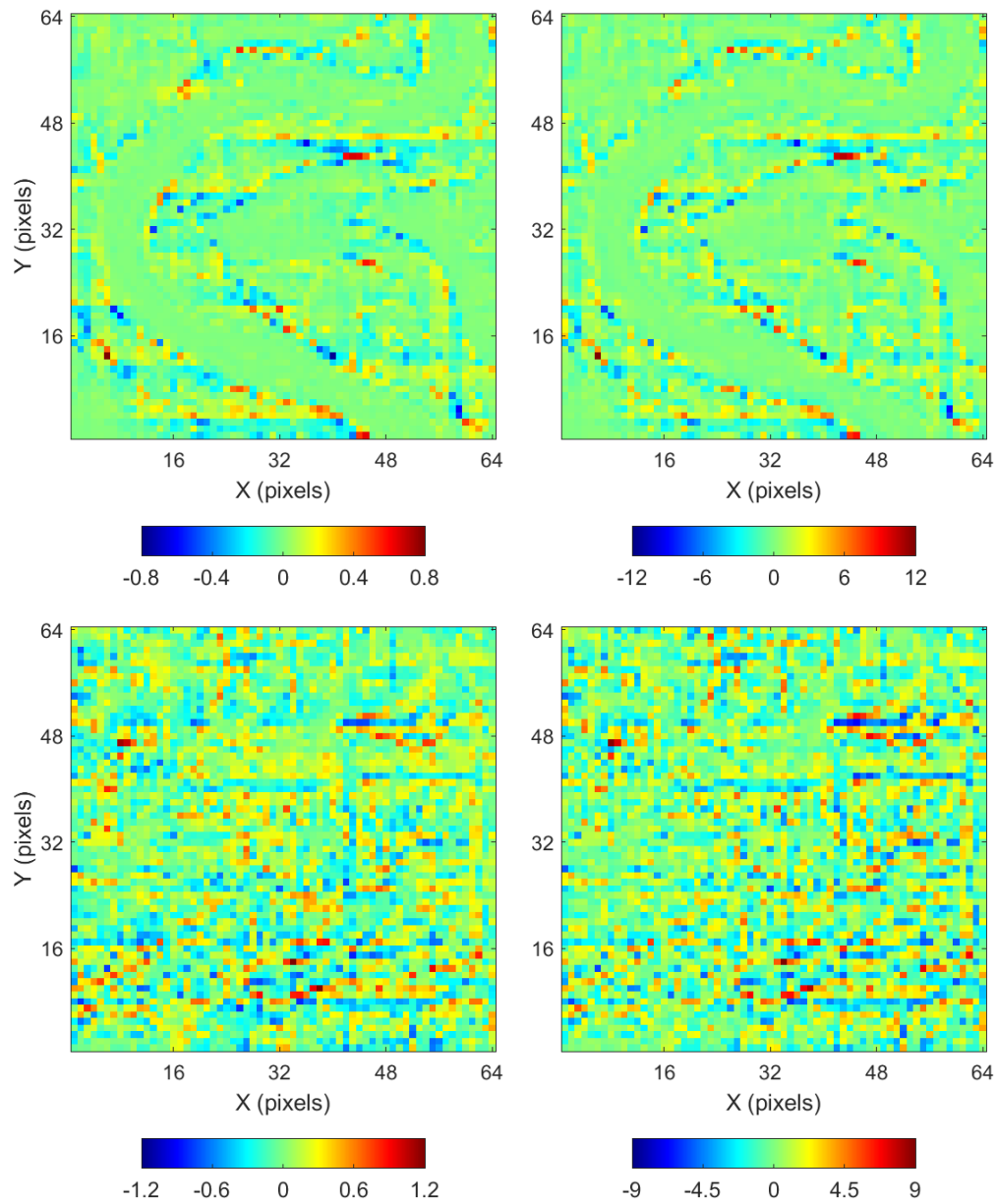
Figure A.7: Errors in the coarse-resolution target DEMs. *Top row*: relative error (%) and absolute residual error (m) in the Colorado Plateau example DEM. *Bottom row*: relative error (%) and absolute residual error (m) in the San Gabriel Mountains example DEM.

A.3 Simulation and validation

Subsections A.3.1 and A.3.2 present the simulation results for the case studies associated with Chapters 4 and 5, respectively. For detailed information about the training data sets, and the downscaling algorithm and data integration parameters used in the experiments, please refer to these two chapters. Subsections A.3.3 summarizes the main findings of the numerical experiments.

A.3.1 Alaska Range, Appalachians, and Central Lowlands examples

Figures A.8–A.10 show sample downscaling realizations of the Alaska Range, the Appalachians, and the Central Lowlands examples. The residual DEMs are generated using the same spatial low-pass filter used in Figures A.1–A.5. The coarse-resolution reference DEMs, in particular, serve to highlight the errors in the target DEMs. Green boxes highlight the magnified areas in the residual DEMs (Figs. A.8–A.10).

Table A.6 lists statistics related to the conditioning quality of simulated realizations to the coarse-resolution target residual DEMs. Statistics are computed based upon the upscaled simulated realizations and the coarse-resolution target residual DEMs. As the upscaling function is not explicitly defined, the conditioning MEs and SDEs associated with each realization are computed by accumulating at each iteration the mismatch between the centroids of the target data events and their corresponding source data events in the training data. Results demonstrate that the downscaling outputs honor the target residual DEMs. The average MEs are close to zero, and the mean SDEs do not exceed 1 m. Errors tend to be larger for $G = 4$ because of the propagation effects across iterations. Slight underprediction and deterioration in the reproduction of the coarse-resolution residual data are observed.

Summary statistics of the medium- and fine-resolution reference and simulated residual DEMs are listed in Table A.7. Most of the reference statistics of the Alaska Range and the Appalachians examples are relatively well reproduced. The standard deviations of the simulated realizations associated with the two data sets are underestimated by approximately 5%. The reference residual minima and maxima are reasonably well reproduced, except the maxima from the Alaska Range example DEM. Measurement errors in the Central Lowlands example target DEM have severely compromised the sub-pixel statistics of simulated realizations, notably their statistical dispersion (Table A.7).

Table A.6: Conditioning to coarse-resolution residual data.

Example	G	ME[1](cm)	SDE[2](cm)	m[3]	r[4]
Alaska Range	2	0.12 ± 0.23	11.58 ± 11.64	1.00 ± 0.00	1.00 ± 0.00
	4	-0.35 ± 1.69	86.50 ± 66.11	1.05 ± 0.00	0.93 ± 0.01
Appalachians	2	-0.23 ± 0.30	20.09 ± 13.39	1.01 ± 0.00	1.00 ± 0.00
	4	-0.42 ± 0.59	34.48 ± 30.57	1.04 ± 0.00	0.78 ± 0.04
Central Lowlands	2	0.38 ± 0.11	24.36 ± 6.87	1.00 ± 0.00	1.00 ± 0.00
	4	1.01 ± 0.19	64.49 ± 12.30	1.01 ± 0.00	0.95 ± 0.01

[1] mean error;   [2] standard deviation of error;   [3] RMA regression slope;
[4] Pearson's linear correlation coefficient; Values represent average statistics plus or minus one standard deviation over 20 realizations

Figures A.11–A.13 illustrate the structural validation of the downscaled DEMs. Results are displayed for the two magnification factors. Spatial statistics refer exclusively to the residual DEMs. Green curves denote the reference data, whereas simulated realizations are indicated in black. The envelopes represent the range covered by 20 simulated realizations. Figures A.11 and A.12 show that the structural statistics of the Alaska Range and Appalachians examples' simulations, in particular, are fairly well reproduced for both magnification factors. However, systematic underestimation of the contributions of the reference empirical variograms, and issues in the reproduction of high-amplitude spikes in the reference Euler characteristic curves are observed. Simulated realizations of the Central Lowlands example were unable to reproduce most of the reference spatial statistics (Fig. A.13), which indicates that the errors in the target DEM have severely compromised the structural quality of the downscaling outputs.
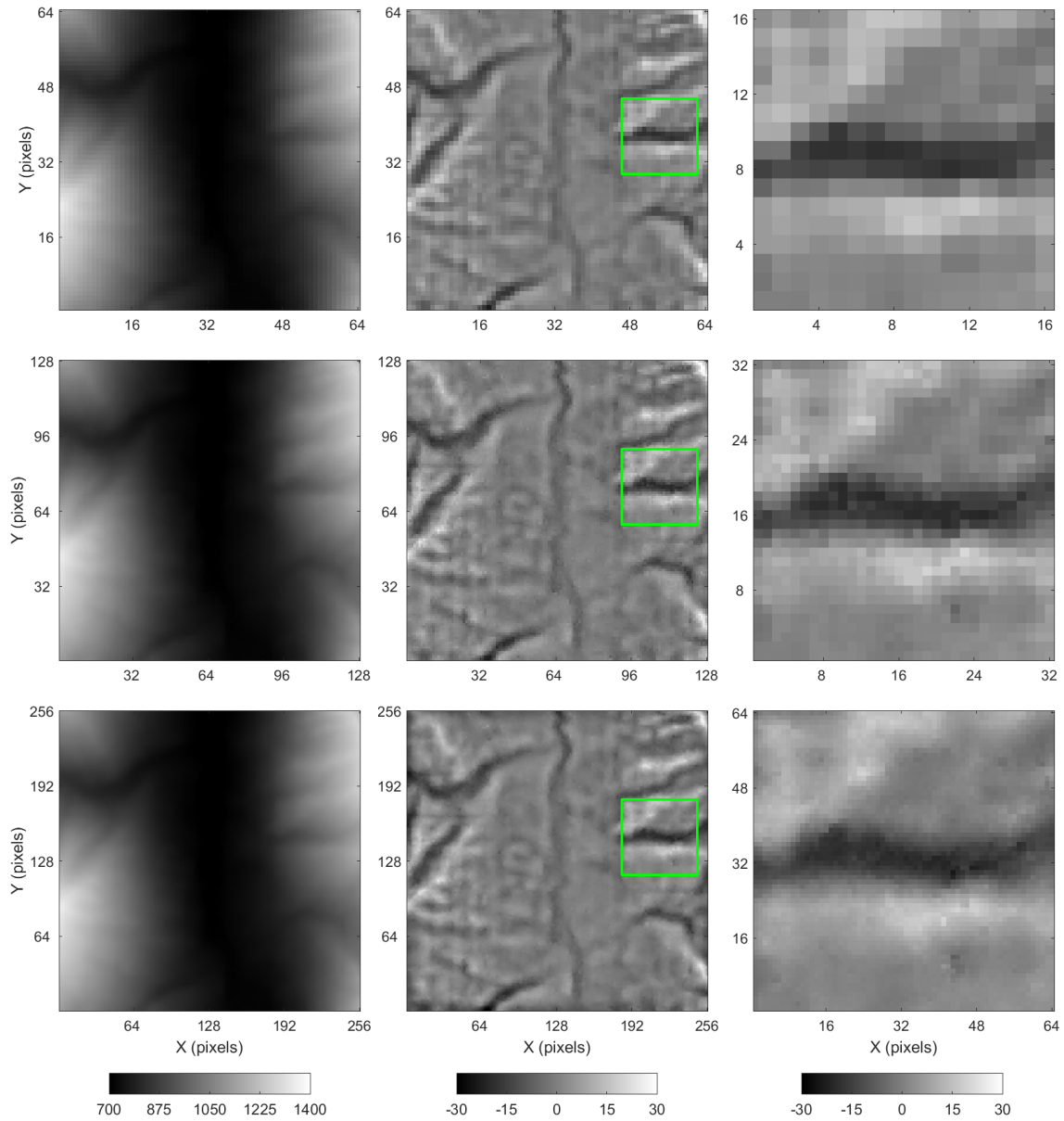
Figure A.8: The Alaska Range example downscaled DEMs. *Top left*: coarse-resolution DEM. *Top center*: coarse-resolution residual DEM. *Top right*: coarse-resolution zoom. *Middle left*: medium-resolution DEM. *Middle center*: medium-resolution residual DEM. *Middle right*: medium-resolution zoom. *Bottom left*: fine-resolution DEM. *Bottom center*: fine-resolution residual DEM. *Bottom right*: fine-resolution zoom. Green boxes highlight the magnified area. Colorbars' unit is m.
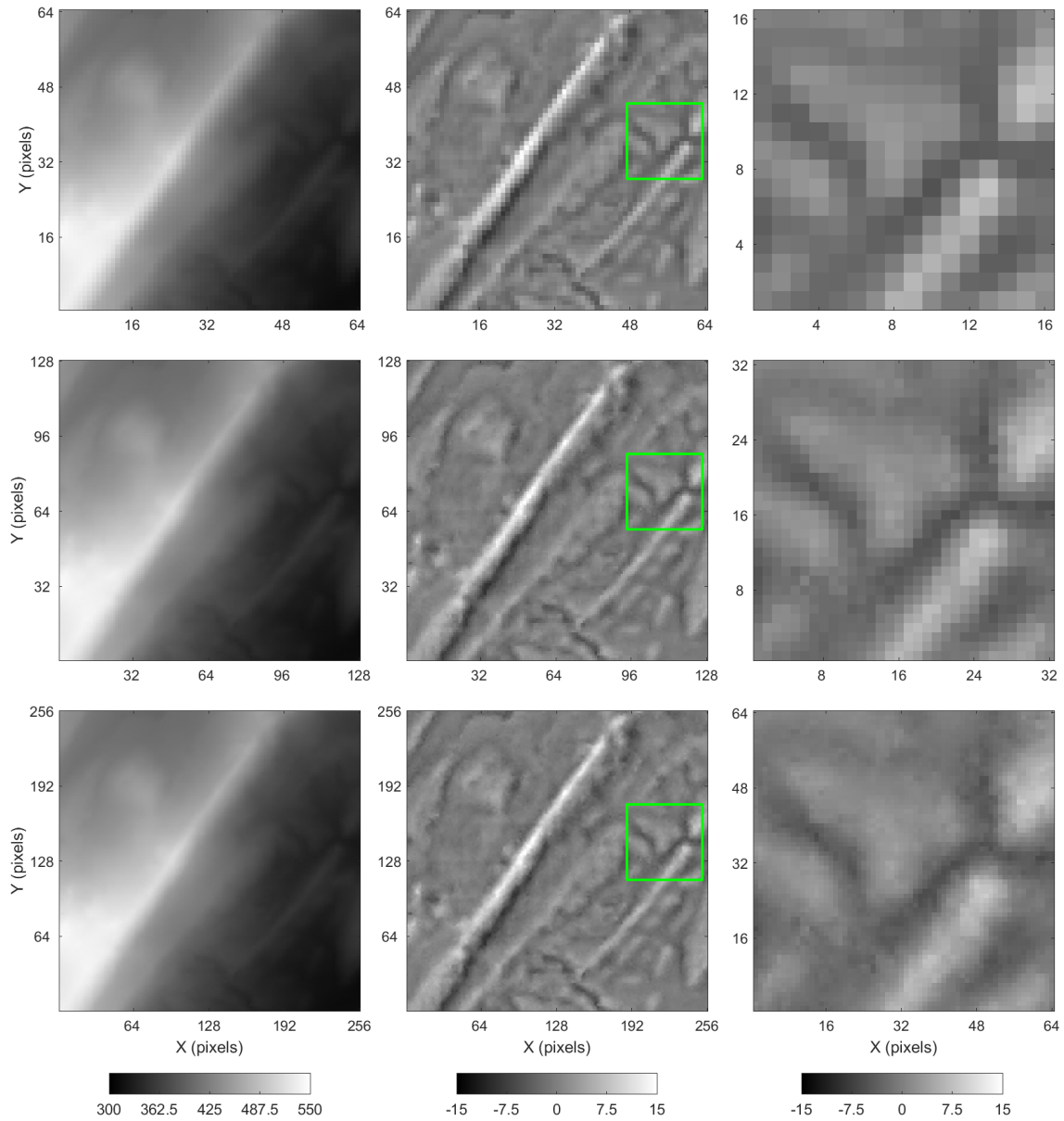
Figure A.9: The Appalachians example downscaled DEMs.   *Top left*: coarse-resolution DEM. *Top center*: coarse-resolution residual DEM. *Top right*: coarse-resolution zoom. *Middle left*: medium-resolution DEM. *Middle center*: medium-resolution residual DEM. *Middle right*: medium-resolution zoom. *Bottom left*: fine-resolution DEM. *Bottom center*: fine-resolution residual DEM. *Bottom right*: fine-resolution zoom. Green boxes highlight the magnified area. Colorbars' unit is m.
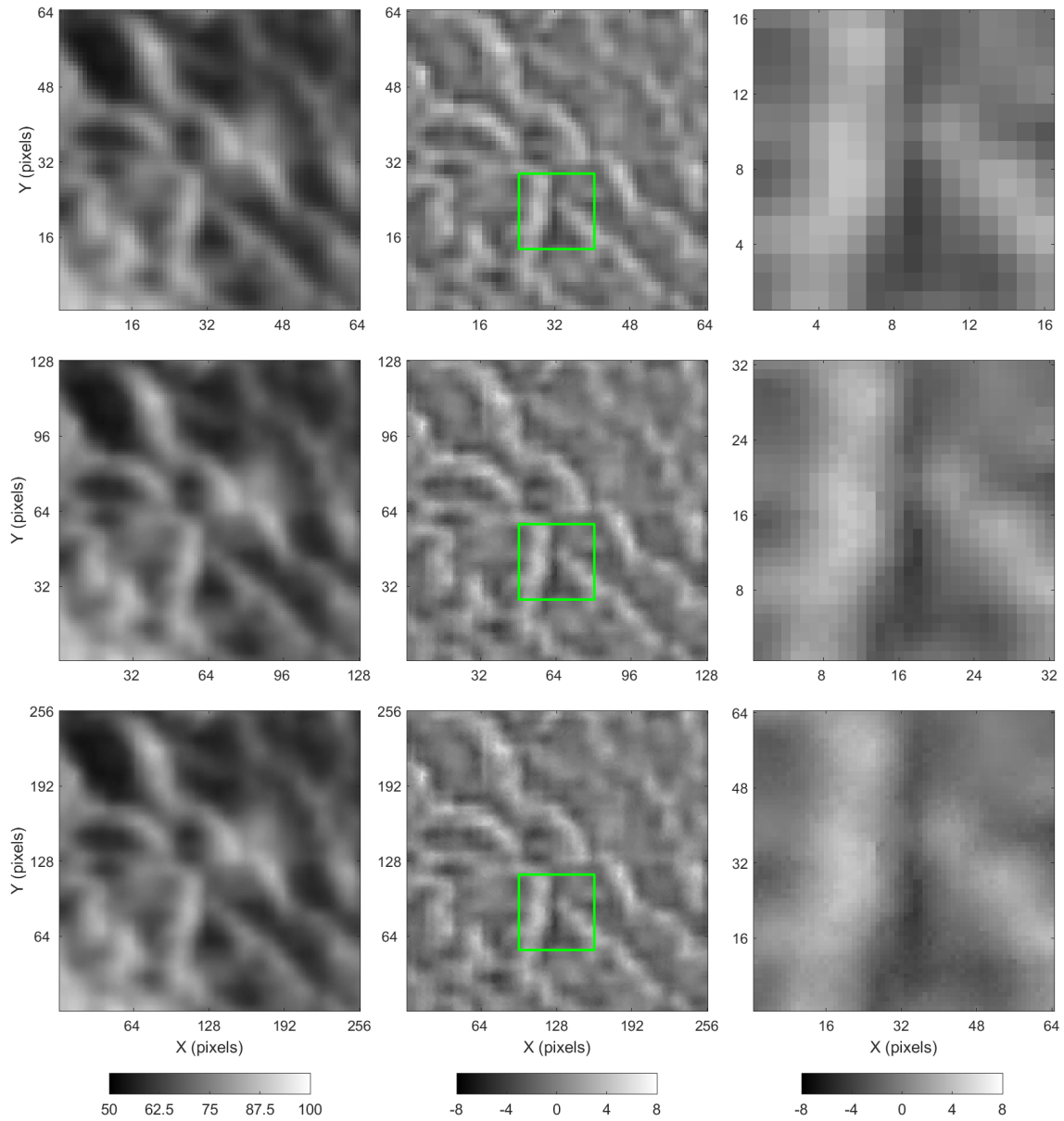
Figure A.10: The Central Lowlands example downscaled DEMs. *Top left*: coarse-resolution DEM. *Top center*: coarse-resolution residual DEM. *Top right*: coarse-resolution zoom. *Middle left*: medium-resolution DEM. *Middle center*: medium-resolution residual DEM. *Middle right*: medium-resolution zoom. *Bottom left*: fine-resolution DEM. *Bottom center*: fine-resolution residual DEM. *Bottom right*: fine-resolution zoom. Green boxes highlight the magnified area. Colorbars' unit is m.

Table A.7: Summary statistics of the medium- and fine-resolution reference and downscaled DEMs from the Alaska Range, the Appalachians, and the Central Lowlands examples.

Example	Data set	G	Mean	SD	Min.	Max.
Alaska Range	Reference	2	−0.36	5.75	−24.44	36.58
		4	−0.35	5.75	−26.16	40.77
	Simulation	2	−0.36 ± 0.00	5.45 ± 0.00	−24.58 ± 1.27	31.26 ± 0.72
		4	−0.94 ± 0.00	5.49 ± 0.00	−30.11 ± 1.58	27.75 ± 1.29
Appalachians	Reference	2	0.03	2.79	−10.45	16.85
		4	0.03	2.79	−10.78	17.34
	Simulation	2	0.03 ± 0.00	2.69 ± 0.00	−9.73 ± 0.26	15.95 ± 0.44
		4	0.03 ± 0.00	2.68 ± 0.00	−10.45 ± 0.41	16.48 ± 0.28
Central Lowlands	Reference	2	−0.02	3.33	−7.79	12.77
		4	−0.02	3.32	−7.89	13.89
	Simulation	2	−0.02 ± 0.00	1.49 ± 0.00	−4.41 ± 0.09	6.08 ± 0.13
		4	−0.03 ± 0.00	1.47 ± 0.00	−4.56 ± 0.15	6.32 ± 0.23

Numbers represent average statistics plus or minus one standard deviation over 20 realizations. Values are in residual elevation (in m)
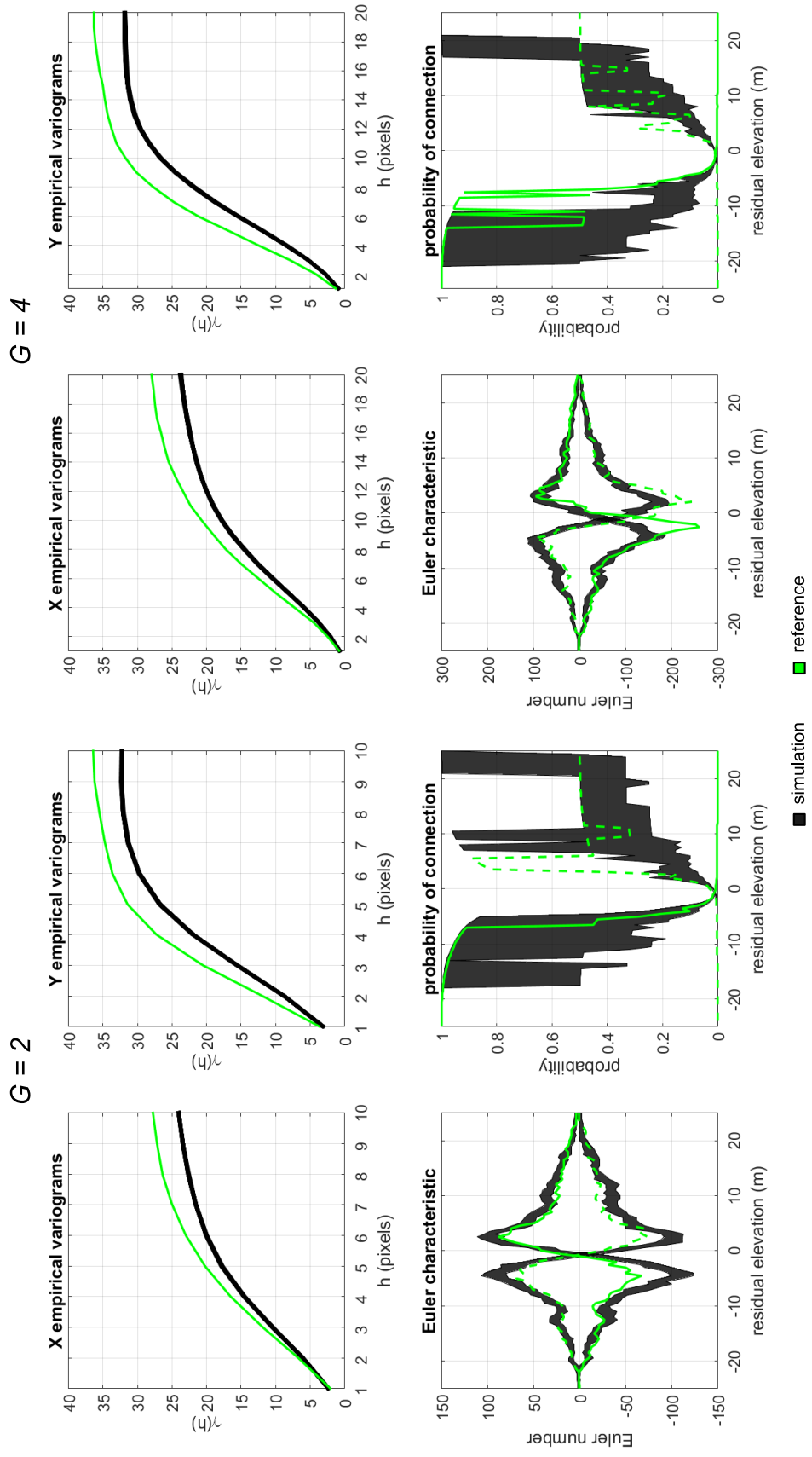
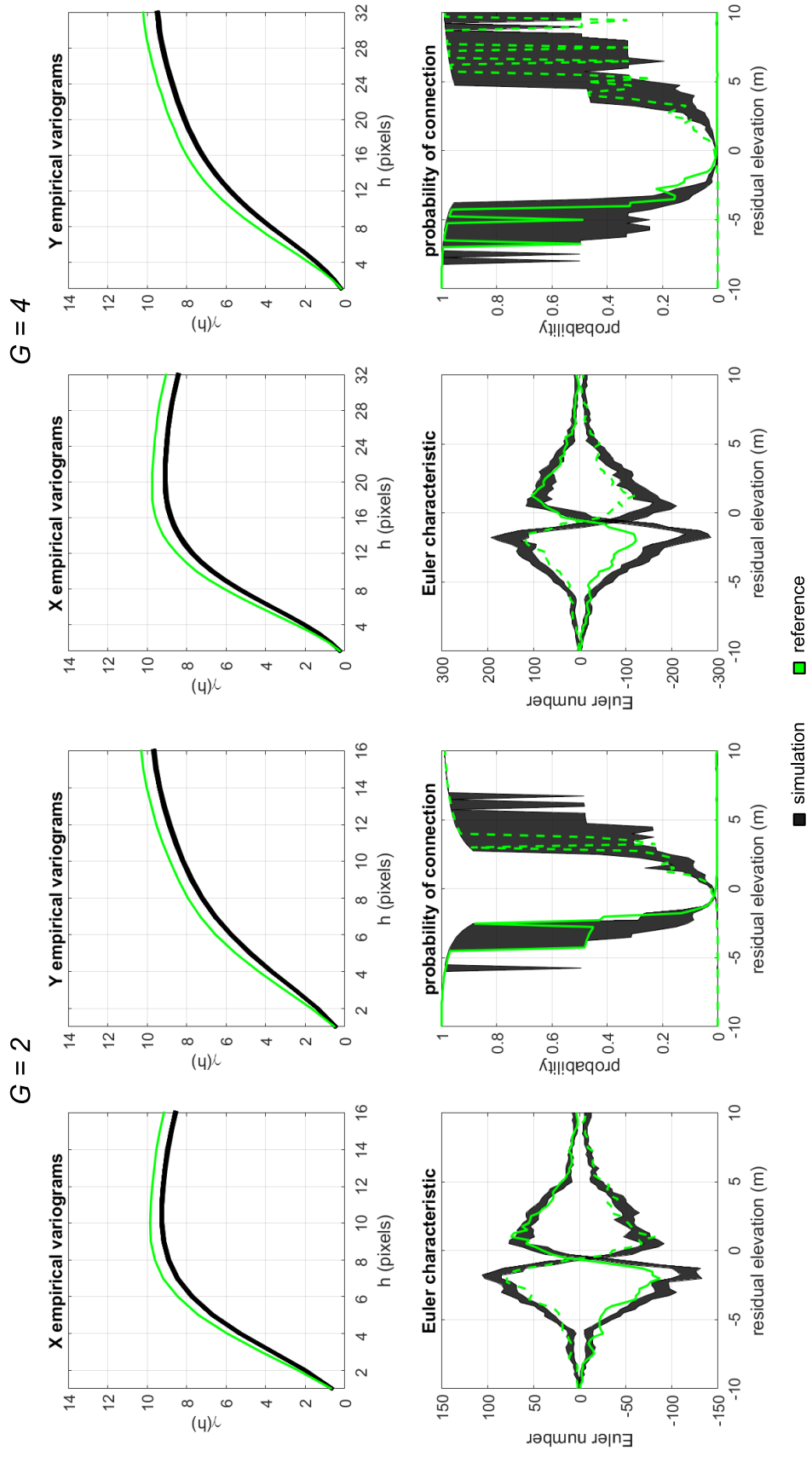Figure A.11: The Alaska Range example structural statistics.

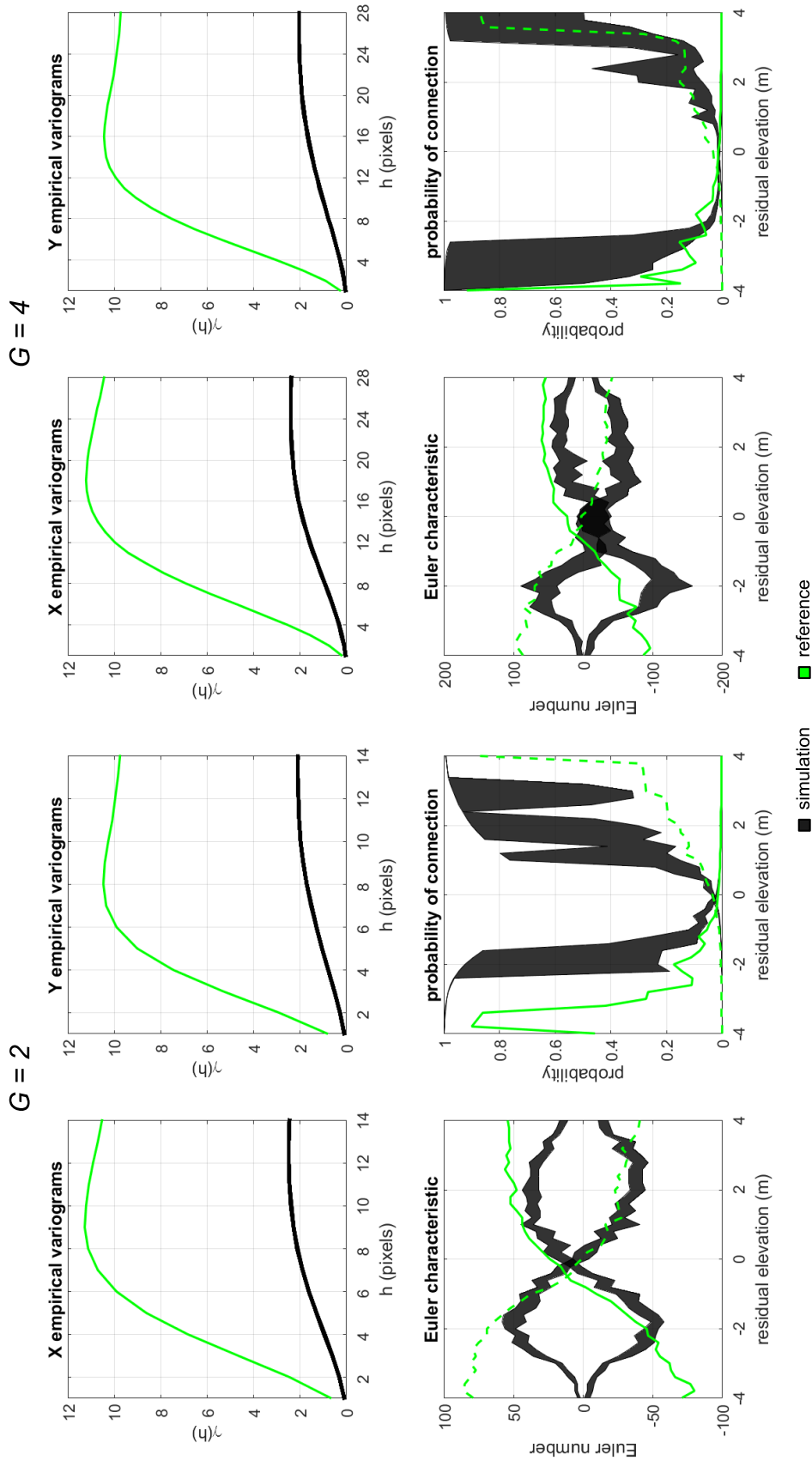Figure A.12: The Appalachians example structural statistics.

Figure A.13: The Central Lowlands example structural statistics.

A.3.2   Colorado Plateau and San Gabriel Mountains examples

Simulated realizations of the downscaling and data integration process for the Colorado Plateau and San Gabriel Mountains examples are shown in Figures A.14–A.19. Green boxes indicate the magnified areas in the residual DEMs. Figures A.16 and A.19 display the medium- and fine-resolution zooms for both reference and simulated DEMs, as well as for the co-registered fine-resolution target MSI (Red and NIR bands).

Table A.8 lists statistics describing the conditioning quality of simulated realizations to the coarse-resolution target residual DEMs. ME and SDE of each realization are calculated implicitly by accumulating the mismatch between the centroids of the target data events and their corresponding source data events in the training data at each iteration. Statistics demonstrate that simulated realizations adequately honor the target residual DEMs. Results are largely in agreement with the coarse-scale conditioning statistics presented in Chapter 5.

Table A.8: Conditioning to coarse-resolution residual data.

Example	Data	G	ME[1](cm)	SDE[2](cm)	m[3]	r[4]
Colorado	DEM	2	0.09 ± 0.26	12.77 ± 11.77	1.00 ± 0.00	1.00 ± 0.00
Plateau		4	0.92 ± 0.73	62.22 ± 41.21	1.02 ± 0.01	0.76 ± 0.06
	DEM/MSI	2	-0.73 ± 0.00	46.92 ± 0.00	1.00 ± 0.00	1.00 ± 0.00
		4	-3.85 ± 0.15	246.66 ± 9.86	0.96 ± 0.00	0.88 ± 0.02
San Gabriel	DEM	2	-0.13 ± 0.44	21.15 ± 19.91	1.00 ± 0.00	1.00 ± 0.00
Mountains		4	2.80 ± 2.70	188.70 ± 162.21	1.03 ± 0.00	0.88 ± 0.02
	DEM/MSI	2	0.04 ± 0.00	2.27 ± 0.00	1.00 ± 0.00	1.00 ± 0.00
		4	-0.21 ± 0.31	19.60 ± 12.90	0.98 ± 0.00	0.93 ± 0.00

[1] mean error;   [2] standard deviation of error;
[3] RMA regression slope;   [4] Pearson's linear correlation coefficient; Values represent average statistics plus or minus one standard deviation over 20 realizations

Summary statistics for the medium- and fine-resolution simulated DEMs are listed in Table A.9. Numerical experiments show that simulated realizations appropriately reproduce the medium- and fine-resolution empirical PDFs. The mean residual elevation of simulated realizations is close to the Colorado Plateau example's reference statistics, but it is systematically underestimated in the San Gabriel Mountains example by both conditioning data configurations. In addition, small underestimation of the reference standard deviation by simulated realizations is observed. The statistical accuracy of the simulated realizations is

comparatively worse due to the presence of errors in the coarse-resolution target DEMs.

Figures A.20 and A.21 show the structural validation of the downscaled DEMs for the Colorado Plateau and San Gabriel Mountains examples. Green curves denote the reference data. Simulated realizations with and without MSI data are indicated by the black and blue curves, respectively. The envelopes represent the range covered by 20 realizations. Results reveal similar patterns observed in the numerical experiments based on artificial target DEMs. Empirical variograms of realizations conditioned to secondary information display lower long-range variability than for those not conditioned to the MSI. The integration of finer-resolution MSI appears to enhance the reproduction of reference Euler characteristic and probability of connection curves for both examples.

Medium- and fine-resolution post-processing maps for the Colorado Plateau and the San Gabriel Mountains examples are shown in Figures A.22 and A.23, respectively. Results suggest that the integration of MSI into the downscaling enables to limit the uncertainty of sub-pixel predictions. The observed spatial patterns in the SD-type maps are similar to the ones presented in Chapter 5. The reduced variability of the predictions is summarized by the statistics listed in Table A.10. Changes in the variability of the SD-type maps display similar behavior to the numerical experiments based on artificial coarse-resolution target DEMs.
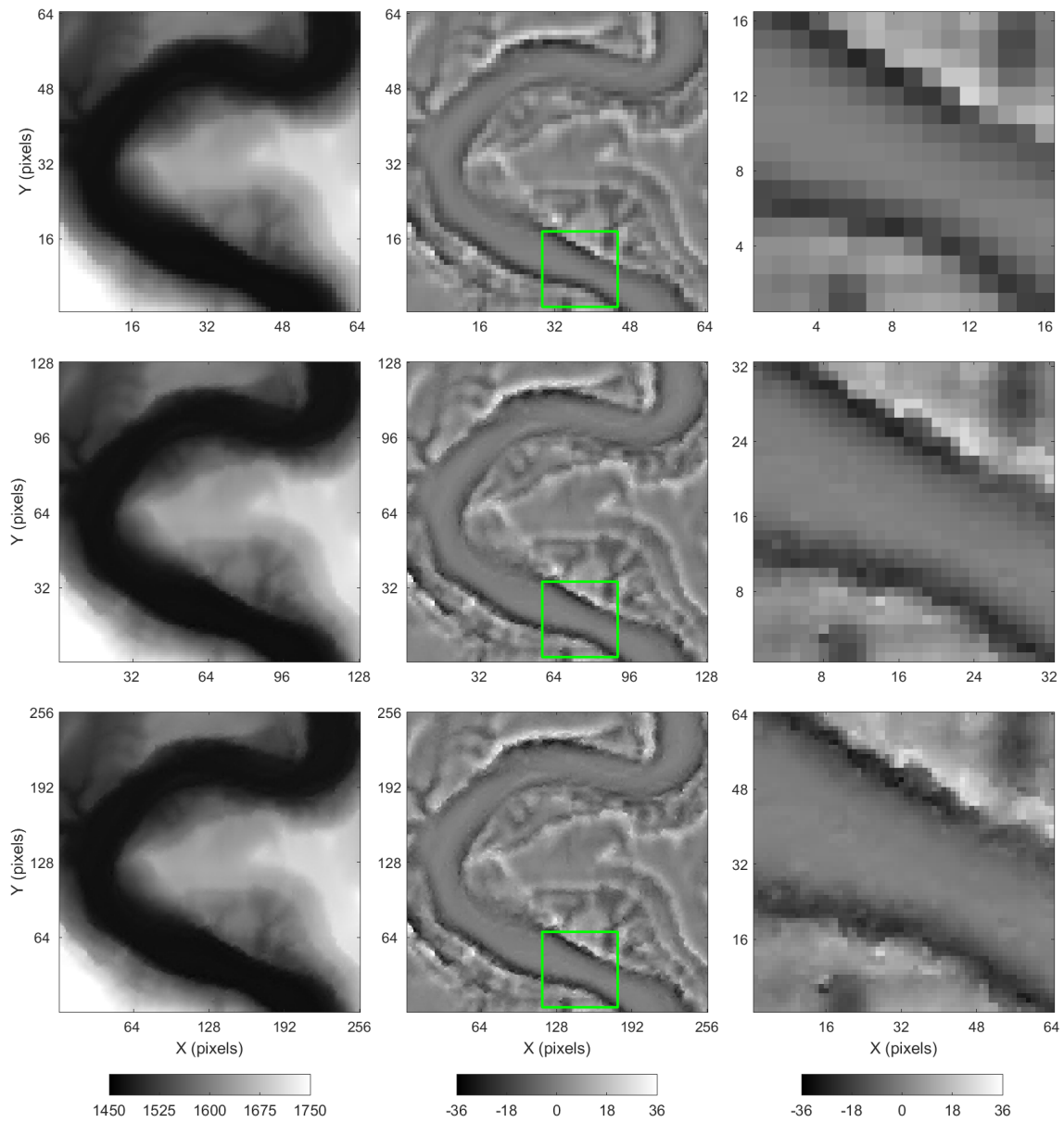
Figure A.14: The Colorado Plateau example downscaled DEMs (without MSI data). *Top left*: coarse-resolution DEM. *Top center*: coarse-resolution residual DEM. *Top right*: coarse-resolution zoom. *Middle left*: medium-resolution DEM. *Middle center*: medium-resolution residual DEM. *Middle right*: medium-resolution zoom. *Bottom left*: fine-resolution DEM. *Bottom center*: fine-resolution residual DEM. *Bottom right*: fine-resolution zoom. Green boxes highlight the magnified area. Colorbars' unit is m.

Figure A.15: The Colorado Plateau example downscaled DEMs (with MSI data). *Top left*: coarse-resolution DEM. *Top center*: coarse-resolution residual DEM. *Top right*: coarse-resolution zoom. *Middle left*: medium-resolution DEM. *Middle center*: medium-resolution residual DEM. *Middle right*: medium-resolution zoom. *Bottom left*: fine-resolution DEM. *Bottom center*: fine-resolution residual DEM. *Bottom right*: fine-resolution zoom. Green boxes highlight the magnified area. Colorbars' unit is m.
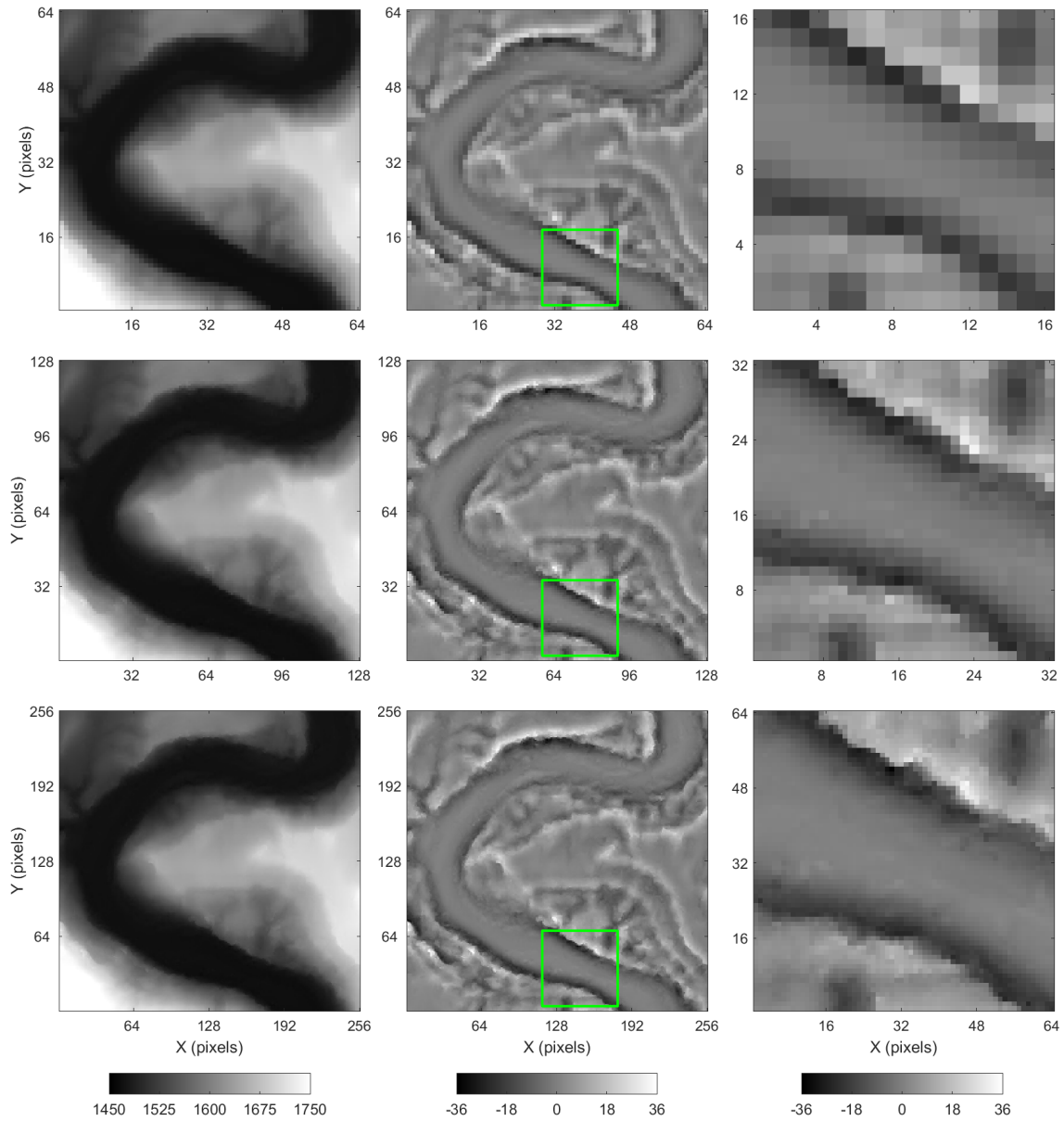
Figure A.16: Medium- and fine-resolution magnified areas of the Colorado Plateau example. Colorbar unit is m.

Figure A.17: The San Gabriel Mountains example downscaled DEMs (without MSI data). *Top left*: coarse-resolution DEM. *Top center*: coarse-resolution residual DEM. *Top right*: coarse-resolution zoom. *Middle left*: medium-resolution DEM. *Middle center*: medium-resolution residual DEM. *Middle right*: medium-resolution zoom. *Bottom left*: fine-resolution DEM. *Bottom center*: fine-resolution residual DEM. *Bottom right*: fine-resolution zoom. Green boxes highlight the magnified area. Colorbars' unit is m.
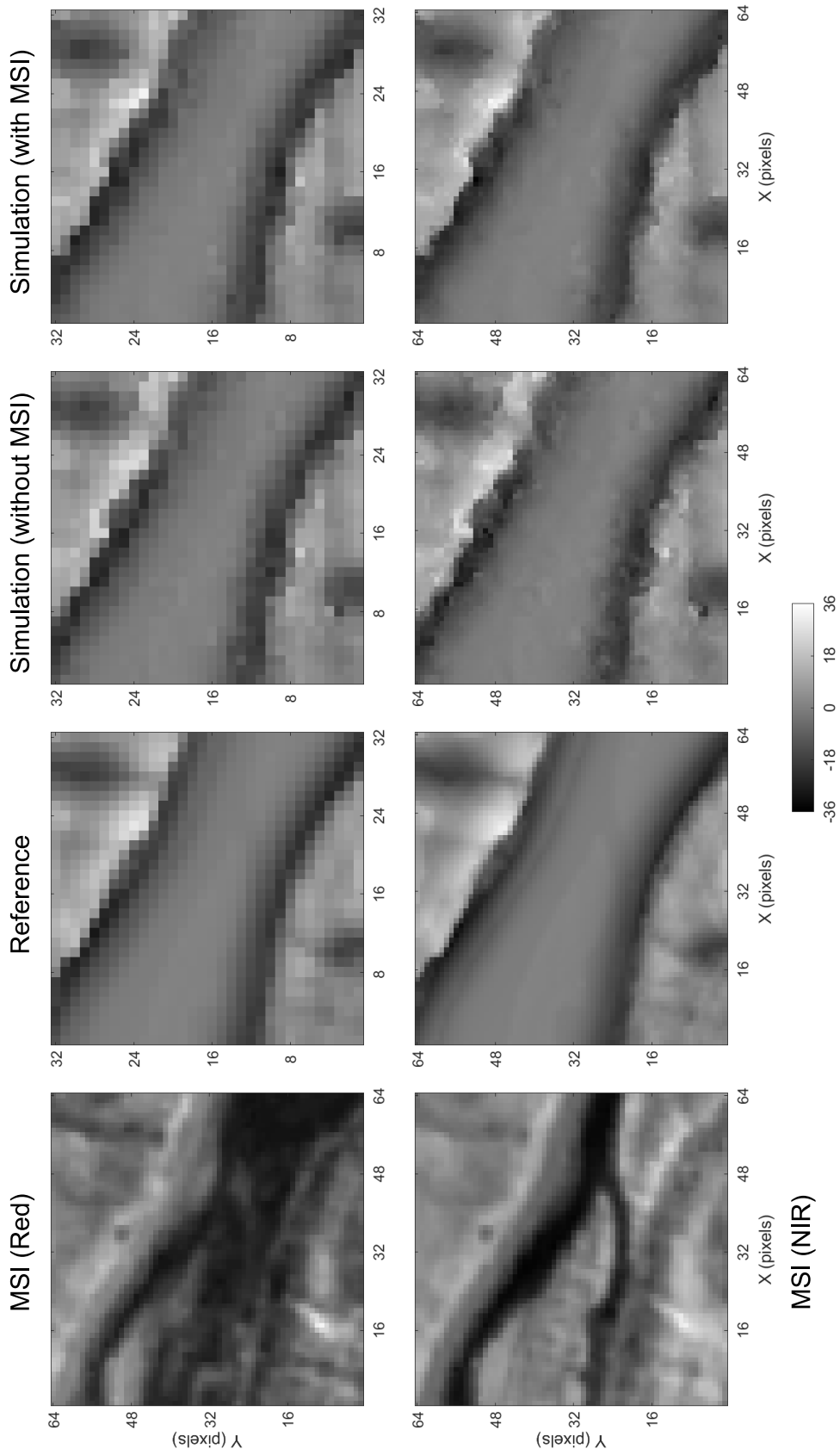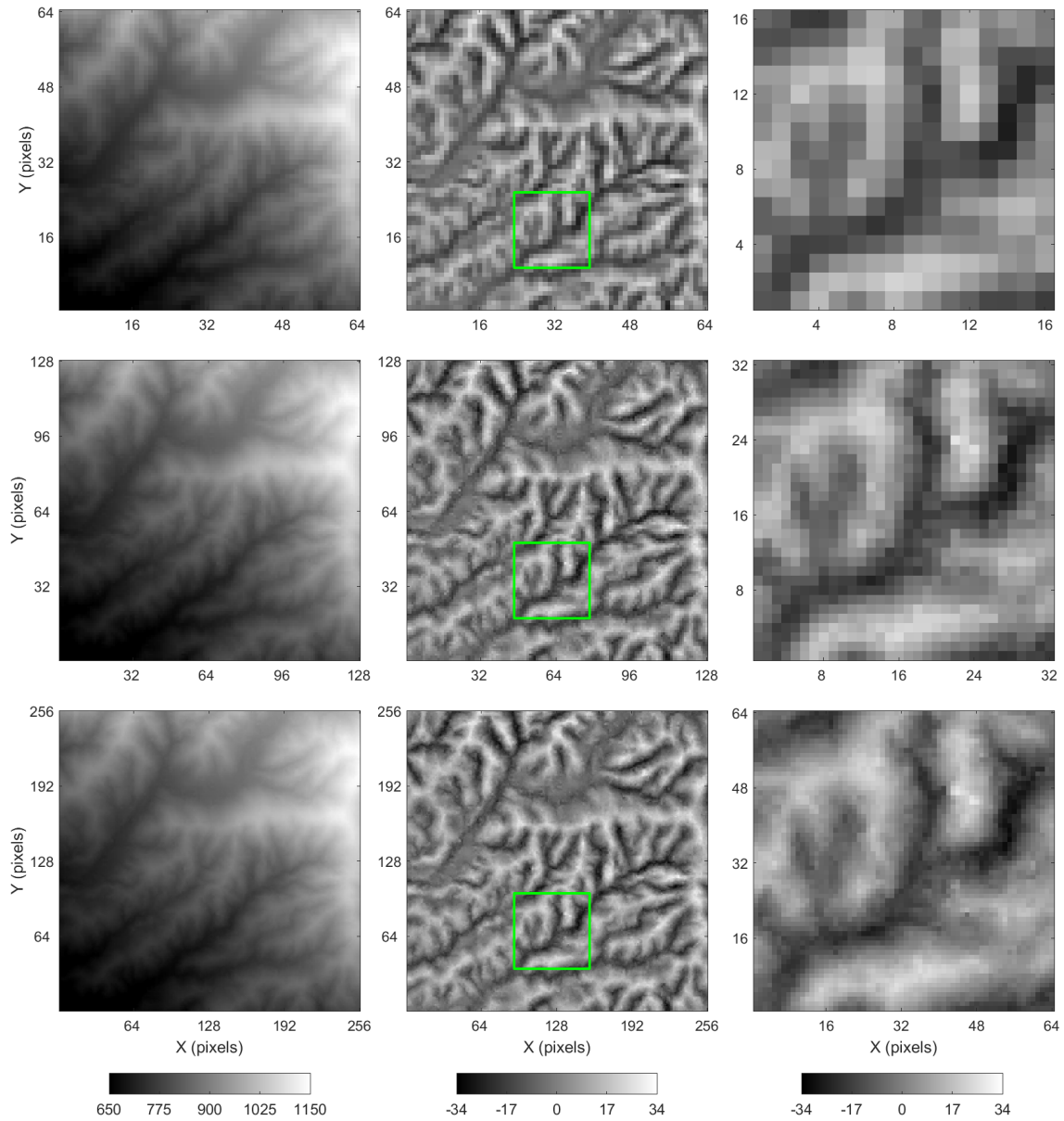
Figure A.18: The San Gabriel Mountains example downscaled DEMs (with MSI data). *Top left*: coarse-resolution DEM. *Top center*: coarse-resolution residual DEM. *Top right*: coarse-resolution zoom. *Middle left*: medium-resolution DEM. *Middle center*: medium-resolution residual DEM. *Middle right*: medium-resolution zoom. *Bottom left*: fine-resolution DEM. *Bottom center*: fine-resolution residual DEM. *Bottom right*: fine-resolution zoom. Green boxes highlight the magnified area. Colorbars' unit is m.
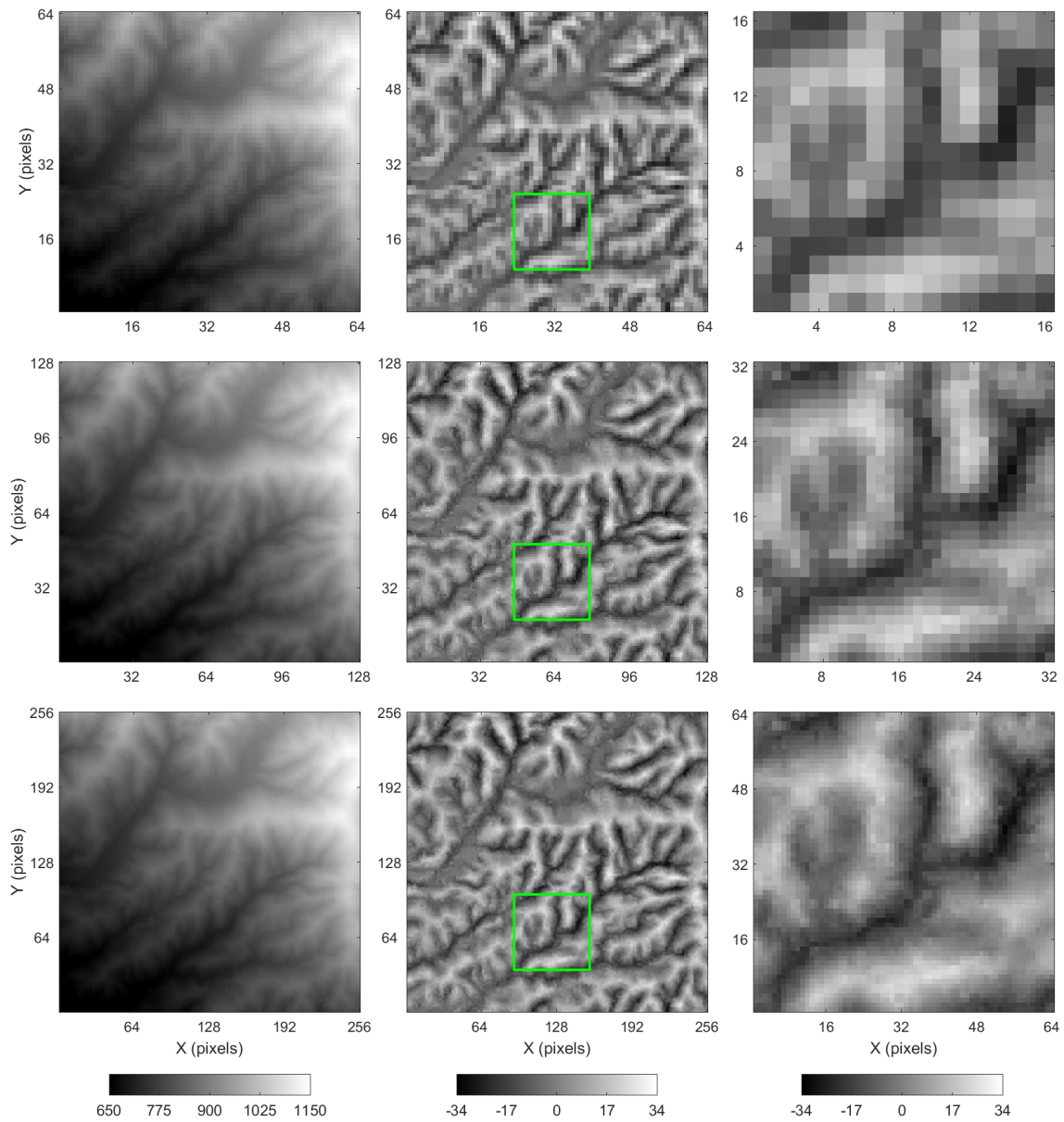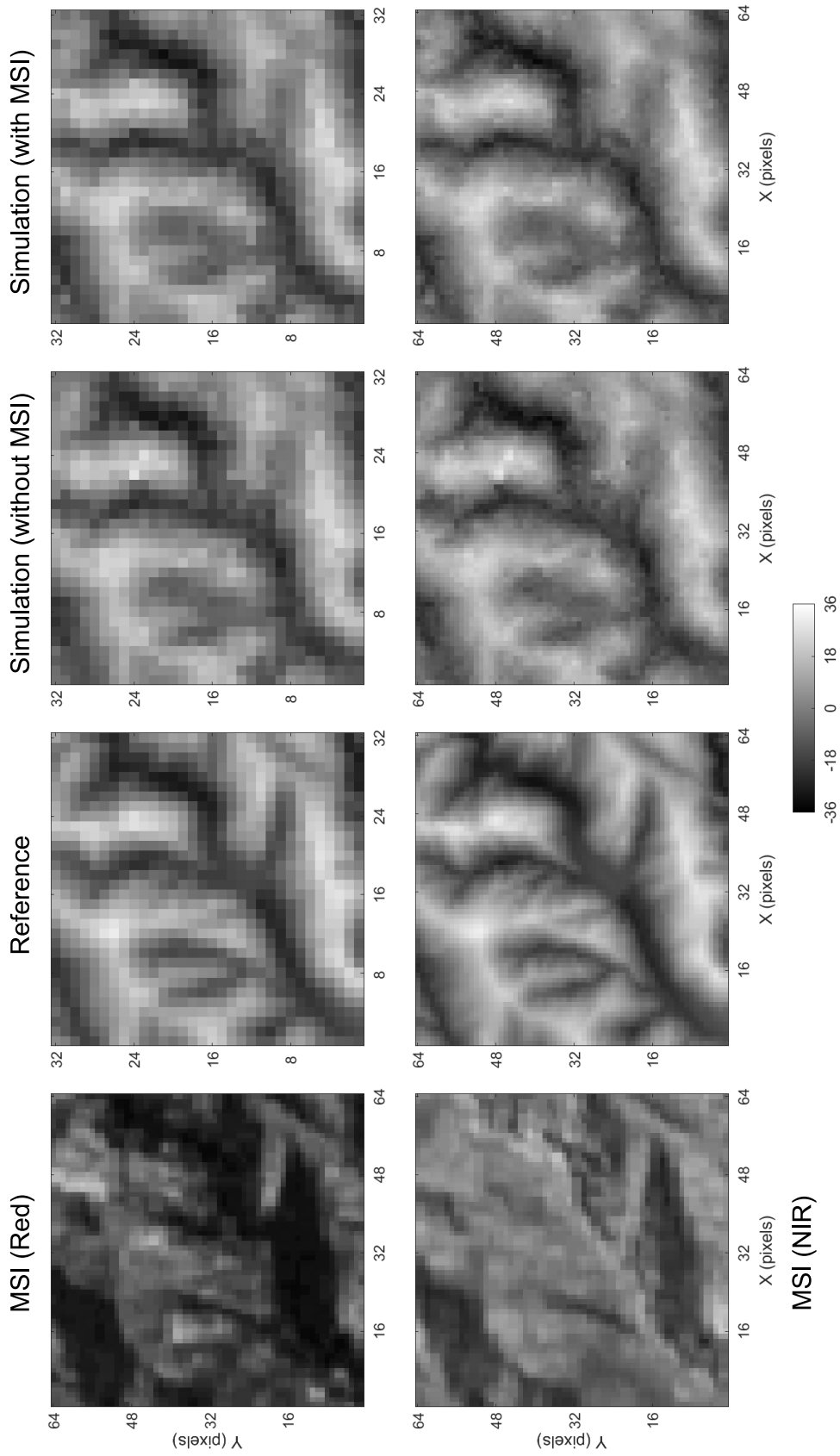
Figure A.19: Medium- and fine-resolution magnified areas of the San Gabriel Mountains example. Colorbar unit is m.

Table A.9: Summary statistics of the medium- and fine-resolution reference and downscaled DEMs from the Colorado Plateau and the San Gabriel Mountains examples.

Example	Data	G	Mean	SD	Min.	Max.
Colorado Plateau	Reference	2	−0.47	7.43	−30.44	33.10
		4	−0.45	7.50	−33.39	36.86
	DEM	2	−0.47 ± 0.00	7.27 ± 0.01	−31.03 ± 1.25	39.37 ± 3.49
		4	−0.45 ± 0.00	7.30 ± 0.01	−35.71 ± 2.51	45.10 ± 3.48
	DEM/MSI	2	−0.47 ± 0.00	7.27 ± 0.01	−31.87 ± 1.46	40.60 ± 3.32
		4	−0.46 ± 0.00	7.26 ± 0.01	−34.37 ± 2.70	44.82 ± 4.37
San Gabriel Mountains	Reference	2	0.25	11.09	−30.99	31.15
		4	0.25	11.18	−34.19	32.69
	DEM	2	0.23 ± 0.00	10.49 ± 0.01	−31.80 ± 1.22	30.82 ± 0.91
		4	0.23 ± 0.00	10.46 ± 0.01	−34.46 ± 1.63	31.95 ± 1.02
	DEM/MSI	2	0.23 ± 0.00	10.46 ± 0.01	−32.63 ± 0.37	30.19 ± 0.14
		4	0.23 ± 0.00	10.43 ± 0.01	−34.22 ± 1.34	31.85 ± 1.07

Numbers represent average statistics plus or minus one standard deviation over 20 realizations. Values are in residual elevation (in m)
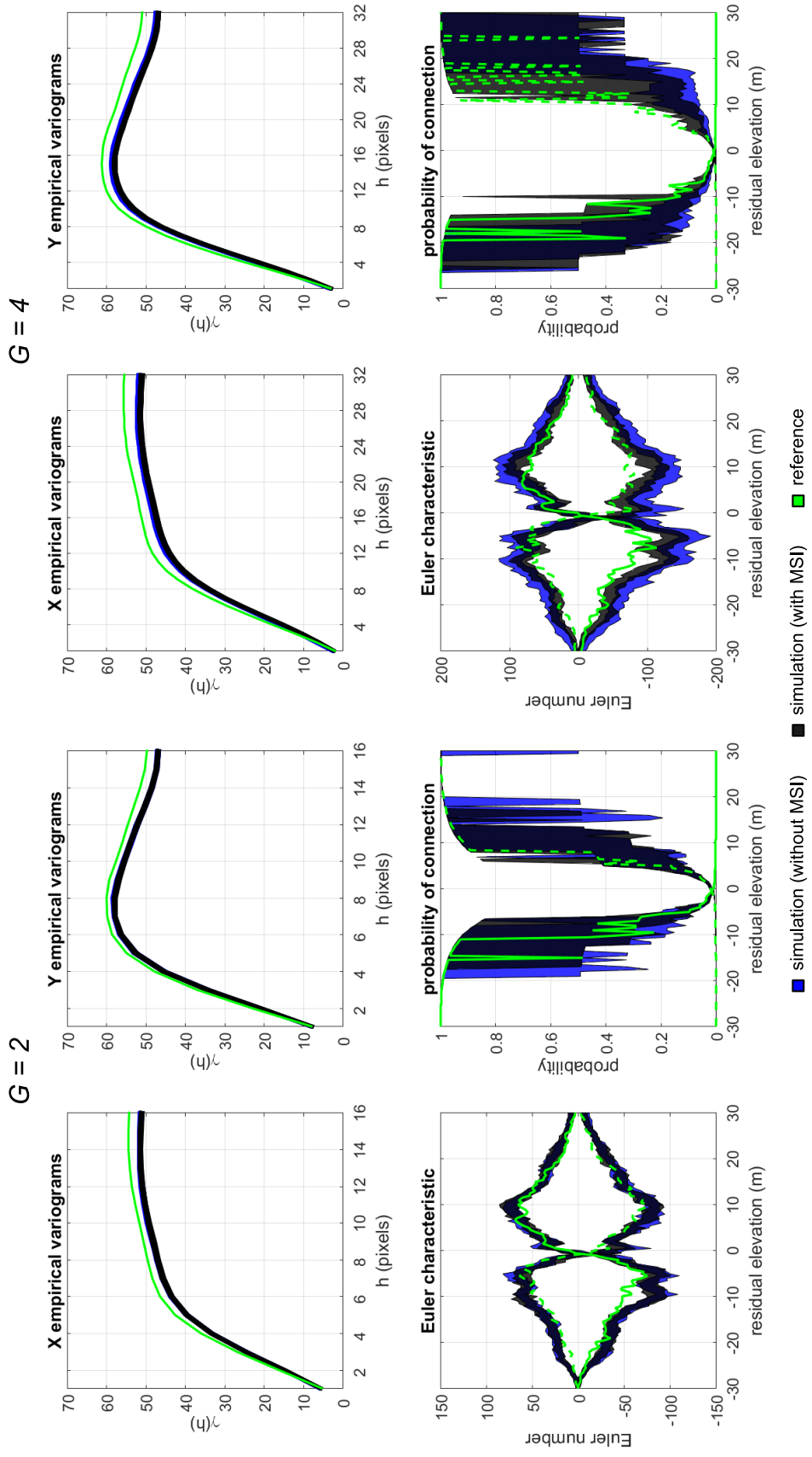
Figure A.20: The Colorado Plateau example structural statistics.
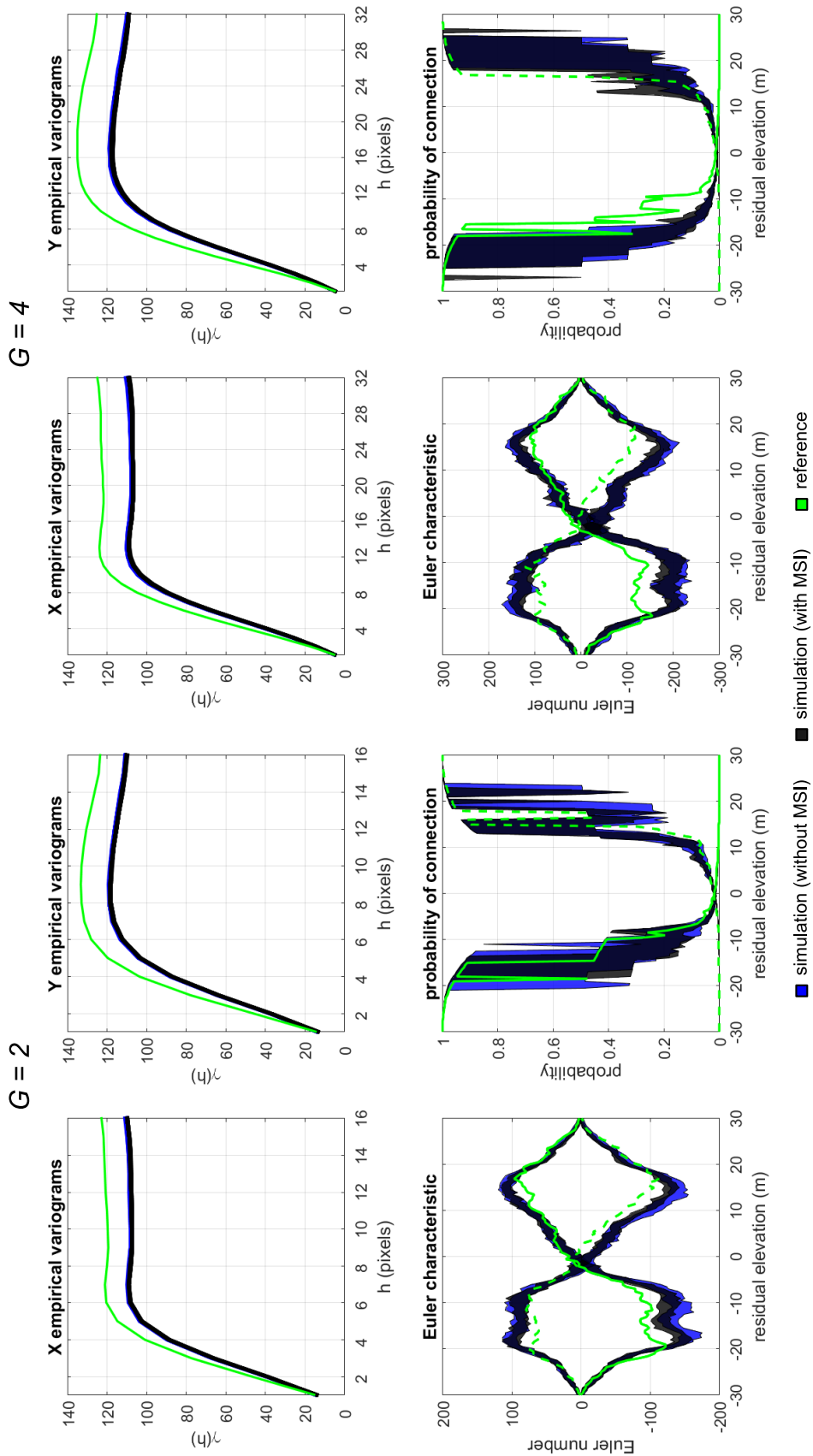
Figure A.21: The San Gabriel Mountains example structural statistics.
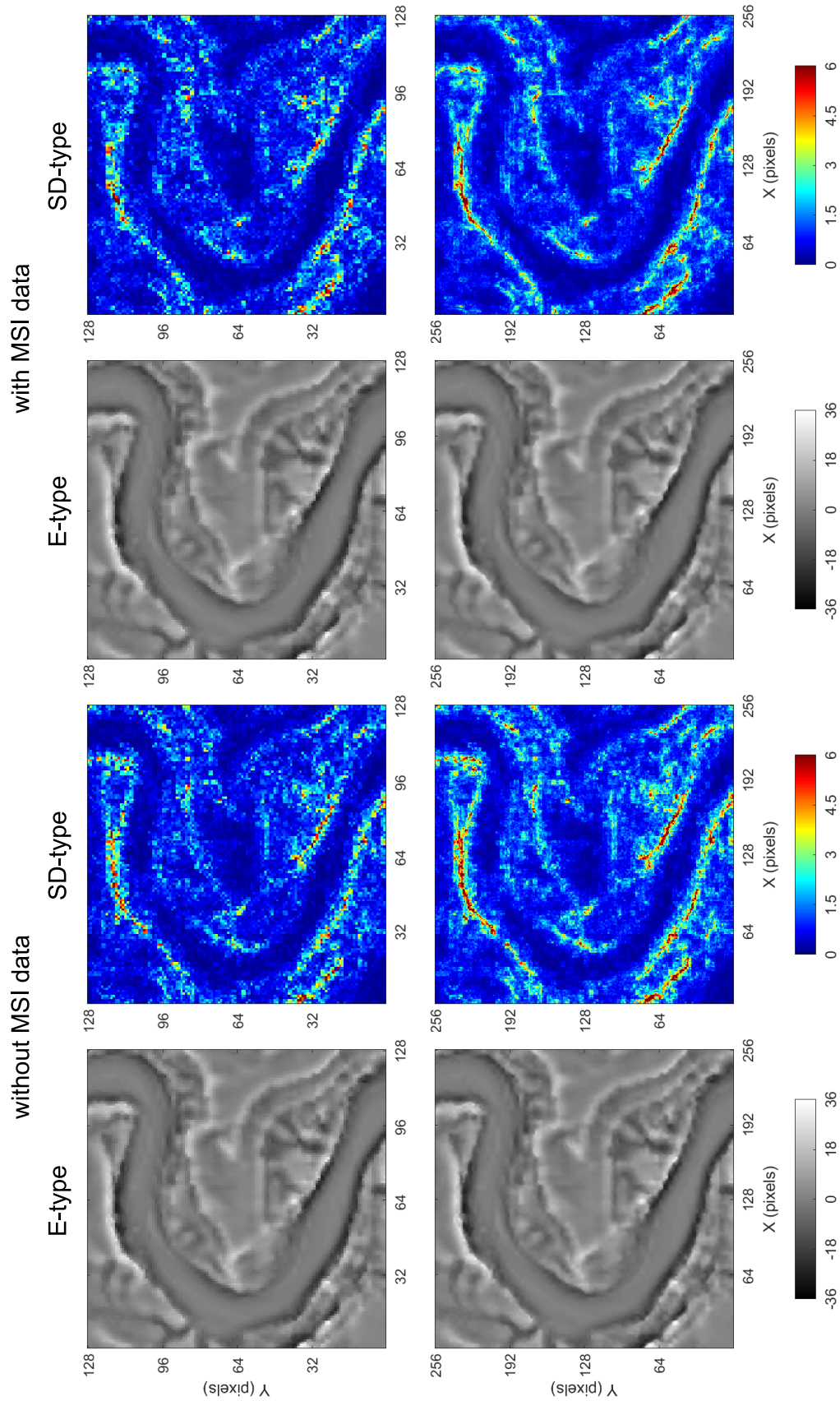
Figure A.22: Post-processing of simulated realizations from the Colorado Plateau example. Values are in residual elevation (in m).
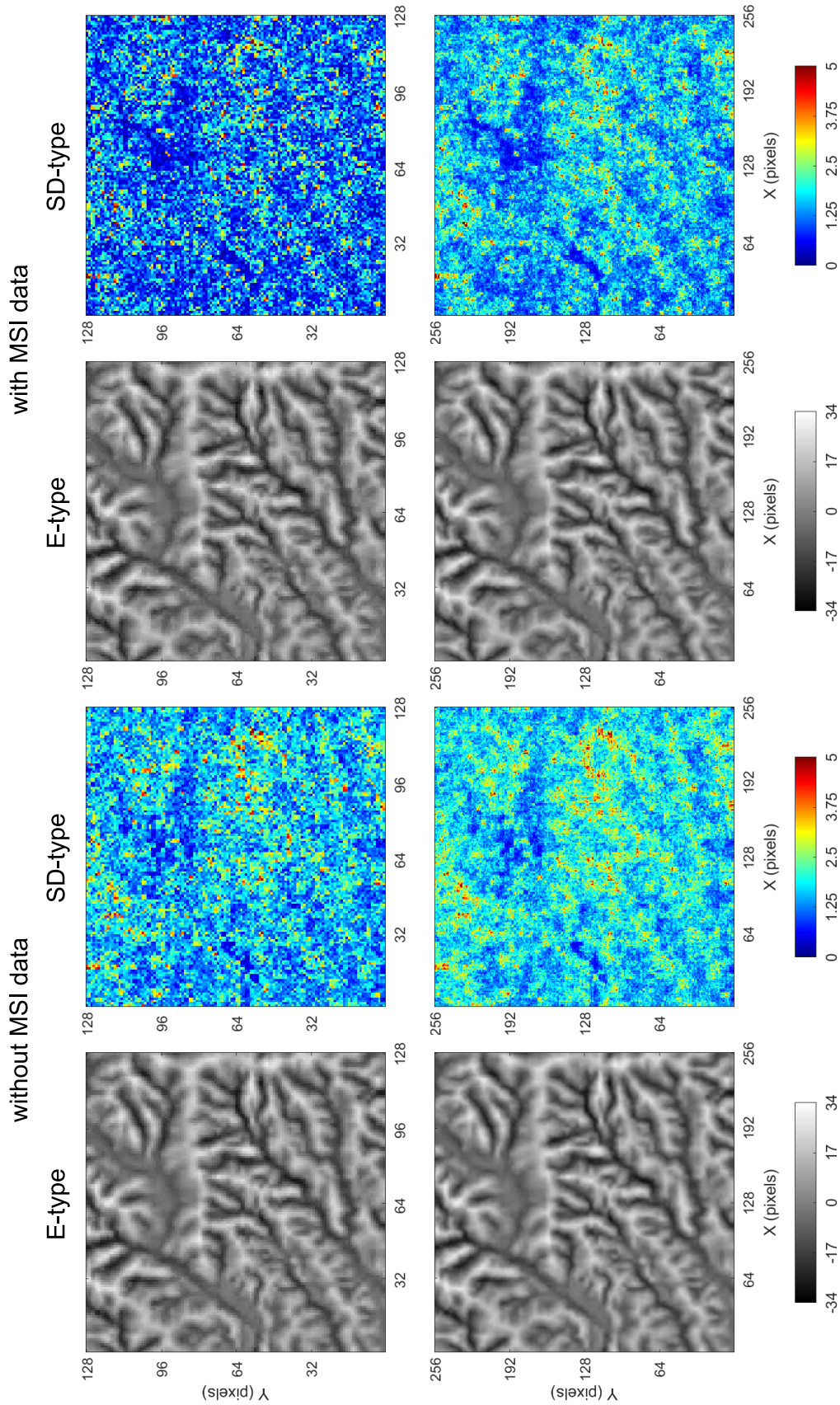
Figure A.23: Post-processing of simulated realizations from the San Gabriel Mountains example. Values are in residual elevation (in m).

Table A.10: SD-type statistics.

Example	Data	G	Mean	SD	Change (%)	
			(m)	(m)	Mean	SD
Colorado	DEM	2	0.88	0.85	–	–
Plateau		4	1.12	0.99	–	–
	DEM/MSI	2	0.86	0.80	-2.89	-5.35
		4	1.00	0.90	-10.63	-9.10
San Gabriel	DEM	2	1.66	0.70	–	–
Mountains		4	1.87	0.62	–	–
	DEM/MSI	2	1.27	0.80	-23.52	$+15.02$
		4	1.62	0.65	-13.24	$+5.18$

A.3.3   Conclusions

Results demonstrate that the presence of errors in the target DEMs can have a significant impact on the statistical and structural accuracy of the downscaling process. Measurement errors in the Central Lowlands example target DEM, in particular, heavily deteriorated the quality of the simulated realizations. Therefore, appropriate identification and subsequent treatment of these errors prior to downscaling is critical.

Bibliography

Allard, D., Comunian, A., and Renard, P. (2012). Probability aggregation methods in geoscience. *Mathematical Geosciences*, 44(5):545–581.

Arroyo, D. and Emery, X. (2015). Simulation of intrinsic random fields of order k with Gaussian generalized increments by Gibbs sampling. *Mathematical Geosciences*, 47(8):955–974.

Atkinson, P. (2005). Super-resolution target mapping from soft classified remotely sensed imagery. *Photogrammetric Engineering and Remote Sensing*, 71(7):839–846.

Atkinson, P., Pardo-Iguzquiza, E., and Chica-Olmo, M. (2008). Downscaling cokriging for super-resolution mapping of continua in remotely sensed images. *IEEE Transactions on Geoscience and Remote Sensing*, 46(2):573–580.

Atkinson, P. M. (2009). Issues of uncertainty in super-resolution mapping and their implications for the design of an inter-comparison study. *International Journal of Remote Sensing*, 30(20):5293–5308.

Atkinson, P. M. (2013). Downscaling in remote sensing. *International Journal of Applied Earth Observation and Geoinformation*, 22:106–114.

Baninajar, E., Sharghi, Y., and Mariethoz, G. (2019). MPS-APO: A rapid and automatic parameter optimizer for multiple-point geostatistics. *Stochastic Environmental Research and Risk Assessment*, 33(11-12):1969–1989.

Barling, R. D., Moore, I. D., and Grayson, R. B. (1994). A quasi-dynamic wetness index for characterizing the spatial distribution of zones of surface saturation and soil water content. *Water Resources Research*, 30(4):1029–1044.

Becker, J., Stewart, C., and Radke, R. J. (2009). LiDAR inpainting from a single image. In *2009 IEEE 12th International Conference on Computer Vision Workshops, ICCV Workshops*. IEEE.

Bergstra, J. and Bengio, Y. (2012). Random search for hyper-parameter optimization. *Journal of Machine Learning Research*, 13:281–305.

Bertero, M. and Boccacci, P. (1998). *Introduction to Inverse Problems in Imaging.* IOP Publishing Ltd.

Bianchi, L., Dorigo, M., Gambardella, L. M., and Gutjahr, W. J. (2009). A survey on metaheuristics for stochastic combinatorial optimization. *Natural Computing*, 8(2):239–287.

Bishop, M. P., James, L. A., Shroder, J. F., and Walsh, S. J. (2012). Geospatial technologies and digital geomorphological mapping: Concepts, issues and research. *Geomorphology*, 137(1):5–26.

Boisvert, J. B., Pyrcz, M. J., and Deutsch, C. V. (2010). Multiple point metrics to assess categorical variable models. *Natural Resources Research*, 19(3):165–175.

Boucher, A. (2009). Sub-pixel mapping of coarse satellite remote sensing images with stochastic simulations from training images. *Mathematical Geosciences*, 41(3):265–290.

Boucher, A. and Kyriakidis, P. C. (2007). Integrating fine scale information in super-resolution land-cover mapping. *Photogrammetric Engineering & Remote Sensing*, 73(8):913–921.

Brown, A. G., Carey, C., Erkens, G., Fuchs, M., Hoffmann, T., Macaire, J.-J., Moldenhauer, K.-M., and Walling, D. E. (2009). From sedimentary records to sediment budgets: Multiple approaches to catchment sediment flux. *Geomorphology*, 108(1-2):35–47.

Burt, P. and Adelson, E. (1983). The Laplacian pyramid as a compact image code. *IEEE Transactions on Communications*, 31(4):532–540.

Cavalli, M., Trevisani, S., Comiti, F., and Marchi, L. (2013). Geomorphometric assessment of spatial sediment connectivity in small Alpine catchments. *Geomorphology*, 188:31–41.

Cawley, G. and Talbot, N. (2010). On over-fitting in model selection and subsequent selection bias in performance evaluation. *Journal of Machine Learning Research*, 11:2079–2107.

Claesen, M. and Moor, B. D. (2015). Hyperparameter search in machine learning. Technical Report arXiv:1502.02127 [cs.LG], ArXiV.

Claessens, L., Heuvelink, G. B. M., Schoorl, J. M., and Veldkamp, A. (2005). DEM resolution effects on shallow landslide hazard and soil redistribution modelling. *Earth Surface Processes and Landforms*, 30(4):461–477.

Clemen, R. T. and Winkler, R. L. (1999). Combining probability distributions from experts in risk analysis. *Risk Analysis*, 19(2):187–203.

Coulthard, T. J. (2001). Landscape evolution models: A software review. *Hydrological Processes*, 15(1):165–173.

Dagasan, Y., Renard, P., Straubhaar, J., Erten, O., and Topal, E. (2018). Automatic parameter tuning of multiple-point statistical simulations for lateritic bauxite deposits. *Minerals*, 8(5):220.

de Carvalho, P. R. M., Rasera, L. G., Costa, J. F. C. L., Araújo, M. G. S., and Varella, L. E. S. (2019). Variogram modeling of broadband artifacts of a seafloor map for filtering with factorial kriging. *Journal of Applied Geophysics*, 161:92–104.

Deutsch, C. V. and Cockerham, P. W. (1994). Practical considerations in the application of simulated annealing to stochastic simulation. *Mathematical Geology*, 26(1):67–82.

Deutsch, C. V. and Wen, X. H. (2000). Integrating large-scale soft data by simulated annealing and probability constraints. *Mathematical Geology*, 32(1):49–67.

Dimitrakopoulos, R. (1990). Conditional simulation of intrinsic random functions of order k. *Mathematical Geology*, 22(3):361–380.

Dimitrakopoulos, R., Mustapha, H., and Gloaguen, E. (2010). High-order statistics of spatial random fields: Exploring spatial cumulants for modeling complex non-Gaussian and non-linear phenomena. *Mathematical Geosciences*, 42(1):65–99.

Doria, D. and Radke, R. J. (2012). Filling large holes in LiDAR data by inpainting depth gradients. In *2012 IEEE Computer Society Conference on Computer Vision and Pattern Recognition Workshops*. IEEE.

Du, Q., Younan, N. H., King, R., and Shah, V. P. (2007). On the performance evaluation of pan-sharpening techniques. *IEEE Geoscience and Remote Sensing Letters*, 4(4):518–522.

Farr, T. G., Rosen, P. A., Caro, E., Crippen, R., Duren, R., Hensley, S., Kobrick, M., Paller, M., Rodriguez, E., Roth, L., Seal, D., Shaffer, S., Shimada, J., Umland, J., Werner, M., Oskin, M., Burbank, D., and Alsdorf, D. (2007). The Shuttle Radar Topography Mission. *Reviews of Geophysics*, 45(2).

Feingersh, T., Ben-Dor, E., and Filin, S. (2010). Correction of reflectance anisotropy: A multi-sensor approach. *International Journal of Remote Sensing*, 31(1):49–74.

Geoscience Australia (2015). Digital Elevation Model (DEM) of Australia derived from LiDAR 5 Metre Grid. Geoscience Australia, Canberra.

Gilbert, L. E. (1989). Are topographic data sets fractal? *Pure and Applied Geophysics*, 131(1-2):241–254.

Goodchild, M. F. (2011). Scale in GIS: An overview. *Geomorphology*, 130(1–2):5–9.

Goovaerts, P. (1997). *Geostatistics for Natural Resources Evaluation*. Oxford University Press, New York.

Gorelick, N., Hancher, M., Dixon, M., Ilyushchenko, S., Thau, D., and Moore, R. (2017). Google Earth Engine: Planetary-scale geospatial analysis for everyone. *Remote Sensing of Environment*, 202:18–27.

Guardiano, F. B. and Srivastava, R. M. (1993). Multivariate geostatistics: Beyond bivariate moments. In *Quantitative Geology and Geostatistics*, pages 133–144. Springer Netherlands.

Hastie, T., Tibshirani, R., and Friedman, J. (2009). *The Elements of Statistical Learning*. Springer New York.

Hengl, T., Bajat, B., Blagojević, D., and Reuter, H. I. (2008). Geostatistical modeling of topography using auxiliary maps. *Computers & Geosciences*, 34(12):1886–1899.

Hengl, T. and Reuter, H., editors (2008). *Geomorphometry: Concepts, Software, Applications*, volume 33. Elsevier, Amsterdam.

Hoang, L., Mukundan, R., Moore, K. E. B., Owens, E. M., and Steenhuis, T. S. (2018). The effect of input data resolution and complexity on the uncertainty of hydrological predictions in a humid vegetated watershed. *Hydrology and Earth System Sciences*, 22(11):5947–5965.

Hoffimann, J., Scheidt, C., Barfod, A., and Caers, J. (2017). Stochastic simulation by image quilting of process-based geological models. *Computers & Geosciences*, 106:18–32.

Hügli, H. and Frei, W. (1983). 49(5).

Jarihani, A. A., Callow, J. N., McVicar, T. R., Niel, T. G. V., and Larsen, J. R. (2015). Satellite-derived digital elevation model (DEM) selection, preparation and correction for

hydrodynamic modelling in large, low-gradient and data-sparse catchments. *Journal of Hydrology*, 524:489–506.

Jha, S. K., Mariethoz, G., Evans, J. P., and McCabe, M. F. (2013). Demonstration of a geostatistical approach to physically consistent downscaling of climate modeling simulations. *Water Resources Research*, 49(1):245–259.

Journel, A. G. (1999). Markov models for cross-covariances. *Mathematical Geology*, 31(8):955–964.

Journel, A. G. (2002). Combining knowledge from diverse sources: An alternative to traditional data independence hypotheses. *Mathematical Geology*, 34(5):573–596.

Journel, A. G. and Deutsch, C. V. (1993). Entropy and spatial disorder. *Mathematical Geology*, 25(3):329–355.

Journel, A. G. and Huijbregts, C. J. (1978). *Mining Geostatistics*. Academic Press, New York.

Journel, A. G. and Rossi, M. E. (1989). When do we need a trend model in kriging? *Mathematical Geology*, 21(7):715–739.

Kasetkasem, T., Arora, M., and Varshney, P. (2005). Super-resolution land cover mapping using a Markov random field based approach. *Remote Sensing of Environment*, 96(3-4):302–314.

Keys, R. (1981). Cubic convolution interpolation for digital image processing. *IEEE Transactions on Acoustics, Speech, and Signal Processing*, 29(6):1153–1160.

Kienzle, S. (2003). The effect of DEM raster resolution on first order, second order and compound terrain derivatives. *Transactions in GIS*, 8(1):83–111.

Kirkpatrick, S., Gelatt, C. D., and Vecchi, M. P. (1983). Optimization by simulated annealing. *Science*, 220(4598):671–680.

Kolecka, N. and Kozak, J. (2014). Assessment of the accuracy of SRTM C- and X-band high mountain elevation data: A case study of the Polish Tatra mountains. *Pure and Applied Geophysics*, 171(6):897–912.

Kwatra, V., Schödl, A., Essa, I., Turk, G., and Bobick, A. (2003). Graphcut textures: Image and video synthesis using graph cuts. *ACM Transactions on Graphics*, 22(3):277–286.

Kyriakidis, P. C., Shortridge, A. M., and Goodchild, M. F. (1999). Geostatistics for conflation and accuracy assessment of digital elevation models. *International Journal of Geographical Information Science*, 13(7):677–707.

Kyriakidis, P. C. and Yoo, E.-H. (2005). Geostatistical prediction and simulation of point values from areal data. *Geographical Analysis*, 37(2):124–151.

Lamichhane, N. and Sharma, S. (2018). Effect of input data in hydraulic modeling for flood warning systems. *Hydrological Sciences Journal*, 63(6):938–956.

Lane, S., Richards, K., and Chandler, J. (1996). Discharge and sediment supply controls on erosion and deposition in a dynamic alluvial channel. *Geomorphology*, 15(1):1–15.

Lane, S. N., Bakker, M., Gabbud, C., Micheletti, N., and Saugy, J.-N. (2017). Sediment export, transient landscape response and catchment-scale connectivity following rapid climate warming and Alpine glacier recession. *Geomorphology*, 277:210–227.

Leitão, J. and de Sousa, L. (2018). Towards the optimal fusion of high-resolution digital elevation models for detailed urban flood assessment. *Journal of Hydrology*, 561:651–661.

Li, M., Qiu, X., Shen, J., Xu, J., Feng, B., He, Y., Shi, G., and Zhu, X. (2019). CFD simulation of the wind field in Jinjiang city using a building data generalization method. *Atmosphere*, 10(6):326.

Li, Z., Zhu, Q., and Gold, C. (2005). *Digital Terrain Modeling: Principles and Methodology*. CRC Press, Boca Raton FL.

Lindquist, M., Lange, E., and Kang, J. (2016). From 3D landscape visualization to environmental simulation: The contribution of sound to the perception of virtual environments. *Landscape and Urban Planning*, 148:216–231.

Liu, Y. (2006). Using the SNESIM program for multiple-point statistical simulation. *Computers & Geosciences*, 32(10):1544–1563.

Liu, Y. and Journel, A. G. (2009). A package for geostatistical integration of coarse and fine scale data. *Computers & Geosciences*, 35(3):527–547.

Mackey, S. D. and Bridge, J. S. (1992). A revised FORTRAN program to simulate alluvial stratigraphy. *Computers & Geosciences*, 18(2-3):119–181.

Maharaja, A. (2008). TiGenerator: Object-based training image generator. *Computers & Geosciences*, 34(12):1753–1761.

Mandelbrot, B. B. (1974). Intermittent turbulence in self-similar cascades: divergence of high moments and dimension of the carrier. *Journal of Fluid Mechanics*, 62(2):331–358.

Marcotte, D. (1996). Fast variogram computation with FFT. *Computers & Geosciences*, 22(10):1175–1186.

Mariethoz, G. and Caers, J. (2014). *Multiple-Point Geostatistics: Stochastic Modeling with Training Images*. John Wiley & Sons, Ltd.

Mariethoz, G., Renard, P., and Straubhaar, J. (2010). The direct sampling method to perform multiple-point geostatistical simulations. *Water Resources Research*, 46(11).

Mariethoz, G., Renard, P., and Straubhaar, J. (2011). Extrapolating the fractal characteristics of an image using scale-invariant multiple-point statistics. *Mathematical Geosciences*, 43(7):783–797.

McKay, M. D., Beckman, R. J., and Conover, W. J. (1979). A comparison of three methods for selecting values of input variables in the analysis of output from a computer code. *Technometrics*, 21(2):239–245.

McMaster, K. J. (2002). Effects of digital elevation model resolution on derived stream network positions. *Water Resources Research*, 38(4):13–1–13–8.

Meerschman, E., Pirot, G., Mariethoz, G., Straubhaar, J., Meirvenne, M. V., and Renard, P. (2013). A practical guide to performing multiple-point statistical simulations with the direct sampling algorithm. *Computers & Geosciences*, 52:307–324.

Melnikova, Y., Zunino, A., Lange, K., Cordua, K. S., and Mosegaard, K. (2015). History matching through a smooth formulation of multiple-point statistics. *Mathematical Geosciences*, 47(4):397–416.

Mertens, K. (2004). Sub-pixel mapping and sub-pixel sharpening using neural network predicted wavelet coefficients. *Remote Sensing of Environment*, 91(2):225–236.

Metropolis, N., Rosenbluth, A. W., Rosenbluth, M. N., Teller, A. H., and Teller, E. (1953). Equation of state calculations by fast computing machines. *The Journal of Chemical Physics*, 21(6):1087–1092.

Montgomery, D. R. and Dietrich, W. E. (1994). A physically based model for the topographic control on shallow landsliding. *Water Resources Research*, 30(4):1153–1171.

Mukherjee, S., Mukherjee, S., Garg, R. D., Bhardwaj, A., and Raju, P. L. N. (2013). Evaluation of topographic index in relation to terrain roughness and DEM grid spacing. *Journal of Earth System Science*, 122(3):869–886.

Mukul, M., Srivastava, V., Jade, S., and Mukul, M. (2017). Uncertainties in the Shuttle Radar Topography Mission (SRTM) heights: Insights from the Indian Himalaya and Peninsula. *Scientific Reports*, 7(1).

Nelson, A., Reuter, H., and Gessler, P. (2009). Chapter 3 DEM production methods and sources. In *Developments in Soil Science*, pages 65–85. Elsevier.

Nguyen, M., Atkinson, P., and Lewis, H. (2005). Super-resolution mapping using a Hopfield neural network with LIDAR data. *IEEE Geoscience and Remote Sensing Letters*, 2(3):366–370.

Nourani, Y. and Andresen, B. (1998). A comparison of simulated annealing cooling strategies. *Journal of Physics A: Mathematical and General*, 31(41):8373–8385.

Oriani, F., Ohana-Levi, N., Marra, F., Straubhaar, J., Mariethoz, G., Renard, P., Karnieli, A., and Morin, E. (2017). Simulating small-scale rainfall fields conditioned by weather state and elevation: A data-driven approach based on rainfall radar images. *Water Resources Research*, 53(10):8512–8532.

Pardo-Igúzquiza, E., Chica-Olmo, M., and Atkinson, P. M. (2006). Downscaling cokriging for image sharpening. *Remote Sensing of Environment*, 102(1-2):86–98.

Pardo-Igúzquiza, E., Rodríguez-Galiano, V., Chica-Olmo, M., and Atkinson, P. M. (2011). Image fusion by spatially adaptive filtering using downscaling cokriging. *ISPRS Journal of Photogrammetry and Remote Sensing*, 66(3):337–346.

Perron, J. T., Kirchner, J. W., and Dietrich, W. E. (2008). Spectral signatures of characteristic spatial scales and nonfractal structure in landscapes. *Journal of Geophysical Research*, 113(F4).

Pirot, G., Straubhaar, J., and Renard, P. (2014). Simulation of braided river elevation model time series with multiple-point statistics. *Geomorphology*, 214:148–156.

Pohjankukka, J., Pahikkala, T., Nevalainen, P., and Heikkonen, J. (2017). Estimating the prediction performance of spatial models via spatial k-fold cross validation. *International Journal of Geographical Information Science*, 31(10):2001–2019.

Porter, C., Morin, P., Howat, I., Noh, M.-J., Bates, B., Peterman, K., Keesey, S., Schlenk, M., Gardiner, J., Tomko, K., Willis, M., Kelleher, C., Cloutier, M., Husby, E., Foga, S., Nakamura, H., Platson, M., Wethington, Michael, J., Williamson, C., Bauer, G., Enos, J., Arnold, G., Kramer, W., Becker, P., Doshi, A., D'Souza, C., Cummens, P., Laurier, F., and Bojesen, M. (2018). ArcticDEM. Harvard Dataverse, V1.

Pouteau, R., Rambal, S., Ratte, J.-P., Gogé, F., Joffre, R., and Winkel, T. (2011). Downscaling MODIS-derived maps using GIS and boosted regression trees: The case of frost occurrence over the arid Andean highlands of Bolivia. *Remote Sensing of Environment*, 115(1):117–129.

Pratt, W. K. (1991). *Digital Image Processing*. John Wiley & Sons, New York.

Putri, A. R. D., Sidiropoulos, P., Muller, J.-P., Walter, S. H., and Michael, G. G. (2019). A new south polar digital terrain model of Mars from the high-resolution stereo camera (HRSC) onboard the ESA Mars Express. *Planetary and Space Science*, 174:43–55.

Pyrcz, M., Boisvert, J., and Deutsch, C. (2008). A library of training images for fluvial and deepwater reservoirs and associated code. *Computers & Geosciences*, 34(5):542–560.

Rasera, L. G., Gravey, M., Lane, S. N., and Mariethoz, G. (2020a). Correction to: Downscaling images with trends using multiple-point statistics simulation: An application to digital elevation models. *Mathematical Geosciences*, 52(2):189–189.

Rasera, L. G., Gravey, M., Lane, S. N., and Mariethoz, G. (2020b). Downscaling images with trends using multiple-point statistics simulation: An application to digital elevation models. *Mathematical Geosciences*, 52(2):145–187.

Rasera, L. G., Lane, S. N., and Mariethoz, G. (2020c). An automation framework for downscaling of digital elevation models with multiple-point statistics simulation. *Mathematical Geosciences*.

Ravalec, M. L., Noetinger, B., and Hu, L. Y. (2000). The FFT moving average (FFT-MA) generator: An efficient numerical method for generating and conditioning Gaussian simulations. *Mathematical Geology*, 32(6):701–723.

Remy, N., Boucher, A., and Wu, J. (2009). *Applied Geostatistics with SGeMS: A User's Guide*. Cambridge University Press.

Renard, P. and Allard, D. (2013). Connectivity metrics for subsurface flow and transport. *Advances in Water Resources*, 51:168–196.

Rubin, D. B. (1981). The Bayesian bootstrap. *The Annals of Statistics*, 9(1):130–134.

Schoorl, J. M., Sonneveld, M. P. W., and Veldkamp, A. (2000). Three-dimensional landscape process modelling: The effect of DEM resolution. *Earth Surface Processes and Landforms*, 25(9):1025–1034.

Sohrabi, M. M., Tonina, D., Benjankar, R., Kumar, M., Kormos, P., Marks, D., and Luce, C. (2019). On the role of spatial resolution on snow estimates using a process-based snow model across a range of climatology and elevation. *Hydrological Processes*, 33(8):1260–1275.

Spall, J. (1992). Multivariate stochastic approximation using a simultaneous perturbation gradient approximation. *IEEE Transactions on Automatic Control*, 37(3):332–341.

Stathopoulou, M. and Cartalis, C. (2009). Downscaling AVHRR land surface temperatures for improved surface urban heat island intensity estimation. *Remote Sensing of Environment*, 113(12):2592–2605.

Straubhaar, J., Renard, P., and Mariethoz, G. (2016). Conditioning multiple-point statistics simulations to block data. *Spatial Statistics*, 16:53–71.

Strebelle, S. (2002). Conditional simulation of complex geological structures using multiple-point statistics. *Mathematical Geology*, 34(1):1–21.

Sudmanns, M., Tiede, D., Augustin, H., and Lang, S. (2019). Assessing global Sentinel-2 coverage dynamics and data availability for operational Earth observation (EO) applications using the EO-Compass. *International Journal of Digital Earth*, pages 1–17.

Sugarbaker, L. J., Eldridge, D. F., Jason, A. L., Lukas, V., Saghy, D. L., Stoker, J. M., and Thunen, D. R. (2017). Status of the 3D Elevation Program, 2015: U.S. Geological Survey Open-File Report 2016–1196.

Szu, H. and Hartley, R. (1987). Fast simulated annealing. *Physics Letters A*, 122(3-4):157–162.

Tadono, T., Nagai, H., Ishida, H., Oda, F., Naito, S., Minakawa, K., and Iwamoto, H. (2016). Generation of the 30 m-mesh global digital surface model by ALOS PRISM. *ISPRS - International Archives of the Photogrammetry, Remote Sensing and Spatial Information Sciences*, XLI-B4:157–162.

Tang, Y., Zhang, J., Jing, L., and Li, H. (2015). Digital elevation data fusion using multiple-point geostatistical simulation. *IEEE Journal of Selected Topics in Applied Earth Observations and Remote Sensing*, 8(10):4922–4934.

Tatem, A. (2002). Super-resolution land cover pattern prediction using a Hopfield neural network. *Remote Sensing of Environment*, 79(1):1–14.

Thomas, C., Ranchin, T., Wald, L., and Chanussot, J. (2008). Synthesis of multispectral images to high spatial resolution: A critical review of fusion methods based on remote sensing physics. *IEEE Transactions on Geoscience and Remote Sensing*, 46(5):1301–1312.

Thornton, M. W., Atkinson, P. M., and Holland, D. A. (2006). Sub-pixel mapping of rural land cover objects from fine spatial resolution satellite sensor imagery using super-resolution pixel-swapping. *International Journal of Remote Sensing*, 27(3):473–491.

Tolpekin, V. and Stein, A. (2009). Quantification of the effects of land-cover-class spectral separability on the accuracy of Markov-random-field-based super-resolution mapping. *IEEE Transactions on Geoscience and Remote Sensing*, 47(9):3283–3297.

Tran, T. T. (1994). Improving variogram reproduction on dense simulation grids. *Computers & Geosciences*, 20(7-8):1161–1168.

Trevisani, S., Cavalli, M., and Marchi, L. (2012). Surface texture analysis of a high-resolution DTM: Interpreting an alpine basin. *Geomorphology*, 161-162:26–39.

Tsai, Y., Stow, D., Chen, H., Lewison, R., An, L., and Shi, L. (2018). Mapping vegetation and land use types in Fanjingshan National Nature Reserve using Google Earth Engine. *Remote Sensing*, 10(6):927.

Tucker, G. E. and Hancock, G. R. (2010). Modelling landscape evolution. *Earth Surface Processes and Landforms*, 35(1):28–50.

Vaze, J., Teng, J., and Spencer, G. (2010). Impact of DEM accuracy and resolution on topographic indices. *Environmental Modelling & Software*, 25(10):1086–1098.

Wang, Z., Bovik, A., Sheikh, H., and Simoncelli, E. (2004). Image quality assessment: From error visibility to structural similarity. *IEEE Transactions on Image Processing*, 13(4):600–612.

Wechsler, S. P. (2007). Uncertainties associated with digital elevation models for hydrologic applications: A review. *Hydrology and Earth System Sciences*, 11(4):1481–1500.

Wen, J., Liu, Q., Xiao, Q., Liu, Q., You, D., Hao, D., Wu, S., and Lin, X. (2018). Characterizing land surface anisotropic reflectance over rugged terrain: A review of concepts and recent developments. *Remote Sensing*, 10(3):370.

Wiederkehr, M. and Möri, A. (2013). SwissALTI3D: A new tool for geological mapping. *Bulletin fuer Angewandte Geologie*, 18(1):61–69.

Wilson, J. and Gallant, J. E., editors (2000). *Terrain Analysis: Principles and Applications.* John Wiley and Sons, New York.

Wilson, J. P. (2012). Digital terrain modeling. *Geomorphology*, 137(1):107–121.

Woodcock, C. E. and Strahler, A. H. (1987). The factor of scale in remote sensing. *Remote Sensing of Environment*, 21(3):311–332.

Yamazaki, D., Ikeshima, D., Tawatari, R., Yamaguchi, T., O'Loughlin, F., Neal, J. C., Sampson, C. C., Kanae, S., and Bates, P. D. (2017). A high-accuracy map of global terrain elevations. *Geophysical Research Letters*, 44(11):5844–5853.

Yokoya, N., Grohnfeldt, C., and Chanussot, J. (2017). Hyperspectral and multispectral data fusion: A comparative review of the recent literature. *IEEE Geoscience and Remote Sensing Magazine*, 5(2):29–56.

Zagayevskiy, Y. and Deutsch, C. V. (2015). Multivariate grid-free geostatistical simulation with point or block scale secondary data. *Stochastic Environmental Research and Risk Assessment*, 30(6):1613–1633.

Zhang, T., Switzer, P., and Journel, A. (2006). Filter-based classification of training image patterns for spatial simulation. *Mathematical Geology*, 38(1):63–80.

Zhang, W. and Montgomery, D. R. (1994). Digital elevation model grid size, landscape representation, and hydrologic simulations. *Water Resources Research*, 30(4):1019–1028.